



Poh, Ping Yi, Leslie (2019) *Experimental and numerical study of silicon nitride for powder injection moulding*. PhD thesis.

<https://theses.gla.ac.uk/41131/>

Copyright and moral rights for this work are retained by the author

A copy can be downloaded for personal non-commercial research or study, without prior permission or charge

This work cannot be reproduced or quoted extensively from without first obtaining permission in writing from the author

The content must not be changed in any way or sold commercially in any format or medium without the formal permission of the author

When referring to this work, full bibliographic details including the author, title, awarding institution and date of the thesis must be given

Enlighten: Theses

<https://theses.gla.ac.uk/>
research-enlighten@glasgow.ac.uk

Experimental and Numerical Study of Silicon Nitride for Powder Injection Moulding



University
of Glasgow

College of Science
& Engineering

By

Poh Ping Yi, Leslie

A THESIS SUBMITTED IN FULFILMENT FOR THE
DEGREE OF DOCTOR OF PHILOSOPHY

IN THE
SCHOOL OF ENGINEERING

April 2019

© Poh Ping Yi, Leslie

Abstract

The continued research interest in ceramic injection moulding originates from the pursue to develop new materials and improve mechanical properties. Mould filling simulation has provided the freedom to test out mould designs and new material numerically with minimal material wastage. Therefore, the use of numerical simulations is useful in the development of ceramic injection moulding. However, extensive material data are required to perform these numerical simulations and the results of which need to be validated for any meaningful conclusions to be made.

At present, the simulation of ceramic injection moulding requires extensive material input data of the powder-based feedstock. It is time consuming and costly to characterise a powder-based feedstock for the necessary thermomechanical properties for simulation. This restricts the use of numerical simulations when a new feedstock material or composition is being developed. Moreover, the phenomena of powder-binder separation that occurs during mould filling are not captured by commercial simulation. The defects caused by this phenomenon will affect the quality of the component and cannot be resolved in latter processes. This is the gap this research aims to fill. The objective of the work presented in this thesis is to develop a hybrid material data that can be used in simulating powder-binder separation observed during mould filling. The research work presented in this thesis is structured into three parts.

First, a hybrid material data of the powder-based feedstock is developed. The hybrid material data consists of a combination of estimated and experimental material data. A comparative study was conducted on experimental material properties of powder-polymer mixture found in literature and existing models that estimates elastic modulus, thermal conductivity, coefficient of thermal expansion and specific volume. The comparative study showed that the estimation models selected for this hybrid material data predicts the material properties better than existing models used in past studies. Experiments are conducted to measure the density, specific heat capacity, viscosity and particle size distribution of the silicon nitride feedstock developed in this research work and the elastic modulus, thermal conductivity, coefficient of thermal expansion and specific volume are estimated with the selected estimation models.

Second, powder distribution analysis methods are developed to measure the powder distribution within the injection moulded green bodies which will be used to validate the numerical simulations. The differential scanning calorimetry (DSC) and thermogravimetric analysis (TGA) are developed to measure the volume fraction of ceramic powder in the feedstock and green bodies. An empirical model is developed using the DSC test results and compared with existing rule-of-mixture model at predicting the volume fraction of silicon nitride powder in green bodies. The empirical model showed results closer to the nominal volume fraction of silicon nitride powder and lower variation in measurements at each point of the green body as compared to the rule-of-mixture model. Between the DSC and TGA methods, the TGA tests measured the closest volume fraction of silicon nitride powder to nominal volume fraction and lowest variation.

Third, a suspension balance model and a two-fluid model are developed to simulate the phenomena of powder-binder separation during mould filling of powder-based feedstock. The effects of overestimating elastic modulus, thermal conductivity and coefficient of thermal expansion on injection moulding numerical results are studied with the newly developed hybrid material data and existing hybrid material data. The filling and packing results from the simulation models were used to investigate the filling patterns of the simulation models and the powder distribution within the green body. The numerical results showed that segregation of powder-binder is more prominent in the regions close to the gate and rear of the green body. This is likewise seen in the experimental results from the powder distribution analysis of the injection moulded silicon nitride test-bar.

This research work contributed to a hybrid material data of a powder-based feedstock that can be used as material input data for powder injection moulding simulation. The powder distribution analysis method that is developed is able to measure the distribution of powder within injection moulded green bodies. Furthermore, injection moulding simulations developed are able to simulate the powder-binder separation in silicon nitride green bodies. By developing a hybrid material data that allows several material properties to be estimated and used for numerical simulation, it provides flexibility and reduces cost for numerical investigation of powder-based feedstock in injection moulding.

Keywords: ceramic injection moulding, silicon nitride, thermomechanical properties, powder-binder segregation, numerical simulation, computational fluid dynamic, powder-binder distribution study.

Table of Contents

Abstract	I
List of Tables	VII
List of Figures	IX
Acknowledgement	XIII
Author’s Declaration	XV
List of publications	XVI
Nomenclature	XVII
Abbreviations	XIX
Chapter 1. Introduction	1
1.1 Ceramic injection moulding process.....	2
1.1.1 Compounding	2
1.1.2 Injection moulding.....	3
1.1.3 Debinding	4
1.1.4 Sintering.....	5
1.2 Challenges faced in powder injection moulding process.....	6
1.3 Simulation programs for powder injection moulding.....	7
1.4 Improvements and developments to powder injection moulding process	9
1.5 Motivation and objectives of this research	10
1.6 Contributions of the thesis	11
1.7 Structure of the thesis.....	12
Chapter 2. Literature Review	15
2.1 Numerical simulation of powder injection moulding	16
2.1.1 Previous studies using two-fluid model.....	17
2.1.2 Previous studies using suspension balance model.....	18
2.2 Characterisation of thermomechanical properties of powder-based feedstock for injection moulding simulation	20

2.2.1	Density	21
2.2.2	Specific heat capacity	22
2.2.3	Viscosity	22
2.2.4	Particle size distribution	24
2.2.5	Elastic modulus.....	25
2.2.6	Thermal conductivity.....	25
2.2.7	Coefficient of thermal expansion.....	26
2.2.8	Specific volume	26
2.3	Theoretical models to predict thermomechanical properties of powder-based feedstock	27
2.4	Experimental validation for powder injection moulding simulation	30
2.4.1	Filling behaviour comparison	30
2.4.2	Powder distribution analysis.....	32
2.5	Summary	35
Chapter 3. Development of two hybrid material data of silicon nitride feedstock ...		36
3.1	Characterising silicon nitride feedstock thermomechanical properties	37
3.1.1	Density	38
3.1.2	Specific heat capacity	39
3.1.3	Viscosity	41
3.1.4	Particle size distribution	44
3.2	Modelling thermomechanical properties of powder-binder mixture	45
3.2.1	Elastic modulus.....	45
3.2.2	Thermal conductivity.....	52
3.2.3	Coefficient of thermal expansion.....	58
3.2.4	Specific Volume	62
3.3	Hybrid material data of silicon nitride feedstock for powder injection moulding simulation	62
3.3.1	Elastic modulus.....	64
3.3.2	Thermal conductivity.....	64

3.3.3	Coefficient of thermal expansion.....	67
3.3.4	Specific volume	68
3.4	Summary	70
Chapter 4.	Powder distribution study of the green bodies.....	71
4.1	Materials for powder distribution study.....	72
4.2	Powder volume fraction measurement using differential scanning calorimetry	73
4.2.1	Heat flow experimental results of binder system and silicon nitride feedstock.....	74
4.3	Powder volume fraction measurement using thermogravimetric analysis.....	76
4.3.1	Weight loss experimental results of binder system and silicon nitride feedstock.....	77
4.4	Powder distribution study using differential scanning calorimetry and thermogravimetric analysis.....	80
4.5	Summary	85
Chapter 5.	Numerical modelling of powder injection moulding of silicon nitride....	86
5.1	Numerical modelling of silicon nitride injection moulding with suspension balance model.....	87
5.1.1	Simulation principles for suspension balance model.....	88
5.1.2	Geometry and mesh	90
5.1.3	Material data	93
5.1.4	Process conditions	97
5.1.5	Computational conditions.....	100
5.1.6	Injection time, pressure, temperature and viscosity results from the filling stage	101
5.1.7	Temperature distribution, part weight, volumetric shrinkage, density and powder concentration results from the packing stage	105
5.1.8	Density results at the end of injection moulding process	109

5.2	Numerical modelling of silicon nitride injection moulding using two-fluid model	111
5.2.1	Simulation principles for two-fluid model	112
5.2.2	Geometry, mesh and boundary conditions	114
5.2.3	Material data	115
5.2.4	Results and discussions.....	116
5.3	Numerical results comparison and experimental validation	127
5.3.1	Filling patterns results of suspension balance models and two-fluid model.....	127
5.3.2	Powder distribution results of simulation models and thermogravimetric analysis.....	130
5.4	Summary	134
Chapter 6.	Conclusions and future work	136
6.1	Conclusions.....	136
6.1.1	Hybrid material data of thermomechanical properties of a silicon nitride feedstock.....	136
6.1.2	Powder distribution analysis method to study the distribution of silicon nitride powder in silicon nitride green bodies.....	137
6.1.3	Develop numerical simulations to simulate moulding process of silicon nitride ceramics.....	138
6.2	Future work.....	139
References	141

List of Tables

Table 1.1. Cause and consequences of defects.	6
Table 2.1. Material properties required for injection moulding simulation and their test methods.	21
Table 2.2. A summary of viscosity models.	23
Table 2.3. Two-domain Tait model.	27
Table 2.4. Summary of theoretical models used to estimate powder-polymer mixture [93].	28
Table 3.1. Composition of binder system and silicon nitride feedstock.	38
Table 3.2. Measured and predicted density of a binder system and silicon nitride feedstock.	38
Table 3.3. A summary of theoretical models to predict viscosity of powder-binder mixture.	41
Table 3.4. Cross-WLF coefficient values.	43
Table 3.5. Characteristic of the silicon nitride particle size.	44
Table 3.6. A summary of theoretical models to predict elastic modulus of powder-binder mixture.	46
Table 3.7 Einstein coefficient and maximum packing fraction [173], [174].	47
Table 3.8 Elastic modulus from experiments presented in the literature for powder-polymer mixture.	48
Table 3.9. The ratio of estimated elastic modulus using various models to experimental data of powder-polymer mixture.	52
Table 3.10. A summary of theoretical models to predict thermal conductivity of powder-polymer mixture.	53
Table 3.11. Thermal conductivity experimental data from literature of powder-polymer mixture.	53
Table 3.12. The ratio of estimated thermal conductivity from various theoretical models to experimental data of powder-polymer mixture.	57
Table 3.13. A summary of theoretical models to predict CTE of powder-polymer mixture.	58
Table 3.14. CTE experimental data from literature of powder-polymer mixture.	59

Table 3.15. The ratio of estimated CTE from various theoretical models to experimental data of powder-polymer mixture.....	61
Table 3.16. Summary of theoretical models and measurements for thermomechanical properties of silicon nitride feedstock.	63
Table 3.17. Estimated elastic modulus of silicon nitride feedstock.	64
Table 3.18. Variation in thermal conductivity of silicon nitride feedstock.	66
Table 3.19. Predicted CTE of silicon nitride feedstock at 185°C.	67
Table 3.20. Two-domain Tait model coefficient values.	69
Table 4.1. TGA results for binder system and silicon nitride feedstock.....	79
Table 4.2. Powder volume fraction in test-bar section based on ROM and EMP.	80
Table 4.3. Average TGA results for all the test-bar sections.	80
Table 4.4. Comparison between TGA and DSC.	84
Table 5.1. Summary of the significant of each material properties.	94
Table 5.2. Summary of thermomechanical properties of silicon nitride feedstock.	95
Table 5.3. Two-domain Tait model coefficient values.	97
Table 5.4. Cross-WLF coefficient values.	97
Table 5.5. Engel ES200/45 HLS injection moulding machine specification.....	98
Table 5.6. Screw specification used for feedstock melt analysis.....	99
Table 5.7. Injection moulding process parameters.....	100
Table 5.8. End of filling pressure results from SBM-NBV and SBM-V.....	103
Table 5.9. End of filling temperatures results from SBM-NBV and SBM-V.....	104
Table 5.10. End of filling viscosity results from SBM-NBV and SBM-V.....	105
Table 5.11. End of packing volumetric shrinkage results from SBM-NBV and SBM-V.	107
Table 5.12. Density results from SBM-NBV and SBM-V at the end of packing.....	108
Table 5.13. Powder concentration results from SBM-NBV and SBM-V.....	109
Table 5.14. Density results from SBM-NBV and SBM-V after cooling.	110
Table 5.15. Material properties of binder system and silicon nitride powder.....	116
Table 5.16. Powder concentration results from SBM-NBV, SBM-V and TFM.....	129

List of Figures

Figure 1.1. Ceramic injection moulding process.	2
Figure 1.2. Schematic diagram of injection moulding machine.	4
Figure 1.3. Workflow of developing the holistic approach to study and develop injection moulding of silicon nitride ceramics using mould filling simulations.....	13
Figure 2.1. Local shear rate gradients and powder movements [63].	19
Figure 3.1. (a) Binder system, (b) silicon nitride feedstock and (c) Scanning Electron Microscope (SEM) imaging of silicon nitride powder.	37
Figure 3.2. Specific heat capacity of binder system and silicon nitride feedstock as a function of temperature.	40
Figure 3.3. Predicted and experimental specific heat capacity of silicon nitride feedstock.	41
Figure 3.4. Comparison of predicted and measured viscosity of silicon nitride feedstock.	42
Figure 3.5. Viscosity of silicon nitride feedstock by experiments and Cross-WLF model.	43
Figure 3.6. (a) Powder particles detected by photo analysis of microscopic photos at 700 times magnification and (b) particle size distribution of the powders.	44
Figure 3.7. Elastic modulus as a function of volume fraction of alumina filler and HDPE matrix. The axis on the right is meant for the Voigt model results.....	48
Figure 3.8. Elastic modulus as a function of volume fraction of HA filler and HDPE matrix. The axis on the right is meant for the Voigt model results.....	49
Figure 3.9. Elastic modulus as a function of volume fraction of silica filler and ester matrix.	49
Figure 3.10. Elastic modulus as a function of volume fraction of SCAN filler and epoxy matrix. The axis on the right is meant for the Voigt model results.....	50
Figure 3.11. Elastic modulus as a function of volume fraction of alumina filler and epoxy matrix. The axis on the right is meant for the Voigt model results.....	50
Figure 3.12. Elastic modulus as a function of volume fraction of silica filler and epoxy matrix.	51
Figure 3.13. Thermal conductivity as a function of volume fraction of SCAN filler and epoxy matrix. The axis on the right is meant for the Voigt model results.	54
Figure 3.14. Thermal conductivity as a function of volume fraction of alumina filler and epoxy matrix. The axis on the right is meant for the Voigt model results.	54

Figure 3.15. Thermal conductivity as a function of volume fraction of silica filler and epoxy matrix.....	55
Figure 3.16. Thermal conductivity as a function of volume fraction of AlN filler and PVDF matrix. The axis on the right is meant for the Voigt model results.....	55
Figure 3.17. Thermal conductivity as a function of volume fraction of silicon nitride filler and epoxy matrix. The axis on the right is meant for the Voigt model results.	56
Figure 3.18. Thermal conductivity as a function of volume fraction of silicon nitride filler and silicone rubber matrix. The axis on the right is meant for the Voigt model results.	56
Figure 3.19. CTE as a function of volume fraction of SCAN filler and epoxy matrix.....	59
Figure 3.20. CTE as a function of volume fraction of alumina filler and epoxy matrix.....	60
Figure 3.21. CTE as a function of volume fraction of silica filler and epoxy matrix.	60
Figure 3.22. CTE as a function of volume fraction of AlN filler and PVDF matrix.	61
Figure 3.23. Specific volume as a function of weight fraction of aluminium filler and polypropylene matrix.	62
Figure 3.24. Predicted thermal conductivity of silicon nitride feedstock using Nielsen model over a function of temperature and pressure.	65
Figure 3.25. Predicted thermal conductivity of silicon nitride feedstock using Voigt model over a function of temperature and pressure.	66
Figure 3.26. Experimental data of HDPE and predicted specific volume of silicon nitride feedstock.	69
Figure 4.1. (a) Silicon nitride test-bar and (b) schematic diagram for powder distribution study. (c) Microscopy imaging at area “1” and (d) at area “3”.....	72
Figure 4.2. Schematic diagram of differential scanning calorimetry set-up for heat of fusion measurement.	73
Figure 4.3. Average heat flow curves of binder system and silicon nitride feedstock.	75
Figure 4.4. Heat of fusion as a function of volume fraction of binder system in silicon nitride feedstock based on experimental data, model 1 (ROM) and model 2 (EMP).....	76
Figure. 4.5. Schematic diagram of thermogravimetric analysis set-up for weight loss measurements.....	77
Figure 4.6. (a) TG curves and (b) derivative TG curves of binder system and silicon nitride feedstock.	78
Figure 4.7. Volume fraction of powders in test-bar based on rule of mixture (ROM) a) Part A and b) Part B.....	81
Figure 4.8. Volume fraction of powders in Test-bar based on empirical model (EMP) a) Part A and b) Part B.	82
Figure. 4.9. Volume fraction of powders in test-bar from TGA a) Part A and b) Part B. ...	83

Figure 4.10. Volume fraction of powders in test-bar from TGA, rule of mixture model (ROM) and empirical model (EMP), a) Part A and b) Part B.....	84
Figure 5.1. Schematic approach for the numerical study of the silicon nitride injection moulding in Moldex3D.....	88
Figure 5.2. Geometries of cavity, runner and cooling channels with dimensions of test-bar, gate and runner.....	91
Figure 5.3. Test-bar meshed with tetrahedral element.....	92
Figure 5.4. (a) Dimension of cooling channel 1 and (b) dimension of cooling channel 2...	92
Figure 5.5. Four main geometries used injection moulding simulation in Moldex3D.....	93
Figure 5.6. Estimated thermal conductivity of silicon nitride feedstock using Nielsen model and Voigt model at 150 MPa.....	95
Figure 5.7. Estimated PVT data of silicon nitride feedstock using Voigt model.....	96
Figure 5.8. Schematic diagram of injection moulding machine showing hydraulic and injection pressure.....	98
Figure 5.9. Melt front time result from SBM-NBV and SBM-V numerical models.....	101
Figure 5.10. Injection pressure results from SBM-NBV and SBM-V numerical models at the end of filling.....	102
Figure 5.11. Temperature results from SBM-NBV and SBM-V numerical models at the end of filling.....	103
Figure 5.12. Viscosity results from SBM-NBV and SBM-V numerical models at the end of filling.....	104
Figure 5.13. Temperature distribution results from SBM-NBV and SBM-V at the end of packing.....	106
Figure 5.14. Volumetric shrinkage results from SBM-NBV and SBM-V numerical models at the end of packing.....	107
Figure 5.15. Density results from SBM-NBV and SBM-V numerical models at the end of packing.....	108
Figure 5.16. Powder concentration results from SBM-NBV and SBM-V numerical models at the end of packing.....	109
Figure 5.17. Density results from SBM-NBV and SBM-V numerical models after ejection and cooling.....	110
Figure 5.18. Systematic approach taken to develop simulation model for powder injection moulding of silicon nitride test-bar using ANSYS-CFX.....	111
Figure 5.19. Dimension of cavity (test-bar) with mesh with inlet and outlet boundaries..	114
Figure 5.20. Location as indicated by a red line (Line Y) in middle of XY-plane at 0.03 m on the Z-axis.....	117

Figure 5.21. Silicon nitride particle velocity on Line Y with reference to the <i>Y</i> -axis.	117
Figure 5.22. Shear strain rate of silicon nitride feedstock on Line Y with reference to the <i>Y</i> -axis.	118
Figure 5.23. Viscosity of silicon nitride feedstock on Line Y with reference to the <i>Y</i> -axis.	119
Figure 5.24. Drag coefficient of silicon nitride particles in binder on Line Y with reference to the <i>Y</i> -axis.....	120
Figure 5.25. Location as indicated by a red line (Line Z) on middle section of <i>YZ</i> -midplane at 0 m on the <i>X</i> -axis.....	120
Figure 5.26. (a) Silicon nitride particle velocity and (b) relative velocity on Line Z with reference to the <i>Z</i> -axis.....	121
Figure 5.27. Shear strain rate of silicon nitride feedstock on Line Z with reference to the <i>Z</i> -axis.	122
Figure 5.28. (a) Viscosity of silicon nitride feedstock and (b) drag coefficient of silicon nitride particles in binder on Line Z with reference to the <i>Z</i> -axis.....	123
Figure 5.29. Volume fraction of silicon nitride powder on Line Z with reference to the <i>Z</i> -axis.	124
Figure 5.30. Temperature distribution of silicon nitride feedstock on Line Z with reference to the <i>Z</i> -axis.....	124
Figure 5.31. (a) Shear strain rate (b) viscosity and (c) drag coefficient distribution on the <i>YZ</i> -plane at 0 m on the <i>X</i> -axis.	126
Figure 5.32. Filling patterns of SBM-NBV, SBM-V and TFM at $T = 0.01s, 0.02s$ and $0.03s$	128
Figure 5.33. Filling patterns of SBM-NBV, SBM-V and TFM at $T = 0.04s, 0.05s$ and $0.06s$	128
Figure 5.34. Silicon nitride volume fraction of SBM-NBV, SBM-V and TFM at the end of filling.	129
Figure 5.35. Schematic diagram for powder distribution study.....	130
Figure 5.36. Silicon nitride powder volume fraction results from the TGA for five test-bars.	131
Figure 5.37. Silicon nitride powder distribution results from filling stage of SBM-NBV, SBM-V and TFM.	132
Figure 5.38. Silicon nitride powder distribution results from packing stage of SBM-NBV and SBM-V and filling stage of TFM.	133
Figure 5.39. Silicon nitride powder distribution results from SBM-NBV, SBM-V, TFM and TGA.....	133

Acknowledgement

I would like to express my sincere appreciation to the following establishments and individuals who have contributed towards this project in terms of opportunity, support, advice, criticisms and ideas. They have been highly constructive and beneficial to the development of the project. First and foremost, I express my earnest thanks to Economic Development Board (EDB), DOU YEE Technologies Pte Ltd and University of Glasgow for having faith in me and providing me with the opportunity to embark on this journey and complete my PhD.

I owe my deepest gratitude to my first supervisor Dr Christian Della. Without his continuous enthusiasm, encouragement, advice and support this study would hardly have been completed. His guidance towards my writing and the challenges that have risen during the years have been essential to this research work. I am especially thankful for his support to think out of the box with when faced with a challenge during the research work. It led me to carry out experiments at the School of Chemistry, University of Glasgow, which has been extremely beneficial to my work.

I am extremely grateful to my second supervisor Dr Cindy Goh. Without her help the research trip to carry out experiments in School of Chemistry, University of Glasgow, would not have happened. Her advices throughout the years have been extremely valuable during the period of thesis writing. I am truly thankful for her continued support and encouragement.

I want to give thanks to Mr Lim Kian Hock, President of DOU YEE Technologies Pte Ltd. The provision of resources and financial support from the company towards the entire research project was vital to several publications. I also want to give special thanks to my industry supervisors Dr Ying Shengjie, and Mr Chen Li for their support at the company and the research work. I am very thankful to my fellow colleague and friend, Mr Alex, who shared an office with me for the most part of the four years spent at the company on my research work. He has been extremely helpful with getting me into the ropes of working in the company and guided me with the use of several equipment. Your continued support and friendship are appreciated and will always be remembered.

I want to extend my thanks to Professor Justin Hargreaves and Mr Andrew Monaghan for welcoming and assisting me with the experiments carried out at the Joseph Black Building, School of Chemistry. The experiments have provided me with valuable results towards the powder-binder distribution study. Professor Yun Li, for his help and support with the writing in the publications despite being in Glasgow. All my fellow postgrads and academic staff at University of Glasgow Singapore who had been with me since the start of my PhD journey.

My friends who have supported me throughout these years, having to listen to me talk about my research work on numerous occasions despite not understanding a single word that I was talking about. Loreta Matulevič, thank you for your support during the toughest time of my life despite the distance we must endure. Thank you for not giving up on us. My family, especially my parents for all you have sacrificed and given throughout my life. I love you all so much.

Author's Declaration

I declare that, except where explicit reference is made to the contribution of others, the substance of this thesis is a presentation of original work and I am the sole author. This work has not previously been presented for an award at University of Glasgow or any other institution. All sources are acknowledged in References.

List of publications

Selected portions of the work described herein have been published, in press or submitted elsewhere as listed below:

- L. Poh, Z. Idris, C. Della, S. Ying, C. Goh and Y. Li, “Modelling powder-binder segregation in powder injection moulding,” in IUMRS-ICEM, Singapore, 2016.
- L. Poh, C. Della, S. Ying, C. Goh and Y. Li, “Modelling powder distribution of powder injection moulded green bodies,” in ECerS, Budapest, 2017.
- L. Poh, C. Della, S. Ying, C. Goh and Y. Li, “Powder distribution on powder injection moulding of ceramic green compacts using thermogravimetric analysis and differential scanning calorimetry,” Powder Technology, 2018.
- L. Poh, C. Della, and C. Goh “Powder injection moulding simulation using hybrid material data of a powder-based feedstock.” (In preparation) to Ceramic International.

Nomenclature

a	: Pre-exponential factor
α	: Coefficient of thermal expansion
A_*	: Data fitted coefficients for Cross-WLF model
b_*	: Data fitted coefficients for two-domain Tait model
$B(T)$: Parameter for pressure sensitivity
C	: Two-domain Tait model constant
C_D	: Drag coefficient
C_p	: Specific heat capacity
C_{p_m}	: Specific heat capacity measured data for sapphire
C_{p_t}	: Specific heat capacity theoretical data for sapphire
d_p	: Mean diameter of particles
D	: Diameter
D_{bp}	: Total drag force
D_c	: Constant for specific heat capacity of aqueous mixture
D_*	: Data fitted coefficients for Cross-WLF model
E	: Elastic modulus
E_a	: Activation energy
ΔH	: Heat of fusion
k	: Thermal conductivity
k_E	: Einstein coefficient
$k(T)$: Temperature dependence
K	: Bulk modulus
KCp_{rev}	: Reversing specific heat capacity
L	: Length
L_*	: Data fitted coefficients for empirical model

m	: Flow consistency index
n	: Flow behaviour index
η	: Viscosity
η_o	: Zero-shear-rate viscosity
p	: Pressure
ρ	: Density
R	: Gas constant
Re_p	: Reynolds number of particles
T	: Temperature
T_t	: Transition temperature
τ^*	: Data fitted coefficients for Cross-WLF model
u	: Velocity
μ	: Shear Modulus
ν	: Poisson's ratio
v	: Specific volume
$v(T, p)$: Specific volume at a given temperature and pressure
$v_o(T)$: Specific volume at zero pressure
$vol. \%$: Volume fraction in percentage
w	: Weight fraction
$wt\%$: Weight fraction in percentage
ϕ	: Volume fraction
ϕ_m	: Maximum packing fraction
Ψ	: Concentration reduction term
$\dot{\gamma}$: Shear rate
λ	: Natural time

Abbreviations

<i>3D</i>	: Three-dimensional
<i>ASTM</i>	: American Society for Testing and Materials
<i>AlN</i>	: Aluminium nitride
<i>CAE</i>	: Computer-aided Engineering
<i>CIM</i>	: Ceramic injection moulding
<i>CTE</i>	: Coefficient of thermal expansion
<i>DSC</i>	: Differential scanning calorimetry
<i>EMP</i>	: Empirical model
<i>HA</i>	: Hydroxyapatite
<i>HDPE</i>	: High density polyethylene
<i>HMD-NBV</i>	: Nielsen-Blackburn-Voigt based hybrid material data
<i>HMD-V</i>	: Voigt based hybrid material data
<i>PIM</i>	: Powder injection moulding
<i>PVDF</i>	: Polyvinylidene fluoride
<i>PVT</i>	: Pressure-Volume-Temperature
<i>PW</i>	: Paraffin wax
<i>ROM</i>	: Rules-of-mixture
<i>SA</i>	: Stearic Acid
<i>SBM</i>	: Suspension balance model
<i>SBM-NBV</i>	: Suspension balance model using HMD-NBV
<i>SBM-V</i>	: Suspension balance model using HMD-V
<i>SCAN</i>	: Silicon-coated aluminium nitride
<i>TFM</i>	: Two-fluid model
<i>TGA</i>	: Thermogravimetric analysis
<i>WLF</i>	: Williams-Landel-Ferry

Chapter 1. Introduction

Manufacturing of advanced ceramic components have been challenging all around the globe, with the focus not just on the reduction of part size, but also determining advanced ceramic-based products that would help industries meet the future goals of energy efficiency and cutback on pollution [1]. Advanced ceramics can be manufactured using several fabrication processes including uniaxial-pressing [2], [3], hot pressing [4], [5], slip casting [6], [7], tape casting [8]–[10], gel casting [11], [12], additive manufacturing [13]–[16] and injection moulding [17]–[20]. These manufacturing methods each have their advantages and disadvantages as a shaping technique for advanced ceramics.

Depending on the complexity of the component shape, cost and volume of production, one method may be more suitable than another. Casting methods can produce near-net shape components, but usually have lower dimensional precision and production rates. Isostatic pressing methods are applicable in general only to low quantity production and the slow processing speed results in its high cost. Free forming of ceramics has demonstrated the capability towards geometry freedom, yet it still lacks quality control on the microstructure of the ceramic components.

Injection moulding of ceramic materials is achieved by mixing ceramic powders with polymers and using conventional plastic injection moulding machines. It is a combination of the design flexibility and productivity of plastic injection moulding and excellent material properties of ceramic material. The process is known as powder injection moulding (PIM) [21], [22] which comprises of ceramic injection moulding (CIM) and metal injection moulding (MIM). In 2014, the global market share of PIM components reached US\$2.0 billion and is expected to reach US\$3.1 billion in 2020 [23]. CIM is a net-shaping process that enables mass production of complex shaped components and it is an economic solution towards the progressively strict requirements for material and component designs. This has enabled CIM to meet the rising trends of component part size getting smaller [24] and expansion of the range of industries [25].

1.1 Ceramic injection moulding process

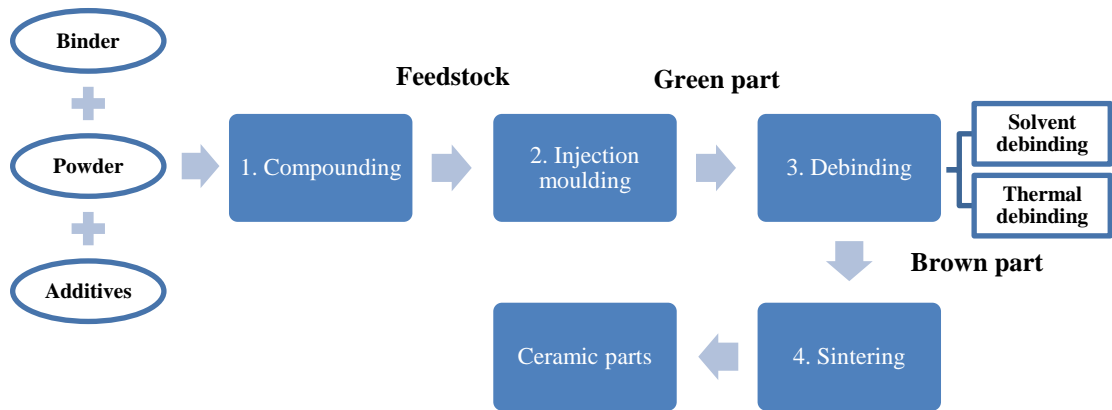


Figure 1.1. Ceramic injection moulding process.

Ceramic injection moulding is defined into four key process stages of compounding, injection moulding, debinding and sintering as depicted in Figure 1.1. It begins with the mixing of ceramic powders, sintering additives and a multi-component binder system at elevated temperatures to form a homogeneous mixture. The cooled mixture is granulated or pelletised into feedstock which are then used as raw materials for the injection moulding machines to be shaped into the required component shapes. At this stage the moulded components are known as green part. The binder system is removed from the green part through solvent and thermal debinding process which results in the brown part. The brown parts are then sintered for densification to achieve desired density, dimensions, mechanical properties and microstructures. The CIM process is an intricate and complex process, where process stages are interconnected to each other. Each process stage has a specific purpose and role to play in the whole CIM process which will be further discussed in this section.

1.1.1 Compounding

The choice of appropriate ceramic powder plays an important role in CIM. The properties of feedstock, final ceramic component and sintering behaviour are influenced by particle size distribution, particle shape, specific surface area, purity and crystalline phase of the powders. Even the slightest change in the particle shape, particle size distribution and the humidity in the air where the powder is kept will influence the properties of the feedstock [26]–[28]. The purpose of compounding is to achieve a homogeneous powder-binder mixture that is free from agglomerates. Agglomeration of particles would cause air pockets to be trapped in between particles thus reducing the solid packing of the green body. Particle agglomerates retained at the end of injection moulding act as fracture initiation sites during

the sintering process. Therefore, the uniform dispersion of powders in the binder system is necessary to achieve homogeneity which offers the feedstock suitable rheological behaviour for injection moulding.

A multi-component binder system in a ceramic feedstock would usually consist of backbone binders, surfactants and plasticisers [29]. The purpose of a binder system is to provide adequate fluidity to the feedstock, help improve wetting and deagglomeration of powder particles to ensure a homogeneous mixture and defect-free moulding process [19]. Known as the 'backbone' binders, they provide the necessary mechanical strength to green bodies for physical handling and shape retention during debinding. The addition of sintering additives is to assist in the densification of the brown part during sintering.

Powder content can range from 50 vol% to 65 vol% and a high powder volume fraction feedstock would entail good sintering capabilities at the expense of increased viscosity [21], [30]. A balance should be achieved between ensuring the good sintering ability while providing adequate viscosity to the feedstock to prevent injection moulding defects from arising during shape forming. The rheology of feedstock is determined by the volume fraction of solid powder, binders, plasticiser, additives and mixing conditions [26]. Increasing mixing speed would increase the mixture homogeneity, however at the same time, it raises the mixing temperature. When mixing temperature is too high, powder-binder separation may take place and this can result in an inhomogeneous feedstock [30]–[32]. An inhomogeneous feedstock will affect the mouldability of the material in the injection moulding stage. This results in added difficulties to the complicated mould filling process which hinders the fabrication of defect-free green parts.

1.1.2 Injection moulding

The process of ceramic injection moulding starts with the granulated or pelletised feedstock being fed into the barrel through the feed hopper. The feedstock is heated to slightly above melting point of the binder to achieve a viscosity that will allow fluid flow when pressure is applied. The viscous material is then forced into the mould cavity through the runner, with pressure and temperature being controlled to ensure the part is homogeneous. The mould temperature is usually at a temperature lower than the feedstock therefore the molten feedstock starts to solidify the moment it enters the cavity. The injection moulding process is essentially a race to fill the mould uniformly before the mixture becomes too viscous to flow. Injection moulded product can be removed once it is rigid enough to be handled

without causing any deformation. The schematic diagram of a conventional injection moulding machine is shown in Figure 1.2.

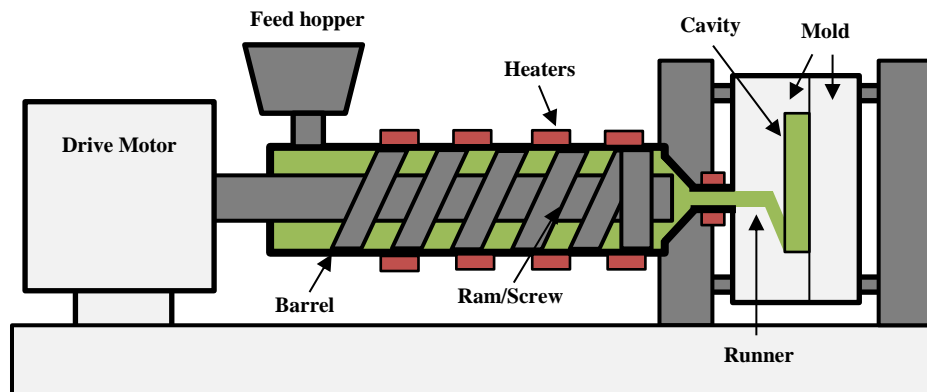


Figure 1.2. Schematic diagram of injection moulding machine.

The objective of injection moulding is to fill the mould completely and uniformly without leaving voids, cracks or other defects behind. The key factors to achieving this are material rheology, injection parameters and mould design [33]. Injection moulded parts are also known as green parts and they are usually fabricated oversized to account for dimensional shrinkages. Dimensional shrinkages occur due to the densification of bodies initiated by grain growth through sintering.

Flawed green parts and runner systems can be recycled and this reduces the cost of material and wastage. However, the breakdown of binders caused by repeated injection moulding process will increase the density of the recycled feedstock. This decreases the amount of shrinkage causing the sintered parts to be out of dimensional tolerance [34]. Due to the high binder content in the moulded green parts, post-moulding steps are required to remove the binders and promote densification of the ceramic parts.

1.1.3 Debinding

After injection moulding, the various components of the binder have to be removed from the green body prior to sintering. This process of binder removal is widely known as debinding. The extraction of wax-based binders involves a two-step debinding process with the first known as solvent debinding and the final step is known as thermal debinding [20], [35]. Solvent debinding involves immersing the green bodies in a liquid that dissolves the soluble binders while leaving at least one non-soluble backbone binder that holds the powder

particles together. The process leaves an open pore structure for the subsequent debinding process [21].

Thermal debinding involves slow volatilization of binder at elevated temperatures which is dependent on its vaporization characteristic. It is carried out in an oxidizing or non-oxidizing atmosphere at ambient pressure or under partial vacuum which has an effect on the rate of removal and carbon residue [36]. To avoid rapid evolution of the vapour that would cause fracture or distortion on the weak ceramic components the temperature is increased slowly. The cycle time of thermal debinding depends on the binder composition and the thickness of the component [36].

Complete removal of the binder without introducing any microstructural defects in the green body is desired in this process [26], [28]. Defects and residual contaminants such as carbon and inorganic ions have adverse effects on the grain growth during sintering and the properties of the ceramic components [28]. Residual carbon content increases with the molecular weight of the polymers used in the binder systems which degrades the mechanical, optical, thermal and electronic properties of the sintered components [36], [37]

1.1.4 Sintering

The purpose of sintering is the removal of any remaining binders and the densification of ceramic components. Sintering parameters such as temperatures and atmosphere are dependent on the type of ceramic powder used and the desired properties of the components [20]. This final stage of ceramic injection moulding process takes place at high temperatures ranging from 60% to 90% of the powder melting point [19]. The sintering temperature in the furnace is high enough to allow recrystallisation and grain growth to take place without melting the powders. Surface diffusion takes place between particles adjacent from each other and leads to the growth of necks between particles.

During this densification process the ceramic component shrinks and reduces in dimension. Therefore, the injection moulded green parts are designed to be larger than the required dimension to compensate for the shrinkage. The ceramic injection moulding process is complex and interconnected where there is room for errors and defects to occur. Precise process control and deep understanding of each stage are necessary to fabricate dense and defect-free ceramic components.

1.2 Challenges faced in powder injection moulding process

The ideal green part should have even distribution of powder across the component body. Visible surface defects should not be observed on the green part and warpage should not occur during post-moulding processes. Defects may occur in any stage of injection moulding and the defects found in early stages of the PIM process will lead to further complications in the latter stages [28]. Therefore, it is important to identify defects in the early stages of injection moulding and their causes. This is to prevent the defects from taking place during the PIM process.

Defects can be categorised into micro-defects or macro-defects [26]. Micro-defects are caused by agglomeration of powder particles and improper particle size distribution which can be resolved by using the right feedstock composition and compounding parameters. Macro-defects can be further divided into subcategories such as mould filling defects and solidification defects. The cause and consequences of some defects are summarised in Table 1.1.

Table 1.1. Cause and consequences of defects.

Cause	Consequences
Poor dispersion of powder in binder	Failure to disperse the powder particles during compounding will lead to mechanical flaws in green parts and warping in sintered parts [30], [33].
Exceeding critical solid loading	Lack of binder to fill the voids between particles may cause inhomogeneity in the feedstock which results in high viscosity and the inability to fill up mould cavity [33], [38].
Poor mould design	Mould geometry and gate position have large impact on the shrinkage behaviour of moulded parts during debinding and sintering. Anisotropic shrinkage causes bending or cracking due to the internal stresses developed during heated processes [39].
Poor injection parameters	Undesirable rheological behaviour during injection moulding leads to separation between powder and binder. This inhomogeneity in the green parts causes anisotropic shrinkage, deformation, warping and cracking during sintering [40]–[43]. Residual stress in green parts that is caused by unsuitable moulding temperature and high injection pressure result in cracking and shape distortion during heated processes [33], [44].
Unsuitable heating conditions	High debinding temperature or heating rate initiate rapid removal of binder components which cause swelling and cracking in the green parts [38].

Desirable process conditions used for compounding, injection moulding, debinding and sintering can be identified by analysing key attributes and verifying with final mechanical properties. There are general principles towards remedying defects and optimising mechanical properties for different feedstock materials or composition and these are often carried out based on the experience of mould operators [44]. Among the four-stage process of PIM, the injection moulding stage lacks a certain degree of freedom in implementing changes to the process. This is due to the fact that once the injection mould is made it is almost irreversible. There are very few changes that can be done to the mould to remedy the defects caused by bad design features. Some common moulding defects are splay marks, sink marks, voids, weld/meld lines, poor surface finish, air traps and burn marks. These undesirable features and defects are not repairable with the latter process and it impairs the quality of the components [26]. Poor mould designs make it harder for the operator to achieve ideal injection moulding parameters. Hence, commercial moulding software are used to design and simulate the mould filling process. This provides mould designers with an analytical tool to create and test new component shape in numerical simulation before fabricating the mould.

The mechanical aspect of mould filling in the PIM process consist of filling and packing the feedstock into the cavity. During this process of filling and packing, the injected material experiences a history of thermal and pressure change that induces thermal residual stresses and a change in mechanical structure [45]. Commercial simulations have been developed to simulate each stage of the mould filling process with the consideration of the material behaviour in order to approximate the quality of the green body. Studies on the mould filling stage using numerical models have shown that the quality of green compact is dependent on the injection moulding parameters such as injection pressure, holding pressure, temperature of the feedstock, mould temperature, filling time, cooling time, thermal and rheological properties of the powder-based feedstock [46]–[48]. This provides mould designers with the capabilities to study the effects of injection moulding parameters on resultant green part quality.

1.3 Simulation programs for powder injection moulding

Several commercial simulation tools for injection moulding have been developed and improved over the years to simulate the behaviour of the material as accurate as possible during mould filling. To aid the development of PIM, these simulation tools can be used to predict the characteristic of the green body or final product. The development and progress

of commercial software for injection moulding are essentially hinged on the scientific understanding of the injection moulding process as well as the state of Computer-Aid Design (CAD) and computers. During the initial works of injection moulding simulation, most of the numerical simulations were performed using Hele-Shaw approximation with two-dimensional [49]–[51], two-and-a-half-dimensional [52] models. However, the Hele-Shaw approximation is unable to simulate the fountain flow and the solutions are unrealistic at the edges of the mould. The advancement in CAD moving from surface and wireframe modelling to three-dimensional (3D) models and the development of more powerful computers allowed 3D modelling to be made possible. Eventually, numerical simulations of injection moulding transited to full 3D analysis [53]–[55] on 3D geometry that allow accurate representation of the material behaviour during the injection moulding process.

Several commercial simulation programs for injection moulding are 3D Timon, PIMSolver, Moldex3D, Moldflow and Sigmasoft. Initial commercial software developed for injection moulding were mainly used for polymeric materials but with the growing market share of powder injection moulding and the competition between commercial software to provide powder injection moulding simulation as an option. 3D Timon [56] and PIMSolver [57], [58] simulate powder-based feedstock as a polymeric material which does not consider the separation between powder and binder that may occur during mould filling. Hence, they are not able to provide analysis of the distribution of powder or segregation found in the green bodies. Some commercial simulation programs such as Moldex3D, Moldflow and Sigmasoft have developed the capabilities to simulate the separation between powder and binder through the means of powder concentration analysis.

Both Moldex3D [59], [60] and Moldflow employ the Suspension Balance Model (SBM) [61], [62] to simulate PIM while Sigmasoft [63], [64] employs the Diffusive Flux Model (DFM) [65]. Both models are continuum-based models where the particle phase is approximated as a pseudo-continuum. Although the DFM is able to capture the basic particle migration phenomena seen in particulate suspension, it is not based on solid physical principles but instead represented by semi-empirical laws to describe movement of particle [62]. Therefore, the SBM is seen as a more popular method to be used to simulate injection moulding of powder-based feedstock. The details of SBM will be further elaborate in Section 2.1.2 where the implementation of SBM in PIM will be reviewed and the simulation principles are detailed in Section 5.1.1. Since the implementation of SBM in Moldflow is more recent in 2017, the current version of Moldflow at Dou Yee Technologies does not include the capabilities for PIM simulation. Therefore, the Moldex3D is selected to simulate

the mould filling process of the silicon nitride feedstock. A compromise to the SBM in Moldex3D is that in order to reduce the computation resources of the numerical simulation, a decouple approach is taken where the moulding filling process is first solved as a single bulk suspension [66]. The resulting velocity field is then used to compute the powder/particle concentration using the SBM. This is also seen in the DFM employed by Sigmasoft [63].

Numerical results from the SBM and DFM essentially shows the variation in powder concentration based on the shear rate history. It does not show the evolution of the separation between the powder and binder during mould filling. The powder-based feedstock used in PIM essentially consists of two phases which are the binder (liquid phase) and powder (solid phase). If PIM were to be simulated in a multiphase simulation environment it would be considered as a particle-fluid flow. The Two-Fluid Model (TFM) has been established as a popular approach to describe particle-fluid flow [67]–[69] where the numerical treatment considers the fluid as a continuous phase and the particles as a dispersed solid/liquid phase. The TFM have been implemented by several studies [70]–[72] have found success in simulating the filling pattern and evolution powder-binder separation during mould filling.

1.4 Improvements and developments to powder injection moulding process

Optimising injection moulding parameters have traditionally been carried out by operators which is based on the experiences gained through multiple trial-and-error [73], [74]. These injection moulding parameters include mould temperature, barrel temperature, melt temperature, injection speed, injection pressure, injection time, fill/pack switchover, packing time, packing pressure, cooling time and clamping force. Injection moulding parameters are often interconnected to each other and changing one parameter to remedy a defect may result in other defects. This compromises the overall performance and renders the optimisation process to be counter effective. This can cause substantial material wastage during the development of a new feedstock material or composition.

Other methods of improvement include the use of statistical approach to study and improve the injection moulding process. Several researchers have been using optimisation models to optimise the quality of green part based on single or multiple process parameters. The Design of Experiments technique was used to optimise single process parameters such as powder variability, powder loading and injection pressure on the powder injection moulding process

[75]–[77]. Analysis of Variance and the Taguchi method was used to study injection moulding parameters and their effect on the impact toughness of the sintered part [78].

Optimisation tools such as genetic algorithm [79], [80] or artificial neural networks [81], [82] have also been used for optimising the injection moulding process for plastic materials as well. Optimisation tools are mainly used to refine the parameters or ensure consistent manufacturability of a developed process. In order to develop new ceramic material or composition, a different method have to be considered. The approach selected in this research thesis and its motivations are discussed in the following section.

1.5 Motivation and objectives of this research

Dou Yee Technologies (DYT) have been manufacturing metal and ceramic materials using powder injection moulding process for more than 20 years. It has a diverse range of products in electronics, telecommunication, medical device, semiconductor and automotive. Despite the success that DYT has had, it is always essential to stay competitive by developing new materials, processes, component geometries and improve the existing PIM process it has. For CIM, DYT have been running mass production with materials like alumina, zirconia and zirconia-toughened-alumina. DYT has interests to develop CIM process for silicon nitride and intents to add silicon nitride ceramics into its profile. The limited PIM feedstock material data in commercial simulation programs for injection moulding is a challenge for industries to simulate the PIM feedstock that they desire. Whenever a new powder-based feedstock is developed or the composition is changed, it needs to be characterised for the necessary material data before it can be used as inputs to the numerical simulation. This is both time consuming and costly to a company if there is a lack of testing equipment as the feedstock needs to be send for testing in external testing labs. The increases cost and time for the development of PIM feedstock limits the use of PIM simulation in industries. Having these motives in mind, this research work aims to develop a method that allows flexible manipulation of material and composition of the powder-based feedstock, which can be used the numerical simulation of mould filling.

The thesis is divided into three areas of focus (material data, experimental validation and numerical simulation) to establish numerical simulations of a silicon nitride feedstock. A silicon nitride feedstock will be developed and characterised for the required thermomechanical properties to be used as input parameters for numerical simulations. This is achieved by a hybrid material data that consist of estimated and experimental material

properties. Powder distribution analysis methods will be developed to measure the point to point silicon nitride volume fraction along the green bodies. The SBM and TFM will be developed to simulate the uneven distribution of silicon nitride powder caused by powder-binder separation and validated with the powder distribution results. Therefore, the three main objectives of this research are:

1. Develop a hybrid material data of the thermomechanical properties of a silicon nitride feedstock that is characterised by using both semi-empirical models and experimental data. Determine the material input parameters for numerical simulations using hybrid material data.
2. Develop powder distribution analysis method to study the distribution of silicon nitride powder in injection moulded silicon nitride green bodies. Conduct experiments to validate the numerical models developed.
3. Develop numerical models (SBM and TFM) to simulate injection moulding process of silicon nitride ceramics in order to study the powder distribution of silicon nitride powder in green bodies.

Through the objectives of this research work, the thesis focuses on providing a method to a better understanding of the various factors that affects the mould filling stage using PIM simulation and develop a method that provides flexibility in estimating various feedstock material and composition. The research work undertaken based on the scope are discussed in subsequent chapters.

1.6 Contributions of the thesis

The research work in this thesis offers a holistic and methodological approach to study and develop ceramic materials using powder injection moulding. The principal contributions of this thesis came from addressing the three main objectives of this research work as outlined in the previous section.

- Existing studies that employ semi-empirical models to characterise the thermomechanical properties of powder-based feedstock have been found to overestimate elastic modulus and thermal conductivity. Based on a comparative study, several estimation models were identified to be able to estimate elastic modulus and

thermal conductivity of powder-based feedstock better than existing models. The result of this study is the development of a hybrid material data that consist of estimated and experimental data that can be used in numerical simulation. Both money and time spent on testing the material properties can be reduced with the used of these estimation models.

- The thesis investigated the use of differential scanning calorimetry (DSC) and thermogravimetric analysis (TGA) to measure powder distribution in injection moulded ceramic green bodies. The study showed that the TGA measured the lowest variation in volume fraction of silicon nitride powder in green bodies as compared to the DSC. The work in this area has been published in Powder Technologies [83]. The experimental results from the study can be used to validate powder injection moulding simulations. This is the first instance where the DSC and TGA are used to measure the powder distribution within a ceramic green body.
- A numerical model was developed based on SBM using the hybrid material data to study the effects of overestimating elastic modulus and thermal conductivity. The numerical models were used to show the overestimation of elastic modulus and thermal conductivity affected the pressure-related, temperature-related and warpage results. A TFM was developed to simulate powder-binder separation in mould filling. Numerical results from the SBM and TFM provided a comparison between two different simulation methods being used for PIM which to the author's knowledge have not been done. Both the SBM and TFM were validated with the powder distribution results measured by the TGA.

1.7 Structure of the thesis

The thesis begins with Chapter 1, where the four stages of the ceramic injection moulding process are introduced with each stage being described in detail. Challenges faced in powder injection moulding and simulation programs for PIM are reviewed. Methods to improve and develop the PIM process were also discussed. The chapter ends with an outline of the motivations and objectives of this research work as well as the subject of the study.

Chapter 2 reviews the existing work that had been carried out by other research in three areas of study. The chapter is divided into three sections for each area, (a) numerical models for mould filling, (b) the characterisation methods for powder-based feedstock and (c) experimental validation methods for PIM simulation. Section 2.1 reviews the existing

numerical models used to simulate the mould filling of powder-based feedstock. Section 2.2 reviews the methods to characterise powder-based feedstock using experimental tests and Section 2.3 reviews the models used to predict the feedstock material data used for powder injection moulding simulations. Section 2.4 reviews the various experimental validation methods for PIM simulation. Figure 1.3 presents a workflow for Chapters 3 to 5 that are devoted to the three main objectives of this thesis with each chapter being represented by a different colour. The workflow presents the development hybrid material data of silicon nitride feedstock for PIM simulation.

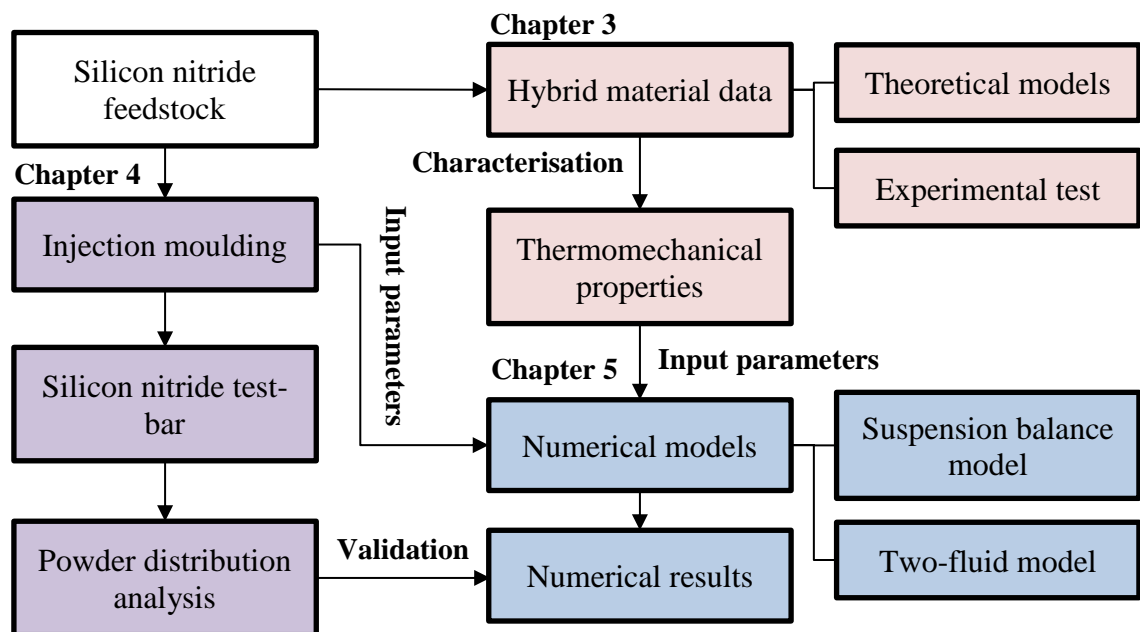


Figure 1.3. Workflow of developing the holistic approach to study and develop injection moulding of silicon nitride ceramics using mould filling simulations.

Chapter 3 presents the development of a hybrid material data of powder-based feedstock that can be used as material input data for mould filling simulations. The composition and compounding parameters for the silicon nitride feedstock developed for this research work is presented in Section 3.1. The silicon nitride feedstock was measured for thermomechanical properties such as density, specific heat capacity, viscosity and particle size distribution. Section 3.2 presents a comparative study between estimated material data using models and experimental data found in literature for powder-polymer mixture. Models were selected from the comparative study to estimate material properties such as elastic modulus, thermal conductivity, coefficient of thermal expansion and specific volume. In Section 3.3, two hybrid material data of the silicon nitride feedstock are developed. Both hybrid material data consist of material data measured in section 3.1. The first hybrid model (HMD-NBV) are based on the estimated material data using the models selected in Section

3.2. while the second hybrid material data (HMD-V) consist of estimated material data using the models used by other studies.

Chapter 4 presents the powder distribution analysis methods developed to analyse the volume fraction of silicon nitride powder in injection moulded green bodies. The methodologies and experimental results of the powder distribution analysis using DSC and TGA are presented. The experimental results are used to evaluate the distribution of silicon nitride in the injection moulded green bodies. Experimental results were able to illustrate the areas of high segregation between the powder and binder in the silicon nitride green parts. The results presented in this chapter have been published as a journal article in Powder Technologies.

In Chapter 5, the numerical models developed to simulate PIM of silicon nitride feedstock are presented. In Section 5.1, the SBM is developed to simulate the different stages of filling and packing in the injection moulding process. The two hybrid material data presented in Chapter 3 are used as material input parameters for the numerical models developed. The numerical results using the hybrid material data showed the sensitivity of overpredicted thermomechanical properties on the filling and packing results. In Section 5.2, the TFM is developed to simulate the powder-binder separation during mould filling of the silicon nitride feedstock. A drag coefficient equation from literature is developed in the model to consider the increase in drag when the particle moves into the flow field. In Section 5.3, the filling and packing results of all the numerical models developed in this research work are presented. Thereafter the powder distribution results from the filling and packing stages are presented with the experimental results from TGA. The numerical and experimental results point out that higher segregation of powder and binder are detected in the areas close to the gate and the rear of the green parts.

Chapter 6 concludes the thesis with a summary of the characterisation of ceramic feedstock using experimental and theoretical methods. Hybrid material data of ceramic feedstock can be characterised and used as material input data for PIM simulation. The powder distribution analysis of injection moulded green bodies using experimental method such as TGA and DSC can be developed to study the powder-binder separation in green bodies. Numerical models can be developed to simulate the powder-binder separation during mould filling. The thesis is closed with a discussion of the future work and direction.

Chapter 2. Literature Review

CIM, a variant of PIM, is an intricate process where the final product is determined by the careful consideration of each process stage. It was noted that the defects that arise during injection moulding pose a challenge to fabricating quality parts as these defects persist unaffected through the post-moulding process [28]. To achieve defect-free injection moulding process, it requires the feedstock to have desirable rheological behaviour, good mould designs and injection moulding parameters [33]. Traditionally the development work in PIM have been done based on the experience of mould designers and operators. However, due to the complexity of mould filling this approach becomes inefficient and sometimes costly. If the mould design is not optimised, it will cause high defect rate during manufacturing which results in material wastage. If a bad mould design is not repairable it may require the fabrication of a new mould to rectify the problem.

Therefore, the implementation of mould filling simulation into the development process of PIM in industries have become prevalent. A key benefit of commercial moulding software is that they allow mould designers to easily test out concepts using various feedstock material available in the database. In addition, it allows operators to numerically simulate the impact of injection moulding parameters on green parts. This provides the means to optimise multiple process parameters simultaneously and evaluate new component shape with minimal material waste. A key area of interest in numerical models of powder injection moulding is the ability to simulate uneven distribution of powder in the green bodies. This inhomogeneity in green parts is caused by the separation between powder and binder that occurs due to high shear rates during injection moulding [40], [84].

Conventional moulding simulation software are predominately for plastic injection moulding where users are given the flexibility to simulate different industry plastic feedstock, make quick changes to mould design and injection parameters and see the resultant impact of those changes numerically. However, the simulation of powder-based feedstock requires more in-depth understanding of material behaviour due to the fluid relationship between the powder and binder. Moreover, the material properties of powder-based feedstock have complex thermomechanical properties that needs to be characterised in order to fully represent the material behaviour in simulation models.

The thermomechanical properties of powder-based feedstock can be estimated using estimation models. These properties are used for mould filling simulations to study the defects caused by powder-binder separation. It is essential for results from these numerical models to be validated with test data to quantify the accuracy of the mould filling models. Therefore, a powder distribution analysis method that measures the powder content within a green body is crucial to the development works of PIM.

The principles of CIM are similar to metal injection moulding. At present, there is limited research work and publications on CIM. In this chapter, the literature survey will encompass research done on powder injection moulding which includes both metal and ceramic materials. This chapter is organised into four sections. Section 2.1 presents the several numerical models developed to simulate the separation between powder and binder during mould filling of powder-based feedstock. Section 2.2 provides a review on the thermomechanical properties of the feedstock required for numerical simulation. The section includes the experimental methods used to characterise each material properties and their significance to the PIM process. Section 2.3 introduces models used by existing research to predict the thermomechanical properties mentioned in Section 2.2. A review on the accuracy of using predicted thermomechanical properties in numerical simulation of mould filling is also presented. Finally, Section 2.4 reviews the experimental techniques used to validate mould filling numerical models. It focuses on the validation of powder distribution measurement techniques.

2.1 Numerical simulation of powder injection moulding

Powder-based feedstock used in PIM consists of two phases which are binder and powder. The binder undergoes a phase change from solid to liquid when temperatures are elevated past its transition temperature during injection moulding. In contrast, the powder remains solid throughout the whole heated process during injection moulding. Taking the differences in physical states between the binder and powder into consideration, the mould filling of powder-based feedstock is considered to be a particle-fluid flow system.

Generally, the Eulerian-Eulerian method and Eulerian-Lagrangian method have been used to model the particle-fluid flow system observed in the mould filling stage of powder injection moulding [54], [70]–[72], [85]–[87]. Multiphase flows are classified by the coupling between the particle movement and its surroundings. The appropriate numerical techniques are determined by the volume fraction of particles which decides the particle-

fluid interactions that governs the overall transport of particles. The continuous flow simulations are generally modelled in a Eulerian reference frame since it is a computationally efficient method for steady flows. The reference frame of the particle phase is classified as either a Eulerian or Lagrangian treatment. The Lagrangian method is considered as a discrete method since it assumes individual identities for each particle or a group of particles.

The main advantage of the Eulerian-Lagrangian method is the flexibility of modelling particles with the consideration of size distribution which is a condition present in any powder used in powder injection moulding. The method considers a finite number of discrete particles and interparticle forces are a result from particle-particle interactions. The key challenge faced in this method is the high computational cost required which restricts the method to be more suitable for low particle volume fraction modelling. In contrast, the Eulerian-Eulerian method is suitable for a wide range of particle volume fractions and have relatively low computational cost. However, the trade-off of the Eulerian-Eulerian method is that the particles are represented by a single particle size which is usually the mean particle size.

2.1.1 Previous studies using two-fluid model

The TFM has been established as a popular approach to describe particle-fluid flow [67]–[69]. The numerical treatment of a particle-fluid flow considers the fluid as a continuous phase and the particles as a dispersed solid/liquid phase. Past studies that have implemented a TFM to model the powder-based feedstock during mould filling are summarised in this section of the thesis.

Wang et al. [70] developed a TFM that consists of a pseudo-liquid phase for the powder and a liquid phase for the binder for micro-PIM mould filling using carbonyl iron feedstock. The authors model the rheological behaviour of the feedstock using the rule-of-mixture and the viscosity of each binder component. The temperature and shear rate dependence of each binder component is considered using the Arrhenius-power-law model. The simulation was used to study the effects of diameter size of the mould on the viscosity, temperature, shear strain rate, velocity and flow distance of the feedstock. However, there was no experimental data to validate their results.

Later, Yin et al. [71] developed a similar TFM for micro-PIM mould filling using carbonyl iron feedstock with the assumption that there was no interaction between the air and

feedstock melt. The model was validated with magnified view of the moulded gear and its morphology. They conclude that the different defects found in micro-PIM gears are due to the position of the gate and velocity field.

Fang et al. [72] developed a similar TFM that consist of a pseudo-liquid phase for the powder and a liquid phase for the binder for mould filling using 316L stainless steel feedstock. The viscosity of the binder was determined using the rule-of-mixture and the viscosity of each binder with the consideration of temperature and shear rate dependence using the Arrhenius-power-law model. The viscosity of the feedstock was measured using a capillary rheometer and the rule-of-mixture model was used to determine a viscosity value for the 316L stainless steel powder using the binder viscosity and experimental data of feedstock viscosity. The reason for doing so was because Fang et al. concluded that the study by Manninen [88] agreed with this principle. However, Manninen [88] concluded that the rule of mixture should not be taken as the definition of the mixture viscosity that has solid particles and suggested that in a TFM the continuous fluid phase should be modelled with the mixture viscosity. The TFM developed by Fang et al. [72] was used to study the powder distribution, temperature, viscosity, shear strain rate, velocity and drag coefficient at the midsection of the part along the lengthwise direction. The model was validated with powder volume fraction experimental results from CT scan images of the part that was characterised based on the local density.

2.1.2 Previous studies using suspension balance model

The hypothesis of SBM is that the driving forces behind powder-binder separation centres around the theory that local shear rate gradients forces the powder particles to leave regions of high shear rate and migrate to lower shear rate regions. The adhesion of the feedstock to the mould wall is similar to the no-slip condition and the shear rate observed close to the wall have higher peaks with low shear rate areas in the middle as seen in Figure 2.1. The non-uniform stress field creates a rotational force on the particles and introduces a change in flow direction of the particles. The SBM was developed to consider the suspension flow of rigid spherical particles in a Newtonian fluid [61], [89]. It describes the migration of particles in a non-colloidal suspension being driven by gradients in the particle-phase stress. The model is based on the interactions between the particles involving viscous, hydrodynamics and non-Brownian forces without external field besides gravity. This model has been implemented by several authors into Finite Volume Method (FVM) to model shear-induced migration of particles and fibres in powder injection moulding.

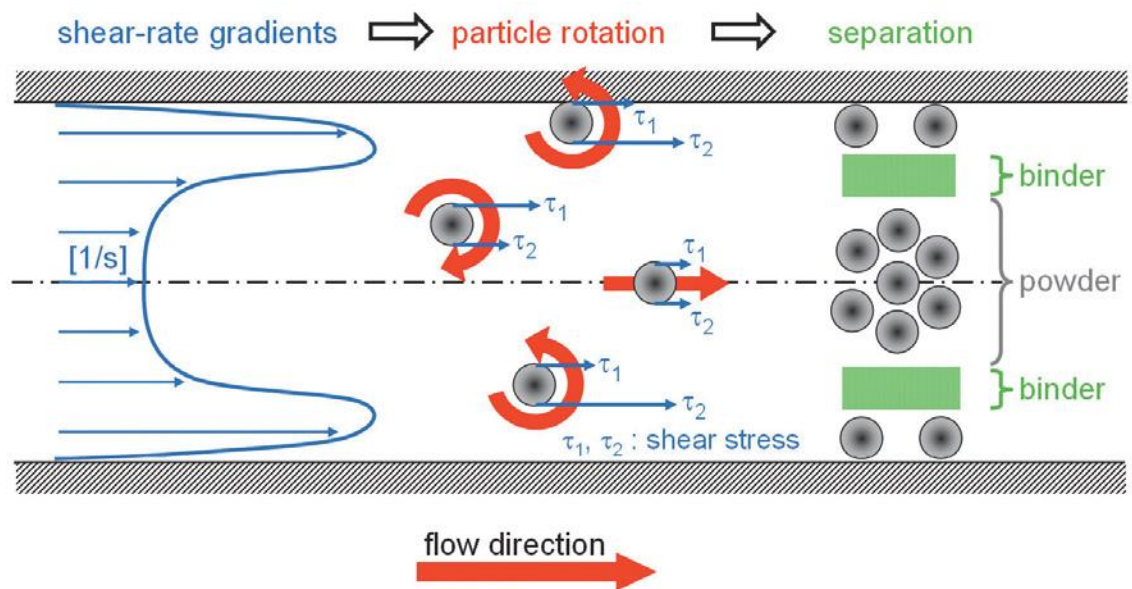


Figure 2.1. Local shear rate gradients and powder movements [63].

Jenni et al. [90] studied the powder distribution of tungsten-based feedstock with the SBM and validated the model with powder content distribution within the green body. The experimental results were measured using the differential scanning calorimetry and computed tomography. Mouldability tests were used to study the effects of nozzle temperature, mould temperature and injection speed on powder-binder separation. The tests showed that the influence of temperature on the rheology of the feedstock should be small.

Tseng [91] developed the SBM to study the shear-induced migration of particles for suspension rheology in geometries that induces expansion and contraction on the suspension fluid flow. The simulation models showed high concentration of powders in the corners when the fluid flow into the contraction region. Tseng studied the surface defects of an injection moulded Catamold 17-4 part together with the simulation models and showed that the black lines are related to low concentration of powder.

Tseng et al. [66] developed the SBM to study the migration behaviour of fibres during injection moulding to predict the fibre concentration within the moulded composite parts. The simulation models were validated with experimental data of fibre concentration located at multiple flow lengths. The results concluded that the core region and shell layers exhibit low flow orientation at high volume fractions and high flow orientation at low volume fractions.

Ilinca et al. [86], [87] developed a diffusive flux model integrated into a 3D injection moulding software developed by the research team to model the separation of dense suspension based on migration of particle. The suspension contained 50 vol% of spherical particles with 3178-micron diameter. The model showed good agreement with experimental data and previous numerical solution. However, the model does not consider slip condition and thermomechanical properties of fluid and particles. The diffusive flux model for particle migration is considered an alternative method to the SBM which has been widely implemented for powder injection moulding simulations [60], [66], [90]–[92].

2.2 Characterisation of thermomechanical properties of powder-based feedstock for injection moulding simulation

To simulate and study mould filling using numerical simulation the powder-based feedstock has to be characterised for a series of material properties. These material properties describe the mechanical and rheological behaviour of a ceramic or metal feedstock during mould filling. Depending on the numerical model that is being developed to simulate the mould filling process, the required material properties can vary with some models requiring more than the others. An example is where fibre characteristics such as orientation, aspect ratio and diameter are needed for injection moulding of fibre reinforced plastics [66]. The material properties of PIM feedstock that are required for PIM simulation can be characterised through experimental tests or predicted using theoretical models [93].

A summary of the material properties with the test methods and standards required for PIM simulation is summarised in Table 2.1. As the molten feedstock experiences a history of pressure and temperature change during mould filling, the whole process is non-isothermal. Therefore, the effects of pressure and temperature changes need to be considered when characterising several material properties that are temperature and pressure dependent. Each material property and the experimental methods to characterise them are presented in the rest of this section.

Table 2.1. Material properties required for injection moulding simulation and their test methods.

Material Property	Equipment/methods	Standards	Reference
Density	Gas pycnometer	ASTM D2638	[94]
	Archimedes' principle	ASTM D792	[95]
Specific heat capacity	Differential scanning calorimetry	ASTM E1269	[96]–[98]
	Modulated Differential Scanning Calorimetry	ASTM E2716	[99]
Viscosity	Capillary rheometer	ASTM D3835	[96]
Particle size distribution	Laser diffraction analysis	ISO 13320	[98]
Elastic modulus	Dynamic thermomechanical analysers	ASTM D4065	[95]
Thermal conductivity	Transient line source method	ASTM D5930	[97], [98]
	Laser flash method	ASTM E1461	[96]
Coefficient of thermal expansion (CTE)	Thermomechanical Analyzer	ASTM E831	[96]
Specific volume	High pressure dilatometer	ISO 17744	[100], [101]

2.2.1 Density

Density is an important attribute to the feedstock in powder injection moulding. Solid loading is the volumetric ratio of solid powder to the total volume of powder and binder. At low solid loading, the measured density typically follows the theoretical density line, but when it reaches critical value the measured density breaks away from the theoretical line [102]. Therefore, by measuring the feedstock density with incremental increase in solid loading, a critical solid loading can be determined. Critical solid loading is where the powder particles in the feedstock are packed as tightly together as possible with all the voids between particles filled with binder.

Measurement of density at various location in a batch of feedstock can be used to determine any inhomogeneity based on the variations of measure density [103]. This method can be used to assess how well the mixing procedures and binder composition is able to achieve homogeneous mixture. Density of the feedstock can be measured by either gas displacement method or water immersion method. The gas displacement method is conducted with the use of a gas pycnometer based on ASTM D2638 [94]. Pressure variation is used to determine volume variation and the density is determined with the mass of the sample. The water immersion method is based on the Archimedes' principle and adhering to ASTM D792 [95]. This method will not work for samples that have lower density than water such as the binder components.

2.2.2 Specific heat capacity

The specific heat capacity of a PIM feedstock is the amount of energy needed to heat up a unit mass of the feedstock for one degree. It also determines the amount of heat energy that can be stored during the heating process and other heat energy due to friction between the feedstock and the barrel [96]. Specific heat capacity of a PIM is dependent on temperature and the binders in the feedstock experience substantial change in specific heat capacity at the transition temperature. The PIM feedstock which usually contains multiple binder components would see multiple changes in specific heat capacity depending on each component's transition temperature. It is important to take note of each transition temperature when considering moulding temperatures to minimise the variation in specific heat capacity of the feedstock melt. The specific heat capacity can be measured using the differential scanning calorimetry (DSC) based on ASTM E1269 or modulated differential scanning calorimetry based on ASTM E2716 [96]–[99]. Measurements should be carried out with cooling rates that closely follow the temperature change experienced by the material in real moulding conditions [104].

2.2.3 Viscosity

Viscous behaviour of a powder-based feedstock is important during mould filling. The rheological behaviour of a powder-based feedstock is sensitive to temperature, pressure and powder loading. The polymers in the PIM feedstock exhibits two regimes of flow behaviour which are Newtonian and non-Newtonian. At low shear rates, it is a Newtonian behaviour where the shear stress is in a linear relationship to the shear rate which means that the viscosity will relatively remain constant and this is known as zero-viscosity. At high shear rates, it is a non-Newtonian behaviour with the viscosity decreasing with the increase in shear rate which is known as shear thinning. For powder-filled polymer like a PIM feedstock, the shear thinning region breaks up into less ordered structure at the critical shear rate and it dissipates more energy during flow due to particle agglomerating and increasing viscosity [105]. In a powder-based feedstock, a yield point can be observed in the region of low shear rate which is an indication of temporary network structure between the particles [106].

Viscosity data is fitted to a viscosity model to describe the rheological behaviour of the feedstock in an equation that can be used in injection moulding simulations. Table 2.2 is a summary of some viscosity models that are commonly used in injection moulding simulation [46], [54], [72], [73], [86], [87], [107]–[109]. The Power-Law model also known as the

Ostwald–de Waele equation, is a type of generalised Newtonian fluid. The power index "n" determines whether the flow behaviour is shear-thinning ($n < 1$) or shear-thickening ($n > 1$). The Power-Law model is popular because it offers the simplest approximation of shear-thinning behaviour, the model can represent the rheological behaviour of a material in high shear rate region, but not at low shear region [107].

Table 2.2. A summary of viscosity models.

Viscosity model	Equation of the model	Equation	Reference
Power-Law	$\eta = m\dot{\gamma}^{n-1}$ <p>where η is the viscosity, m is a flow consistency index, n is a flow behaviour index and $\dot{\gamma}$ is shear rate</p>	(2.1)	[107], [110]
Cross	$\eta = \frac{\eta_o}{1 + (\lambda\dot{\gamma})^{1-n}}$ <p>where η_o is the zero-shear-rate viscosity and λ is the natural time</p>	(2.2)	[111]
Arrhenius	$\eta(T) = \eta(\dot{\gamma})k(T)$	(2.3)	[107]
	$k(T) = ae^{\frac{E_a}{RT}}$	(2.4)	
	$\ln(k) = \ln(a) + \frac{E_a}{R} \left(\frac{1}{T} \right)$ <p>where, a is a pre-exponential factor, E_a is the activation energy for reaction, R is the universal gas constant, T is absolute temperature.</p>	(2.5)	
Cross-WFL	$\eta = \frac{\eta_o}{1 + \left(\frac{\eta_o \dot{\gamma}}{\tau^*} \right)^{1-n}}$	(2.6)	[110]
	$\eta_o = D_1 e^{\left[\frac{-A_1(T-T^*)}{A_2+(T-T^*)} \right]}$ <p>where D_1, A_1, T^*, n, τ^* are curve fitted coefficients (WLF) and A_2 is a constant, 52.6 K</p>	(2.7)	

The Cross model assumes that pseudo-plastic flow that correlates to the formation and breaking of structural linkages in the material [111]. It is commonly used to describe the low-shear-rate behaviour of the viscosity. However, both the Power-Law model and Cross model are not able to link the temperature dependence of the material to the viscosity. The flow during injection moulding is non-isothermal due to the temperature difference between the molten feedstock and mould temperature. In this case, the temperature dependence of the viscosity must be included along with the shear rate to represent the rheological behaviour of the feedstock accurately. In Table 2.2, the Arrhenius equation can be data fitted with viscosity models to determine the temperature sensitivity of the feedstock. A mouldability index has been proposed to consider parameters such as viscosity flow behaviour index and

activation energy [112]. This index can be used to determine the optimal powder loading of the feedstock [113]–[115].

The Cross-WLF model is the most common model used in commercial injection moulding simulation because it offers the best fit for a wide range of material viscosity data. It describes the dependency of viscosity on temperature, shear rate and pressure. The model requires experimental data over a range of temperature, shear rate to data fit for coefficients of the model. Rheological behaviour of a PIM feedstock can be measured with a capillary rheometer based on ASTM D3835 for shear rate region ranging from 1 s^{-1} to 10000 s^{-1} and a rotational rheometer based on ASTM D4440 for low shear rate region ranging from 0.01 s^{-1} to 100 s^{-1} [95], [96]. The viscosity of a feedstock is measured over a range of shear rates at multiple temperature points.

2.2.4 Particle size distribution

Particle size distribution plays a dominant role in the viscoelastic functions of highly filled powder-polymer mixture as well as its debinding and sintering behaviour. The size of powder particles affects the feedstock in terms of homogeneity, mouldability and debinding duration. Fine powders with particle size from 0.1 to $20 \mu\text{m}$ has a tendency towards particles agglomeration resulting in inhomogeneity, increased viscosity and reduced size of capillary paths which would slow the debinding process [19], [116]. However, the use of fine powders provides some benefits such as better surface finish, better microstructural shape retention, increased material strength and lowered injection temperature [117], [118]. Coarse powders with particle size up to $250 \mu\text{m}$ would see a reduction in debinding duration and cost, but have disadvantages such as large open pores after debinding, reduced sinterability due to smaller surface area of particle and undesirable rheological properties [119], [120].

Nanosized powders possess a larger surface contact area for interaction with binder and interparticle friction [121]. The larger surface contact area decreases the activation energy of the feedstock and has lower power law exponent of the viscous behaviour [116], [121]. It leads to the increase in flow resistance thus the viscosity of the feedstock [116]. Nanosized powder makes it harder for binder removal through debinding process, but improves the shape retention and densification process [122], [123]. One solution to this is to consider bimodal powder which is achieved by mixing nanosized and micro sized powder together. The bimodal feedstock has seen slight decrease in critical solid loading and viscosity in the feedstock [124], [125]. The injected green part from the bimodal feedstock showed better

sintering behaviour than feedstock containing only micro sized powders [124]. The particle size distribution of powders can be measured by laser diffraction analysis by adhering to ISO13320 [98].

2.2.5 Elastic modulus

The elastic modulus of feedstock is important as it determines the strength of injection moulded green bodies. It is important to achieve adequate strength in green bodies to withstand mechanical operations and reduce warpage caused by residual thermal stress during cooling [126]. High green strength will allow the green parts to withstand mechanical damage during the manufacturing process up to firing [127]. The elastic properties of the injection moulded green bodies essentially determine the mechanical strength of the green body. The elastic modulus of polymers or powder injection moulding feedstock can be measured using dynamic mechanical analysers based on ASTM D4065 [95].

2.2.6 Thermal conductivity

The metal or ceramic powders in feedstock raise the thermal conductivity of the mixture as they usually have relatively higher thermal conductivity than the binders. During mould filling, the high thermal conductivity of feedstock can lead to untimely freezing of the molten feedstock. This is caused by the sensitivity of PIM feedstock towards the temperature difference between the mould and melt flow as it begins to dissipate heat to its surroundings. The feedstock is subjected to high pressure and temperature differences during the injection moulding process. Therefore, it is important to characterise the temperature and pressure dependence of the material thermal conductivity.

As of now the thermal conductivity of the feedstock are characterised at pressures close to the actual injection moulding pressure. This is because currently the thermal conductivity models for material data in commercial injection moulding software only considers the dependence of temperature. However, it has been shown that the thermal conductivity of polymers is dependent on both temperature and pressure [128]–[131]. The thermal conductivity measurements were carried out in a high-pressure dilatometer with a thermal conductivity probe in the cylinder. In future, perhaps a temperature and pressure dependent model can be developed to represent the thermal conductivity of the PIM feedstock as well as a method of measurement. The thermal conductivity of PIM feedstock can be measured

using the transient line source method based on ASTM D5930 and laser flash method based on ASTM E1461 [96]–[98].

2.2.7 Coefficient of thermal expansion

Coefficient of thermal expansion (CTE) is a measurement of the fractional changes in size per degree change in temperature. During cooling, the huge difference in coefficient of thermal expansion between the binder and powders can cause residual thermal stresses and lead to warping and cracking in green bodies. With binders having higher CTE, this would lead to decrease in solid loading during heating as the binders expand in volume. The decrease in solid loading would result in the decrease in viscosity thus making it easier to mould. The coefficient of thermal expansion of PIM feedstock can be measured with a thermomechanical analyser based on ASTM E831 [96].

2.2.8 Specific volume

Specific volume of polymers and PIM feedstock are described by Pressure-Volume-Temperature (PVT) diagram as a function of pressure and temperature. The polymers in the feedstock undergoes a significant volumetric change over temperature and pressure. Therefore, characterising the PVT relationship of the feedstock is essential to determine the compressibility of material during packing phase and the resultant part shrinkage and warpage after ejection [100]. Polymers used as binders in powder injection moulding are usually classified between amorphous and semi-crystalline. The main difference between the two types of polymers are the arrangement of the molecular chains and how they behave with the change in temperature. Amorphous polymers have wider transition temperature range as compared to semi-crystalline polymers. Although having a sharp transition temperature makes semi-crystalline polymers difficult to thermoform, they can achieve more uniform melt consistency. This gives consistent dimensions and moulding performance of the injection moulded green bodies. Concerns with regards to using semi-crystalline polymers includes under-packing, which can cause sinks and voids to arise during moulding and incomplete crystallisation which results in warpage and uneven shrinkage.

The PVT experimental data of a feedstock is measured over a range of pressure at multiple temperature points. A specific volume model is used to data fit the experimental data measured by a high-pressure dilatometer to represent the behaviour of the property over a function of temperature and pressure. In Table 2.3, the two-domain Tait model [132], [133]

is widely used in injection moulding simulation packages for simulating mould filling. The two-domain Tait model considers separation expressions for solid and melt regions which are defined by the transition temperature. The transition temperature $T_t(p)$ is dependent on pressure. The PVT of PIM feedstock can be measured with a high-pressure dilatometer based on ISO 17744.

Table 2.3. Two-domain Tait model.

Region	Equation of the model	Equation
	$v(T, p) = v_o(T) \left[1 - C \ln \left(1 + \frac{p}{B(T)} \right) + v_t(T, p) \right]$	(2.8)
	<i>where $v(T, p)$ is the specific volume, $v_o(T)$ is the specific volume at zero pressure, T is temperature, p is pressure and C is a constant (0.0894), $B(T)$ is a parameter that accounts for the pressure sensitivity</i>	
	$v_o = b_{1m} + b_{2m}(T - b_5)$	(2.9)
Melt region ($T > T_t$),	$B(T) = b_{3m} e^{[-b_{4m}(T - b_5)]}$	(2.10)
	$v_t(T, p) = 0$	(2.11)
	<i>where $b_{1m}, b_{2m}, b_{3m}, b_{4m}$ and b_5 are data fitted coefficients</i>	
Solid region ($T < T_t$),	$v_o = b_{1s} + b_{2s}(T - b_5)$	(2.12)
	$B(T) = b_{3s} e^{[-b_{4s}(T - b_5)]}$	(2.13)
	$v_t(T, p) = b_7 e^{[b_8(T - b_5) - (b_9 p)]}$	(2.14)
	<i>where $b_{1s}, b_{2s}, b_{3s}, b_{4s}, b_5, b_7, b_8$ and b_9 are data fitted coefficients</i>	
	$T_t(p) = b_5 + b_6(p)$	(2.15)
	<i>where $T_t(p)$ is the transition temperature and b_6 is data fitted coefficient</i>	

2.3 Theoretical models to predict thermomechanical properties of powder-based feedstock

Other than characterising the powder-based feedstock using experiments, theoretical models for mixture property can be used to predict the thermomechanical properties. A material database system was developed to predict thermomechanical properties of powder-based feedstock [93], [134], [135]. Kate et al. [93] employed the method by first measuring each thermomechanical property of the aluminium nitride (AlN) feedstock at 0 and 0.52 volume fractions of AlN powder. Thereafter, the thermomechanical properties for the AlN feedstock at volume fractions from 0.48 to 0.51 are interpolated using the theoretical models. The

Chapter 2

theoretical models used by the material database are summarised in Table 2.4. The feedstock properties at different volume fractions were used in simulation models to understand the effects of material composition on moulding results such as part weight, peak injection pressure, freeze time and volumetric shrinkages. However, the simulation models were not validated.

Table 2.4. Summary of theoretical models used to estimate powder-polymer mixture [93].

Material Property	Theoretical model	Equation
Density	$\frac{1}{\rho_f} = \frac{w_b}{\rho_b} + \frac{w_p}{\rho_p}$	(2.16)
Specific Heat Capacity	$C_{p_f} = [C_{p_b}w_b + C_{p_p}w_p] \times [1 + D_c \times w_bw_p]$	(2.17)
Thermal Conductivity	$k_f = k_b\phi_b + k_p\phi_p$	(2.18)
CTE	$\alpha_f = \alpha_b\phi_b + \alpha_p\phi_p$	(2.19)
Elastic Modulus	$E_f = E_b\phi_b + E_p\phi_p$	(2.20)
Viscosity	$\eta_f = \eta_b \left(1 - \frac{\phi_p}{\phi_m}\right)^{-2.5\phi_m}$	(2.21)
Specific Volume	$v_f = [v_bw_b + v_pw_p]$	(2.22)

where ρ is density, w is weight fraction, C_p is specific heat capacity, D_c is a constant optimised for each system, k is thermal conductivity, ϕ is volume fraction, α is coefficient of thermal expansion, E is elastic modulus, η is viscosity, ϕ_m is the maximum packing fraction and v is specific volume. The subscripts f , b and p represent feedstock, binder and powder respectively.

The same material database system was validated by using experimental data of powder-polymer mixture found in literature [134]. The experimental data of powder-polymer mixture taken from literature included powders that consisted of a wide range of metal, ceramic, carbon nanotubes, glass beads and glass fibres. The range of polymers include paraffin wax, polypropylene, high density polyethylene (HDPE), low density polyethylene, cyanate ester, polyvinylidene fluoride and polybutadiene. The theoretical models were able to provide good prediction for the various material properties except for elastic modulus and shear modulus that showed moderate fitting.

The same material database system was used to develop the material properties of a bimodal AlN-based feedstock consisting of micro and nanosized powders [135]. It was performed by measuring the properties of the feedstock at 0 and 0.6 volume fractions of AlN powder. Thereafter, the thermomechanical properties for bimodal AlN feedstock at volume fractions

from 0.52 to 0.58 were interpolated using the theoretical models. The properties were used as inputs to numerical simulations of mould filling to investigate the effects of powder content on process parameters and defects evolution. The results suggest that the likelihood of defects occurring increase with increasing part complexity and powder volume fraction. However, the numerical simulation was not validated with any form of experiments.

The material database system is not a fully theoretical method that predicts thermomechanical properties using only the binder and powder properties. It is rather a semi-empirical method that uses measured thermomechanical properties of a certain volume fraction of powder to interpolate for properties with slight increments of volume fraction. From Table 2.4, Equation (2.18) to (2.20) and (2.22), are an upper bound rule-of-mixture model also known as the Voigt model [136]. The simplicity of the Voigt model makes it attractive as a theoretical model to predict material property.

A study was conducted using the Voigt model to predict the thermomechanical properties of a variety of ceramic feedstock that includes silicon carbide, AlN, silicon nitride, mullite composite, zirconia composite, alumina and barium titanate [137]. The study showed that the material database system was able to estimate density and specific volume well. The coefficient of determination for different ceramic feedstock was 0.96 and 0.97 for density and specific volume. However, the method faced problems with specific heat capacity, viscosity and thermal conductivity. Specific heat capacity, viscosity and thermal conductivity was 0.64, 0.61 and 0.23 respectively [137]. In the same research work, mould filling simulations were developed using experimental and estimated thermomechanical properties of AlN-based feedstock. The feedstock properties were estimated using the theoretical models summarised in Table 2.4. The numerical results showed that temperature related output parameters had errors ranging from 1% to 6% and pressure related output parameters were overestimated by a factor of 10. The study showed the effects of poorly predicted thermomechanical properties on simulation results.

A research study using the material databased was conducted to compare mould filling numerical results between a set of estimated thermomechanical properties and a hybrid material data of a lead-zirconate-titanate feedstock [138]. The hybrid material consists of estimated and experimental thermomechanical properties of a feedstock. In this study, the hybrid material data is made up of experimental viscosity data and estimated material properties for density, specific heat capacity, thermal conductivity and specific volume. The numerical results were compared with experimental results to accuracy of using

experimental viscosity data. From the numerical results, it was observed that volumetric shrinkage from numerical model using the hybrid material data had 0.5% variation from the experimental results while the numerical model using all estimated properties had 2% variation. The numerical model using the hybrid material data observed 5% variation in part weight from the experimental results while the numerical model using all estimated properties had 7% variation.

These studies showed that if theoretical models have to be used when characterising a powder-based feedstock, a combination of theoretical models and experimental data should be used. Material properties such as viscosity which is a parameter that changes over a range of temperature and shear rate affects the accuracy of mould filling numerical results. Therefore, the viscosity of a powder-based feedstock should be measured to provide accurate viscosity data to the simulation models. However, these studies did not address the overestimation of using the Voigt model to estimate elastic modulus, thermal conductivity and CTE.

2.4 Experimental validation for powder injection moulding simulation

The material data of a powder-based feedstock is usually characterised using experimental methods. These material properties are then used for mould filling simulations. Numerical models developed to simulate the PIM process require several assumptions and approximation. Therefore, the numerical results from these models must be validated with experimental results to come to any meaningful conclusion. Taking into consideration that if some of the material properties are estimated using theoretical models, there are added importance to validate these numerical models. There are several methods that have been used to validate the numerical results from mould filling. The methods for validation can be categorised into two main types which are comparing filling behaviour of the numerical models with the moulding process and powder distribution of the green body. These methods are reviewed in this section.

2.4.1 Filling behaviour comparison

Filling behaviour or pattern comparison are experimental methods that are set up to study and record the physical behaviour of the molten feedstock filling the injection mould during a standard process. One of these methods is the short shot method. The short shot method is

done by injecting insufficient feedstock into the mould cavity whereby the feedstock melts starts to enter the mould. The partially filled green part is removed from the mould and the next injection shot is done with small increments. This process is repeated until the cavity is completely filled. Short shot method allows visual determination of the flow path of the flow front. The method was developed to validate the flow patterns during the initial stages when numerical models were being developed to simulate mould filling [54], [139], [140]. Short shot method is also used by operators to determine the amount of material that needs to be injected into the mould to prevent damage to the mould caused by overpacking. It can be used to determine the uniformity of material filling in the mould especially for multi-cavity moulds as well [54].

Pressure sensors and thermocouples can be fitted into the cavity of the mould to study the evolution of pressure and temperature during the mould filling process [53], [141]. Pressure curves from the sensors are used to validate the viscosity models used in the numerical models and identify the main stages of the injection moulding process [141]. Bilovol et al. [142] designed an experimental mould with changeable gating locations, thermocouples and pressure transducers for the two cavities. Mould filling numerical models were developed in three commercial moulding software (ProCAST, Moldflow and C-Mold) to study the difference between the moulding software and their accuracy in simulating mould filling of BASF 316L stainless steel feedstock. The study compared numerical results from the commercial moulding software with in-cavity pressure and surface temperature measured by the sensors. Numerical results from C-Mold showed that despite being able to provide better agreements for pressure and temperature data with the experimental results had less accurate flow patterns compared to ProCAST and Moldflow. Short shot method was used to validate the flow patterns of the numerical models and it showed that the C-Mold provided less accurate flow patterns than Moldflow and ProCAST. Despite using a powder-based feedstock, the commercial moulding software used at that point of time were not able to consider the effects of powder in the simulations.

Ahn et al. [57] placed pressure transducers in three locations of the mould; near the gate, at the start and end of the cavity. A numerical model was developed in the integrated Computer-aided Engineering (CAE) package, PIM Solver, that considers the filling, packing and cooling stages of injection moulding. The numerical model took into consideration of slip behaviour in a particle filled material that assumes the existence of only pure binder in the thin slip layer. A comparison between the simulated and experimental results showed that

the numerical model with slip behaviour and coupled analysis stages provided more accurate results than the numerical model with no slip.

High speed camera can be used to observe the ceramic injection moulding process by fitting it to a mould with transparent glass windows [143]. Dvorak et al. [143] used a high speed charge-coupled device camera to capture images of jetting phenomena during moulding. Jetting occurs when injected material enters the mould at high speed, hits the end of the cavity and fills the mould from the back in a reverse filling sequence. The flow visualisation from high speed camera, pressure sensors and thermocouple can provide a direct visual comparison of injection moulded parts with numerical models [108]. It is a better method as compared to the short shot method which is hard to achieve repeatability of the experiments. The use of high-speed camera can be used to determine the injection parameters to prevent jetting and achieve complete filling.

However, all of these methods are mainly used to determine the right injection parameters to prevent defects caused by poor filling and for the development of fluid models. They are used to validate the flow patterns of the numerical models developed in simulation, but there are occasions where the experimental results disagree with the flow patterns. These experimental methods are not able to observe the separation between the powder and binder and they do not determine the resultant mechanical properties of the green bodies which is highly useful in determining the sintered part characteristic. A way to observe the separation between the powder and binder during moulding is through the study of powder distribution. Powder distribution can be determined by measuring density distribution or weight fraction of powder within the green body. Since the simulation of powder-binder separation phenomena during mould filling is the main focus of this numerical study, it is ideal to use powder distribution experiments to validate the numerical models developed in this research.

2.4.2 Powder distribution analysis

The powder distribution analysis of a green body can be determined by measuring the powder content at various locations of the green body. This can be achieved by either measuring the powder content directly or determined using mixing rules from measured densities. Petera [144] measured the average density of 28 points on a 120 mm by 10 mm by 4 mm injection moulded test-bar with the use of Archimedes' principle. The test-bar was divided into seven by four sections and density measurements were taken for each section. An alumina-based feedstock was used to fabricate the specimens and the experimental

results were used to determine the effects of holding pressure on the quality of the green bodies. Two holding pressure was used, 150 bar and 300 bar, and the results showed that the holding pressure of 300 bar gave the green body a more homogeneous powder distribution as compared to 150 bar. This method can be further developed by using the rule-of-mixture equation to determine the volume or weight fraction of powder in each section. However, errors in measurement may arise due to surface tension effects between the wire that suspends the specimen and the immersion fluid. Therefore, surfactant can be added to reduce the surface tension while only increasing the immersion fluid density by very small amounts.

Another method used to measure the density distribution in a green body is X-ray computed tomography (CT). X-ray CT is a non-destructive inspection method that provides cross-sectional images of a sample in multiple planes. Phillips and Lannutti [145] developed the method based on the Lambert-Beer law that relates the intensity of the X-ray beam crossing through a layer of material with the initial intensity and the linear attenuation coefficient. The linear attenuation coefficient is dependent on the mass attenuation coefficient and density.

Yang et al. [146], [147] used X-ray CT to analyse the density distribution of an injection moulded silicon carbide green body by first establishing a linear fitting equation that relates density to grey value of different materials measured using X-ray CT. The solid loading which is the volume fraction of powder in each section is determined using the density measurements of each component and the rule-of-mixture equation.

Wei et al. [72] used X-ray CT to analyse the powder distribution of injection moulded 316L stainless steel green bodies. The experimental results were used as reference data for a two-phase model for mould filling simulation. Powder volume fraction data were measured in the mid-section along the length to formulate the distribution of powder along the line. Numerical results that were collected in the same position showed similar results as the experimental data. The numerical model was used to study the effects of injection rate on powder-binder separation and filling patterns. The study concluded that high injection rate causes more separation between the powder and binder.

The use of X-ray CT as a non-destructive inspection method to analyse injection moulded green body is becoming an attractive technique. This is because the technique is able to create a virtual 3D volume showing the internal structures of the green body and characterise defects, porosity and inclusions [148]. However, a key limitation of X-ray CT is the

penetrating ability of the X-rays are relative to the density of the green body where high-energy X-rays are required for dense material such as metals and very small samples [148], [149]. If the material phases have large differences in X-ray absorption, it would result in CT scan images with poor contrast within the less absorptive phases [148]. Other major disadvantages of X-ray CT are the high capital and operating cost for instrumentation [150]–[152].

The DSC is an experimental method that has multiple use case for the powder injection moulding process and one of them is to measure the powder distribution in green body. Jenni et al. [90], [92], [153] used DSC to measure the powder distribution of tungsten in injection moulded green bodies. The enthalpy of fusion of the binder system and feedstock with multiple volume fraction of powder were first measured. Subsequently, experimental results showed that the enthalpy of fusion of the feedstock is dependent on the weight fraction of the binder system. Therefore, the volume fraction of powder at different locations of a green body can be determined using mixing rules and density of each components. Characterisation moulds were used to exaggerate the powder-binder separation during injection moulding. The powder distribution within the green bodies were measured to validate the numerical model developed based on the SBM. The investigation showed that reducing the temperature at the nozzle and mould can decrease the separation occurring during moulding. The DSC can be used to measure the heat flow data of the feedstock. This can be used to determine suitable mixing temperatures for mixing the powders and binders into feedstock [30]. The DSC is also useful in measuring the specific heat capacity of the feedstock which is used as material input data for mould filling simulations.

Another experimental method that has multiple use case for powder injection moulding process is the TGA. Demers et al. [103] measured the volume fraction of powder in injection moulded Inconel 718 superalloy green bodies using the pycnometer, DSC and TGA. The pycnometer was able to achieve an estimated variation of 0.5 vol.% in each measurement. However, the pycnometer requires significantly larger mass to perform each experiment, therefore making it only useful for determining the homogeneity in feedstock. The DSC method showed an estimated variation of 1 vol.% in the measurements which is well adapted to measure localised segregations effects in the green bodies. However, the method requires a calibration curve which is dependent on the feedstock formulation. Direct measurements of the weight fraction of powder were done using the TGA by measuring mass remaining after the binder burnout through controlled heating. The volume fraction of powder can be determined using the density of each component and the rule-of-mixture equation. The

method showed variations of 0.5 vol.% in the point to point measurements on the green body. The TGA was not dependent on a calibration curve based on feedstock formulation and requires small amounts of mass. From the study, the TGA was shown to be more suitable to determine segregation effect in injection moulded green bodies.

Demers et al. [154] did another study with the use of low pressure injection moulding of Inconel 718 feedstock. The results showed that the use of thermogravimetric analysis to measure the volume fraction of powder had variations of 0.25 vol% in measurements which was lower than before. The study also showed that the mixtures containing paraffin wax had the best trade-off between mouldability and segregation. The TGA allows the observation of binder weight loss in a controlled heated environment similar to thermal debinding. With the use of TGA, thermal debinding process parameters such as holding temperature and duration can be determined and refined [155].

2.5 Summary

In this chapter, a literature survey is conducted in areas needed to establish a complete approach to improve and develop ceramic materials. The literature survey in characterisation of powder-based feedstock highlighted the reliance on experimental data of feedstock when estimating thermomechanical properties using theoretical models. Existing theoretical models used to estimate thermomechanical properties have been shown to overestimate thermal conductivity and specific heat capacity. It was also showed that the material data estimated are only sufficient for standard injection moulding simulation that considers the powder-based feedstock as a single-phase fluid. In the area of experimental validation of the injection moulding simulation, the survey found that little research work was done to validate the mould filling simulation of ceramic-based feedstock and the DSC and TGA have multiple use case in powder injection moulding development. The SBM has been found to be widely implemented in powder injection moulding simulation which can be used to test out the hybrid material data developed to characterise powder-based feedstock. The interactions between the powder and binder during mould filling which are not simulated in SBM can be simulated with the TFM. The existing TFM of powder injection moulding can be further improved to consider mixture viscosity as binder viscosity. With these considerations, the development of a holistic approach to improve and develop ceramic feedstock is presented in the next few chapters.

Chapter 3. Development of two hybrid material data of silicon nitride feedstock

In this chapter, two hybrid material data are developed by combining experimental and estimated thermomechanical properties of powder-polymer mixture. The hybrid material data are used material input parameters that can be used in numerical models to simulate the injection moulding process. The estimation of material properties reduces the time and cost to acquire the required material data for numerical simulation. This added flexibility and cost-saving will allow the implementation of numerical simulation to industry workflow more appealing and help with the designing of geometrical attributes of the mould, material systems, feedstock compositions and optimisation of injection moulding parameters.

In Section 3.1, the composition of each powder and binder components used in the silicon nitride feedstock are presented. The compounding process conditions and procedure are described in detail in this section. Next, the methodology and characterisation for thermomechanical properties such as density, specific heat, viscosity and particle size distribution of silicon nitride feedstock are presented. The compounding process and thermomechanical properties measurement were carried out at Dou Yee Technologies and the University of Glasgow. These experimental data are used in both hybrid material data.

In Section 3.2, a comparative study between theoretical models used to predict thermomechanical properties of powder-polymer mixtures and experimental data found in literature is presented. The properties include elastic modulus, thermal conductivity, coefficient of thermal expansion and specific volume. Estimation models are then selected based on the accuracy of the estimation results, which will be used to estimate the required material properties in hybrid material data shown in Section 3.3.

In Section 3.3, two hybrid material data based on experimental and estimated results are presented. The first hybrid material data is HMD-NBV which comprises of models from different authors that were selected from the comparative study in Section 3.2. The second hybrid material data is HMD-V which uses only the Voigt model that was mainly used by Kate et al. [93] in the material database system. Voigt model is the theoretical upper-bound of mixture properties, therefore it resulted in overestimation of elastic modulus and thermal

conductivity. The effects of overestimating thermomechanical properties can be observed by using the material input data from HMD-NBV and HMD-V for numerical models developed in Chapter 5.

3.1 Characterising silicon nitride feedstock thermomechanical properties

A binder system and a silicon nitride feedstock were developed in this study, as shown in Figure 3.1(a) and (b). The silicon nitride (Si_3N_4) powder used in this study had 99.9% purity and α -phase crystalline structure. Low weight fractions of sintering aids such as yttrium oxide (Y_2O_3) powders and magnesium oxide (MgO) powders were used and they had 99.95% and 99.9% purity. In Figure 3.1(c), the microscopic imaging of the silicon nitride powders is captured with the JSM-5310 scanning electron microscope (SEM) paired with the Oxford Instruments EDS detector. It can be observed from Figure 3.1(c), that the silicon nitride particles are agglomerated. Therefore, it will be important for the compounding process deagglomerates the particles to ensure a homogeneous feedstock.

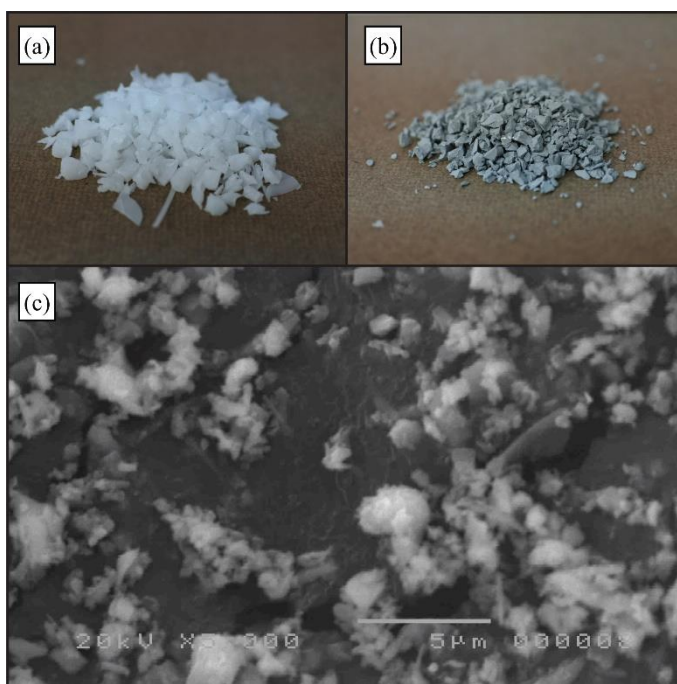


Figure 3.1. (a) Binder system, (b) silicon nitride feedstock and (c) Scanning Electron Microscope (SEM) imaging of silicon nitride powder.

The binder system consists of HDPE with melt index of 18 g/10 min and density of 0.955 g/cc, paraffin wax (PW) with melting point ranging 58°C to 60°C and stearic acid (SA). The composition of binder system and a silicon nitride feedstock are shown in Table 3.1. The feedstock was prepared in the IKA HKV-10 vertical kneading machine for 6 hr with a

rotation frequency of 15 rpm to 40 rpm and temperatures from 140°C to 160°C. Vacuum de-airing was added to the end of the mixing cycle to ensure the homogeneity of the feedstock.

Table 3.1. Composition of binder system and silicon nitride feedstock.

Specimen	Si₃N₄ + MgO + Y₂O₃ vol% (wt%)	HDPE vol% (wt%)	PW+ SA vol% (wt%)
Binder system	-	51.37 (52)	48.63 (48)
Silicon nitride feedstock	45.08 (74)	28.21 (13.52)	26.71 (12.48)

The thermomechanical properties of the silicon nitride feedstock must be characterised to get the input material data for the simulation models. It is important to develop an accurate material profile of the silicon nitride feedstock so that the feedstock will have the necessary thermomechanical properties to simulate its behaviour during mould filling through numerical models. The experimental results and theoretical models used to determine the thermomechanical profile of the feedstock are presented in the rest of Chapter 3.

3.1.1 Density

The density of the powder, binder and feedstock were measured using a Micromeritics AccuPyc II 1340 Gas Pycnometer using helium gas. Three tests with mass ranging from 2 g to 7 g were carried out on both binder system and silicon nitride feedstock. The measured density of the binder system and silicon nitride feedstock are shown in Table 3.2. Despite its simple form, the use of rule-of-mixture models to predict density of a powder-binder mixture have been widely documented to show good estimation [93], [134], [135]. Density of the binder system and silicon nitride feedstock used in this study are predicted using Equation (2.16). In Table 3.2, the measured density showed variations of 0.645% and 0.06% from predicted density of binder system and silicon nitride feedstock, respectively. The low variations in densities shows that the compounding conditions were able to achieve homogeneity in the binder system and feedstock. The predicted and measured density of binder system and feedstock indicated that the rule-of-mixture models are able to provide good estimation of mixture density.

Table 3.2. Measured and predicted density of a binder system and silicon nitride feedstock.

Specimen	Composition (wt%)	Measured Density (g/cm³)	Predicted Density (g/cm³)
Binder system	52% HDPE and 48% PW+SA	0.9241	0.9301
Silicon nitride feedstock	74% Si ₃ N ₄ +MgO+Y ₂ O ₃ , 13.52% HDPE, 12.48% PW+SA	1.9633	1.9645

3.1.2 Specific heat capacity

Specific heat capacity measurement for the binder system and silicon nitride feedstock are presented in this section. Modulated DSC experiments were performed in accordance to ASTM E2716 on a TA instrument Q100 to determine the specific heat capacity of the binder system and silicon nitride feedstock with N₂ purge gas flow rate of 50 mL/min over a temperature range from ambient temperature to 240°C. Hermetic aluminium pans and lids were selected for these experiments. DSC tests were carried out on 4 samples of binder system and silicon nitride feedstock with weight range of 6.0 - 7.1 mg and 7.4 – 9.0 mg. A calibration experiment is carried out to determine the correction factor for the specific heat capacity results. A calibration experiment is carried out on a standard sapphire sample from TA instruments. The experiment results and theoretical data from TA instruments are used to evaluate the calibration constant [156]. The specific heat capacity calibration constant [157] is determined using:

$$KC_{p_{rev}} = C_{p_t} / C_{p_m} \quad (3.1)$$

where $KC_{p_{rev}}$ is the reversing specific heat capacity calibration constant, C_{p_t} is the specific heat capacity theoretical data for sapphire and C_{p_m} is the specific heat capacity measured data for sapphire. The calibration constant is used as a correction factor for the measurements made on the binder system and silicon nitride feedstock. This experimental data can be used to represent the specific heat capacity of the feedstock during simulation. It is a thermodynamic property that determines the amount of heat required to raise a unit of mass by one degree in temperature.

Figure 3.2. shows the average specific heat capacity results of the binder system and silicon nitride feedstock which are based on four DSC tests each. The binder system results showed two transition temperatures around 50 °C and 110 °C. This signified that the components in the binder system has different melting points. The first transition temperature is due to the stearic acid and paraffin wax which have lower melting points and the second transition temperature is due to the HDPE in the binder system which has a higher melting temperature. Much like the binder system results, the silicon nitride feedstock results showed two transition temperature in similar temperature zones. Figure 3.2. shows that the specific heat capacity of the silicon nitride feedstock is stable at temperature ranging from 150 °C to 240 °C. Moulding should occur in temperatures in this range to avoid variations in specific heat capacity during the process.

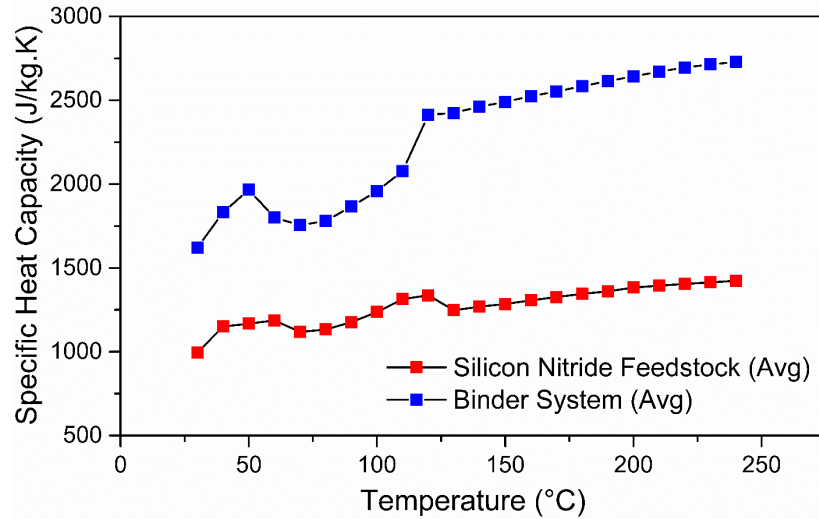


Figure 3.2. Specific heat capacity of binder system and silicon nitride feedstock as a function of temperature.

The material database system showed that specific heat capacity of a powder-binder mixture can be predicted using theoretical models [93], [97], [135]. Voigt model [158], [159] is used to predict the specific heat capacity of mixtures and is given by:

$$C_{p_f} = [C_{p_b}w_b + C_{p_p}w_p] \quad (3.2)$$

where w is the weight fraction and C_p is the specific heat capacity. The subscripts f , b and p represent feedstock, binder and powder respectively. Presented in the material database in Section 2.3, Equation (2.17) was proposed by Jamieson and Cartwright [158], [159] to predict the specific heat capacity of the aqueous mixture. The constant (D_c) which is optimised for each system is set as 0.2, similar to the study by Kate et al. [93]. Equation (2.17) and Equation (3.2) are used to predict the specific heat capacity of the silicon nitride feedstock by using specific heat capacity experimental results of the binder system and specific heat capacity of silicon nitride found in literature [160].

Figure 3.3. shows the estimated specific heat capacity using Equations (2.17) and (3.2) with the silicon nitride feedstock experimental results. The comparison was done in temperature range suitable for moulding which ranges from 150°C to 240°C. From temperatures ranging from 150°C to 240°C, Equation (3.2) was able to provide prediction with variations up to 2.29% and Equation (2.17) had variations up to 5.36%. This shows that Equation (3.2) is more adequate in predicting the specific heat capacity of silicon nitride feedstock used in this study.

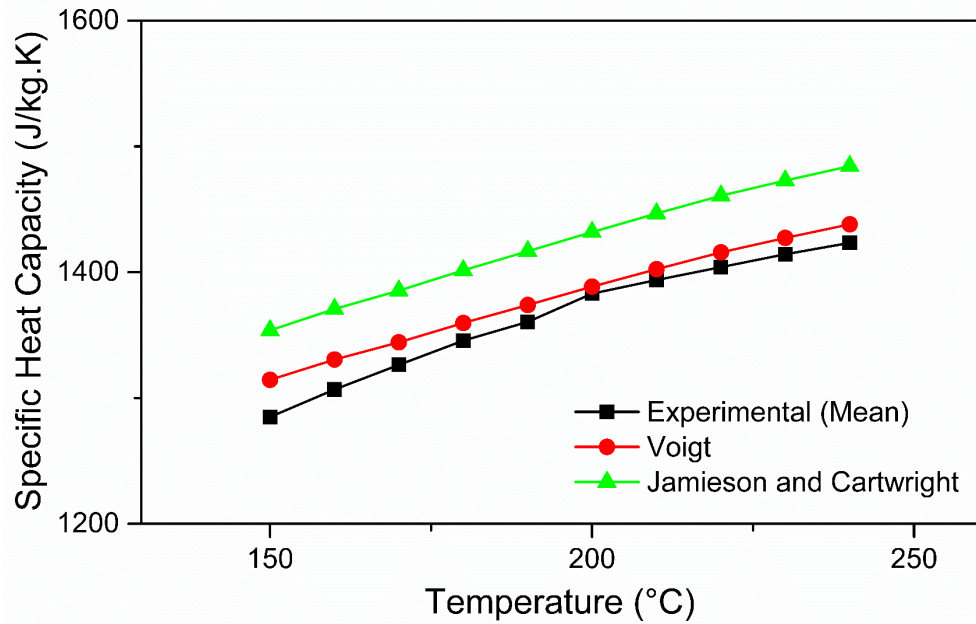


Figure 3.3. Predicted and experimental specific heat capacity of silicon nitride feedstock.

3.1.3 Viscosity

Rheological behaviour of the binder system and silicon nitride feedstock were measured using a Yasuda capillary rheometer (No. 140 SAS). Viscosity of the binder system and silicon nitride feedstock were measured at temperatures from 150°C to 200°C with 10°C increments. Shear rate range of 102.1 s⁻¹ to 5836.8 s⁻¹ were measured for binder system and 5.8 s⁻¹ to 5836.8 s⁻¹ for silicon nitride feedstock. Experimental viscosity results of the binder system are used to predict the viscosity of silicon nitride feedstock using theoretical models. Predicted and experimental viscosity results of the silicon nitride feedstock are compared to determine the accuracy of the theoretical model. In Table 3.3, the theoretical models used are simple as they only require the viscosity of the binder system and volume fraction of powder.

Table 3.3. A summary of theoretical models to predict viscosity of powder-binder mixture.

Model	Theoretical model	Equation	Reference
Einstein	$\eta_f = \eta_b(1 + 2.5\phi_p)$	(3.3)	[161], [162]
Mooney	$\eta_f = \eta_b \left(e^{\frac{2.5\phi_p}{1-\phi_p/\phi_m}} \right)$	(3.4)	[163]
Krieger and Dougherty	$\eta_f = \eta_b \left(1 - \frac{\phi_p}{\phi_m} \right)^{-2.5\phi_m}$	(3.5)	[164]

where η is viscosity, ϕ is volume fraction and ϕ_m is the maximum packing fraction, 0.637. The subscripts f , b and p represent feedstock, binder and powder respectively.

The Einstein equation [161], [162], Equation (3.3), is used to predict viscosity behaviour of a dilute suspension. Equation (3.4) shows an exponential model developed by Mooney [163] from extending the Einstein equation for viscosity to suspension of finite concentration. It considers the variation in particle size and particle interactions for higher concentration. In Equation (3.5), Krieger and Dougherty [164] developed a power-law model that considers the interactions between neighbouring spherical particles. When particle concentrations are low, the model is reduced to the Einstein equation. In Figure 3.4, predicted viscosity from the three models and experimental viscosity results of silicon nitride feedstock are compared at temperatures 160 °C, 180 °C and 200 °C.

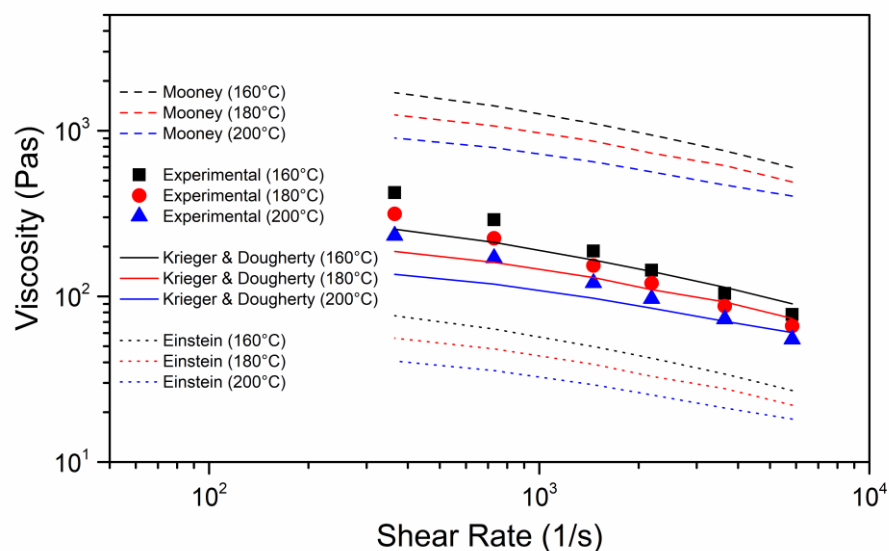


Figure 3.4. Comparison of predicted and measured viscosity of silicon nitride feedstock.

Figure 3.4 shows that the Einstein equation underpredicts the silicon nitride feedstock viscosity as it is primarily used for dilute volume fractions of particles. On the other hand, the Mooney model overpredicts the silicon nitride feedstock viscosity. Krieger and Dougherty model was able to provide better prediction of feedstock viscosity as compared to Einstein equation and Mooney model. At higher shear rate regions ($\geq 2188.8 \text{ s}^{-1}$), Krieger and Dougherty model predicted highest difference of 16.72 %, but as the shear rate decreases ($\leq 2188.8 \text{ s}^{-1}$), the model starts to underpredict the viscosity of the silicon nitride feedstock by highest difference of 41.64 % at 200 °C and 364.8 s^{-1} . There were no experimental viscosity results of the binder system to verify the predictions for low shear rate regions of 5.8 s^{-1} to 364.8 s^{-1} . However, the Krieger and Dougherty model is expected to underpredict the silicon nitride feedstock viscosity in low shear rate region.

Chapter 3

Currently, there are no universal theoretical model that can predict the viscosity of powder-based feedstock at different volume fractions and low shear rate regions [165]. Therefore, the viscosity experimental results of powder-based feedstocks are usually curve fitted with a viscosity model. In Section 2.2.3, Equation (2.6) known as Cross-WLF model describes the rheological behaviour of the feedstock and its dependency of temperature, shear rate and pressure. It is important that the viscosity model is able to represent the rheological behaviours of the feedstock well to ensure good rheological representation in the numerical models. In Table 3.4, Cross-WLF coefficients are data fitted from the viscosity experimental results of the silicon nitride feedstock.

Table 3.4. Cross-WLF coefficient values.

Coefficient	A_1	A_2	D_1	T^*	n	τ^*
Value	17.96	51.6	1.646×10^9	325.81	0.482	8758.27

At first glance in Figure 3.5, the Cross-WLF model can be seen to fit the silicon nitride feedstock experimental results well. Upon observation the experimental data of the viscosity at low shear rate region of 5.8 s^{-1} to 102.1 s^{-1} is fitted well by the Cross-WLF model. However, at higher shear rate region noticeable difference can be observed. In shear rate region of 364.8 s^{-1} to 5836.8 s^{-1} , the Cross-WLF model underpredicts the viscosity at lower temperature and overpredicts at higher temperature. Figure 3.5 also shows that the viscosity of the silicon nitride feedstock is less sensitive to temperature in the high shear rate regions.

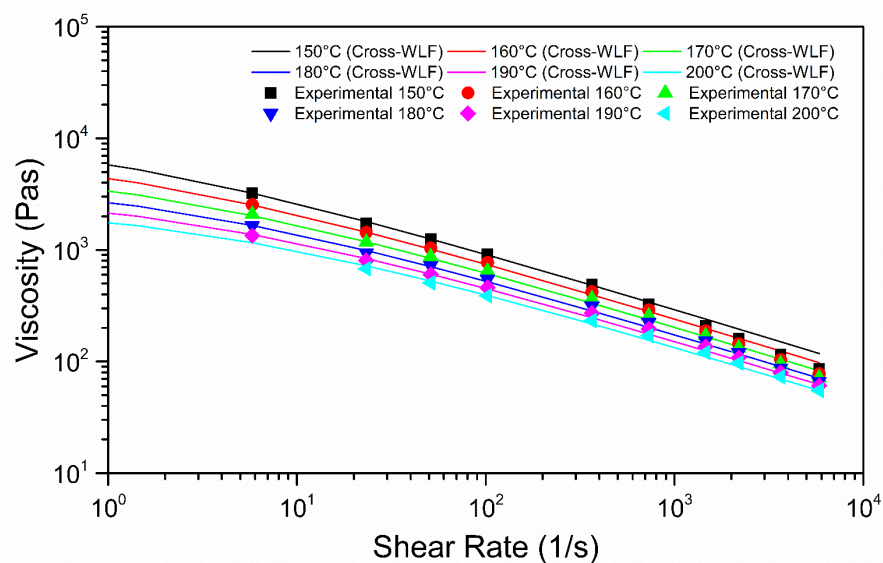


Figure 3.5. Viscosity of silicon nitride feedstock by experiments and Cross-WLF model.

3.1.4 Particle size distribution

In Figure 3.6(a), a digital microscope, Keyence VHX-5000, is used to conduct photo analysis of the silicon nitride powders to determine the particle size distribution. The samples were prepared by diluting 5g of silicon nitride powders in 100ml of acetone and mixed to ensure dispersion [166]. A few drops of the solution were dripped on white filter paper and left to dry. In Figure 3.6(a), microscopic photos of the powders are taken at 700 times magnification and the particles were detected and indicated in red. Photo analysis of the microscopic photos analysed 1917 particles the vertical and horizontal feret diameter of each particle. The average vertical and horizontal feret diameter for each particle is the same at 3.7 μm , therefore the particle can be assumed to be spherical. The average equivalent circle diameter of the particles is 3.6. μm , which shows that the assumption is acceptable. Figure 3.6(b) shows the particle size distribution of the powders used in the silicon nitride feedstock and the characteristic of the particle size distribution are reported in Table 3.5.

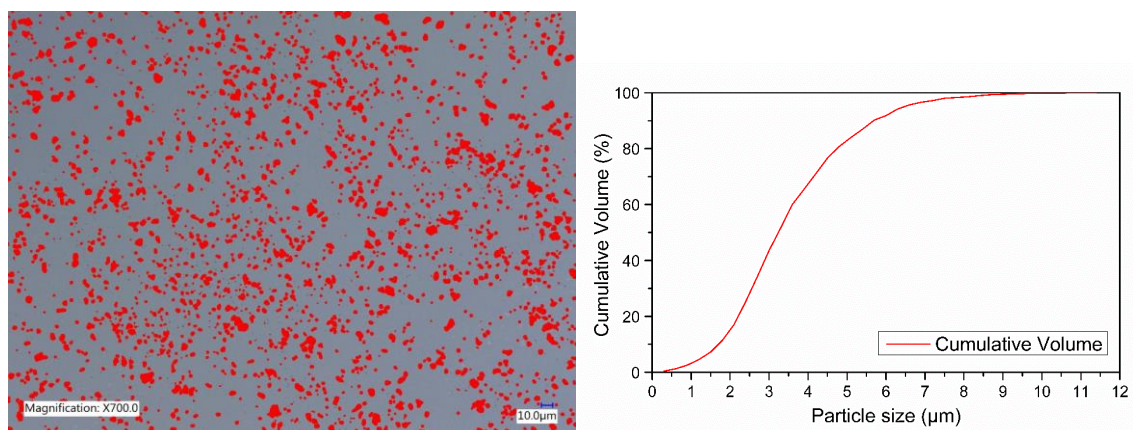


Figure 3.6. (a) Powder particles detected by photo analysis of microscopic photos at 700 times magnification and (b) particle size distribution of the powders.

Table 3.5. Characteristic of the silicon nitride particle size.

Particle size mean (μm)	Particle size, D_{10} (μm)	Particle size, D_{50} (μm)	Particle size, D_{90} (μm)
3.6	1.8	3.3	5.7

Since the moulding filling simulation models developed in this research work are based on the Eulerian-Eulerian method, the disperse phase particles are assumed to be spherical and can only be defined by a single particle size. The assumption of spherical particle is suitable for this case since the silicon nitride particles are observed to be so. However, a single particle size cannot be used to represent a particle size distribution which is what would be present in any powder-based feedstock. Simulating with one particle size greatly reduces the

computation complexity and efforts. The trade-off of reduced computational time and cost allows for more simulation parameters to be tested and in turn shorten the whole numerical process of optimising the injection moulding process. The silicon nitride mean particle size is used in the numerical models developed in this thesis to simulate powder-binder separation in PIM.

3.2 Modelling thermomechanical properties of powder-binder mixture

A comparative study between predicted and measured thermomechanical properties such as elastic modulus, thermal conductivity, coefficient of thermal expansion and specific volume are presented in this section. Experimental data of properties such as elastic modulus, thermal conductivity, coefficient of thermal expansion and specific volume found in various literature are compared with thermomechanical properties predicted by several theoretical models. Since the silicon nitride feedstock is made up of ceramic powders and polymers, the study is narrowed down to include only experimental data of powder-polymer mixtures. Since powder content of the silicon nitride feedstock is approximately 45 vol%, a criterion for the theoretical models is that they need to be able to provide close estimates of properties for high volume fraction of fillers (40-60 vol%). This study is conducted to identify theoretical models suitable for predicting thermomechanical properties of powder-based feedstock from the properties of each components. Models that are identified in this section are used to develop the hybrid material data in Section 3.3.

3.2.1 Elastic modulus

Equation (3.2) is a general rule-of-mixture model, Voigt model, that can be used to predict the elastic modulus of the composites such as a powder-binder mixture. The Voigt model [136] is based on the assumption that the constituents are subjected to same strain. In Table 3.6, several theoretical models that are also identified to predict elastic modulus of a powder-binder mixture are presented. The Reuss model [167] shown in Equation (3.6) is where the constituents are subjected to same stress. Based on the study by Kate et al. [134], the Voigt model showed moderate and better prediction as compared to the Reuss model for predicting elastic modulus of polymer-filler mixtures. However, these simple models do not take into consideration the effects of filler orientation, size of filler, shape of filler and filler-polymer adhesion.

Fu et al. [168] investigated the effects of particle size, particle-matrix interface adhesion and particle loading on the mechanical properties of the composites. They concluded that the elastic modulus of a composite is largely dependent on the particle loading and not the particle-matrix adhesion. It was also found that there is a critical particle size where at below nanoscale the stiffness of the composite is greatly enhanced. Equation (3.3) was originally derived to study the effective shear viscosity for dilute suspensions of rigid spheres can also be used to predict the effective elastic modulus of mixture [161], [162]. The Einstein equation for elastic modulus is valid only at small concentrations of filler and it assumes ideal adhesion between the filler and matrix.

Table 3.6. A summary of theoretical models to predict elastic modulus of powder-binder mixture.

Theoretical Model	Equation of the model	Equation	Reference
Reuss	$E_f = \frac{E_b E_p}{E_b \phi_p + E_p \phi_b}$	(3.6)	[167]
Guth	$E_f = E_b (1 + 2.5 \phi_p + 1 + 14.1 \phi_p^2)$	(3.7)	[169]
Kerner	$E_f = E_b + E_b \frac{15 \phi_p (1 - \nu_b)}{\phi_b (8 - 10 \nu_b)}$	(3.8)	[170]
Nielsen	$E_f = E_b \frac{1 + AB \phi_p}{1 - B \Psi \phi_p}$	(3.9)	[171]
	$A = k_E - 1$	(3.10)	[171]
	$B = \frac{E_p/E_b - 1}{E_p/E_b + A}$	(3.11)	[171]
	$\Psi = 1 + [(1 - \phi_m)/\phi_m^2] \phi_p$	(3.12)	[171]

where ϕ is the volume fraction, E is the elastic modulus, ν is the Poisson ratio, k_E is the Einstein coefficient, ϕ_m is the maximum packing fraction of the powder and Ψ is a reduced concentration term dependent upon the maximum packing fraction. The subscripts f , b and p represent feedstock, binder and powder respectively

Equation (3.7) shows the Guth model [169] that was modified from the Einstein equation to include particle interaction. The linear term accounts for the stiffening effect of each particles and the power term accounts for the particle interaction. Kerner [170] developed a modified version of self-consistent approach that considered the spherical particles were embedded in concentric shells of matrix material and the shells in turn have the properties of the composite. The Kerner model is shown in Equation (3.8). Nielsen model [171], Equations (3.9) to (3.12), were equations modified from Kerner and Halpin-Tsai for properties of two phase system with dispersed spherical particles. Nielsen [172], [173] first theorised the generalised equation for elastic modulus of composite material and later

Chapter 3

considers the effects of agglomeration of particle on the elastic properties of filled polymers which determines the Einstein constant used in the equation.

The Einstein coefficient is determine by morphology of the system which can be obtained from tabulated values presented in literature [173], [174]. Table 3.7 summarises the value for Einstein coefficient and maximum packing fraction for various fillers. In this study, the powder particles are considered to be spherical in shape and closely packed in random order with presence of aggregates in the polymers. Therefore, the Einstein coefficient and the maximum packing factor used in the Nielsen model is considered to be $2.5/\phi_m$ and 0.637.

Table 3.7 Einstein coefficient and maximum packing fraction [173], [174].

Filler phase	k_E	Type of particle	ϕ_m
Spheres	2.5	Sphere (Hexagonal close)	0.7405
Aggregates of spheres	$2.5/\phi_m$	Sphere (Face-centered cubic)	0.7405
Randomly oriented rods (Aspect ratio = 2)	2.58	Sphere (Body-centered cubic)	0.6
Randomly oriented rods (Aspect ratio = 4)	3.08	Sphere (Simple cubic)	0.524
Randomly oriented rods (Aspect ratio = 6)	3.8	Sphere (Random close)	0.637
Randomly oriented rods (Aspect ratio = 8)	3.8	Sphere (Random loose)	0.601
Randomly oriented rods (Aspect ratio = 10)	5.93	Fibre (Uniaxial hexagonal close)	0.907
Randomly oriented rods (Aspect ratio = 15)	9.4	Fibre (Uniaxial simple cubic)	0.785
Uniaxial fibre (parallel)	$1+2L/D$	Fibre (Uniaxial random)	0.82
Uniaxial fibre (perpendicular)	1.5	Fibre (3D random)	0.52

Table 3.8 summarises the elastic modulus, composition, type of filler and matrix taken from literature [175]–[177]. The experimental data for filler and matrix were used to predict the elastic modulus of the powder-polymer mixture using the theoretical models presented in this section. The predicted and experimental data of the powder-polymer mixture were compared to identify the most suitable model for predicting the elastic modulus of a powder-based feedstock. The selected model is used to predict the elastic modulus of the silicon nitride feedstock and the material data is used as input data in the numerical simulation developed in this thesis.

Table 3.8 Elastic modulus from experiments presented in the literature for powder-polymer mixture.

Filler	E_p (GPa)	Matrix	E_b (GPa)	Composition	Ref.
Alumina	385	HDPE	0.71	10 – 45 vol%	[175]
HA	80	HDPE	0.71	10 – 45 vol%	[175]
Silica	73	Ester	> 3	8.9 – 56 vol%	[176]
SCAN	330	Epoxy	2.25	10 – 50 vol%	[177]
Alumina	385	Epoxy	2.25	10– 50 vol%	[177]
Silica	73	Epoxy	2.25	10 – 50 vol%	[177]

Figure 3.7 to Figure 3.12 show the comparisons of estimated and experimental data of elastic moduli of various mixture with filler content of up to 56 vol%. The figures provide an insight to study the suitability of each presented theoretical models in predicting elastic modulus of powder-polymer mixtures. Hill [178] proved that the Voigt and Reuss models are theoretical upper and lower bound for composite elastic modulus. Figure 3.7 and Figure 3.8 show the estimated and experimental data of elastic modulus for alumina and HA fillers with HDPE matrix. In Figure 3.7 and Figure 3.8, the theoretical models by Guth [169] and Nielsen [171] can be observed to give better estimates as compared to the models by Voigt, Reuss, Einstein and Kerner. Figure 3.7 and Figure 3.8 show that the Guth model fails to provide good estimates at above 40 vol% of fillers while the Nielsen model is able to do so. The Reuss model, Einstein equation and Kerner model provided similar estimates for elastic modulus of powder-polymer mixture.

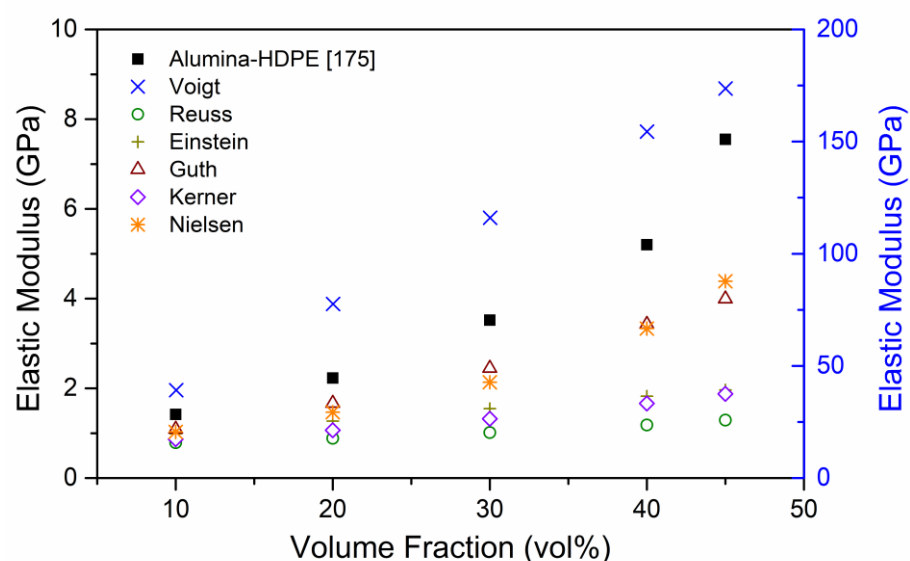


Figure 3.7. Elastic modulus as a function of volume fraction of alumina filler and HDPE matrix. The axis on the right is meant for the Voigt model results.

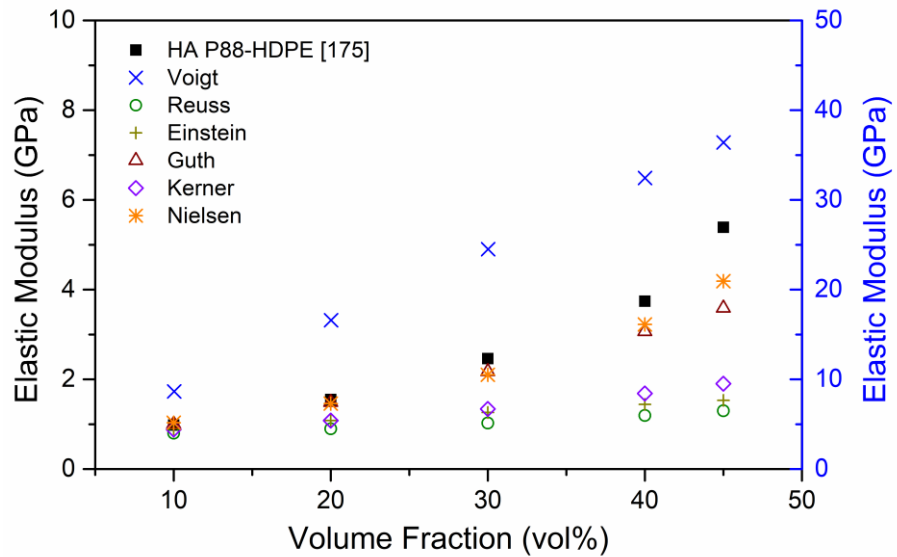


Figure 3.8. Elastic modulus as a function of volume fraction of HA filler and HDPE matrix. The axis on the right is meant for the Voigt model results.

The Nielsen model can be seen to provide better estimate for the HA-HDPE mixture (Figure 3.8) as compared to the alumina-HDPE mixture (Figure 3.7). It is important to note that the elastic modulus ratio between the filler and matrix for the alumina-HDPE mixture is much higher than the HA-HDPE mixture and this could be an aspect that affects the accuracy of the theoretical models. The elastic modulus ratio between the filler and matrix is the lowest in Figure 3.9 and the Kerner model can be observed to provide the best estimation among the theoretical models.

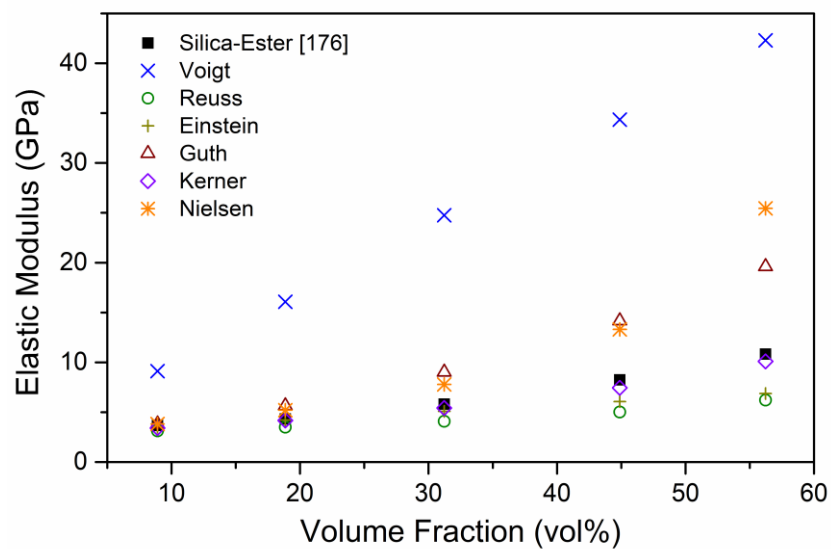


Figure 3.9. Elastic modulus as a function of volume fraction of silica filler and ester matrix.

Figure 3.10 to Figure 3.12 show the estimated and experimental data of elastic modulus of mixtures with epoxy matrix. The fillers consist of silicon-coated aluminium nitride (SCAN), alumina and silica which have different elastic modulus. Despite having the highest elastic modulus ratio between the filler and matrix, the alumina-epoxy mixture does not have a higher elastic modulus as compared to the SCAN-epoxy mixture that has a lower elastic modulus ratio. This shows that the elastic modulus of the mixtures is not dependent on the elastic modulus ratio between the filler and matrix and there might be other attributes that affect the elastic modulus of the mixtures.

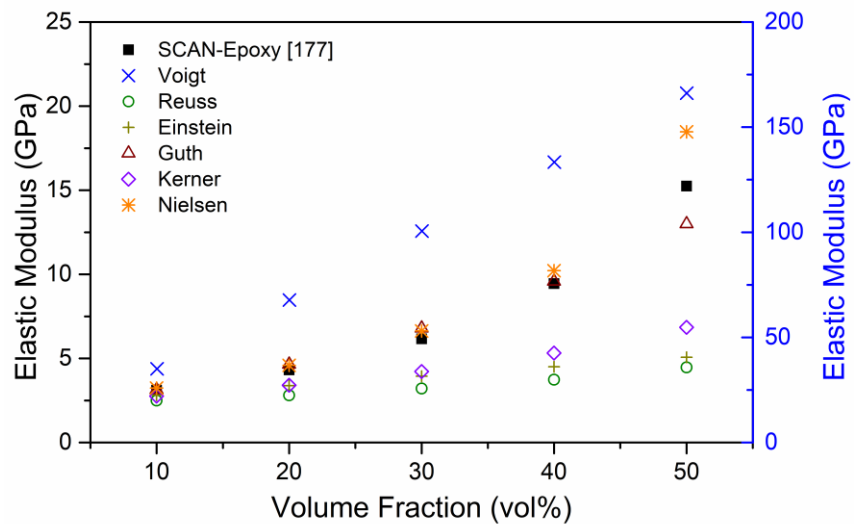


Figure 3.10. Elastic modulus as a function of volume fraction of SCAN filler and epoxy matrix. The axis on the right is meant for the Voigt model results.

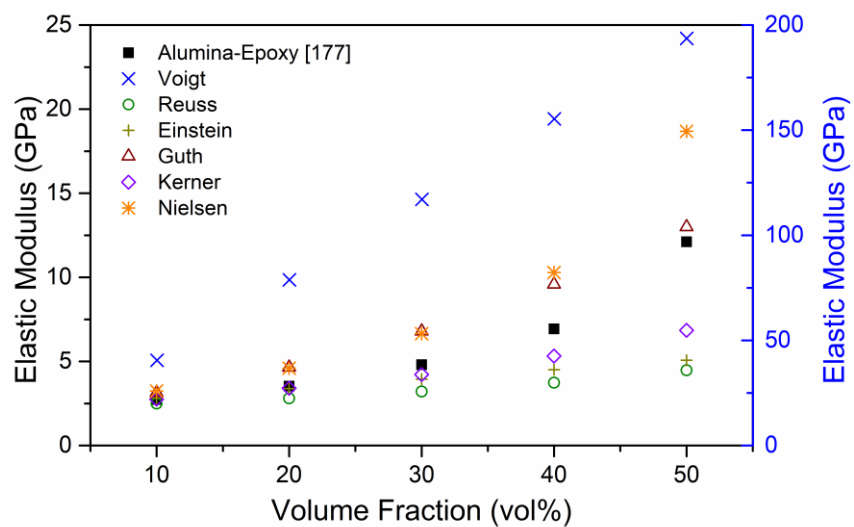


Figure 3.11. Elastic modulus as a function of volume fraction of alumina filler and epoxy matrix. The axis on the right is meant for the Voigt model results.

The elastic modulus of silicon nitride is closer to the SCAN and alumina. From Figure 3.7, Figure 3.10 and Figure 3.11, it can be observed that models by Guth and Nielsen were able to predict the elastic modulus of SCAN and alumina mixture with better confidence.

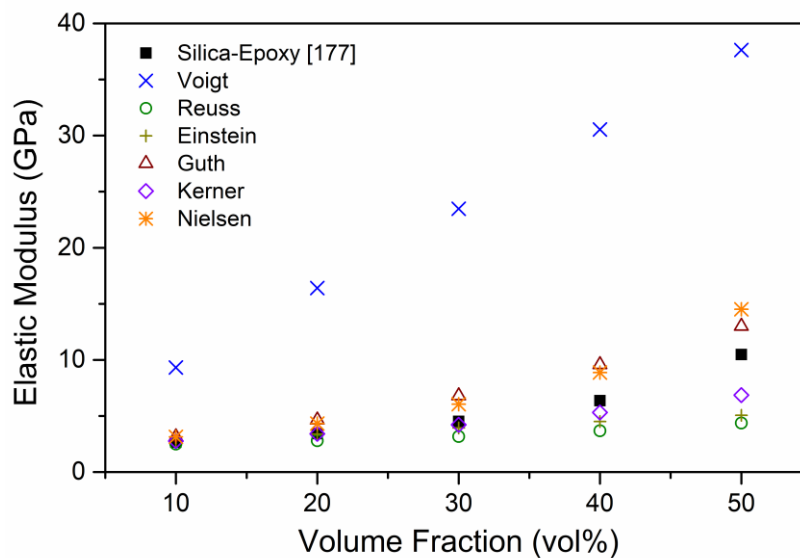


Figure 3.12. Elastic modulus as a function of volume fraction of silica filler and epoxy matrix.

Table 3.9 summarises the ratio of estimated elastic modulus to experimental elastic modulus data for volume fraction above 40 vol%. The comparison is done on volume fractions above 40 vol% as the silicon nitride feedstock used in this study has a 45% solid loading and most powder-based feedstocks have a solid loading from 50 % to 65 % [21], [30]. In Table 3.9, when the ratio is at 1, it means that the estimated data matches the experimental data. When the ratio is less than 1, it shows that the model underestimated the elastic modulus and when the ratio is more than 1, it shows that the model overestimated the elastic modulus. From Table 3.9, it can be observed that the Guth model and Nielsen model have better estimates for Alumina-HDPE, HA-HDPE, SCAN-Epoxy and Alumina-Epoxy mixtures compared to the rest.

Nielsen model has better estimates for mixtures with HDPE matrix. The Kerner model is able to provide good estimates for Silica-Ester mixture. The results from Table 3.9 also show that the Voigt model greatly overestimate the elastic modulus of the mixtures especially when the difference in elastic modulus between the filler and matrix is high. On the other hand, the Reuss model underestimates the elastic modulus of every mixture. This is due to the fact that the Voigt and Reuss models are known to provide theoretical upper and lower bounds on composite elastic properties [178]. To conclude, the Guth model and Nielsen

Chapter 3

model have more flexibility and are better suited in estimating mixtures with different elastic modulus ratio between filler-matrix. Since the silicon nitride feedstock used in the research work has HDPE as the main binder component, the Nielsen model was chosen to estimate the elastic modulus in the hybrid material data (HMD-NBV) as well as due to its versatility and better accuracy at high volume fractions.

Table 3.9. The ratio of estimated elastic modulus using various models to experimental data of powder-polymer mixture.

Filler-Matrix	Vol%	Voigt	Reuss	Einstein	Guth	Kerner	Nielsen
Alumina-HDPE	40	29.69	0.23	0.35	0.66	0.32	0.64
	45	22.99	0.17	0.26	0.53	0.25	0.58
HA-HDPE	40	8.67	0.32	0.39	0.82	0.45	0.86
	45	6.75	0.24	0.28	0.67	0.35	0.78
Silica-Ester	44	4.17	0.61	0.74	1.72	0.90	1.61
	46	3.91	0.57	0.64	1.81	0.93	2.35
SCAN-Epoxy	40	14.11	0.40	0.48	1.01	0.56	1.08
	50	10.90	0.29	0.33	0.85	0.45	1.21
Alumina-Epoxy	40	22.42	0.54	0.65	1.38	0.77	1.48
	50	15.99	0.37	0.42	1.07	0.57	1.54
Silica-Epoxy	40	4.80	0.58	0.71	1.51	0.84	1.40
	50	3.59	0.42	0.48	1.24	0.65	1.38

3.2.2 Thermal conductivity

Several models have been used to predict the thermal conductivity of a powder-polymer mixture and they are compared in this section to identify the suitable model for predicting thermal conductivity of a PIM feedstock. Some of these theoretical models are repeated from the previous section which were used to predict the elastic modulus of powder-polymer mixture. The equations to those theoretical models will not be repeated in this section. The repeated theoretical models are the Voigt, Reuss and Nielsen models which are Equation (3.2), (3.6) and (3.9), respectively. For thermal conductivity of mixture, the Voigt and Reuss models also represent the upper and lower bound.

The Nielsen model [174], [179] can be used to predict the thermal conductivity of two-phase systems. The Einstein coefficient and maximum packing factor used for thermal conductivity will be similar to the ones used for elastic modulus estimation. The Lichtenecker model [180], Equation (3.13), known as the geometric-mean model has a two-component form and it was developed for randomly distributed fillers in a mixture. Equation

(3.14) shows the Maxwell equation [181] that can be used to predict the effective thermal conductivity of non-interacting homogeneous suspension containing spherical particles. Both theoretical models are presented in Table 3.10.

Table 3.10. A summary of theoretical models to predict thermal conductivity of powder-polymer mixture.

Theoretical Model	Equation of the model	Equation	Reference
Lichtenecker	$k_f = k_p^{\phi_p} k_b^{\phi_b}$	(3.13)	[180]
Maxwell	$k_f = k_b \frac{k_p + 2k_b + 2\phi_p(k_p - k_b)}{k_p + 2k_b - \phi_p(k_p - k_b)}$	(3.14)	[181]

where, k is the thermal conductivity and ϕ is the volume fraction. The subscripts f, b and p represent feedstock, binder and powder respectively.

Table 3.11 summarises the thermal conductivity, composition, types of filler and matrix taken from literature [177], [182]–[184]. The experimental data of fillers and matrix were used to predict the thermal conductivity of powder-polymer mixture using the theoretical models presented in this section. The predicted and experimental data of the powder-polymer mixture were compared to identify the most suitable model for predicting the thermal conductivity of a powder-based feedstock. The highlighted model is used to predict the thermal conductivity of the silicon nitride feedstock and the material data is used as input data in the numerical simulation developed in this thesis.

Table 3.11. Thermal conductivity experimental data from literature of powder-polymer mixture.

Filler	k_p (W/mK)	Matrix	k_b (W/mK)	Composition	Ref.
SCAN	220	Epoxy	0.195	10 – 50 vol%	[177]
Alumina	36	Epoxy	0.195	10 – 50 vol%	[177]
Silica	1.5	Epoxy	0.195	10 – 50 vol%	[177]
AlN	185	PVDF	0.12	50 - 60 vol%	[182]
Silicon nitride	150	Epoxy	0.2	20 – 60 vol%	[183]
Silicon nitride	80	Silicone rubber	0.2	5 – 60 vol%	[184]

Figure 3.13 to Figure 3.18 show the comparisons of predicted and experimental data of thermal conductivity of various mixture with filler content of up to 73 vol%. Figure 3.13 to Figure 3.15 show the estimated and experimental data of thermal conductivity of mixtures with epoxy matrix. The fillers consist of SCAN, alumina and silica which have different thermal conductivity.

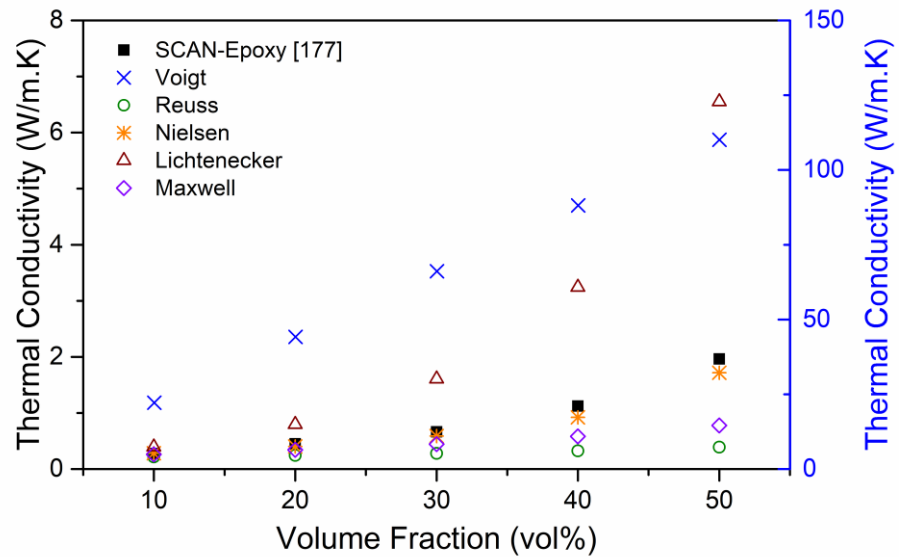


Figure 3.13. Thermal conductivity as a function of volume fraction of SCAN filler and epoxy matrix. The axis on the right is meant for the Voigt model results.

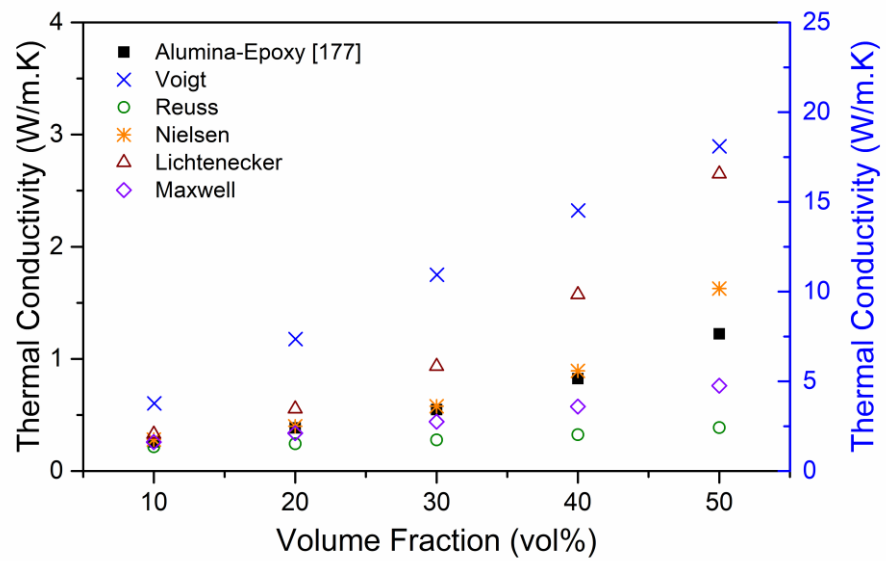


Figure 3.14. Thermal conductivity as a function of volume fraction of alumina filler and epoxy matrix. The axis on the right is meant for the Voigt model results.

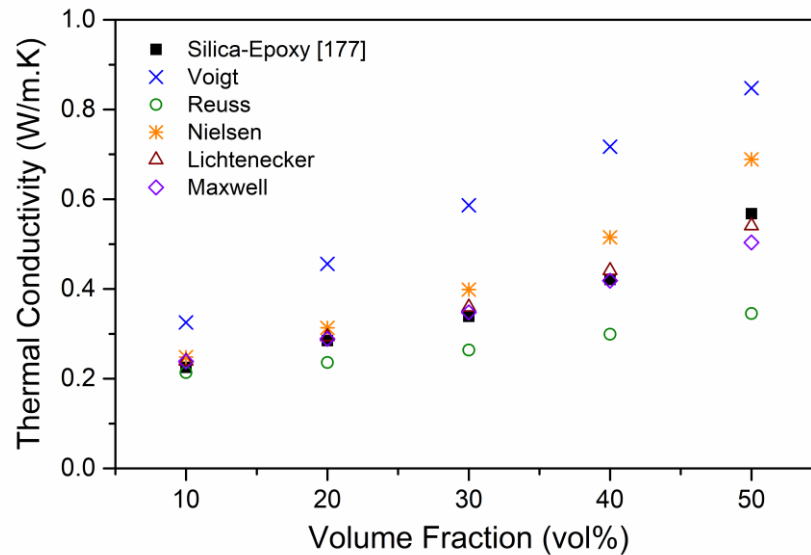


Figure 3.15. Thermal conductivity as a function of volume fraction of silica filler and epoxy matrix.

The thermal conductivity of the three fillers provides a wide range of thermal conductivity ratio between the filler and matrix with SCAN-epoxy having the highest and silica-epoxy having the lowest. The Nielsen model [174], [179] gave better estimations for thermal conductivity for SCAN and alumina fillers while the Lichtenecker model and Maxwell equation did better for silica fillers. It is observed from Figure 3.16 to Figure 3.18 that despite being able to provide better estimates of thermal conductivity of the powder-polymer mixtures, the Nielsen model [174], [179] is noticed to drastically increase in estimation of material properties when it gets close to 60 vol% of filler content. This is due to the maximum packing fraction which is limiting constant in the equation.

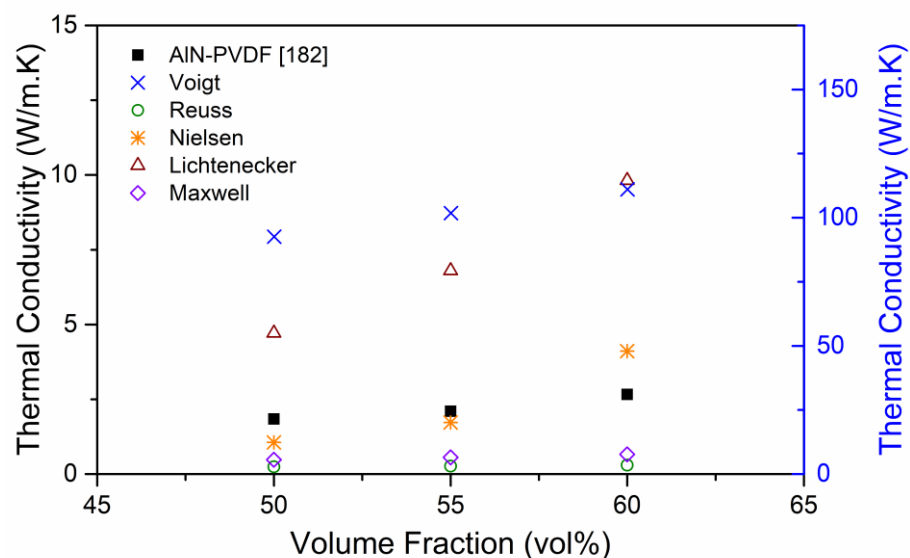


Figure 3.16. Thermal conductivity as a function of volume fraction of AlN filler and PVDF matrix. The axis on the right is meant for the Voigt model results.

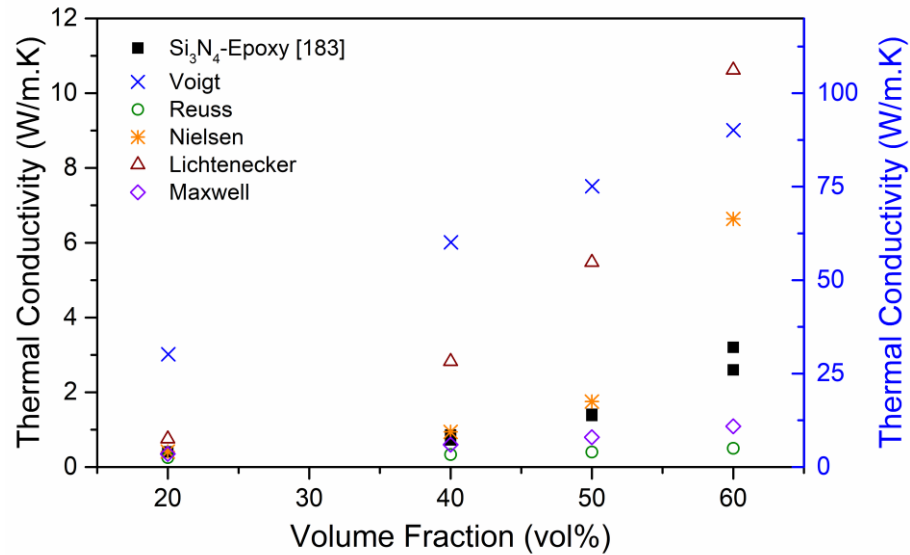


Figure 3.17. Thermal conductivity as a function of volume fraction of silicon nitride filler and epoxy matrix. The axis on the right is meant for the Voigt model results.

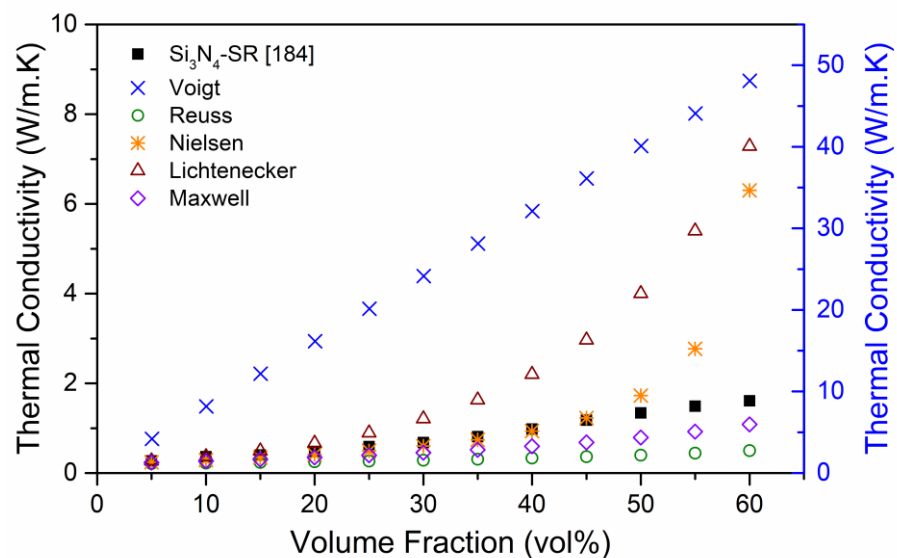


Figure 3.18. Thermal conductivity as a function of volume fraction of silicon nitride filler and silicone rubber matrix. The axis on the right is meant for the Voigt model results.

From Figure 3.13 to Figure 3.18, Lichtenecker model consistently overpredicts while the Maxwell equation consistently underpredicts the thermal conductivity of powder-polymer mixture with the only exception for silica-epoxy mixture. Therefore, it is not advisable to use the Lichtenecker model or Maxwell equation to predict thermal conductivity of a powder-based feedstock that has high thermal conductivity ratio of filler to matrix. Table 3.12 summarises the ratio of estimated thermal conductivity to experimental thermal conductivity data for volume fractions above 40%. In Table 3.12, when the ratio is at 1, it means that the estimated data matches the experimental data. When the ratio is less than 1,

it shows that the model underestimated the elastic modulus and when the ratio is more than 1, it shows that the model overestimated the elastic modulus. It is observed in Table 3.12 that the Voigt model and Reuss model are faced with similar problems when predicting the thermal conductivity of powder-polymer mixture. Much like the estimation for elastic modulus, the Voigt and Reuss models were the theoretical upper and lower bounds of mixture thermal conductivity. Therefore, the Voigt model overestimates the thermal conductivity of the mixtures significantly and the Reuss model underpredicts the thermal conductivity of every mixture. The Nielsen model performs the best out of all the other models at estimating thermal conductivity of various powder-polymer mixtures. However, the Nielsen model is observed to be have difficulty in estimating properties of powder-polymer mixtures above 60 vol% of powder content. This is due to the estimates reaching close to the maximum packing fraction, ϕ_m . To conclude, the Nielsen model was chosen to estimate the thermal conductivity of powder-based feedstock in the HMD-NBV. However, the Nielsen model will face problems when the estimates contain 60 vol% of powder.

Table 3.12. The ratio of estimated thermal conductivity from various theoretical models to experimental data of powder-polymer mixture.

Filler-Matrix	Vol%	Voigt	Reuss	Nielsen	Lichtenecker	Maxwell
SCAN-Epoxy	40	78.55	0.29	0.82	2.89	0.52
	50	56.12	0.20	0.88	3.34	0.40
Alumina-Epoxy	40	17.63	0.39	1.09	1.91	0.70
	50	14.79	0.32	1.33	2.16	0.62
Silica-Epoxy	40	1.70	0.71	1.22	1.05	0.99
	50	1.49	0.61	1.21	0.95	0.89
AlN-PVDF	50	0.13	50.30	0.58	2.56	0.26
	55	0.13	48.48	0.82	3.24	0.27
	60	0.11	41.75	1.55	3.69	0.25
Silicon nitride-Epoxy	40	0.39	70.23	1.10	3.30	0.70
	50	0.28	53.26	1.24	3.88	0.56
	60	0.16	28.15	2.07	3.32	0.34
Silicon nitride-silicone rubber	40	0.34	32.81	0.95	2.24	0.61
	45	0.31	30.64	1.04	2.52	0.58
	50	0.30	29.92	1.29	2.98	0.59
	55	0.30	29.62	1.86	3.63	0.62
	60	0.31	29.85	3.91	4.52	0.67

3.2.3 Coefficient of thermal expansion

Most binders have a higher CTE as compared to the powders and in this work when we compare the main binder component, HDPE, to the main powder component, silicon nitride, it amounts to approximately thirty times more. The huge difference in coefficient of thermal expansion between the HDPE and silicon nitride can cause residual thermal stresses. This can lead to warping and cracking defects to occur in green bodies. Several models have been used to predict the CTE of a powder-polymer mixture and they are compared in this section to identify a suitable model for predicting CTE of a PIM feedstock.

Some of these theoretical models are repeated from the previous section which were used to predict elastic modulus and thermal conductivity of powder-polymer mixture. The theoretical models are the Voigt model, Equation (3.2), and Reuss model, Equation (3.6), which are the upper and lower bounds of mixture properties. The equations will not be repeated in this section. In Equation (3.15), the Turner model is based on the basic assumption that the shear deformation is negligible and each component changes dimension over the function of temperature at the same rate [185]. In Equation (3.16), the Blackburn model [186], [187] was derived for spherical particles in a matrix at low concentration.

Table 3.13. A summary of theoretical models to predict CTE of powder-polymer mixture.

Theoretical Model	Equation of the model	Equation	Reference
Turner	$\alpha_f = \frac{\alpha_b K_b \phi_b + \alpha_p K_p \phi_p}{K_b \phi_b + K_p \phi_p}$	(3.15)	[185]
Blackburn	$\alpha_f = \alpha_b - \frac{3E_p \phi_p (1 - \nu_b)(\alpha_b - \alpha_p)}{[(1 + \nu_b) - 2\phi_b(1 - 2\nu_b)]E_p + 2\phi_b E_b(1 - 2\nu_b)}$	(3.16)	[186], [187]

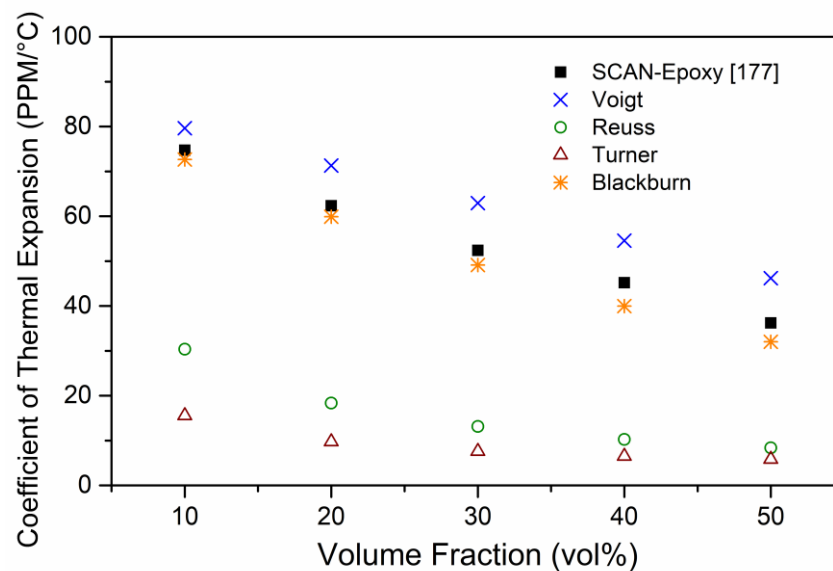
where, α is the coefficient of thermal expansion, ϕ is the volume fraction, K is the bulk modulus, K is the bulk modulus and ν is the Poisson ratio. The subscripts f , b and p represent feedstock, binder and powder respectively.

Table 3.14 summarises the CTE, elastic modulus, bulk modulus and Poisson's ratio of various filler and matrix taken from literature [177], [182], [184]. The experimental data of filler and matrix were used to predict the CTE of powder-polymer mixture using the theoretical models presented in this section. The predicted and experimental data of the powder-polymer mixture were compared to identify the most suitable theoretical model for predicting the CTE of a powder-based feedstock. The highlighted theoretical model is used to predict the CTE of the silicon nitride feedstock and the material data is used as input data in the numerical simulation developed in this thesis.

Table 3.14. CTE experimental data from literature of powder-polymer mixture.

Material	α (W/mK)	E (GPa)	K (GPa)	ν	Ref.
SCAN	4.4	330	220	0.25	[177]
Alumina	6.6	385	247	0.24	[177]
Silica	0.5	73	39	0.19	[177]
AlN	5.6	348	240	0.27	[182]
Epoxy	88	2.25	3.75	0.19	[177]
PVDF	137	2.125	2.213	0.34	[182]

Figure 3.19 to Figure 3.22 show the comparisons of predicted and experimental data of CTE of various mixture with filler content from 10 vol% to 73 vol%. Figure 3.19 to Figure 3.21 show the estimated and experimental data of CTE of mixtures with epoxy matrix. The fillers consist of SCAN, alumina and silica which have different CTE. The CTE for the matrix is much higher than the fillers so the CTE ratio between the filler and matrix are all low for the mixtures used in this study. In Figure 3.19 to Figure 3.21, the Blackburn model and Voigt model are seen to provide good estimates for CTE of a powder-polymer mixture. The Blackburn model [186], [187] is seen to be more consistent and accurate at predicting the CTE of powder-polymer mixture.

**Figure 3.19. CTE as a function of volume fraction of SCAN filler and epoxy matrix.**

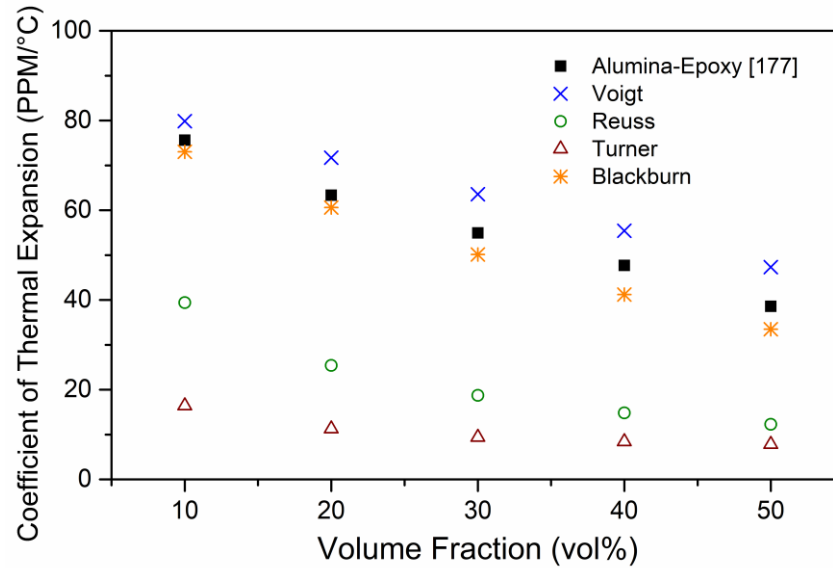


Figure 3.20. CTE as a function of volume fraction of alumina filler and epoxy matrix.

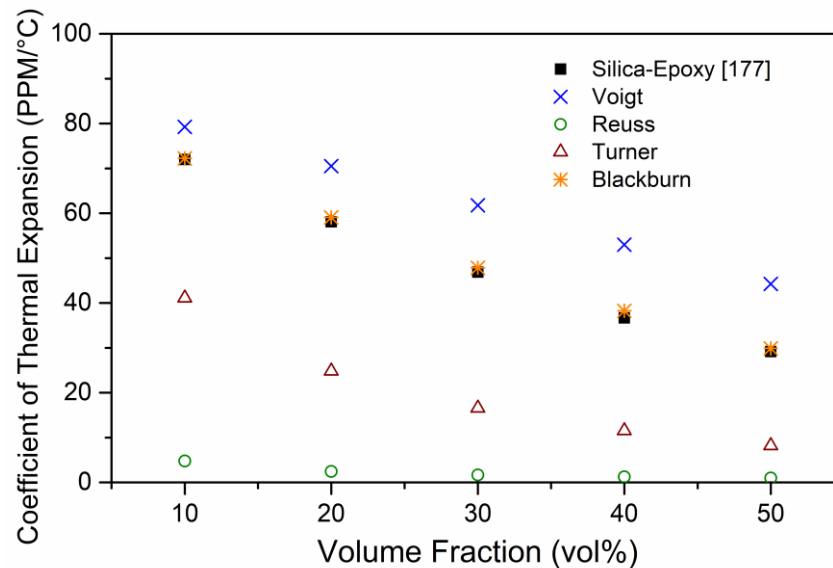


Figure 3.21. CTE as a function of volume fraction of silica filler and epoxy matrix.

In Figure 3.22, the theoretical models attempt to predict the CTE of AlN-PVDF mixture at volume fractions up to 73 vol%. Figure 3.22 shows the experimental data of the mixture starting at close to the upper bounds at 50 vol% and as the AlN content gets higher the experimental CTE results of the mixture deviates towards the lower bounds. Therefore, a lower-bound model might be more suitable to estimate the CTE of mixture above 65 vol%.

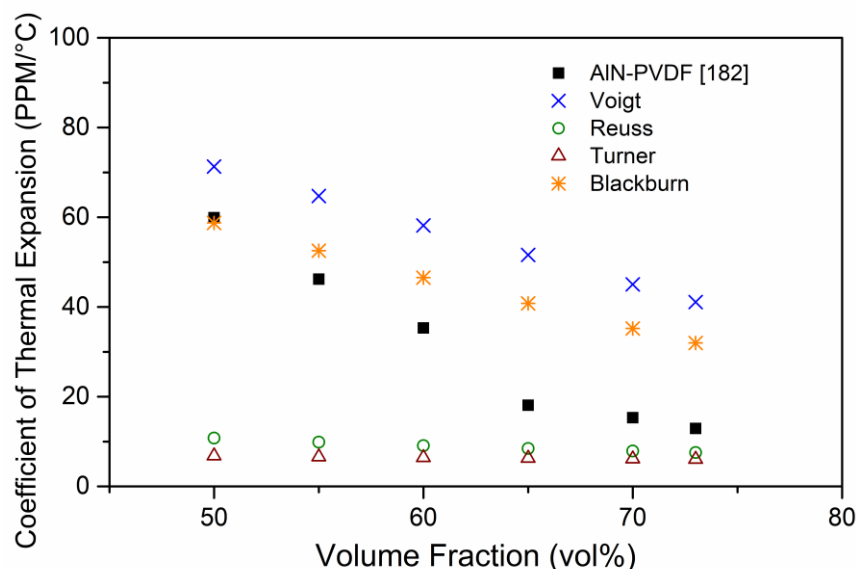


Figure 3.22. CTE as a function of volume fraction of AlN filler and PVDF matrix.

Table 3.15 summarises the ratio of estimated CTE to experimental CTE data found in literature. From Figure 3.19 to Figure 3.22, the Reuss model and Turner model can be seen to be predicting the lower-bounds CTE of the various powder-polymer mixtures while the Voigt model and Blackburn model are predicting the upper-bounds CTE of the various powder-polymer mixtures. The Voigt model and Blackburn model performs better among all the other theoretical models at estimating CTE of various powder-polymer mixtures. However, the Voigt model and Blackburn model are observed to be have difficulty in estimating CTE of powder-polymer mixture above 60 vol% of powder content. Based on the ratio of estimated CTE to experimental CTE data in Table 3.15, the Blackburn model has slightly better estimation when compared to the Voigt model. Therefore, the Blackburn model was chosen to be used to predict the CTE of powder-based feedstock in HMD-NBV. However, it should be noted that the Blackburn model would start to overestimate the CTE when powder content is more than 60 vol%.

Table 3.15. The ratio of estimated CTE from various theoretical models to experimental data of powder-polymer mixture.

Filler-Matrix	Voigt	Reuss	Turner	Blackburn	Vol%	Ref.
SCAN-Epoxy	1.06-1.27	0.22-0.40	0.14-0.20	0.88-0.97	10 – 50	[177]
Alumina-Epoxy	1.05-1.22	0.31-0.52	0.17-0.21	0.86-0.96	10 – 50	[177]
Silica-Epoxy	1.10-1.51	0.03-0.66	0.28-0.57	1.00-1.04	10 – 50	[177]
AlN-PVDF	1.19-3.18	0.17-0.58	0.11-0.46	0.98-2.47	50 – 73	[182]

3.2.4 Specific Volume

Density is the multiplicative inverse of specific volume therefore a model that can be used to predict the specific volume of a powder-binder mixture is inverse of the model shown in Equation (2.16). The inverse of that model is to use the Voigt model with weight fractions of the powder instead of volume fraction seen in Equation (3.2). The Voigt model has previously been identified as an adequate model to predict the specific volume of a powder-polymer mixture [137]. In Figure 3.23, experimental data [188] and predicted specific volume of aluminium-polypropylene composite were compared to verify the accuracy of the Voigt model. Figure 3.23 shows the Voigt model providing good predictions for specific volume of the mixture. Therefore, the Voigt model is chosen to be used to predict the specific volume of powder-based feedstock due to the good estimation while having a simple form.

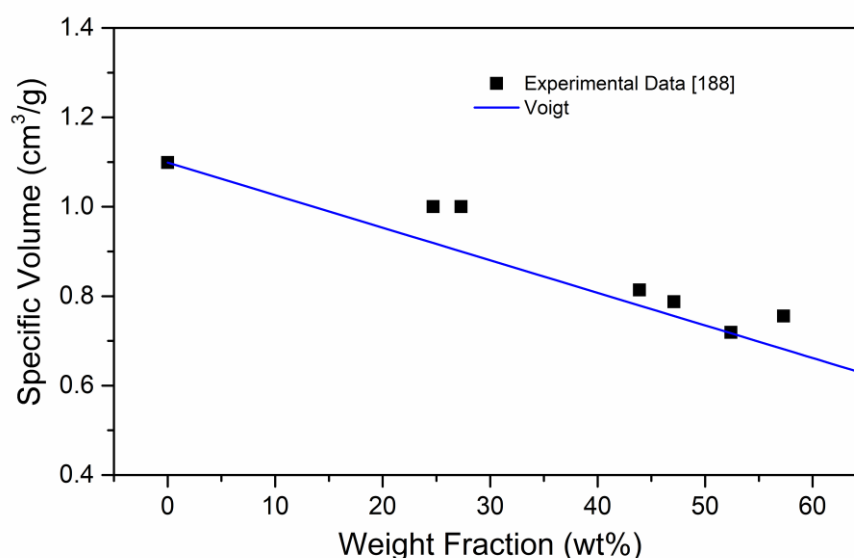


Figure 3.23. Specific volume as a function of weight fraction of aluminium filler and polypropylene matrix.

3.3 Hybrid material data of silicon nitride feedstock for powder injection moulding simulation

Two hybrid material data developed based on experimental and estimated results are presented in this section. In Table 3.16, HMD-NBV is developed based on the comparative study presented in Section 3.2. In the comparative study, several models were shown to provide good prediction for elastic modulus, thermal conductivity, coefficient of thermal expansion and specific volume of powder-polymer mixture. The first part “HMD” denotes hybrid material data and “NBV” are the initials of the authors that developed the theoretical models which in this case is Nielsen model, Blackburn model and Voigt model. Presented

Chapter 3

in Section 2.3, the HMD-V is developed based on the theoretical models identified by Kate et al. [93], [134], [135] in the material database system which mainly uses the Voigt model. The method devised by Kate et al. have been used to estimated material properties of feedstock for numerical simulations. The numerical simulation [138] showed errors ranging from 1% to 6% for temperature related output parameters and pressure related output parameters were overestimated by a factor of 10.

Table 3.16. Summary of theoretical models and measurements for thermomechanical properties of silicon nitride feedstock.

Thermomechanical properties	HMD-NBV	HMD-V
Elastic modulus	Nielsen	Voigt
Thermal conductivity	Nielsen	Voigt
Coefficient of thermal expansion	Blackburn	Voigt
Specific volume	Voigt	
Density	Gas pycnometer	
Specific heat capacity	Differential scanning calorimetry	
Viscosity	Capillary rheometer	
Particle size distribution	Digital microscope	

Both hybrid material data will use experimental results of density, specific heat capacity, viscosity and particle size distribution that are characterised in Section 3.1. The models used in the hybrid material data will be used to estimate the elastic modulus, thermal conductivity and CTE required as material input data for the numerical models developed in this thesis. In Table 3.16, the main difference between the two hybrid material data are the estimation models used to predict elastic modulus, thermal conductivity and coefficient of thermal expansion. It was shown with the comparative study in Section 3.2 that the Voigt model is the theoretical upper-bound of these material properties. Therefore, using the Voigt model to predict these thermomechanical properties of the silicon nitride feedstock will result in overestimation of values. More importantly, capturing accurate behaviour of the feedstock are an important step towards developing numerical models that would give results that are comparable to experimental results. Therefore, the effects of overestimation of thermomechanical properties can be observed by comparing the numerical results derived from the hybrid material data.

The estimation models used in the hybrid material data are designed to provide estimation for a two-component mixture. Therefore, the composition of the silicon nitride feedstock is simplified by considering having the binder system (matrix) to be represented by the main

component, HDPE, and the powder (filler) to be represented by silicon nitride. The properties of HDPE and silicon nitride are used when estimating the thermomechanical properties of silicon nitride feedstock for elastic modulus, thermal conductivity, coefficient of thermal expansion and specific volume

3.3.1 Elastic modulus

Section 3.2 showed that the Nielsen model [171] is adequate in predicting the elastic modulus of powder-polymer mixture. The Nielsen model and the Voigt model are used to estimate the elastic modulus of the silicon nitride feedstock. Table 3.17 shows the estimation of elastic modulus of the silicon nitride feedstock for several volume fractions. Elastic modulus of the silicon nitride feedstock are predicted using average elastic modulus of HDPE and silicon nitride found in literature [160], [189], [190]. The elastic modulus of the binder (HDPE) is denoted by 0 volume fraction of powder (silicon nitride) and vice-versa the elastic modulus of the silicon nitride is denoted by 1.

Table 3.17. Estimated elastic modulus of silicon nitride feedstock.

Volume fraction of powder (ϕ)	Elastic modulus Nielsen (GPa)	Elastic modulus Voigt (GPa)
0	0.953	0.953
0.42	4.920	132.573
0.45	5.858	142.233
0.48	7.069	151.375
1	314.333	314.333

As an upper-bound model for estimating mixture properties, the Voigt model gave estimation of 24.28 times the estimated elastic modulus by the Nielsen model at 0.45 volume fraction of powder. In Section 3.2, the Nielsen model was shown to provide estimates of elastic modulus ranging from 0.58 to 2.35 times the experimental data while the Voigt model provided estimates ranging from 2.46 to 34.87 times. This means that in numerical models that uses the material data from HMD-V will see significantly higher mechanical properties in the feedstock and green bodies as compared to HMD-NBV.

3.3.2 Thermal conductivity

Thermal conductivity of polymers has been found to be affected by the change in pressure and temperature [128]–[130]. Thermal conductivity changes due to the effects of temperature have also been observed in silicon nitride [160]. In injection moulding

simulation, the thermal conductivity of feedstock over a function of temperature are usually used without the consideration of pressure effects. During the injection moulding process, the feedstock experiences drastic change in pressure. Therefore, it is important to consider the effects of pressure in the predictions. Section 3.2 shows that the Nielsen model [174], [179] used for predicting elastic modulus of powder-polymer mixture have been found to be able to estimate thermal conductivity as well. In Section 3.2, the Nielsen model was shown to provide estimates of thermal conductivity ranging from 0.57 to 3.91 times the experimental data while the Voigt model provided estimates ranging from 1.44 to 99.85 times. However, the experimental results found in literature did not consider the effects of temperature and pressure on thermal conductivity.

Using the Nielsen model and Voigt model, thermal conductivity of the silicon nitride feedstock is estimated by using the average experimental data of silicon nitride and HDPE found in literature [128], [160], [189], [190]. A solid loading of 45 vol% of silicon nitride powder is used in the estimations. Figure 3.24 and Figure 3.25 show the estimation of thermal conductivity of the silicon nitride feedstock over a function of temperature and at various pressure. The predicted thermal conductivity of the silicon nitride feedstock can be observed to decrease over a function of temperature and increase with pressure. In Figure 3.24, the predicted thermal conductivity of the silicon nitride feedstock from the Nielsen model shows a distinct change in thermal conductivity. It is an indication of the transition temperature in which the material changes from solid to liquid. In Figure 3.25, the predicted thermal conductivity of the silicon nitride feedstock from the Voigt model does not show a distinct change in thermal conductivity like the Nielsen model.

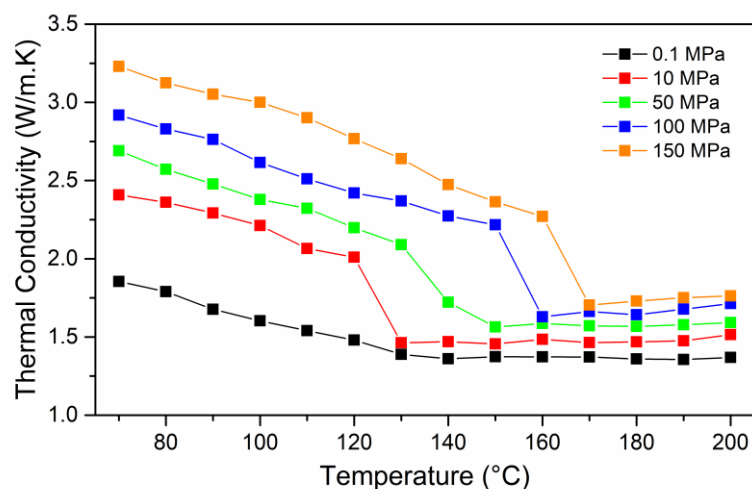


Figure 3.24. Predicted thermal conductivity of silicon nitride feedstock using Nielsen model over a function of temperature and pressure.

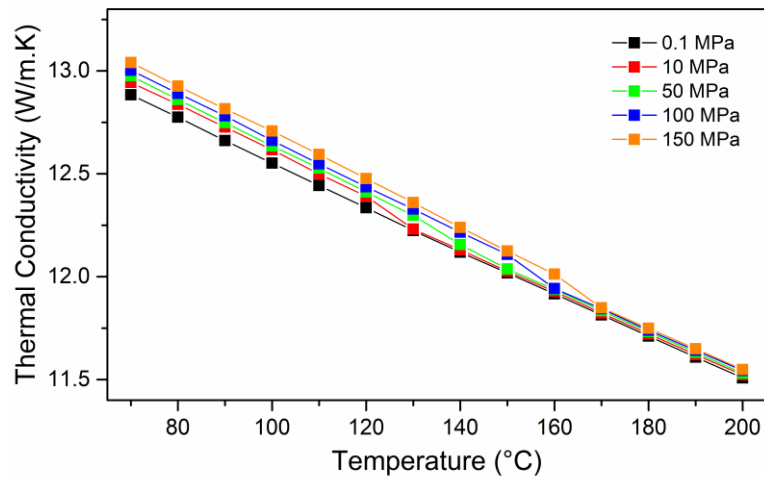


Figure 3.25. Predicted thermal conductivity of silicon nitride feedstock using Voigt model over a function of temperature and pressure.

Table 3.18 shows a summary of the thermal conductivity variation in HDPE and predicted silicon nitride feedstock by the theoretical models. The highest variation in thermal conductivity of HDPE and predicted silicon nitride feedstock was observed at 130°C between pressures of 0.1 MPa and 150 MPa. The lowest variation in thermal conductivity of HDPE and predicted silicon nitride feedstock was observed at 170°C between pressures of 0.1MPa and 150MPa. From the variations in thermal conductivity of HDPE and silicon nitride feedstock, the predicted thermal conductivity by Nielsen model have similar behaviour as the HDPE. Overall the thermal conductivity predicted by the Voigt model had low dependence to the effects of pressure.

Table 3.18. Variation in thermal conductivity of silicon nitride feedstock.

Thermal conductivity (W/mK)	Highest variation between pressure	Lowest variation between pressure
HDPE	104%	27%
Silicon nitride feedstock (Nielsen)	90%	24%
Silicon nitride feedstock (Voigt)	1.24%	0.29%

In numerical simulation of mould filling, material data inputs only considered the effects of temperature changes on the thermal conductivity of the feedstock melt. Thermal conductivity plays an important role in the computation of cycle time predictions, part temperature distribution, melt cooling estimation during moulding filling and packing. Bad feedstock thermal conductivity predictions can produce miscalculation in numerical results. Currently, there are no commercial injection moulding simulation packages that considers thermal conductivity model to consider both the effects of temperature and pressure. The

thermal conductivity of the feedstock is only considered over a function of temperature. Therefore, the thermal conductivity of the silicon nitride feedstock is selected close to the injection moulding pressure used in this study to fabricate the green bodies. In this study, the injection pressure used to fabricate the green bodies is 157.6 MPa and therefore the predicted thermal conductivity of the silicon nitride feedstock is selected at 150MPa. At 150MPa, the average thermal conductivity of silicon nitride feedstock predicted by the Voigt model is 4.94 times more than the predicted thermal conductivity by Nielsen model.

3.3.3 Coefficient of thermal expansion

Identified in Section 3.2, the Blackburn model [186], [187] is adequate at predicting the CTE of powder-polymer mixture. The Blackburn model and Voigt model are used to estimate the CTE of the silicon nitride feedstock. Table 3.19 shows the estimation of CTE of the silicon nitride feedstock for several volume fraction. The CTE of silicon nitride is dependent on temperature, but commercial injection moulding simulation only allows for the input of a single value to represent the CTE of the feedstock. Hence the melt temperature of the silicon nitride feedstock which is at 185°C is considered when predicting the CTE of the silicon nitride feedstock. The CTE of the silicon nitride feedstock is predicted using average CTE of HDPE and silicon nitride at 185°C found in literature [160], [189], [190]. The CTE of the binder (HDPE) is denoted by 0 volume fraction of powder (silicon nitride) and vice-versa the CTE of the silicon nitride is denoted by 1.

Table 3.19. Predicted CTE of silicon nitride feedstock at 185°C.

Volume fraction of powder (ϕ)	CTE-Blackburn (PPM/°C)	CTE-Voigt (PPM/°C)
0	152	152
0.42	85.29	89.10
0.45	80.62	84.48
0.48	76.23	80.11
1	2.24	2.24

The silicon nitride feedstock CTE estimation from Voigt and Blackburn models are close to each other, with variations of 4.47%, 4.79% and 5.09% for volume fraction of 0.42, 0.45 and 0.48 respectively. This was similar to the estimation of powder-polymer mixture CTE seen in Section 3.2. Currently, commercial simulation package used in the industry only considers a constant for CTE value of the feedstock. This disregard the effects of temperature change on the thermal expansion of the feedstock. The stress analysis derived from numerical

simulations are dependent on the CTE of the feedstock. Therefore, it would be beneficial to consider the possible effects of thermal expansion with respect to temperature or pressure in future. The variations in CTE predicted by the Blackburn model and Voigt model are low. Therefore, profound difference in numerical results may be hard to observe in the injection moulding simulations developed in Chapter 5.

3.3.4 Specific volume

Specific volume or PVT data of a powder-based feedstock has been found to be affected by the change in pressure and temperature. During the injection moulding process, the feedstock experiences drastic change in pressure and temperature. Therefore, it is important to consider the effects of pressure and temperature in the predictions. Section 3.2.4 showed that the Voigt model, Equation (3.2), is an adequate model at predicting specific volume of powder-polymer mixture. A solid loading of 45.08 vol% of silicon nitride powder is used in the estimations. Using the Voigt model, specific volume of the silicon nitride feedstock is estimated by using the inverse of measured silicon nitride powder density (3.224 g/cm^3) and experimental data of HDPE found in literature [191]. The measurement of silicon nitride powder density was previously presented in Section 3.1.1.

Figure 3.26 shows the estimation of PVT data of the silicon nitride feedstock over a function of temperature and at various pressure together with the experimental results of HDPE. The predicted specific volume of the silicon nitride feedstock can be observed to increase over a function of temperature and decrease with pressure which is the opposite behaviour from the thermal conductivity of the silicon nitride feedstock. The transition temperature of HDPE at different pressure can be seen by the sharp increase in specific volume after 130°C . It can be observed that the lower pressures data have a shorter transition temperature than the higher pressures data with a temperature range of 130°C to 170°C . The predicted data shows similar behaviour to the HDPE, but at a lower magnitude.

Predicted specific volume of the silicon nitride feedstock increases with the increase in temperature with transition temperatures in the same range as HDPE and the increase in pressure would result in a decrease in specific volume. With the predicted specific volume of the silicon nitride feedstock, the data can be curve-fitted with the two-domain Tait model to get its coefficients. In Section 2.2.8, the two-domain Tait model was presented as a model that provides specific volume data of a material over a range of temperature and pressure.

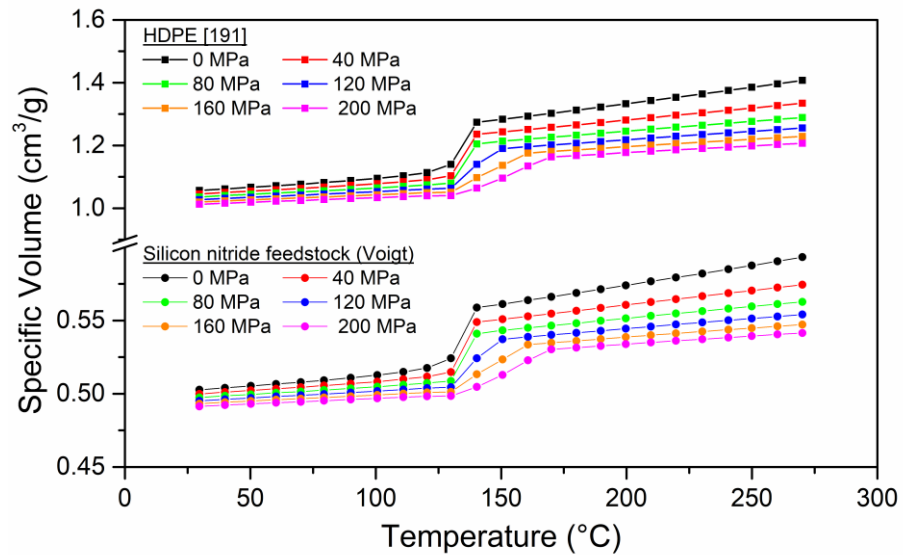


Figure 3.26. Experimental data of HDPE and predicted specific volume of silicon nitride feedstock.

Table 3.20 shows the data fitted coefficient values of the two-domain Tait model [132], [133] for the specific volume of silicon nitride feedstock predicted with the Voigt model. With these coefficients, specific volume behaviour of the silicon nitride feedstock can be represented in numerical simulations to simulate the mould filling process. By capturing the compressibility behaviour of the material, final part shrinkage and warpage of the green body can be simulated and analysed.

Table 3.20. Two-domain Tait model coefficient values.

Coefficient	Value	Unit	Coefficient	Value	Unit
b_{1m}	0.5566	cm ³ /g	b_{1s}	0.5124	cm ³ /g
b_{2m}	0.00026	cm ³ /gK	b_{2s}	8.36E-05	cm ³ /gK
b_{3m}	2.14E+09	dyne/cm ²	b_{3s}	5.35E+09	dyne/cm ²
b_{4m}	0.004433	1/K	b_{4s}	0.001927	1/K
b_5	407.99	K	b_6	1.00E-08	cm ² /dyne
b_7	0.0321	cm ³ /g	b_8	0.1	1/K
b_9	1.07E-09	cm ² /dyne	C	8.94E-02	-

3.4 Summary

In this chapter, the characterisation of silicon nitride feedstock to develop a material profile is presented. The measurements of silicon nitride feedstock density, specific heat capacity, viscosity and particle size distribution are presented in Section 3.1. In Section 3.2, a comparative study is conducted to identify accurate theoretical models that can estimate the rest of the thermomechanical properties required. The comparative study shows that the models used in hybrid material data or material database that were found in literature are inadequate in predicting thermomechanical properties such as viscosity, elastic modulus, thermal conductivity and coefficient of thermal expansion. These theoretical models have been shown to overpredict elastic modulus and thermal conductivity of powder-polymer mixtures.

Therefore, the HMD-NBV was developed using the Nielsen model to estimate elastic modulus and thermal conductivity, Blackburn model to estimate CTE and Voigt model to estimate specific volume. The HMD-V used only the Voigt model to estimate elastic modulus, thermal conductivity, CTE and specific volume. Both hybrid material data contain similar experimental data for density, specific heat capacity, viscosity and particle size for the silicon nitride feedstock. By developing numerical models using the material data from HMD-NBV and HMD-V, the effects of overestimating elastic modulus and thermal conductivity can be studied.

Chapter 4. Powder distribution study of the green bodies

Uniform distribution of powder content in the green body is important to minimise defects that occurs during the debinding and sintering process. Uneven powder distribution causes thermal expansion within the green compacts to vary. During thermal decomposition and densification, the compacts experience anisotropic shrinkages which may lead to cracking and warpage to occur in brown or sintered parts. The capability to measure powder distribution within the green body will allow the early detection of defects. Furthermore, the experimental results can be used to validate the two numerical models, SBM and TFM, that will be used to simulate the powder injection moulding process.

In this chapter, powder distribution measurement methods are developed to measure the distribution of silicon nitride powder within the injection moulded green body. Powder distribution measurements using DSC [90], [92], [103], [153] and TGA [103] have previously been used on tungsten and Inconel 718 injection moulded green bodies. Demers et al. [103] showed that the DSC measured the volume fraction of Inconel 718 powders at variations of 1 vol.% and the TGA measured with variations of 0.5 vol.%. These measurement methods have not yet been developed for ceramic-based injection moulded green bodies. Therefore, in this research work the DSC and TGA have been developed using similar principles to measure the distribution of silicon nitride powder within the injection moulded green body.

In Section 4.1, the process conditions and parameters for the fabrication of silicon nitride test-bars using an injection moulding machine are presented. Microscopy images of the green body surfaces are examined and the locations where tests will be carried out using the DSC and TGA are shown. In Section 4.2, the methodologies and experimental conditions of powder distribution analysis using the DSC are presented. A rule-of-mixture model and an empirical model are developed with heat flow data to evaluate the volume fraction of silicon nitride powder within the green body. In Section 4.3, the methodologies and experimental conditions of powder distribution analysis using the TGA are presented. The remaining weight fraction from binder burnout is used to evaluate the volume fraction of silicon nitride powder within the green body. In Section 4.4, the experimental results from the powder

Chapter 4

distribution analysis using the DSC and TGA are presented in comparison. The experimental methods are compared and discussed on the sensitivity and suitability for measuring powder distribution within an injection moulded silicon nitride green body. Finally, the chapter is summarised in Section 4.5. The methods and results presented in this chapter have been published as a journal article in Powder Technologies [83].

4.1 Materials for powder distribution study

The silicon nitride feedstock developed in Section 3.1 was used to fabricate the silicon nitride test-bar shown in Figure 4.1(a) using an injection moulding machine (Engel, ES 200/45 HLS). The injection moulding parameters used were a barrel temperature of 185°C, mould temperature of 110°C, injection speed ranging from 70 mm/s to 90 mm/s and injection pressure of 150 bar. The test-bar had a dimension of 60 mm by 12 mm by 3.5 mm and they were divided into 2 by 5 section shown in Figure 4.1(b). Figure 4.1(b) shows the upper and lower sections which are denoted by (A) and (B) and 5 smaller sections denoted from 1 to 5. Smaller pieces of the specimens were cut out and weighed for the TGA and DSC test. A digital microscope (Keyence VHX-5000) was used to inspect the surface of the injection moulded silicon nitride test-bars. In Figure 4.1(c) and Figure 4.1(d), microscopy imaging in the area of “1” which is near the gate shows surface defects and the area in “3” shows no visible defects. Surface defects in the areas of “1” are likely due to high shear stress in the flow at the gate.

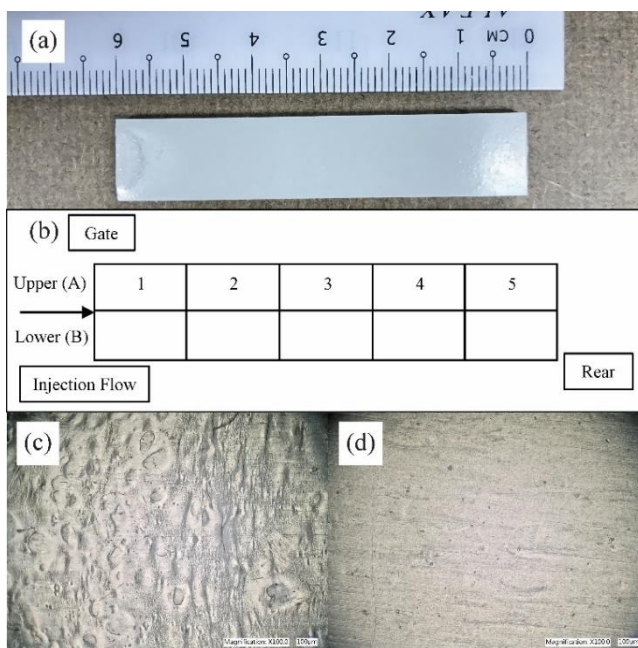


Figure 4.1. (a) Silicon nitride test-bar and (b) schematic diagram for powder distribution study. (c) Microscopy imaging at area “1” and (d) at area “3”.

4.2 Powder volume fraction measurement using differential scanning calorimetry

In Figure 4.2, the DSC is a thermal analysis technique in which the difference in the amount of heat required to increase the temperature of the sample and reference is measured as a function of temperature. Both the sample and reference are maintained at nearly the same temperature throughout the experiment. The experiments were performed on a DSC (TA instrument Q100) in temperature range from 25°C to 200°C with ramp temperature of 5 °C/min and air purge gas flow rate of 50 mL/min. Hermetic aluminium pans and lids were used to provide a sealed environment for the samples during the experiments.

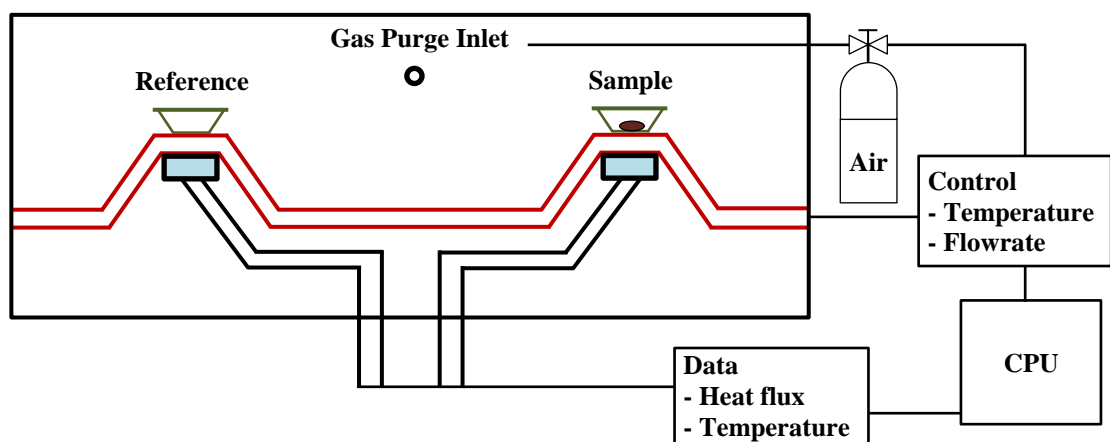


Figure 4.2. Schematic diagram of differential scanning calorimetry set-up for heat of fusion measurement.

Melting points of the binder system, silicon nitride feedstock and test-bar specimens can be determined by observing heat flow data. The melting points determined using the DSC corresponds to each of the binder components found in the test samples. The heat flow data can also be used to determine suitable mixing parameters for the compound and mixing the powders and binders into feedstock [30]. TA Universal Analysis software was used to calculate the heat of fusion in the specimens by integrating the area under the DSC peaks.

Thermal properties of a powdered feedstock such as specific heat capacity and heat of fusion are considered proportional to the weight fraction of the binder components [90], [92], [103], [153]. Demers et al. [103] theorised that the increase in powder solid loading would result in a decrease in the heat of fusion of the feedstock. This is due to the fact that most metal powders have a lower heat of fusion as compared to the binders found in metal-based feedstock. In Section 3.1.2, the specific heat capacity of the silicon nitride feedstock and binder system were measured. The experimental result of the silicon nitride feedstock was

shown to be proportional to the weight fraction of the binder system. In this section, two models are presented to predict the volume fraction of silicon nitride powder with heat of fusion data. In Equation (4.1), the rule-of-mixture model (ROM) was shown by Demers et al. [103] to predict the heat of fusion of metal powdered feedstock with the use of a calibration curve and the heat of fusion of every binder component.

$$\Delta H_f = \sum_i^n w_{b,i} \times \Delta H_{b,i} \quad (4.1)$$

where ΔH is the heat of fusion and w is the weight fraction. The subscripts f and b represent feedstock and binder respectively. n is the number of binder component in the binder system. For this method, instead of measuring the heat of fusion of each binder component, the heat of fusion of the binder system is measured. The volume fraction of silicon nitride powder can then be determined by using the weight fraction of binder system and the densities of the components.

The second model is an empirical equation (EMP) that is developed based on the heat of fusion experimental data of the binder system and the silicon nitride. The assumption made here is that the heat of fusion proportional to the volume fraction of the binder in the feedstock. Equation (4.2) shows the empirical equation in a form of a power-law model developed by data fitting experimental data of the binder system and silicon nitride feedstock for coefficients. The volume fraction of binder system in the samples can then be determined based on the heat of fusion:

$$\Delta H = L_1 vol\%_b^{L_2} \quad (4.2)$$

where $vol\%_b$ is the volume percent of binder, L_1 and L_2 are constants fitted from empirical data.

4.2.1 Heat flow experimental results of binder system and silicon nitride feedstock

Heat flow results of the binder system and silicon nitride feedstock were used to determine the average heat of fusion in the binder system and silicon nitride feedstock, respectively. DSC tests were repeated on 5 samples of the binder system and silicon nitride feedstock with weight range of 2.1 - 3.9 mg and 2.1 - 8.8 mg respectively. Presented in Figure 4.3, the DSC results of both the binder system and silicon nitride showed two peaks. The first peak

contains SA and PW and the second peak consist of HDPE. The two peaks indicate that the material goes through two endothermic reactions. Each endothermic reaction is the transit temperature where the binder components are melting. The two temperature peaks observed in the binder system occurred at 59.7°C and 123.3°C. The two temperature peaks observed in the silicon nitride feedstock occurred at 60.0°C and 122.7°C. The heat of fusion of the tests can be determined by integrating the area under the curve for each peak.

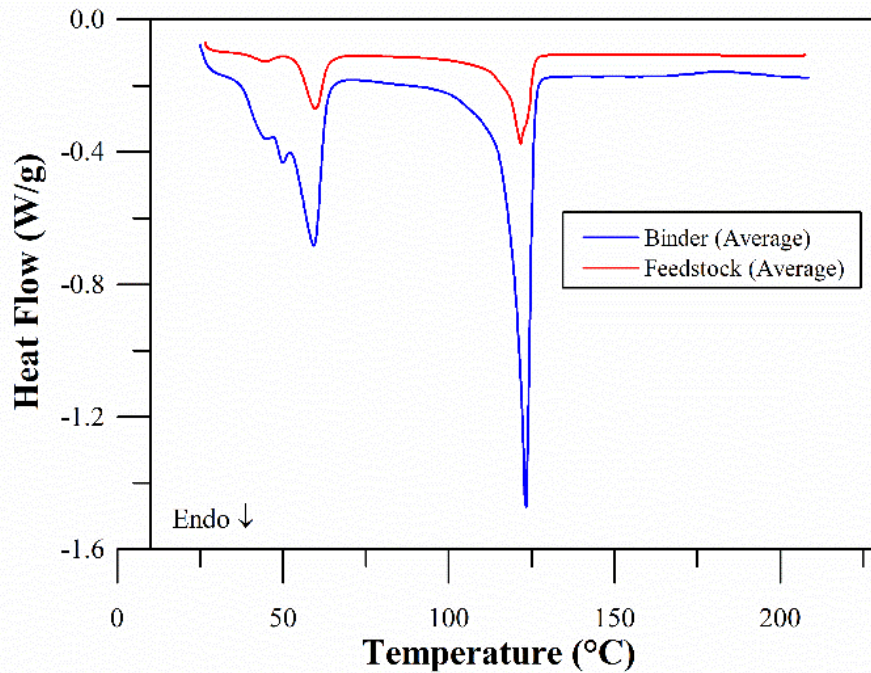


Figure 4.3. Average heat flow curves of binder system and silicon nitride feedstock.

In Figure 4.3, the average heat of fusion of the binder system for the first peak is 73.28 J/g and the second peak is 95.97 J/g. This gives a total of 169.25 J/g. The average heat of fusion of the silicon nitride feedstock for the first peak is 14.52 J/g and the second peak is 23.99 J/g. This gives a total of 38.51 J/g. From Equation (4.2), the constants are data fitted based on heat of fusion experimental data of the binder system and the silicon nitride feedstock from the DSC. Equation (4.3) shows the values of the data fitted constants.

$$\Delta H = 0.00198 vol\%_b^{2.4655} \quad (4.3)$$

Figure 4.4 shows the estimated heat of fusion over a function of volume fraction of binder system from the ROM and EMP models. From Figure 4.4, the ROM is showing overprediction of heat of fusion for silicon nitride feedstock by up to 12.5%. This means that if the ROM model was used to predict the volume fraction of binders in the silicon nitride green body, it would overestimate the volume fraction of silicon nitride powder in the tests.

The EMP model on the other hand was empirically calibrated based on the experimental data of the silicon nitride feedstock. The EMP model is expected to provide measurements of powder fractions within the green bodies with better accuracy considering that the volume fraction of binder system observed in the green bodies is expected to be close to the feedstock.

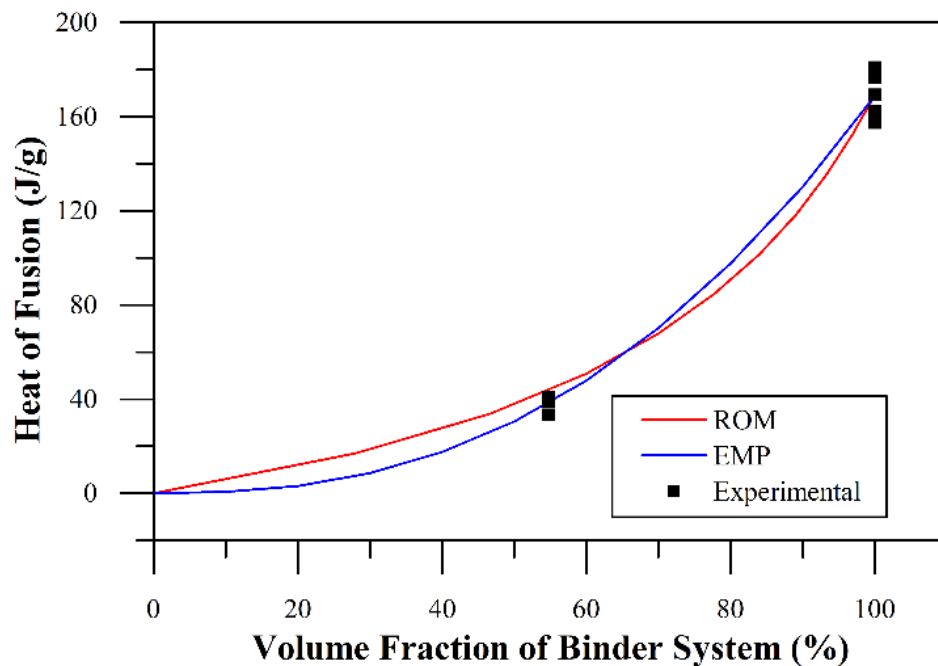


Figure 4.4. Heat of fusion as a function of volume fraction of binder system in silicon nitride feedstock based on experimental data, model 1 (ROM) and model 2 (EMP).

4.3 Powder volume fraction measurement using thermogravimetric analysis

In Figure. 4.5, the TGA is a method of thermal analysis which measures the change in weight of a material, either as a function of increasing temperature or time in a controlled atmosphere of air, nitrogen or oxygen. With the TGA experiments, the powder content in the feedstock or green bodies can be determined by the remaining weight fraction from the tests. The volume fraction of powder is then determined using mixing rules and measured densities of the powder and binder system. TGA experiments were performed on a TA Instrument Q500 to determine the weight loss of the binder system, silicon nitride feedstock and test-bar sections at ramp temperature of 10°C/min with N₂ purge gas flow rate of 90 mL/min over a temperature ranging from ambient to 700°C. 100 µL platinum pans were selected for the experiments.

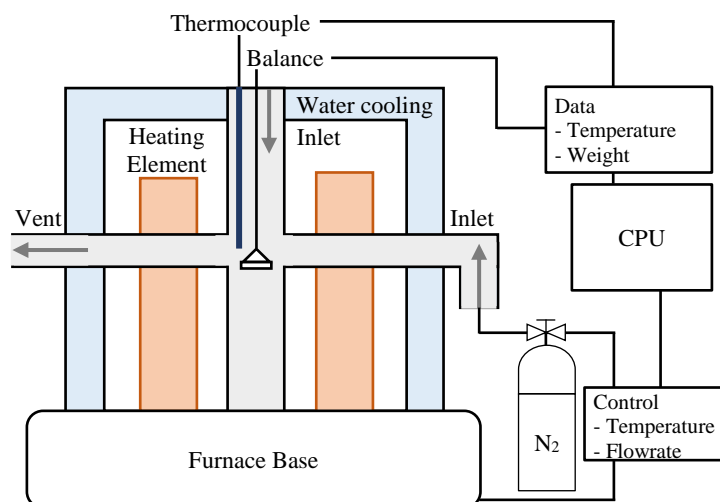


Figure. 4.5. Schematic diagram of thermogravimetric analysis set-up for weight loss measurements.

4.3.1 Weight loss experimental results of binder system and silicon nitride feedstock

TGA tests were repeated on 5 samples of the binder system and silicon nitride feedstock with weight range of 8 – 17 mg and 23 – 47 mg respectively. During the TGA tests, the samples undergo similar heat process as thermal debinding. Therefore, by observing the weight loss of feedstock during the TGA test, thermal debinding process parameters can be determined and improved to ensure that the binders are burnout [155]. Any phenomenal weight gains that may occur will be recorded during the experiments. This would help determine the optimal process parameters for solvent and thermal debinding. Average TGA results of the binder system and the silicon nitride feedstock were taken to determine the temperature at which weight loss occurs and the weight fraction of powder after binder burnout. Figure 4.6(a) shows a two-stage weight loss curves observed from the binder system and silicon nitride feedstock. This is due to the different decomposition temperature of the binder components.

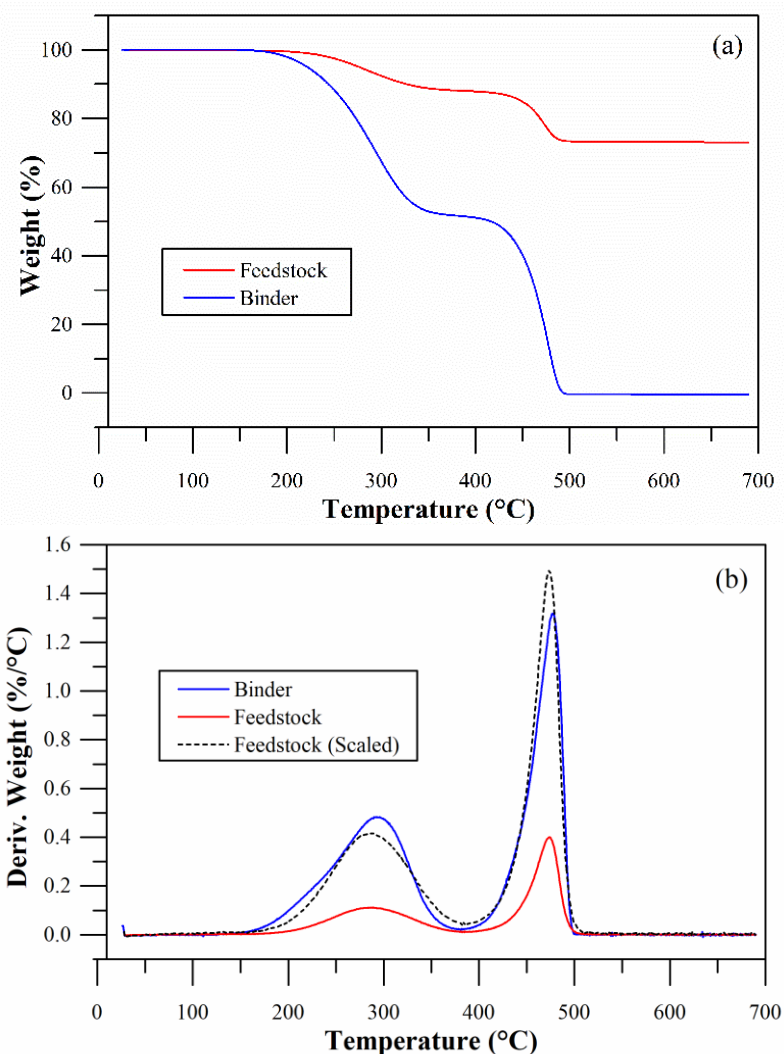


Figure 4.6. (a) TG curves and (b) derivative TG curves of binder system and silicon nitride feedstock.

Figure 4.6(b) shows the derivative weight loss of each binder components and the two-stage weight loss resulted in two derivative weight loss peaks. The derivative weight loss observed in the silicon nitride feedstock was scaled with respect to the weight loss observed in the binder system. This allows better comparison between binder system and silicon nitride feedstock. The two derivative weight loss peaks of the binder system are at 291°C with weight loss rate of 0.483 wt./°C and at 477 °C with weight loss rate of 1.316 wt./°C. The two derivative weight loss peaks of the silicon nitride feedstock are at 289°C with weight loss rate 0.111 wt%/°C and at 473°C with weight loss rate 0.4 wt./°C. The peak temperature results do not show significant difference between the binder system and silicon nitride feedstock.

When the derivative weight loss result of the silicon nitride feedstock is scaled to 100% of weight loss, the weight loss rate of silicon nitride feedstock becomes 0.417 wt./°C and 1.496 wt./°C for first and second peaks. The first peak shows lower rate of loss in weight which is

Chapter 4

due to the restriction in degradation of the paraffin wax and stearic acid. The restriction was caused by the burnout only occurring on the surface of the specimen and capillary action driving the binders to the surface of the specimens. The first derivative weight loss peak result also showed that there were leftover binder components of PW and SA in the feedstock before it reached the second peak. The second peak showed higher rate of loss in weight due to the burnout of the remaining binder components that were not decomposed in the first peak.

Initial degradation temperatures of the binder system and silicon nitride feedstock are considered when 5 wt% weight loss of binder system is measured. Table 4.1 shows the TGA results for the binder system and silicon nitride feedstock. Table 4.1 shows that the silicon nitride feedstock has higher initial degradation temperature as compared to the binder system. This is due to the obstruction of silicon nitride powders that prevents the binders from decomposing. The first stage of decomposition ended when the weight loss begins to plateau at 380 °C for the binder system and 382 °C for the silicon nitride feedstock. The weight loss for binder system and silicon nitride feedstock at the end of the first stage were 48.6 wt% and 11.9 wt% respectively. This should correspond to the weight fraction of PW and SA in the binder system (48 wt%) and silicon nitride feedstock (12.48 wt%).

Table 4.1. TGA results for binder system and silicon nitride feedstock.

Properties	Binder system	Silicon nitride feedstock
Weight Range (mg)	8 – 17	23 – 47
Initial Degradation Temperature (IDT), T_{d5} (°C)	221	229
Maximum Derivative Rate (wt%/°C)	1.316	0.4
Maximum Derivative Rate (Scaled)	-	1.496
Final Residue (wt%)	0	73.2
Final Residue (vol%)	0	43.9

The second stage of decomposition occurred at 398 °C for the binder system and 392 °C for the silicon nitride feedstock. The second stage of decomposition ended at 505 °C for the binder system and 525 °C for the silicon nitride feedstock. Binder system was fully decomposed and silicon nitride feedstock with a weight loss of 14.9 wt%. The weight fraction of HDPE in silicon nitride feedstock is 13.52 wt%, therefore the leftover PW and SA was decomposed in the second stage. The final residue of the silicon nitride feedstock will determine the powder content of the silicon nitride feedstock.

4.4 Powder distribution study using differential scanning calorimetry and thermogravimetric analysis

The silicon nitride test-bars were segmented into 2 by 5 sections based on the schematic diagram shown in Figure 4.1(b). DSC experiments were carried out for each segmented silicon nitride test-bars section. Table 4.2 shows the weight range of sample, average volume fraction of silicon nitride and variations determined based on the ROM and EMP models. The results from the ROM model show significantly higher volume fraction of silicon nitride and variations in measurements as compared to the EMP model.

Table 4.2. Powder volume fraction in test-bar section based on ROM and EMP.

Model	Properties	Test-bar (1)	Test-bar (2)	Test-bar (3)	Test-bar (4)	Test-bar (5)
ROM	Weight (mg)	3.5-11.1	3.6-7.7	1.9-11.3	3.5-9.7	2.7-7.8
	Average Volume% of Powders (vol%)	49.79	50.88	52.04	51.55	50.72
	Variation (vol.%)	1.019	0.986	1.604	1.503	1.515
EMP	Average Volume% of Powders (vol%)	45.43	46.18	46.96	46.63	46.06
	Variation (vol.%)	0.699	0.674	1.092	1.023	1.035

These results agree with the hypothesis that the ROM model overestimates the volume fraction of silicon nitride in the test-bars. TGA experiments were carried out for each segmented silicon nitride test-bars section. Table 4.3 shows the weight range of sample, average volume fraction of silicon nitride and the variation in volume fractions. Despite the wide weight range of specimens, the measured volume fraction of each section is within a close range of 43.97-44.10 vol% with highest variation of 0.119. This shows that the measurements of silicon nitride content by the TGA were not affected by the specimen weight. The uneven distribution of silicon nitride can be determined by the variation in the volume fraction of silicon nitride measured in the test-bar.

Table 4.3. Average TGA results for all the test-bar sections.

Properties	Test-bar (1)	Test-bar (2)	Test-bar (3)	Test-bar (4)	Test-bar (5)
Weight (mg)	26-65	77-111	34-95	52-108	49-89
Average Volume% of Powders (vol%)	44.10	44.09	44.09	44.08	43.97
Variation/Standard Deviation (vol%)	0.112	0.0854	0.119	0.0961	0.0603

Chapter 4

The points and error bars in Figure 4.7 to Figure 4.10 illustrate the volume fraction of powder and the variation in the measurements. Figure 4.7 shows the average volume fraction of powder and variation in each section along the test-bar for part (A) and (B) using the ROM model. The ROM model was meant to have a calibration curve based on the heat of fusion data of each binder component and densities of powder, binder and feedstock. Therefore, ROM model is not ideal in this application where only the binder system was measured for heat of fusion.

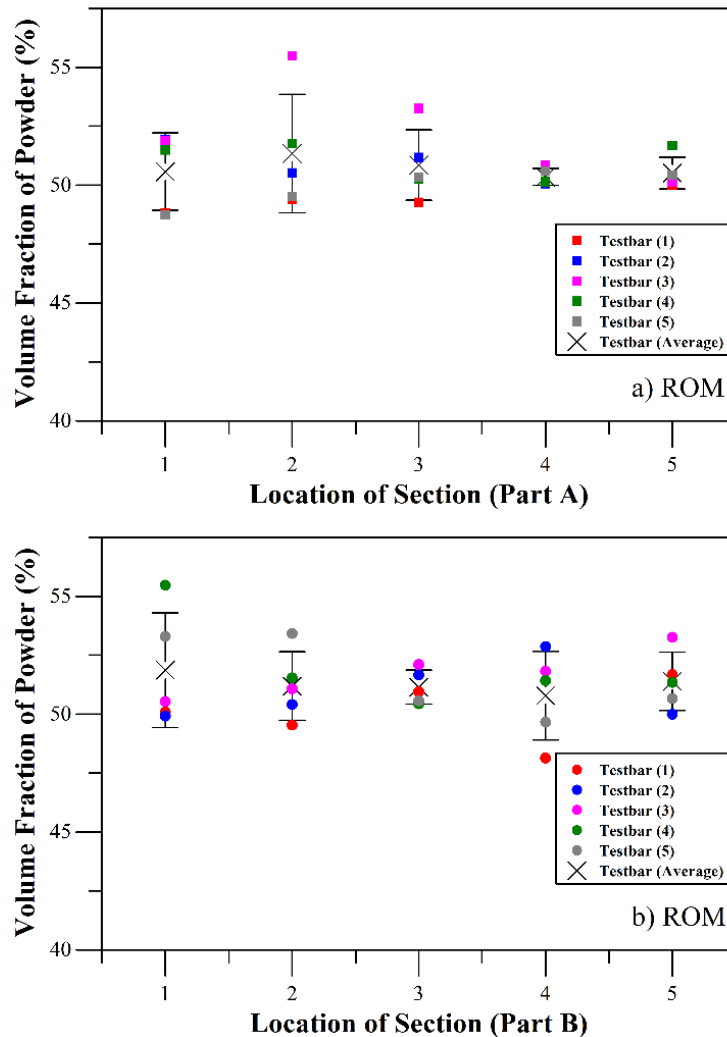


Figure 4.7. Volume fraction of powders in test-bar based on rule of mixture (ROM) a) Part A and b) Part B.

Figure 4.8 shows the average volume fraction of powder and variation in each section along the test-bar for part (A) and (B) using the EMP model. The EMP model shows lower variations and closer to nominal volume fraction of powder results as compared to the ROM model. Both methods are essentially empirical relations that is based off proportion of heat of fusion to weight or volume fraction of binder in each section. Therefore, they have similar trends. However, the measurements from the EMP model will be more suitable for validation

of numerical results as the measurements are closer to the theoretical volume fraction of silicon nitride powder.

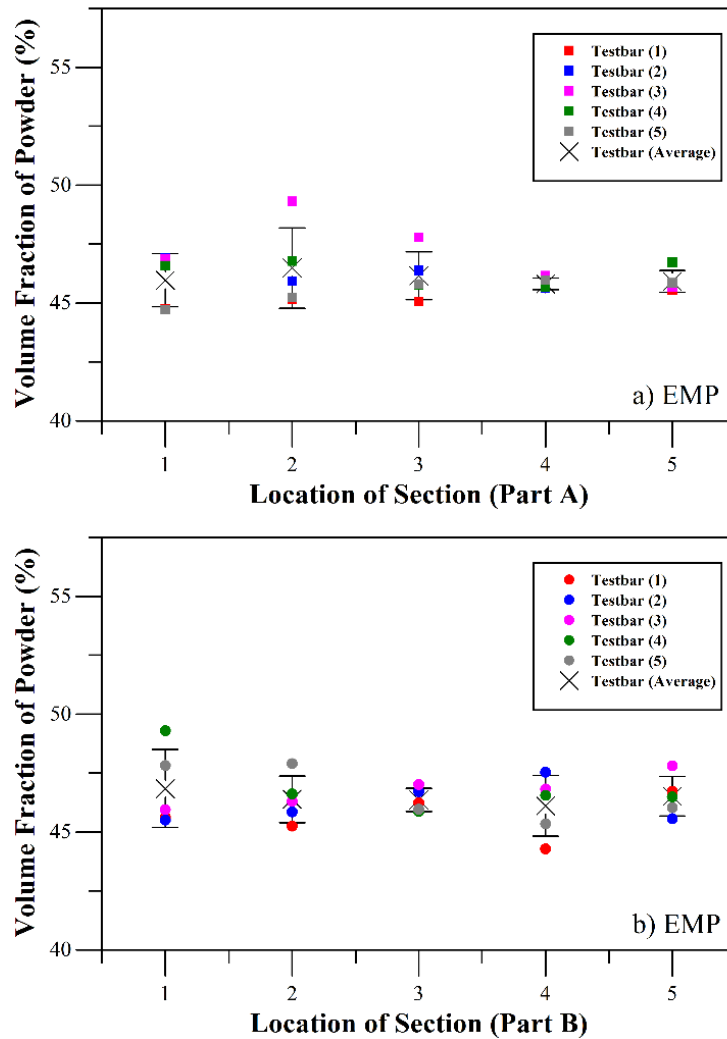


Figure 4.8. Volume fraction of powders in Test-bar based on empirical model (EMP) a) Part A and b) Part B.

Figure. 4.9 shows the average volume fraction of powder in each section along the test-bar for part (A) and (B) using the TGA results. From Figure. 4.9, the TGA results for part A and B show slight decrease in sections 3 and 4 of the test-bar. This indicates lower volume fraction of powder in the middle section of the test-bars. This uneven distribution of powder in the test-bar can cause warpage during firing.

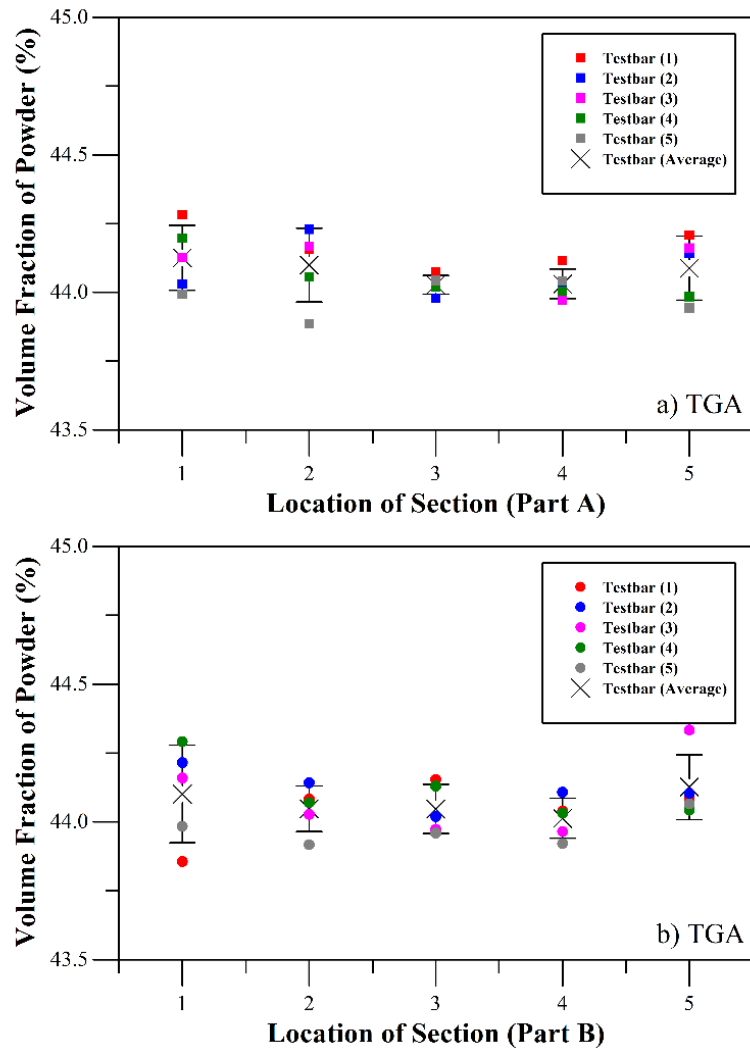


Figure. 4.9. Volume fraction of powders in test-bar from TGA a) Part A and b) Part B.

Figure 4.10 shows the average volume fraction of powder and variation in each section along the test-bar for part (A) and (B) using the TGA and the DSC results. The comparison shows the sensitivity of each measurement technique with the TGA having the lowest variation in measurements and closest to nominal volume fraction of silicon nitride powder in the silicon nitride feedstock. Table 4.4 presents the comparison of both methods and models. The methods are compared on the difference from nominal volume fraction of silicon nitride powder, variation in measurements and time taken for each test.

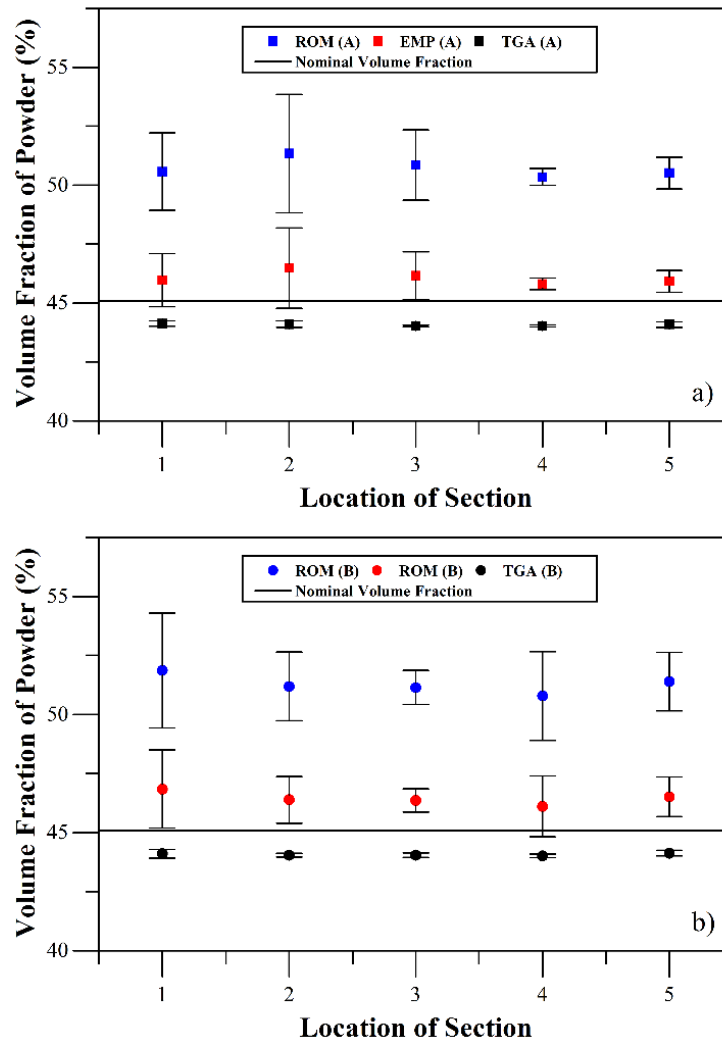


Figure 4.10. Volume fraction of powders in test-bar from TGA, rule of mixture model (ROM) and empirical model (EMP), a) Part A and b) Part B.

The TGA results have a variation of 0.177 for the five experiments and up to 1.07 vol% difference from the nominal volume fraction of powder (45.08 vol%). The DSC results using the rule of mixture (ROM) have a variation of 2.510 for the five experiments and up to a 6.78 vol% difference while the empirical model (EMP) gives a variation of 1.710 for the five experiments and up to a 1.78 vol% difference the nominal volume fraction of powder.

Table 4.4. Comparison between TGA and DSC.

Measurement technique	Difference (vol.%)	Variation (vol.%)	Ramp (°C/min)	Time taken (min)
TGA	1.07	0.177	10	68.5
DSC	6.78 (ROM) 1.76 (EMP)	2.510 (ROM) 1.710 (EMP)	5	36.8

The low variation in the TGA measurements indicates that the TGA can measure the powder content in feedstock and green bodies with good accuracy. In Table 4.4, the variation in volume fraction of powder across the test-bars is a good indication of the magnitude of segregation. Even though the DSC results have higher deviations compared to the TGA results, the results showed similar trend in terms of the powder distribution. The ROM model did not give reasonable accuracy to measure the powder volume fraction along the green body. However, the EMP model shows potential as a method to determine the point to point powder distribution in a green body. If the ramp temperature used in the DSC tests are increased to 10 °C/min, it would shorten the time taken for each experiment. This would allow the DSC tests to be 3 times faster than the TGA test at quantifying the powder distribution in a green body.

4.5 Summary

In this chapter, the experimental analysis of powder distribution within an injection moulded silicon nitride green body is presented. The DSC and TGA were developed to measure the volume fraction of silicon nitride powder in injection moulded test-bars. The ROM model and EMP model were developed with the DSC to determine the volume fraction of silicon nitride based on the heat fusion data of each test. The TGA measures the volume fraction of silicon nitride in the test-bar by measuring the residual weight after a heated process.

The experimental results show that the TGA has better accuracy at measuring point to point volume fraction of silicon nitride as compared to the DSC method using the ROM model and EMP model. The EMP model shows potential to be further developed as a method to measure the powder distribution in a green body. The experimental results from the TGA will be used to validate the powder distribution simulation results from the numerical models developed in Chapter 5.

Chapter 5. Numerical modelling of powder injection moulding of silicon nitride

The addition of ceramic or metal powders to polymers in powder injection moulding complicates the behaviour of the feedstock during mould filling. Typical injection moulding simulation only considers the material behaviour of the powder-based feedstock in the numerical models without considering the relationship between the powder and binder during moulding conditions. Powder-binder separation is a common, yet challenging issue during injection moulding which leads to inhomogeneity in the green bodies. In Chapter 5, two types of numerical models developed to simulate the powder-binder separation phenomenon during the powder injection moulding process are presented. The material input parameters used in the numerical models are based on the HMD-NBV and HMD-V presented in Chapter 3.

In Section 5.1, a numerical model is developed based on the SBM to model the shear-induced migration of particles in a suspension fluid. The numerical model is implemented using the Moldex3D, a Computer-aided Engineering software to simulate the multiple stages of the injection moulding process. Presented in Chapter 3, the HMD-NBV and HMD-V are used to develop the required material input parameters for the numerical models. The numerical models are used to simulate the filling and packing stages and the numerical results in each stage are studied. The numerical results show the effects of overpredicted material properties from the HMD-NBV and HMD-V have on the green bodies.

In Section 5.2, a simulation model is developed based on the Eulerian-Eulerian method by using a TFM to simulate powder-binder separation during mould filling. The numerical model is implemented in ANSYS-CFX to consider the interphase drag forces between the silicon nitride powder and the binder. The interphase drag forces are modelled based on a drag coefficient equation from literature [192]. Thereafter, numerical results are analysed to study the effects of local shear strain gradient on the flow, viscosity and drag coefficient.

The initial and boundary conditions in both simulations are kept as close to the real conditions used to fabricate the silicon nitride test-bars as possible. However, there are a number of differences in boundary conditions and input parameter between simulation

software used for SBM and TFM. For example, in the moulding software used for SBM, the geometries of cavity, runner, cooling channels and mould were considered while the software used for the TFM considered only a simplified geometry of the cavity. There are also difference in the fluid mechanics between the SBM and TFM where the SBM considers the silicon nitride feedstock as a Newtonian fluid which only uses the material properties of the feedstock. Whereas, TFM considers the silicon nitride feedstock as two phases where silicon nitride powder and binder system are modelled individually. Therefore, material properties of the silicon nitride powder and the binder system are used in TFM.

Finally, in Section 5.3, the numerical results for filling patterns and powder distribution are compared between the SBM and TFM based numerical models. The powder distribution results from all the numerical models will be validated using the experimental results of the silicon nitride powder distribution in green bodies presented in Chapter 4.

5.1 Numerical modelling of silicon nitride injection moulding with suspension balance model

The use of SBMs to simulate PIM have been developed by several authors to study the flow-induced migration of particles or fibres in injection moulding. Jenni et al. [90], [92] studied the powder distribution of with the SBM developed in Matlab and validated the powder distribution results using the DSC. Tseng et al. [60] developed a SBM to study the powder concentration in a gear that was injection moulded with BASF 316L feedstock. Tseng et al. [66] further develop the model to study the migration behaviour of fibres during injection moulding to predict the fibre concentration with in the moulded composites. This SBM has been shown to be useful in simulating PIM.

Moldex3D developed a CAE approach for the injection moulding simulation and the PIM package was used to simulate the filling and packing stage close to the physical conditions used to fabricate the silicon nitride test-bars. Figure 5.1 shows a flow diagram that describes the methodical steps taken to develop the numerical models in this section. First, the geometries used for the simulation models were created and meshed. Thereafter, silicon nitride feedstock material profiles were developed using the material input parameters from HMD-NBV and HMD-V presented in Section 3.3. Next, the injection moulding machine was selected based on the model, make and specifications. This defines the dimensions of the barrel and process limits for the numerical models. The appropriate solver setting was selected with the desired analysis mode and output results. The initial and boundary

condition in all the simulation was kept as close to the actual powder injection moulding process conditions as possible. Throughout Section 5.1, several assumptions were made to develop the numerical models and the assumptions in each step will be discussed in detail in the following sections. In the next section, the equations modelling the flow and the discretisation method that is used by Moldex3D will be defined.

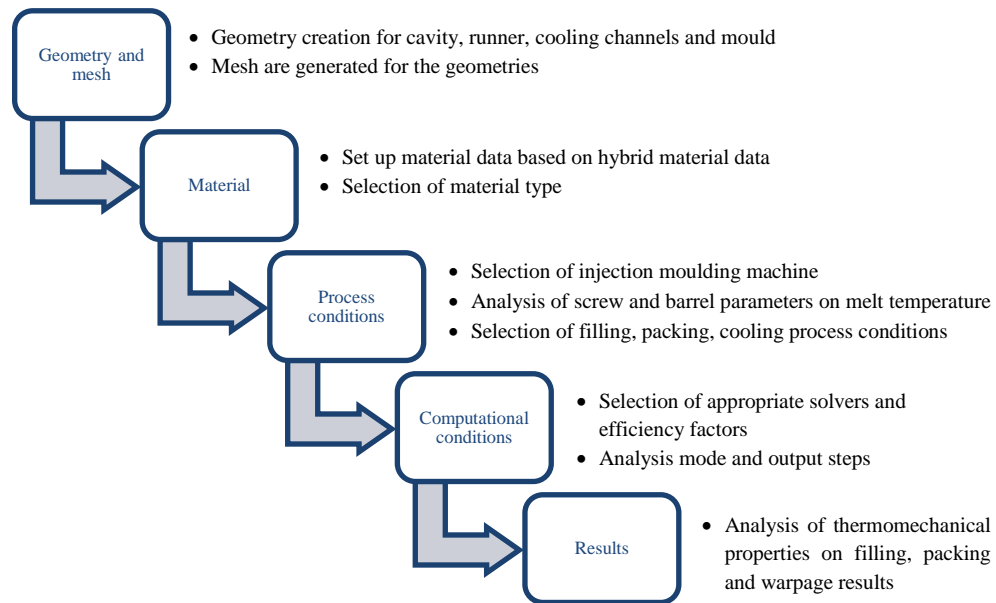


Figure 5.1. Schematic approach for the numerical study of the silicon nitride injection moulding in Moldex3D.

5.1.1 Simulation principles for suspension balance model

There are various discretization methods employed for solving the governing equations used in numerical simulations developed for powder injection moulding. The discretisation method used in Moldex3D for solid geometries is based on the Finite Volume Method (FVM), which can deal with complex geometry and it is used for its robustness and efficiency to solve transient flow field in three dimensional models. The incompressible Navier-Stokes equations are discretised and solved using the collocated FVM with pressure and velocity coupled using the Semi-Implicit Method for Pressure Linked Equations (SIMPLE) algorithm. A more detailed explanation to discretization method can be found in the paper by Chang and Yang [193]. In this study, the silicon nitride feedstock is assumed to be transient, non-Newtonian and non-isothermal. The governing equations [194] to describe the transient and non-isothermal flow are shown in Equations (5.1) to (5.4), where the equation of continuity is given by:

$$\frac{\partial \rho}{\partial t} + \nabla \cdot (\rho U) = 0 \quad (5.1)$$

where ρ is the fluid density, U the velocity vector and ∇ denotes the gradient operator. The equation of motion is given by:

$$\frac{\partial \rho}{\partial t} (\rho U) + \nabla \cdot (\rho U U - \sigma) = \rho g \quad (5.2)$$

where g is the acceleration vector of gravity and the total stress tensor σ is defined as:

$$\sigma = -pI + \eta(\nabla U + \nabla U^T) \quad (5.3)$$

where p is pressure, I is the unit tensor, T the temperature and η the viscosity. The equation of energy is given by:

$$\rho C_p \left(\frac{\partial T}{\partial t} + U \cdot \nabla T \right) = \nabla \cdot (k \nabla T) + \eta \dot{\gamma}^2 \quad (5.4)$$

where C_p is the specific heat capacity, k the thermal conductivity and $\dot{\gamma}$ the shear rate. The volume/density as a function of temperature and pressure of the silicon nitride feedstock is expressed by the two-domain Tait model. The viscosity of the silicon nitride feedstock is represented by the Cross-WLF model, which describes the viscosity of the fluid as a function of temperature, pressure and shear rate. The equations to these models can be found in Section 2.1 and the data-fitted coefficients can be found in Section 5.1.3. SBM considers the suspension flow of inelastic spherical particles in a Newtonian fluid. The interaction between the particles are driven by viscous, hydrodynamic and non-Brownian forces with no external field with the exception of gravity. After averaging over the particulate volume and dividing by density of the particle, the particle-phase conservation equation [61], [89] is given by:

$$\frac{\partial \phi_p}{\partial t} + \langle U \rangle \cdot \nabla \phi_p = -\nabla \cdot j_{\perp} \quad (5.5)$$

$$j_{\perp} = \phi_p (U_p - \langle U \rangle) \quad (5.6)$$

where ϕ_p is the particle volume fraction, $\langle U \rangle$ is the suspension average velocity, j_{\perp} is the particle flux relative to the mean suspension motion and U_p is the local average velocity of the particle phase. Assuming Stokes flow, the particle flux as seen in Equation (5.7) can be acquired by averaging the general momentum balance over the particulate phase, focusing on the low Reynolds numbers and impartially buoyant condition.

$$j_{\perp} = \frac{2r_p^2}{9\eta_f} f(\phi) \nabla \cdot \Sigma_p \quad (5.7)$$

where r_p is the particle radius, η_f is the viscosity of the suspending fluid, Σ_p is the particle contribution to stress and $f(\phi)$ is the sedimentation hindrance function. The details to the particle stress tensor can be found in these papers [61], [195]. The sedimentation hindrance function is a modified form of the function defined Richardson and Zaki [196] to ensure that particle migration ceases when the particle concentration approaches maximum packing. The sedimentation hindrance function is given by:

$$f(\phi) = (1 - \phi_p/\phi_m)(1 - \phi_p)^{a_f-1} \quad (5.8)$$

where ϕ_m is the maximum packing fraction and a_f is an index of particle friction. The maximum packing fraction cannot be controlled in Moldex3D and index of particle friction is suggested from a range of 2 to 4. The index of particle friction a_f as defined by Moldex3D [60] is based on the fluidisation experiments by Richardson and Zaki [196] for spherical and non-spherical particles in water, glycerol and oil. Richardson and Zaki [196] observed the a_f to be in the range of 2 to 5. experimental observations of Hampton et al. [197] in tube flow and Miller [62] for channel flow suggests a value of $a_f = 2$. Therefore, the index of particle friction used in the Moldex3D simulation is 2.

5.1.2 Geometry and mesh

The four main geometries of cavity, runner, cooling channels and mould were developed for the simulation models in Moldex3D. Figure 5.2 shows the geometries and dimensions of the cavity (test-bar), runner and two cooling channels. The cavity is a depression in the mould that holds the shape of the component. The runner is a channel that is cut into the mould. It is the point of entry for feedstock melt to enter into the cavity from the nozzle of the injection barrel. The cooling channels are passages for coolants to flow through the mould to cool the

component uniformly before it is ejected. Lastly, the mould is the tooling that holds all the components together in an injection moulding machine. The simple geometry of a test-bar is selected as it allows distinct sectioning of the geometry for the powder distribution measurements using the DSC and TGA which can be used to validate the numerical models developed in this study.

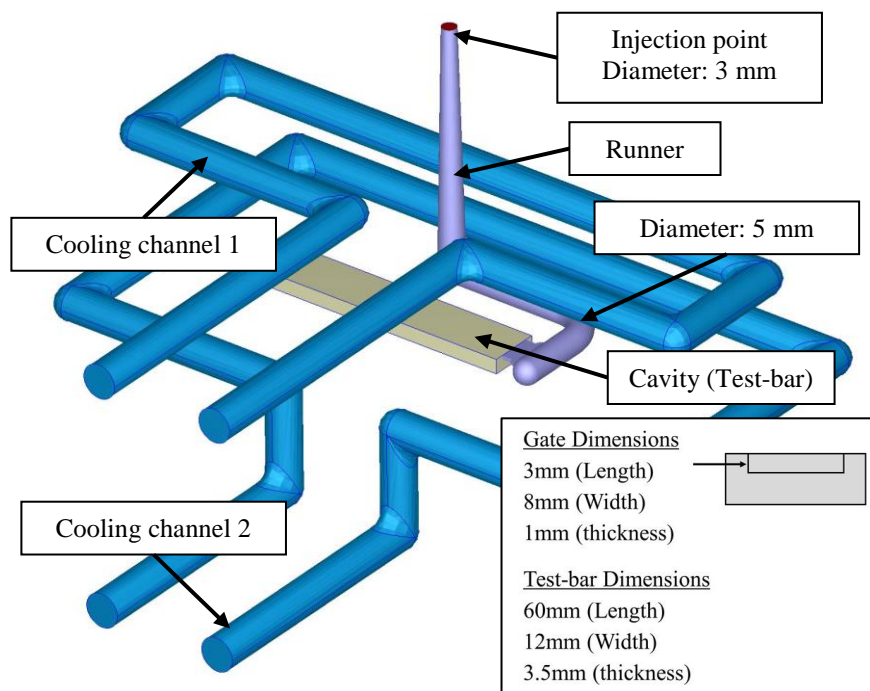


Figure 5.2. Geometries of cavity, runner and cooling channels with dimensions of test-bar, gate and runner.

The cavity and runner were created in SolidWorks and have a total volume of 2.519 cm^3 and 2.798 cm^3 , respectively. The Step files of the cavity and runner were then imported into Moldex3D eDesign where they were defined by component type for Moldex3D to recognise each component. Solid mesh was generated for the test-bar, runner and cooling channels. The Moldex3D eDesign was used to generate the mesh. In Figure 5.3 and the test-bar has mesh node count of 110,897 and mesh element count of 100,627. The size of the element on the surface was generally around 0.5 mm and the eDesign tool ensure that were sufficient layers in the internal mesh.

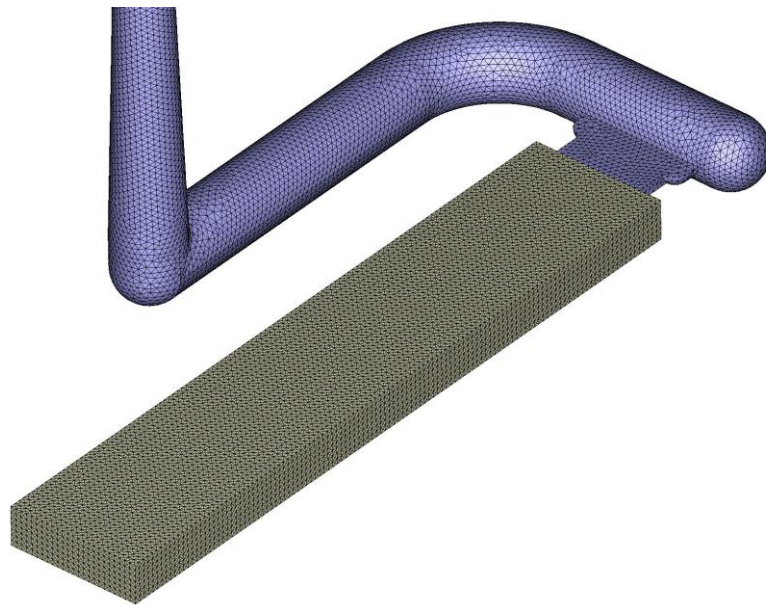


Figure 5.3. Test-bar meshed with tetrahedral element.

In Figure 5.4(a) and (b), the dimensions to the geometries for the cooling channels are presented. The cooling channels were created in the Moldex3D eDesign. The dimensions of the geometries and the positions of each component were defined exactly as close to the real-life conditions as possible. Component type were defined for the cooling channels.

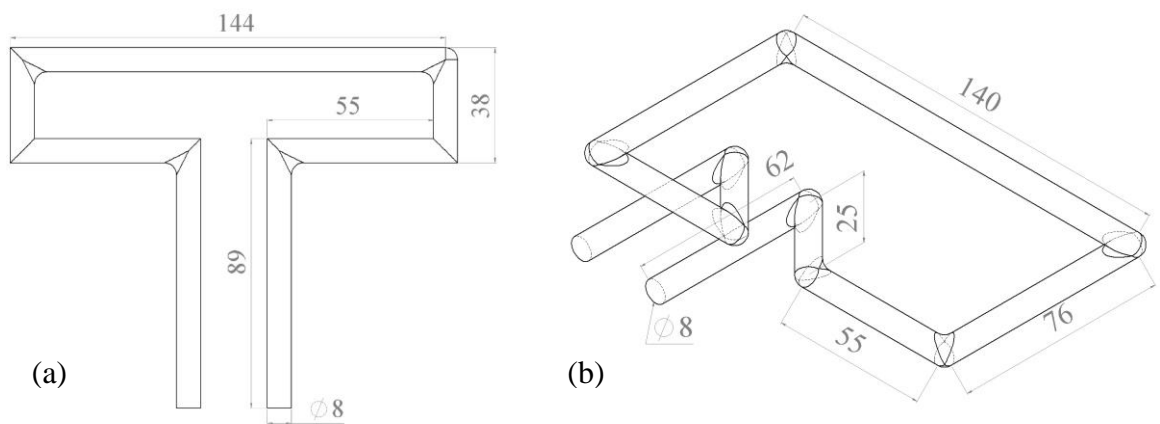


Figure 5.4. (a) Dimension of cooling channel 1 and (b) dimension of cooling channel 2.

Figure 5.5 shows the four geometries assembled with the dimensions of the mould. The location of the parting line on the mould was specified and indicated by the red line shown in Figure 5.5. This is where the mould will separate after injection moulding process is completed. The parting and closing direction of the mould were indicated by the yellow arrows shown in Figure 5.5. The perimeter around the cavity where the parting line meets is

where the venting was defined. Venting is the where the atmosphere in the cavity is vent out of the mould during injection moulding. In Figure 5.5, the cooling channel inlet and outlet were specified for coolant fluid to flow in and out of the channels. Oil is used as the coolant fluid in the real-life injection moulding process of the silicon nitride test-bar and it was used in these numerical models.

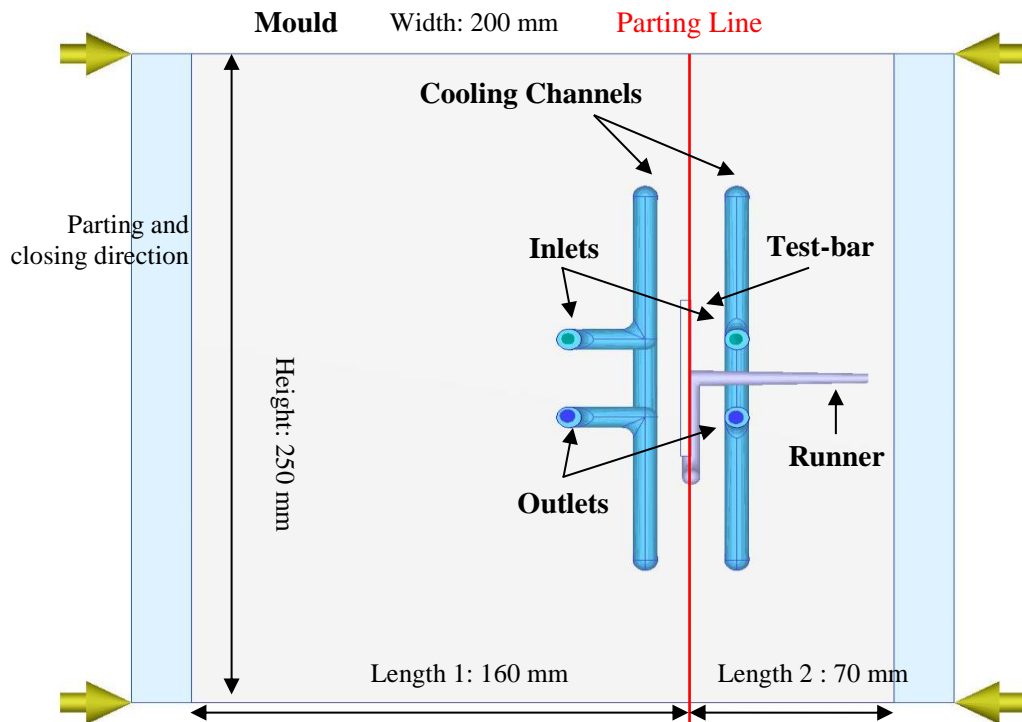


Figure 5.5. Four main geometries used injection moulding simulation in Moldex3D.

5.1.3 Material data

Moldex3D can be developed for a wide variety of injection moulding processes such as multi-component injection moulding, co-injection moulding, resin transfer moulding and powder injection moulding. Depending on the area of application, the material profile developed for it will require more sets of material properties. In the case of PIM, the material properties needed are density, specific heat capacity, viscosity, particle size distribution, elastic modulus, thermal conductivity, coefficient of thermal expansion and specific volume. The significance of each property in the powder injection moulding simulation is summarised in Table 5.1. The injection moulding process is a dynamic non-isothermal process with temperature and pressure change that occurs in a short period of time. Therefore, several material properties in the Moldex3D material profile need to be characterised over a function of temperature and pressure.

Table 5.1. Summary of the significant of each material properties.

Material property	Type of analysis needed
Density	Filling and packing analysis
Specific heat capacity	Filling, packing and cooling analysis
Viscosity	Filling and packing analysis
Powder size	Powder concentration analysis
Powder volume fraction	Powder concentration analysis
Elastic modulus	Filling and packing analysis
Poisson ratio	Filling and packing analysis
Thermal conductivity	Filling, packing and cooling analysis
Coefficient of thermal expansion	Thermal analysis
Specific volume	Filling and packing analysis

Presented in Chapter 3, the hybrid material data are a combination of estimated and experimental material data that can be used as material input parameters for powder-based feedstock. In Section 5.1, to develop the thermomechanical properties of the silicon nitride feedstock based on HMD-NBV and HMD-V were used in the numerical models. The experimental data of density, viscosity, specific heat capacity and particle size distribution were tested at Dou Yee Technologies and University of Glasgow while material properties such as thermal conductivity, elastic modulus, specific volume and coefficient of thermal expansion were estimated using theoretical models and material data available in literature.

Table 5.2 summarises single value thermomechanical properties used in the Moldex3D material profile. The elastic modulus and CTE were estimated using the HMD-NBV and HMD-V. The density, powder volume fraction and mean particle size were determined using pycnometer, digital microscope and TGA presented in Section 3.1 and 4.3. The estimated elastic modulus by Nielsen model is 24.28 times lower than the elastic modulus estimated by Voigt model. This is due the overestimation of elastic modulus by the Voigt model as it is an upper-bound model. In Section 3.2, the Voigt model has been shown to overestimate the elastic modulus of powder-polymer mixture ranging from 2.46 to 34.87 times the experimental data. The elastic modulus is an important material attribute as it determines the strength of the green body and overestimating the elastic modulus may affect the moulding results from the numerical models.

Table 5.2. Summary of thermomechanical properties of silicon nitride feedstock.

Thermomechanical properties	HMD-NBV	HMD-V
Elastic modulus	5.858 GPa (Nielsen)	142.233 (Voigt)
CTE	80.62 PPM/°C (Blackburn)	84.48 (Voigt)
Density	1.9633 g/cm ³	
Powder volume fraction	43.9 vol%	
Mean particle size	3.6 μm	

The effects of temperature, pressure and shear rate are considered for the rest of the thermomechanical properties such as thermal conductivity, specific volume, specific heat capacity and viscosity. Figure 5.6 shows the thermal conductivity of silicon nitride feedstock estimated using the HMD-NBV and HMD-V. Taking into consideration the actual injection pressure applied onto the feedstock melt of 157.6 MPa, the thermal conductivity data of the silicon nitride feedstock at 150 MPa was used. The HMD-NBV uses the Nielsen model to estimate thermal conductivity while HMD-V uses the Voigt model. In the Moldex3D material profile of the silicon nitride feedstock, the thermal conductivity was compiled as tabulated thermal conductivity data for the two hybrid material data. A transition temperature should be observed in the thermal conductivity as silicon nitride feedstock melts into molten state when heated in the injection machine barrel. In Figure 5.6, the transition temperature for HMD-NBV can be observed between 160 and 170°C while HMD-V does not have an apparent transition temperature. Moreover, the average thermal conductivity of silicon nitride feedstock predicted by the Voigt model is 4.94 times more than the predicted thermal conductivity by Nielsen model.

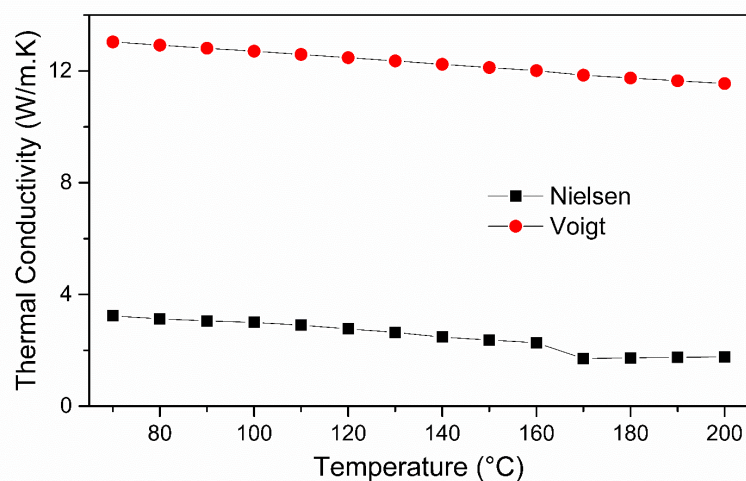


Figure 5.6. Estimated thermal conductivity of silicon nitride feedstock using Nielsen model and Voigt model at 150 MPa.

In Section 3.3.4, the Voigt model was used to estimate the PVT data of the silicon nitride feedstock using measured density of silicon nitride and specific volume data of HDPE found in literature [191]. Both HMD-NBV and HMD-V are using the same PVT data estimated from the Voigt model. Figure 5.7 shows the estimated PVT data of the silicon nitride feedstock. From Figure 5.7, the PVT data is observed to encompass a wide range of temperature and pressure. The advantage of having the vast range of PVT data of a feedstock enables unconventional moulding conditions to be tested out in simulations. The predicted PVT data is curve-fitted by the two-domain Tait model [132], [133] to represent the specific volume of the silicon nitride feedstock over a range of temperature and pressure.

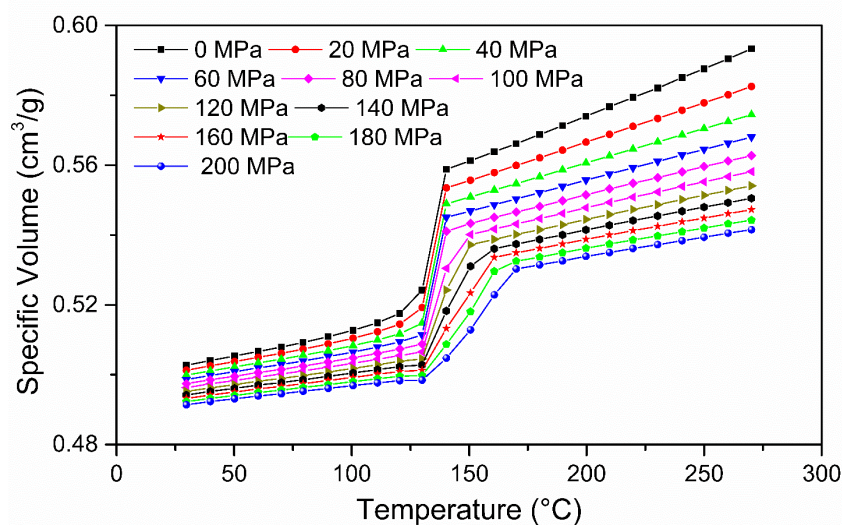


Figure 5.7. Estimated PVT data of silicon nitride feedstock using Voigt model.

Table 5.3 summarises the coefficient values for the two-domain Tait model that are input parameters for the Moldex3D material profile. With the coefficient values, the simulation models will be able to calculate the specific volume of the silicon nitride feedstock at the given temperature and pressure depending on the moulding conditions. In Section 3.1.2, the average specific heat capacity of the silicon nitride feedstock was determined using the differential scanning calorimetry. Figure 3.2. shows the average specific heat capacity of the silicon nitride feedstock given over a function of temperature which is used in both HMD-NBV and HMD-V. In Section 3.1.3, the viscosity of silicon nitride feedstock was determined using a capillary rheometer and curve-fitted with the Cross-WLF model [110]. Figure 3.5 shows the viscosity data which is used in both hybrid material data. The viscosity data are observed to encompass a wide temperature and shear rate range. The advantage of having a

wide range of viscosity data of a feedstock ensures that the rheological behaviour of the feedstock is well represented during moulding.

Table 5.3. Two-domain Tait model coefficient values.

Coefficient	Value	Coefficient	Value
b_{1m}	0.5566	b_{1s}	0.5124
b_{2m}	0.00026	b_{2s}	8.36E-05
b_{3m}	2.14E+09	b_{3s}	5.35E+09
b_{4m}	0.004433	b_{4s}	0.001927
b_5	407.99	b_6	1.00E-08
b_7	0.0321	b_8	0.1
b_9	1.07E-09	C	8.94E-02

Table 5.4 summarises the coefficient values for the Cross-WLF model that will be used as input parameters for the Moldex3D material profile. With the coefficient values, the simulation models will be able to calculate the viscosity of the silicon nitride feedstock at a given temperature and shear rate depending on the moulding conditions. By capturing the rheological behaviour of a feedstock, the filling patterns of unconventional moulding conditions can be tested out and studied in simulations.

Table 5.4. Cross-WLF coefficient values.

Coefficient	A_1	A_2	D_1	T^*	n	τ^*
Value	17.96	51.6	1.646 x 10 ⁹	325.81	0.482	8758.27

5.1.4 Process conditions

In comparison to other injection moulding analysis packages, Moldex3D provides the user with the ability to customise the injection moulding machine specifications. This will match the simulation models closely to the actual injection moulding conditions and machine limits. The simulation models can only be defined with injection parameters that are within the working limits of the actual injection moulding machine used. An Engel ES200/45 HLS injection moulding machine was used to fabricate the silicon nitride test-bars with aforementioned dimensions. The Moldex3D injection moulding machine database did not have the Engel ES200/45 HLS. A model (Engel VC200/80) that closely match the Engel ES200/45 HLS in terms of specification was used instead. The specification of Engel VC200/80 in Moldex3D was modified to fit the technical specification of Engel ES200/45

HLS. Table 5.5 summarised the injection moulding machine specification of the Engel ES200/45 HLS.

Table 5.5. Engel ES200/45 HLS injection moulding machine specification.

Machine attribute	Value (units)
Maximum hydraulic pressure	151 (bar)
Machine intensification ratio	10.43
Maximum injection pressure	1576 (bar)
Maximum injection speed	211 (mm/s)
Maximum injection rate	104 (cm ³ /s)
Maximum clamping force	450 (kN)
Barrel diameter	25 (mm)
Nozzle diameter	2 (mm)
Screw stroke	140 (mm)

Figure 5.8 shows a schematic diagram of an injection moulding machine and where the hydraulic pressure and injection pressure are applied. The hydraulic pressure is the pressure supplied by the hydraulic pump which is controlled by the input parameters on the control panel of the injection machine. The injection pressure is the pressure applied directly to the feedstock melt by the ram.

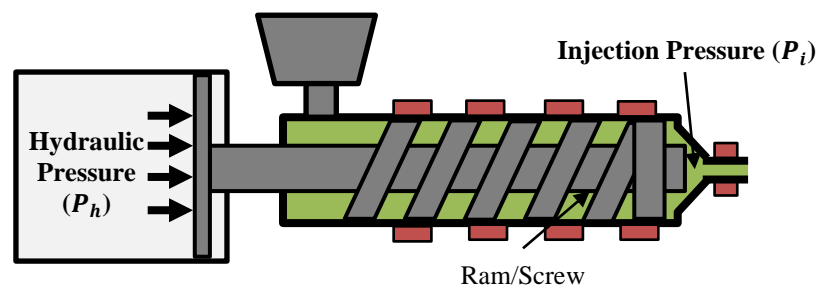


Figure 5.8. Schematic diagram of injection moulding machine showing hydraulic and injection pressure.

In Figure 5.8, the hydraulic pressure supplied to the injection machine is translated to the injection pressure and this relationship is described by a machine intensification ratio given by:

$$\frac{P_h}{P_i} = IR \tag{5.9}$$

where P_h is the hydraulic pressure, P_i is the injection pressure and IR is the intensification ratio. Moldex3D uses the injection pressure applied to feedstock melt for its numerical models. Therefore, the Engel ES200/45 HLS pressure parameters that were used to fabricate the silicon nitride test-bars need to be translated into equivalent injection pressure data for

the simulation models. The input parameters include injection pressure, holding pressure and back pressure. Usually the nozzle temperature or last zone temperature is used as the melt temperature for an injection moulding simulation. However, this is not a realistic estimation of the melt temperature expected from the real-life injection moulding conditions. The shearing from the screw during moulding and the material properties of the feedstock may result in an increase or decrease in the melt temperature after heating. The ScrewPlus is an analysis package in Moldex3D that takes the design of the screw, process conditions and thermomechanical properties of the feedstock to estimate the melt temperature of the feedstock.

For the suspension models developed in Section 5.1, ScrewPlus is used to estimate the true melt temperature of the silicon nitride feedstock based on the dimension of the barrel and screw used in the Engel ES200/45 HLS, temperature parameters of the barrel, back pressure input parameter and the thermomechanical properties of the feedstock. Considering the difference in thermomechanical properties between HMD-NBV and HMD-V, the estimated melt temperatures of silicon nitride feedstock for HMD-NBV and HMD-V are expected to be different. The injection machine barrel related process conditions and dimensions for barrel and screw are summarised in Table 5.6.

Table 5.6. Screw specification used for feedstock melt analysis.

Machine attribute	Value (units)	Machine attribute	Value (units)
Barrel length	635 (mm)	Barrel zone 1 (length)	185 (mm)
Screw length	635 (mm)	Barrel zone 2 (length)	150 (mm)
Back pressure	0.06 (MPa)	Barrel zone 3 (length)	150 (mm)
Barrel zone 1 (temperature)	185 (°C)	Barrel zone 4 (length)	150 (mm)
Barrel zone 2 (temperature)	185 (°C)	Channel depth	2.2 (mm)
Barrel zone 3 (temperature)	185 (°C)	Flight pitch	30 (mm)
Barrel zone 4 (temperature)	185 (°C)	Flight width	3 (mm)
Nozzle temperature	185 (°C)	Number of flights	1

Through the ScrewPlus analysis, a melt temperature of 190 °C was determined for using the material properties from HMD-NBV while HMD-V gave a melt temperature of 194.9 °C. As presented in Section 3.3, the difference in thermomechanical properties between the two hybrid material data are the elastic modulus, CTE and thermal conductivity. It is hypothesised that the higher melt temperature estimated by the ScrewPlus analysis is due to the significantly higher thermal conductivity in the HMD-V (4.94 times) than the HMD-

NBV. By having a higher melt temperature, the silicon nitride feedstock in the numerical model with material profile based on the HMD-NBV may result in lower density, viscosity and higher specific heat capacity than using HMD-V. The estimates from the ScrewPlus analysis showed that the process conditions used resulted in melt temperatures higher than barrel temperatures.

5.1.5 Computational conditions

The injection moulding process was performed at injection speed from 90 to 70 mm/s, with barrel temperature of 185 °C, mould temperature of 110 °C, injection pressure of 157.6 MPa and holding pressure of 20.9 MPa. The injection mould was heated by oil which was pumped through the cooling channels and the mould temperature was assumed to be uniform. The injection speed used is separated into 3 stages starting at 90 mm/s with decrements of 10 mm/s to 70 mm/s. Each stage of injection speed is defined by the position of the ram/screw. During each injection moulding cycle, the ram/screw moves to a pre-defined backward position to allow feedstock melt to fill the front of the barrel. This defined backward position is an input parameter known as ram position. This is essentially the volume of feedstock required to fill the cavity completely. The ram position used to fabricate the silicon nitride test-bars in the injection moulding machine was 14 mm. Table 5.7 summarises the boundary conditions that were used in the simulation models.

Table 5.7. Injection moulding process parameters.

Process parameter	Value (units)
Barrel temperature (Zone 1 to 4)	185, 185, 185, 185 (°C)
Nozzle temperature	185 (°C)
Mould temperature	110 (°C)
Cavity volume	5.318 (cm ³)
Dosage/Ram position	13 (mm)
Injection speed 1 (0 to 5.2 mm)	90 (mm/s)
Injection speed 2 (5.2 to 9.1 mm)	80 (mm/s)
Injection speed 3 (9.1 to 13 mm)	70 (mm/s)
Estimate stroke time	1.377 (s)
Maximum injection pressure	157.6 (MPa)
Packing pressure	20.9 (MPa)

The initial and boundary conditions used in Moldex3D simulations were kept as close to the real injection moulding process as possible. Moldex3D requires the injection speed to be

determined based on the percentage of the fill or the ram position. Besides that, Moldex3D estimates the ram position by dividing the total volume of the cavity and runner system by the cross-section of the barrel. The ram position estimated by the software was 13mm which is slightly lower than the input parameters used in the actual moulding. This is due to the cushion setting in the actual moulding. Injection moulding cycles have a cushion to ensure consistent filling at every cycle during mass production. The estimation of the required ram position by Moldex3D can save the need to conduct short-shots study to determine the ram position. The actual injection speed is adjusted to fit the 13 mm ram position used in the numerical models shown in Table 5.7. The stroke time is determined by the simulation package based on the injection moulding speed defined and the estimated ram position.

5.1.6 Injection time, pressure, temperature and viscosity results from the filling stage

The simulation of the mould filling process is considered complete when the cavity was completely filled with the silicon nitride feedstock. The simulation models developed in Moldex3D were based on the SBM using material properties from the two hybrid material data. These are denoted as SBM-NBV and SBM-V for SBM developed with material data from HMD-NBV and HMD-V, respectively. Figure 5.9 shows the numerical observation of the filling pattern and melt front time from SBM-NBV and SBM-V. In Table 5.7, the stroke time estimated by Moldex3D is shorter than the filling time determined by the numerical simulation because it was estimated based on stepwise injection speed while the simulation models considered the gradual change in injection speed for each change in injection speed.

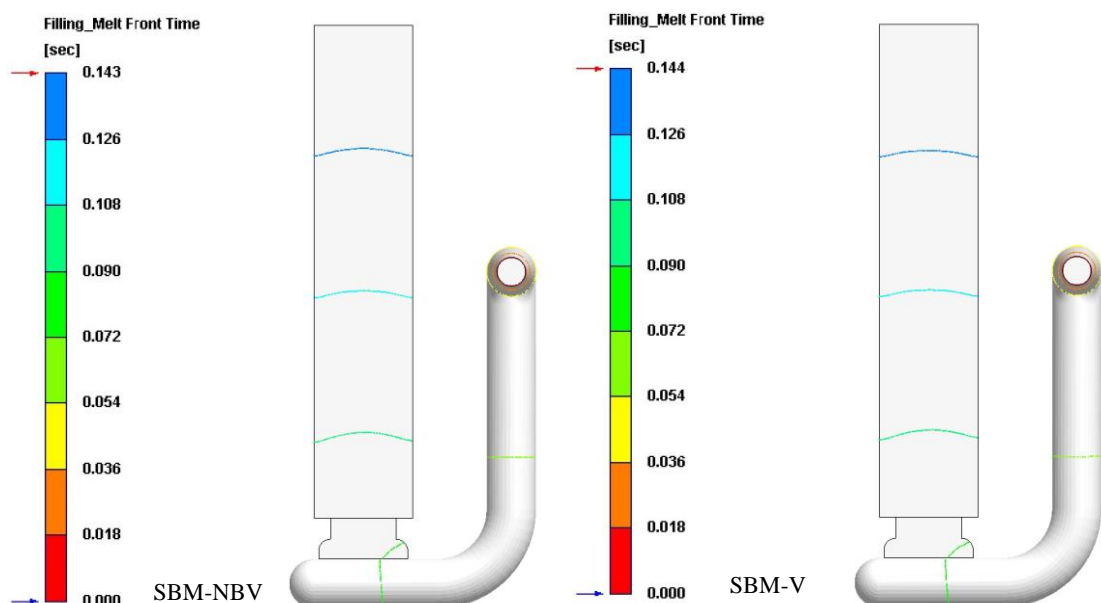


Figure 5.9. Melt front time result from SBM-NBV and SBM-V numerical models.

Chapter 5

The impact of the difference in material data between the HMD-NBV and HMD-V on the filling time is small. The time taken for SBM-NBV and SBM-V to reach the end of fill were 0.143 s and 0.144 s respectively. Considering the difference in elastic modulus between the HMD-NBV and HMD-V is large, it is hypothesised that the elastic modulus did not affect the filling time. The filling time is segmented into 8 contour sections. These are defined by the melt front location at each time interval. The filling patterns from both simulation models can be observed to be similar. The longer filling time observed in SBM-V would suggest that there is more hesitation in the feedstock melt for SBM-V. As the feedstock melt entered the mould, which is at a lower temperature, it started to solidify in the areas that are in contact with the mould. This formed a frozen layer and caused retardation in the movements of the feedstock to fill up the cavity.

The higher thermal conductivity of the silicon nitride feedstock in SBM-V would result in faster rate of heat loss to the mould walls from the feedstock melt and forming the frozen layers sooner than in SBM-NBV. The injection pressure needed to fill the cavity is an indicator of the resistance faced by the feedstock melt. Figure 5.10 shows the injection pressure results between the SBM-NBV and SBM-V at the end of mould filling. The numerical results for injection pressure are segmented into 8 contour sections with similar pressure range for both SBM-NBV and SBM-V. The numerical results for maximum, minimum and mean injection moulding pressure observed in the cavity for SBM-NBV and SBM-V are summarised in Table 5.8. Overall higher injection pressure is required in SBM-V to fill up the cavity.

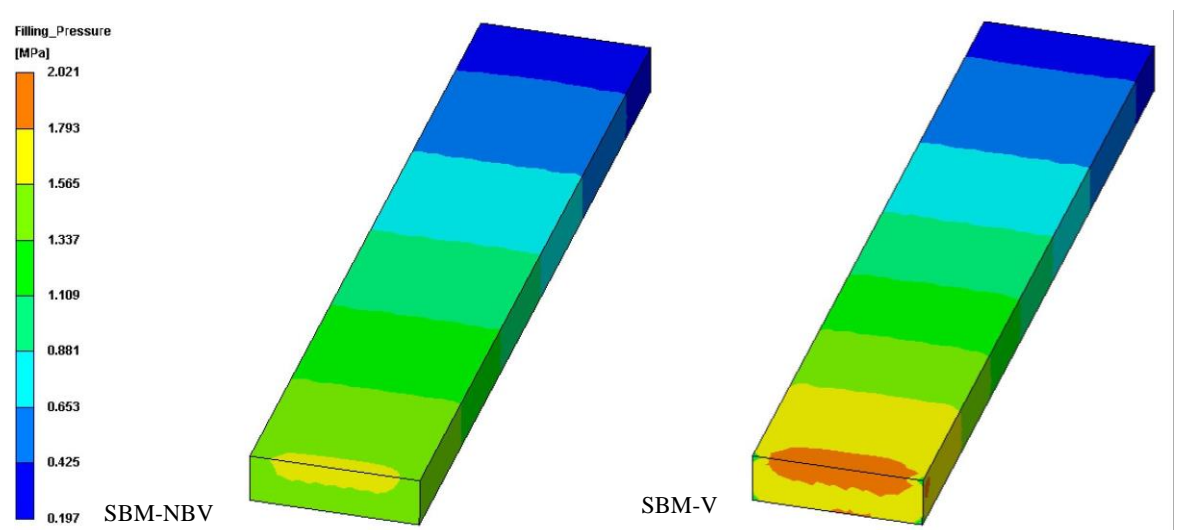


Figure 5.10. Injection pressure results from SBM-NBV and SBM-V numerical models at the end of filling.

Chapter 5

The mean injection pressure in SBM-V is 10.96 % higher in SBM-NBV. This shows that there was significantly more resistance faced by the feedstock melt during mould filling in the SBM-V. The highest pressure in the cavity were recorded at the gate which is the entry point to the cavity. The effective cross-section of the gate is smaller than that of the test-bar and resulted in a smaller flow path. Therefore, as the resistance to the flow is higher in this area, higher shear rates are expected in the areas surrounding the gate due to the high pressure.

Table 5.8. End of filling pressure results from SBM-NBV and SBM-V.

	Max (MPa)	Min (MPa)	Mean (MPa)
SBM-NBV	1.787	0.198	0.921
SBM-V	2.020	0.265	1.022

Figure 5.11 shows the temperature distribution results between the SBM-NBV and SBM-V at the end of mould filling. The numerical results for temperature are segmented into 8 contour sections with similar temperature range for both SBM-NBV and SBM-V. The numerical results for maximum, minimum and mean injection moulding pressure observed in the cavity for SBM-NBV and SBM-V are summarised in Table 5.9. The higher maximum temperature in SBM-V is due to the higher melt temperature used in the simulation. The lower minimum temperature in SBM-V is due to the higher thermal conductivity of the silicon nitride feedstock which resulted in a fast rate of heat loss. As a consequence, the formation of frozen layer in the SBM-V numerical model was faster, resulting in a wider temperature difference in the SBM-V.

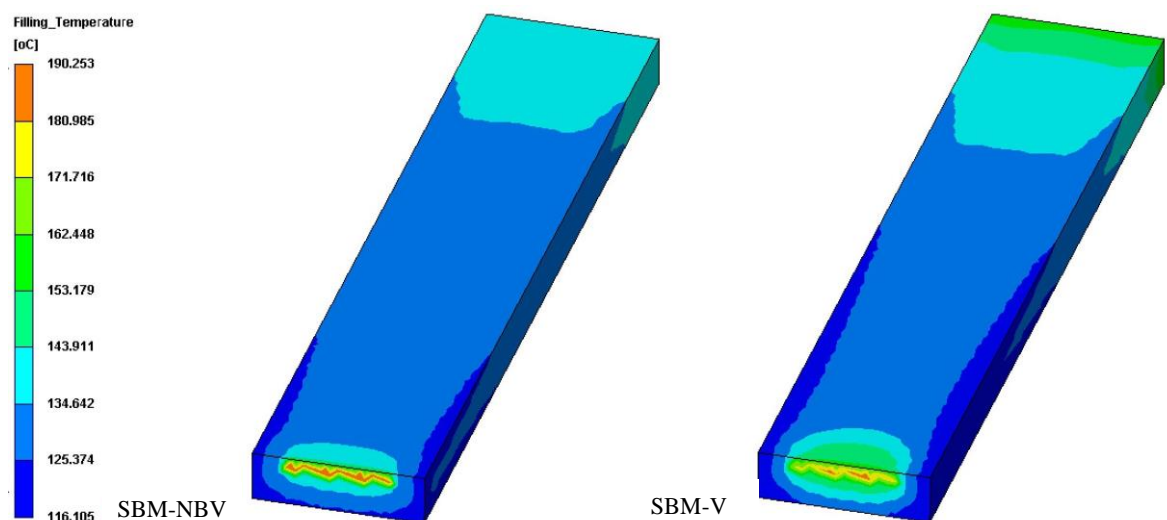


Figure 5.11. Temperature results from SBM-NBV and SBM-V numerical models at the end of filling.

Chapter 5

The temperature difference in the cavity for the SBM-V numerical model was observed to be 74.148 °C while SBM-NBV observed a temperature difference of 69.386 °C. The higher thermal conductivity of the silicon nitride feedstock in SBM-V also resulted in lower average temperature. The average temperature in SBM-V was 168.046 °C while SBM-NBV was 178.173 °C. In Figure 5.11, despite having lower average temperatures in SBM-V, the temperature at the rear of the test-bar can be observed to be higher than SBM-NBV. This shows that the temperatures of the green body are significantly lower at the regions close to the gate. This is because it had longer time to lose heat to the mould walls as compared to the rear.

Table 5.9. End of filling temperatures results from SBM-NBV and SBM-V.

	Max (°C)	Min (°C)	Mean (°C)
SBM-NBV	189.649	120.263	178.173
SBM-V	190.253	116.105	168.046

Figure 5.12 shows the viscosity results of the silicon nitride test-bar between the SBM-NBV and SBM-V at the end of mould filling. The numerical results for viscosity are segmented into 8 contour sections with similar viscosity range for both SBM-NBV and SBM-V. From Figure 5.11 and Figure 5.12, it can be observed that in the regions of low temperature the viscosity of the silicon nitride feedstock is high. This correlates with the viscosity behaviour of the silicon nitride feedstock shown in Figure 3.5. The high viscosity is also an indication that the feedstock has transited into solid state.

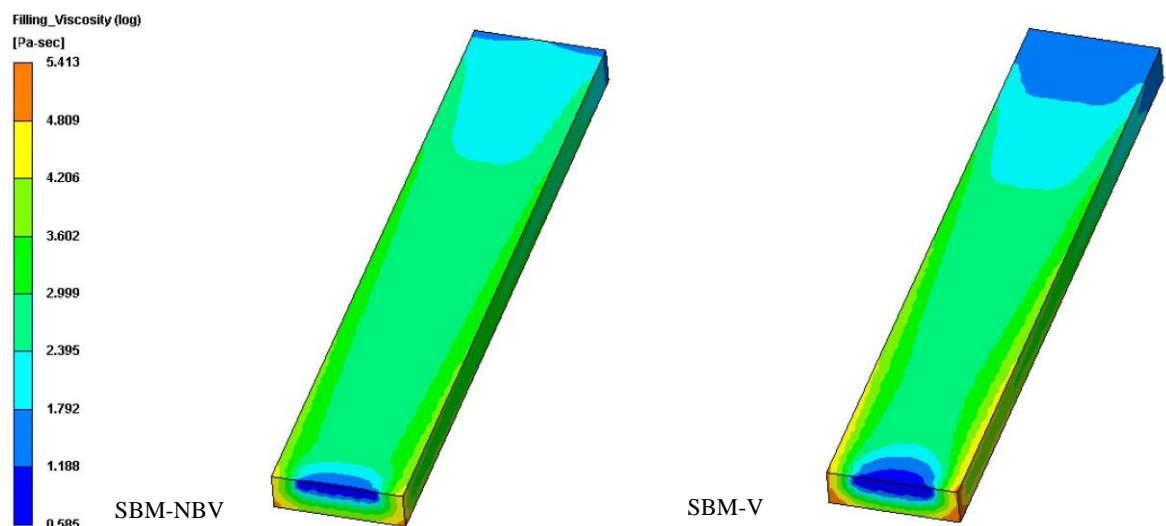


Figure 5.12. Viscosity results from SBM-NBV and SBM-V numerical models at the end of filling.

The viscosity results from the numerical models were in log value and they were converted to integer value. The numerical results for maximum, minimum and mean viscosity observed in the cavity for SBM-NBV and SBM-V are summarised in Table 5.10. A wide viscosity range can be observed in the simulation models. However, the mean viscosity of the silicon nitride feedstock seen in the numerical models are relatively low. This implies that the injection moulding parameters will result in adequate viscosity for moulding. Nonetheless, the wide range of viscosity observed in the cavity meant that the viscosity model used to represent the rheological behaviour of the feedstock has to be characterised with a wide range of experimental data to provide accurate simulation models. The filling results from the numerical models showed that thermal conductivity played an important role towards the thermal related numerical results. The effects of thermal conductivity are further studied with the packing results from the numerical models.

Table 5.10. End of filling viscosity results from SBM-NBV and SBM-V.

	Max (Pa.s)	Min (Pa.s)	Mean (Pa.s)
SBM-NBV	108143.39	3.84	29.10
SBM-V	258821.29	4.89	38.54

5.1.7 Temperature distribution, part weight, volumetric shrinkage, density and powder concentration results from the packing stage

The packing stage starts when the mould is 98% filled as indicated by a switchover sequence. Temperature, volumetric shrinkage, density and powder concentration results were observed from the simulation results. Figure 5.13 shows the temperature distribution results of the silicon nitride test-bar between the SBM-NBV and SBM-V at the end of packing. The numerical results for temperature are segmented into 8 contour sections with similar temperature range for both SBM-NBV and SBM-V. Based on the numerical results, the temperature of the green body has cooled close to the temperature of the oil in the cooling channels.

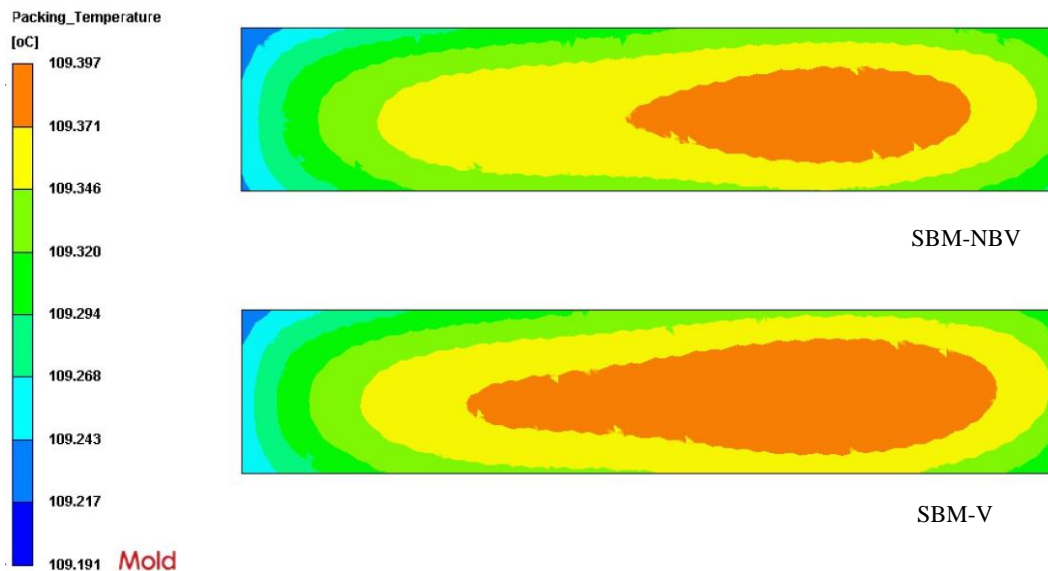


Figure 5.13. Temperature distribution results from SBM-NBV and SBM-V at the end of packing.

The temperature variation throughout the green body is as low as 0.18 % for both SBM-NBV and SBM-V. The maximum and minimum temperatures of the SBM-V simulation model is 109.397 °C and 109.199 °C which is higher than SBM-NBV at 109.388 °C and 109.191 °C. The thermal equilibrium in the cavity was reached at 10.228 s and 4.14 s for SBM-NBV and SBM-V respectively. The higher thermal conductivity of the silicon nitride feedstock in the SBM-V numerical model resulted in the green body reaching thermal equilibrium faster than SBM-NBV.

Figure 5.14 shows the volumetric shrinkage results of the silicon nitride test-bar in comparison between the SBM-NBV and SBM-V at the end of packing. The numerical results for volumetric shrinkage are segmented into 8 contour sections with similar volumetric shrinkage range for both SBM-NBV and SBM-V. The volumetric shrinkage results from the simulation models are close to the that are observed in the powder injection moulding simulation results found literature, which ranged from 0.98 – 4.77% [137], [198], [199]. The volumetric shrinkage results seen in the SBM-NBV is higher than those in SBM-V. The numerical results for maximum, minimum and mean volumetric shrinkages observed in the cavity for SBM-NBV and SBM-V are summarised in Table 5.11.

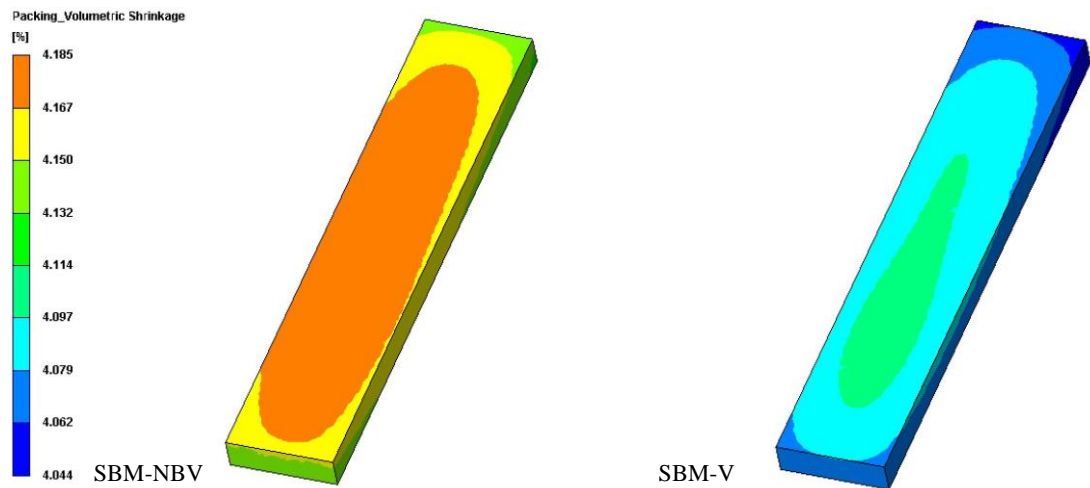


Figure 5.14. Volumetric shrinkage results from SBM-NBV and SBM-V numerical models at the end of packing.

Considering the average temperature observed in SBM-NBV during mould filling was 6 % higher than SBM-V, the temperature drop during packing for SBM-NBV was higher than SBM-V. The 6% higher temperature drop which is approximated 10 °C resulted in 2% more volumetric shrinkage in SBM-NBV. The volumetric shrinkage results showed the change in part volume as it transits from high temperature and pressure experienced through moulding to ambient temperature and pressure. It is determined based on the PVT data of the feedstock. The average part weight of the test-bar measured is 4.55 g. By dividing the weight of the test-bar by the density of the silicon nitride feedstock, the total volume of the injection moulded test-bar is determined as 2.317 cm³. By comparing this volume to the volume of the cavity, the total volumetric shrinkage of the silicon nitride test-bar can be determined as 8%. The is almost twice the volumetric shrinkage calculated by the simulation models and the reason of this is likely due to the lack of accurate PVT data of the silicon nitride feedstock. Hence, the estimation model used to estimate the PVT data requires more validation and perhaps a more accurate model.

Table 5.11. End of packing volumetric shrinkage results from SBM-NBV and SBM-V.

	Max (%)	Min (%)	Mean (%)
SBM-NBV	4.185	4.128	4.163
SBM-V	4.102	4.044	4.080

Figure 5.15 shows the density distribution results of the silicon nitride test-bar between the SBM-NBV and SBM-V at the end of packing. The numerical results for density are segmented into 8 contour sections with similar density range for both SBM-NBV and SBM-V. The numerical results for maximum, minimum and mean packing density observed in the

cavity for SBM-NBV and SBM-V are summarised in Table 5.12. Both numerical models observed lower densities in the region right after the gate, but the SBM-V numerical model can be seen to have a greater drop in density.

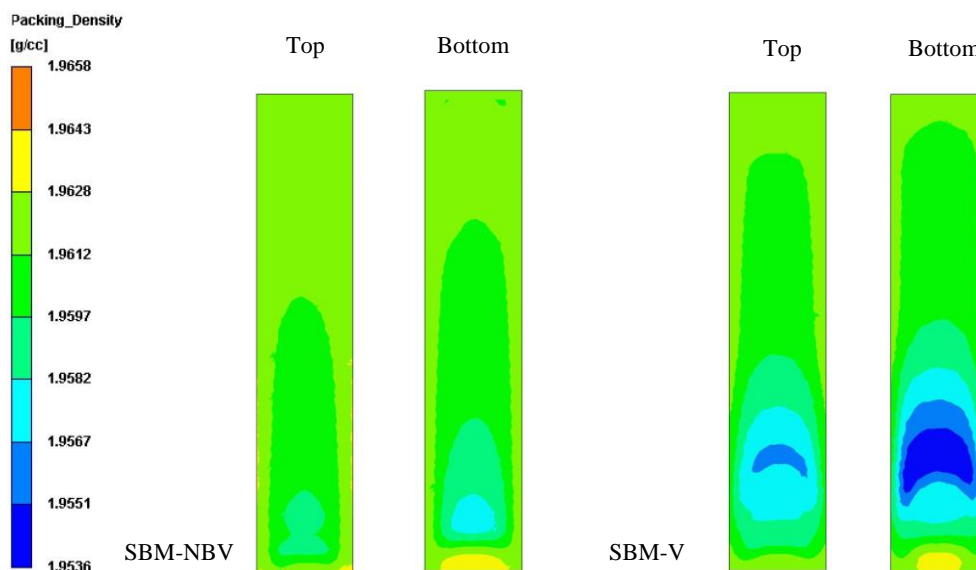


Figure 5.15. Density results from SBM-NBV and SBM-V numerical models at the end of packing.

In Table 5.12, the average density of the silicon nitride test-bar shows that the density difference between the simulation models are not profound. The average density of the silicon nitride test-bar of SBM-NBV and SBM-V were 1.962 g/cm³ and 1.963 g/cm³ respectively. This is close to the measured silicon nitride feedstock density of 1.9633 g/cm³. However, it is hypothesised that the density results are expected to increase due to contraction when the silicon nitride test-bars are cooled to room temperature. The reason is because the numerical models determined the density distribution in the cavity using the PVT data as the input parameter and not the density data.

Table 5.12. Density results from SBM-NBV and SBM-V at the end of packing.

	Max (g/cm ³)	Min (g/cm ³)	Mean (g/cm ³)
SBM-NBV	1.965	1.957	1.962
SBM-V	1.966	1.954	1.963

Figure 5.16 shows the powder concentration results of the silicon nitride test-bar between the SBM-NBV and SBM-V at the end of packing. The numerical results for powder concentration are segmented into 8 contour sections with similar powder concentration ranges for both SBM-NBV and SBM-V. From Figure 5.15 and Figure 5.16, it is noted that the density results from both numerical models have similar trends as the powder

concentration results. This is observed because density is a mechanical property that is directly proportional to the volume fraction of powder.

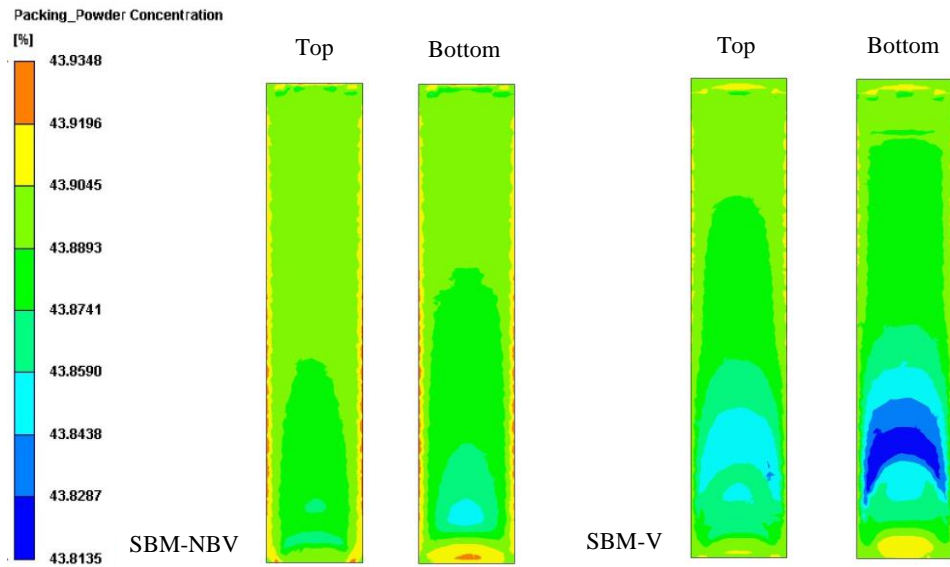


Figure 5.16. Powder concentration results from SBM-NBV and SBM-V numerical models at the end of packing.

The numerical results for maximum, minimum and mean powder concentration observed in the cavity for SBM-NBV and SBM-V are summarised in Table 5.13. The powder concentration differences observed between the simulation models are not profound. This is shown in the average powder concentration of the silicon nitride test-bar. Similar to the density results of the SBM-V numerical model, the powder concentration in the region after the gate was observed to be lower than the rest of the test-bar.

Table 5.13. Powder concentration results from SBM-NBV and SBM-V.

	Max (vol%)	Min (vol%)	Mean (vol%)
SBM-NBV	43.934	43.852	43.903
SBM-V	43.935	43.814	43.908

5.1.8 Density results at the end of injection moulding process

Figure 5.17 shows the density distribution results of the silicon nitride feedstock in comparison between the SBM-NBV and SBM-V after the part is ejected and cooled to ambient temperature. The numerical results for density are segmented into 8 contour sections with similar density range for both SBM-NBV and SBM-V. The numerical results for

maximum, minimum and mean packing density observed in the cavity for SBM-NBV and SBM-V are summarised in Table 5.14.

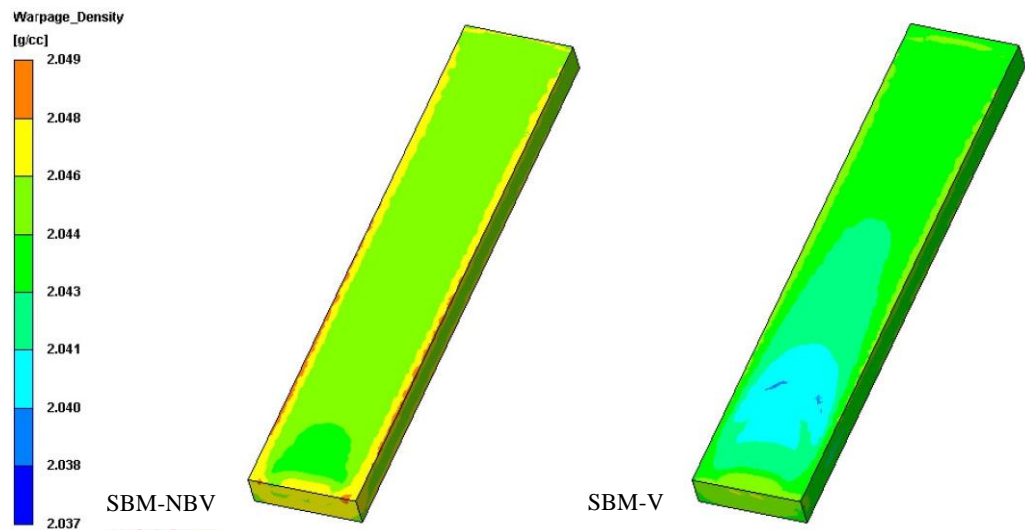


Figure 5.17. Density results from SBM-NBV and SBM-V numerical models after ejection and cooling.

The density numerical results confirmed the hypothesis that the PVT data is used by the numerical models to determine the density distribution of the part. The PVT data used in these numerical models are not experimental data, but it is estimated from experimental data of HDPE and silicon nitride powder found in literature. Therefore, the average density does not match the density of the feedstock. The density distribution numerical results of the silicon nitride test-bar shown here should only be used as a reference and not a definitive density results of the test-bar.

Table 5.14. Density results from SBM-NBV and SBM-V after cooling.

	Max (mm)	Min (mm)	Mean (mm)
SBM-NBV	2.049	2.042	2.046
SBM-V	2.047	2.037	2.045

5.2 Numerical modelling of silicon nitride injection moulding using two-fluid model

In this section, the TFM has been developed to simulate the PIM of silicon nitride test-bar. The use of TFM in simulating the mould filling of PIM feedstock [70]–[72] has become more popular over the years. This is because the powder and binder phases are simulated as interpenetrating continua which allows the behaviour of powder-binder separation to be captured and visualised unlike the SBM that only captures a distribution of the powder concentration based on the velocity field. The objective of the numerical model is to simulate the powder-binder separation occurrence during mould filling. Figure 5.18 shows a flow diagram that described the approach taken to develop the powder injection moulding simulation model using ANSYS-CFX.

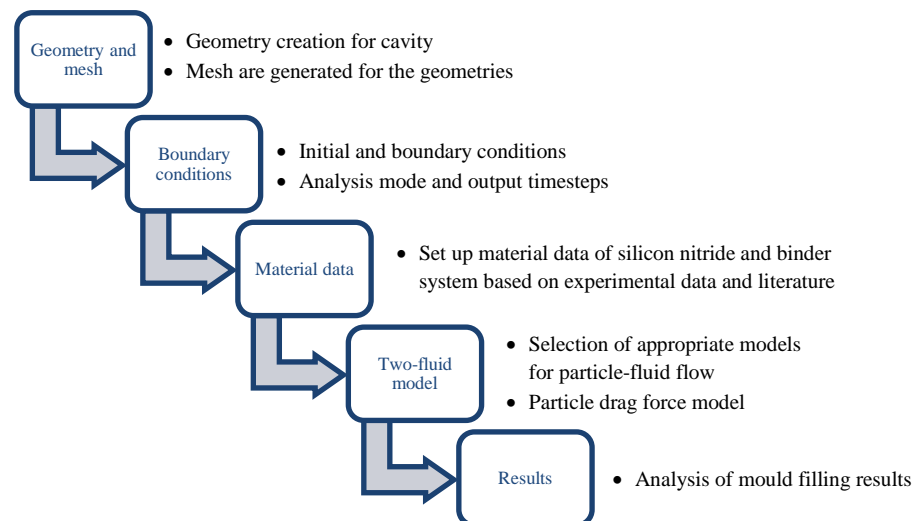


Figure 5.18. Systematic approach taken to develop simulation model for powder injection moulding of silicon nitride test-bar using ANSYS-CFX.

The TFM modelled each phase individually where fluid mechanics interactions between the phases are imposed. In this model, only the geometry of the cavity is considered and the dimension of the cavity (test-bar) is similar to the CAD model used in Moldex3D. The TFM requires the material data of the binder system and the silicon nitride powder. The material data of the binder system and silicon nitride powder were developed based on experimental data and material data found in literature. A particle model was used to model the relationship between the silicon nitride powder and binder system. The particle model is developed based on a drag coefficient equation [192]. The initial and boundary conditions in all the simulations were kept as close to the real silicon nitride injection moulding process conditions as possible. The appropriate solver settings were selected with the desired

analysis mode and output results. The relationships between viscosity, shear rate, drag coefficient, relative velocity and silicon nitride volume fraction are studied.

5.2.1 Simulation principles for two-fluid model

In this work, the TFM based on the Eulerian-Eulerian method was used to develop the fluid models to simulate the mould filling of the silicon nitride test-bar. The model considered a multiphase model that consisted of air as a continuous fluid phase and a TFM made up of a dispersed-fluid phase for the silicon nitride powder in a continuous fluid phase for the binder system. It is assumed that there is no interaction between the powder and air. ANSYS-CFX uses an element-based Finite Volume approach to discretise the Navier-Stokes equations. The continuity equation for a two-fluid model is given by:

$$\frac{\partial(\phi_k \rho_k)}{\partial t} + \nabla \cdot (\phi_k \rho_k U_k) = 0 \quad (5.10)$$

where the subscript k refers to each phase in the model and U is the mean velocity field. The momentum equation is given by:

$$\frac{\partial(\phi_k \rho_k U_k)}{\partial t} + \nabla \cdot (\rho_k U_k U_k) = -\phi_k \nabla p + \nabla \cdot (\phi_k \tau_k) + \phi_k \rho_k g_k + S_M + M_k \quad (5.11)$$

Where p is the mean pressure shared by the phases, τ is viscous stress tensor, g is the gravity vector, S_M is the momentum sources due to external body forces and M_k is the interfacial forces acting on phase k due to the presence of other phases. The interfacial forces acting on the phases are driven by the interphase drag between the phases. The interphase drag model between the dispersed-fluid (powder particles) and continuous fluid (binder) is described by a particle model that is based on drag coefficient from the literature [192]. As for the interphase drag model between the two continuous fluid, binder and air, the mixture model is employed. The total drag force unit per volume between the binder and silicon nitride powder was developed together with the Cross-WLF model and an empirical drag coefficient equation based on literature [192]. The difference between the relative velocity of binder and silicon nitride powder led to the separation between them. The total drag force per unit volume between the binder (continuous fluid) and powders (dispersed fluid particles) is given by:

$$D_{bp} = \frac{3 C_D}{4 d_p} \phi_p \rho_b |v_p - v_b| (v_p - v_b) \quad (5.12)$$

Where C_D is the drag coefficient, d_p is the mean diameter of particles, v is the relative velocity and the subscripts, p and b , represents powder and binder respectively. During mould filling, the increase in presence of other particles caused a distortion to the flow field which led to each particle experiencing an increase in flow resistance [88].

This led to an increase in drag coefficient and therefore the viscosity of the continuous phase in the Reynolds number should be replaced with the apparent viscosity of the mixture [88]. The reason for developing an empirical drag coefficient equation is due to the volume fraction limits on the drag coefficient models in ANSYS-CFX. These drag coefficient models considers volume fraction that ranges from sparsely to densely distributed particles and they require a surface tension coefficient between particles and binder to be defined. With the surface tension coefficient, the interface between the particle and fluid would be considered as immiscible. However, the silicon nitride particles are considered to be miscible with the binder and the feedstock is considered to be rather homogeneous. Therefore, there is no need for surface tension coefficient as a boundary condition. In order to achieve this, a drag coefficient model that does not require surface tension coefficient was developed in the TFM. The drag coefficient equation [192] used in this simulation model is given in Equation (5.13).

$$C_D = \frac{24}{Re} (1 + 0.27Re)^{0.43} + 0.47[1 - \exp(-0.04Re^{0.38})] \quad (5.13)$$

where the Reynolds numbers is defined by.

$$Re_p = \frac{d_p |v_p - v_b| \rho_b}{\eta_f} \quad (5.14)$$

The feedstock viscosity, η_f , is defined by the Cross-WLF model. The five-parameter drag coefficient equation is simple and it represents the drag coefficient data better than the available drag coefficient models in ANSYS-CFX [192]. The drag coefficient and Reynolds number are implemented into ANSYS-CFX as expressions and a small value of 1e-14 is added to the Reynolds number to prevent dividing zero when the relative velocity is zero.

5.2.2 Geometry, mesh and boundary conditions

The CAD model of the test-bar was developed in SolidWorks and imported into ANSYS-CFX 16 for meshing. Figure 5.19 shows the geometry of the test-bar used for the numerical simulation with dimension for the inlet and outlet boundary conditions. Mapped meshing was used to generate tetrahedral mesh of 20,749 elements and 4566 nodes for the test-bar. Map meshing was used to ensure that there was even distribution of elements with no bad aspect ratio. The cavity has a total volume of 2.544 cm³ with maximum element size of 1mm and minimum element size of 0.2mm. The mesh profile, inlet and outlet boundary conditions are depicted in Figure 5.19. The model is simplified by not adding the runner, which will not significantly affect the results.

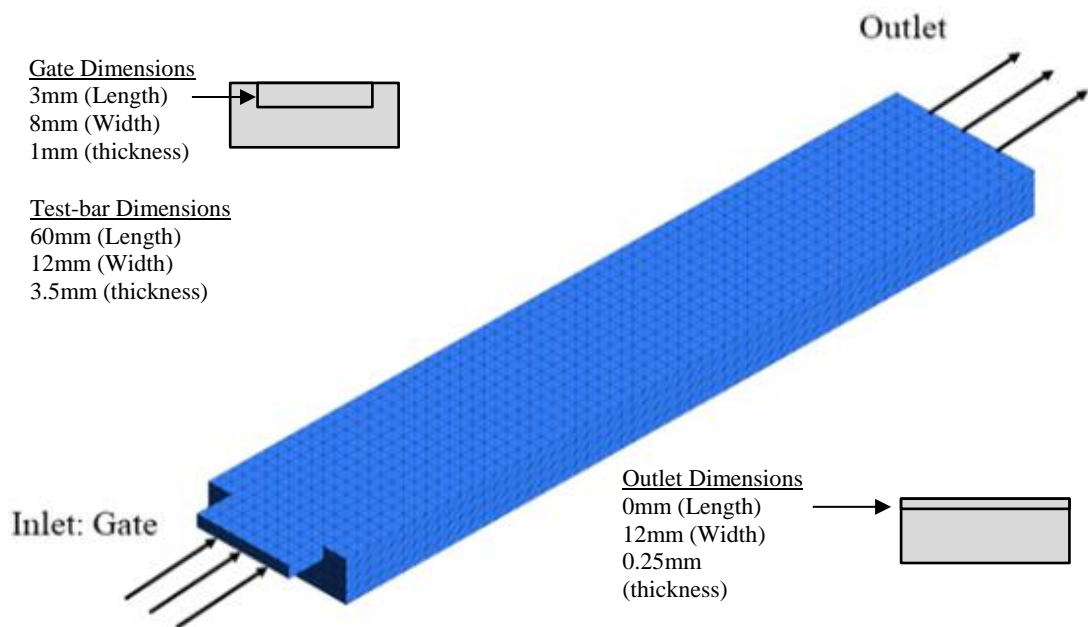


Figure 5.19. Dimension of cavity (test-bar) with mesh with inlet and outlet boundaries.

The TFM developed in ANSYS-CFX consisted of two continuous fluid phases for air and binder system and a dispersed fluid particles phase for silicon nitride powders. In this model the dispersed fluid particles were defined with silicon nitride solid particles properties. This is done so that the physics are dominated by interphase drag. For the flow, it is assumed that the Reynolds number is sufficiently small and neutrally buoyant particles similar to the SBM [62]. Therefore, laminar flow is considered as the turbulence model and buoyancy is not considered. The volume fraction of silicon nitride powder measured using the TGA, shown in Section 4.3.1, is used as the inlet boundary condition for the silicon nitride powder. Initial

boundary conditions at the inlet were assigned with the volume fraction of air as 0, silicon nitride powder as 0.439 and binder system as the constraint 0.561. The mass flow rate used in SBM simulations is applied to the TFM. The mass flow rate at the inlet was determined by considering the ram position after the feedstock melt had filled the runner system and the injection speed at that point with the dimensions of the injection barrel. The mass flow rate determined were 77.12 g/s from 0 to 0.01832 s and 67.48 g/s from 0.01832 s onwards.

The temperature of the binder system and silicon nitride powder was set at 185°C. The cavity domain was assigned with only air in it at atmospheric pressure and 110°C. Buoyancy is not considered. The mould temperature of 110°C was assigned to the wall temperature with no slip wall boundary condition assigned to the binder system while free slip boundary condition is assigned to air and silicon nitride powder. The outlet boundary has atmospheric pressure imposed and is specified as an opening for the air in the cavity to leave through the outlet. Mould filling was expected to complete within 0.075 s, but the simulation time was set to 0.09 s to ensure sufficient run time for mould filling to be completed. Adaptive time steps were used to adjust a smaller timestep if it is required. This is based on the Courant number conditions of below 1. The analysis condition has an initial timestep of 0.0001s, minimum timestep of 0.00004s and maximum timestep of 0.0001s.

5.2.3 Material data

The numerical model consists of three phases, air (continuous), binder system (continuous) and silicon nitride powder (disperse fluid). The default 'Ideal Air Gas' in ANSYS CFX is used for the air modelled in this simulation. The material properties for binder system and silicon nitride powder are summarised in Table 5.15. The density of the binder system and silicon nitride powder were determined using a Micromeritics AccuPyc II 1340 Gas Pycnometer with helium gas which was presented previously in Section 3.1.1. Specific heat capacity of the binder system and silicon nitride powder at 185°C were used for the simulation model. Specific heat capacity of the binder system was determined using the DSC which was presented previously in Section 3.1.2. Specific heat capacity of the silicon nitride powder was taken from literature [160]. The thermal conductivity of the binder system and silicon nitride powder at 185°C were taken from literature [128], [160], [189], [190].

Table 5.15. Material properties of binder system and silicon nitride powder.

Material	Density (kg/m³)	Specific Heat Capacity (J/kg.K)	Thermal Conductivity (W/m.K)	Viscosity (Pa.s)
Binder system	924.1	2599.103	0.305	Cross-WLF model (Table 5.4)
Silicon nitride	3224.78	933.816	25.4	0.1

As mentioned in Section 2.1, the TFMs found in literature were developed to simulate powder injection moulding by using viscosity of binder and powder which were determined using the rule of mixture equation and feedstock viscosity experimental data [70]–[72]. This means that both the binder system and powder particles have viscosity values. However, Manninen [88] concluded that the rule of mixture should not be taken as the definition of the mixture viscosity that has solid particles and suggested that in a TFM the continuous fluid phase should be modelled with the mixture viscosity. In the TFM developed in this thesis, the viscosity of the binder system was represented by the Cross-WLF model with the coefficients shown in Table 5.4 and a small insignificant molecular viscosity of 0.1 Pa.s was assigned to the silicon nitride powder so that physics will be dominated by interphase drag.

5.2.4 Results and discussions

Numerical results were collected in two locations on the test-bar shown in Figure 5.20 and Figure 5.25. In Figure 5.20, the numerical results collected along the *Y*-axis were indicated by a line, Line Y. The line is on a *XY*-plane that is located at 0.03m on the *Z*-axis and numerical data were collected on 15 points along the line. The numerical results of powder velocity, shear strain rate, viscosity and drag coefficient were selected. This is to show the local shear strain gradient and investigate the relationship of the local shear strain gradient with the other parameters.

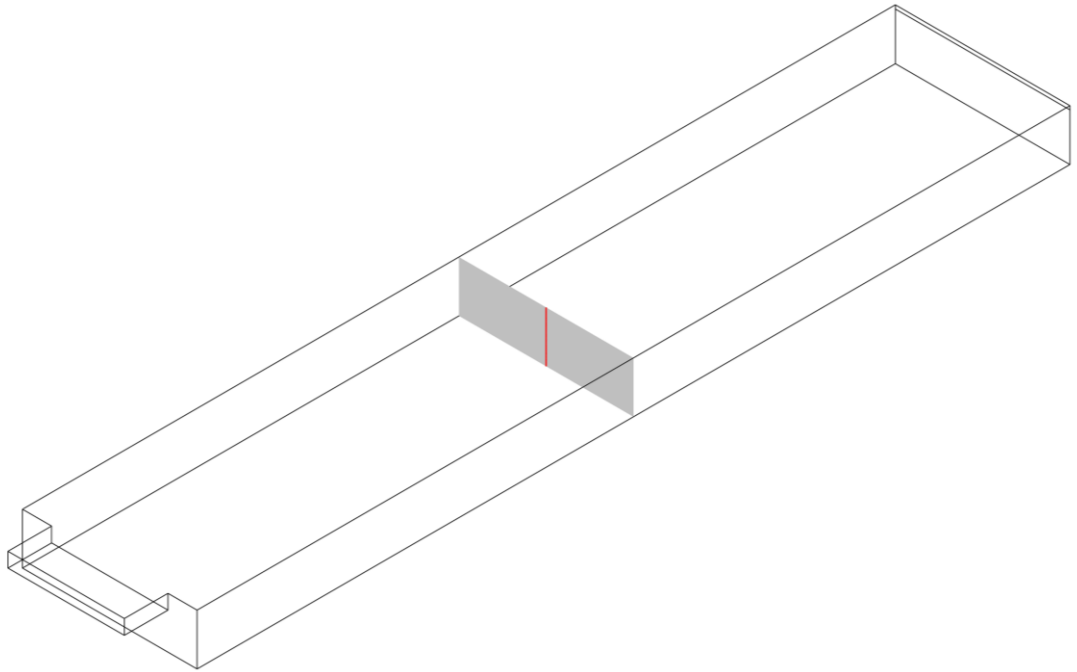


Figure 5.20. Location as indicated by a red line (Line Y) in middle of XY -plane at 0.03 m on the Z -axis.

Figure 5.21 shows the silicon nitride particle velocity results that were collected along Line Y and plotted with reference to the Y -axis. The velocity profile of the silicon nitride particles were dependent on the viscosity model that was used to describe the rheological behaviour of the silicon nitride feedstock [64]. The velocity profile seen in Figure 5.21 is similar to the numerical results of PIM simulations that uses the Cross-WLF viscosity model [63], [64]. It is hypothesised that the velocity profile determines the local shear strain rate gradient of the flow.

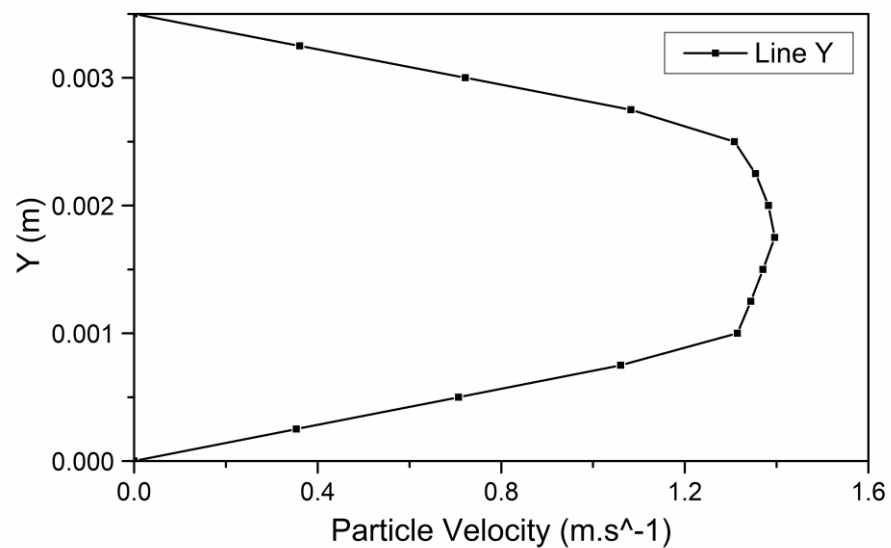


Figure 5.21. Silicon nitride particle velocity on Line Y with reference to the Y -axis.

Figure 5.22 shows the shear strain rate numerical results that were collected along Line Y and plotted with reference to the Y-axis. The local shear strain rate is depicted in the graph with higher shear strain observed close to the walls of the mould and low shear strain in the middle region. The gradients of the shear strain rate seen in Figure 5.22 will cause rotation in the silicon nitride particles. This in turn creates movement of particles towards the middle region of the flow. Based on the Cross-WLF model which was used to model the rheological behaviour of the silicon nitride feedstock, the low shear strain rate regions resulted in high viscosity and vice-versa for high shear strain rate.

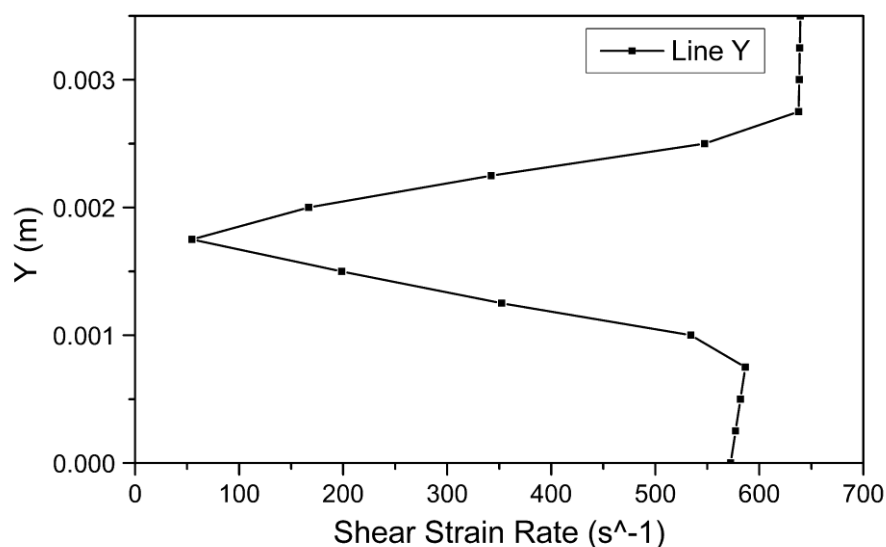


Figure 5.22. Shear strain rate of silicon nitride feedstock on Line Y with reference to the Y-axis.

Figure 5.23 shows the viscosity numerical results that were collected along Line Y and plotted with reference to the Y-axis. High viscosity was observed in the points close to the mould walls which was due to the low wall temperatures. However, because phase change was not modelled in this simulation model, therefore the frozen layers of feedstock next to the mould walls was not observed. Nonetheless, the high viscosity seen at the walls of the mould mimic the behaviour of having frozen layers. The viscosity profile can be observed to adhere to the Cross-WLF model where higher viscosity found in the middle region is due to the low shear strain rate.

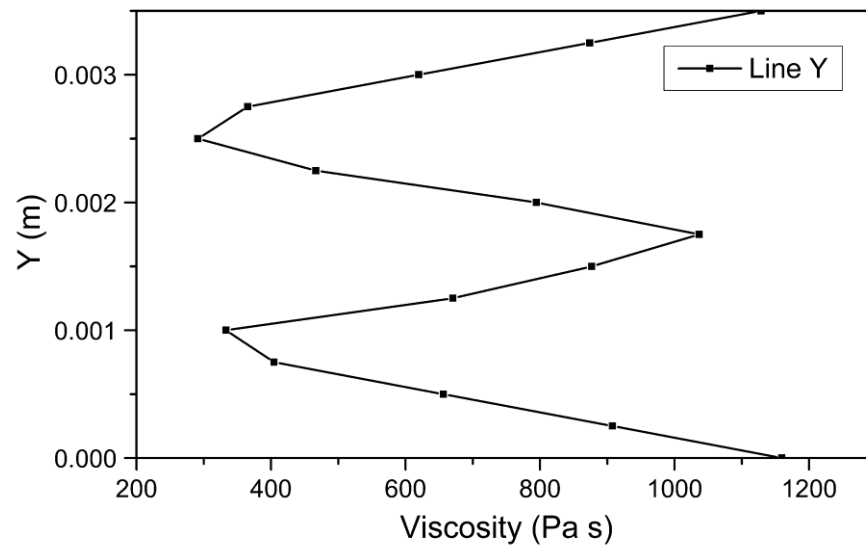


Figure 5.23. Viscosity of silicon nitride feedstock on Line Y with reference to the Y-axis.

Figure 5.24 shows the drag coefficient numerical results that were collected along Line Y and plotted with reference to the Y-axis. The conservative values of the drag coefficients are considered for this plot as the no-slip boundary conditions meant that the velocity at the wall is zero and this would cause an enormous drag coefficient values for the nodes close to the wall. Instead the velocity value calculated at the mesh node on the wall is based upon the ‘average’ in the control volume surrounding that node which returns a low velocity value shown in Figure 5.21. This would provide reasonable drag coefficient values for the nodes close to the wall. It can be observed from Figure 5.24 that the distortion to the flow field caused by the movements of particles resulted in the increase in drag coefficient in the middle region of the flow.

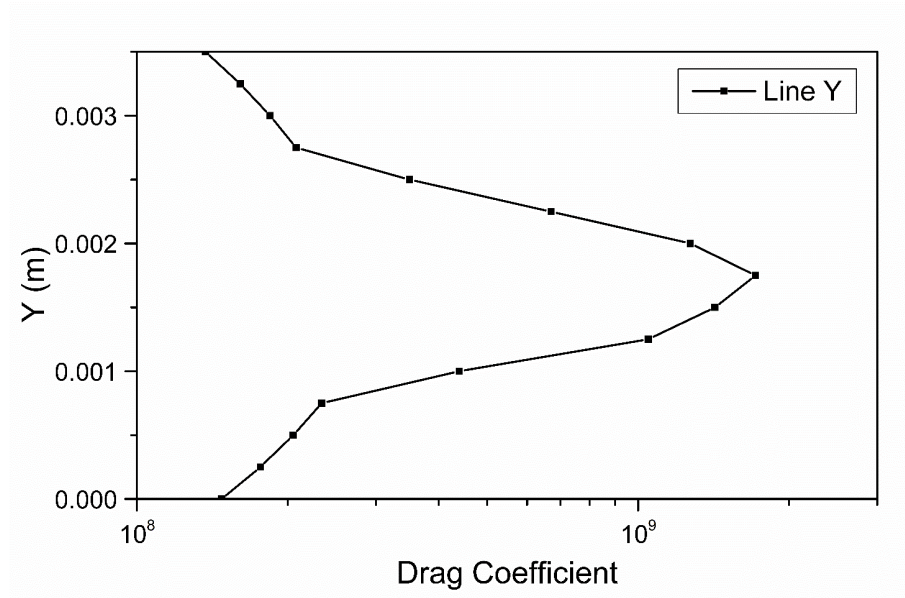


Figure 5.24. Drag coefficient of silicon nitride particles in binder on Line Y with reference to the Y-axis.

Figure 5.25 shows location where numerical results were collected along the Z-axis as indicated by Line Z. The line is on a YZ-plane that is located at 0 m on the X-axis and numerical data were collected on 60 points along the line. Numerical data of powder velocity, shear strain rate, viscosity, drag coefficient, temperature and volume fraction of powder were selected to investigate the flow behaviour throughout the test-bar and distribution along Line Z.

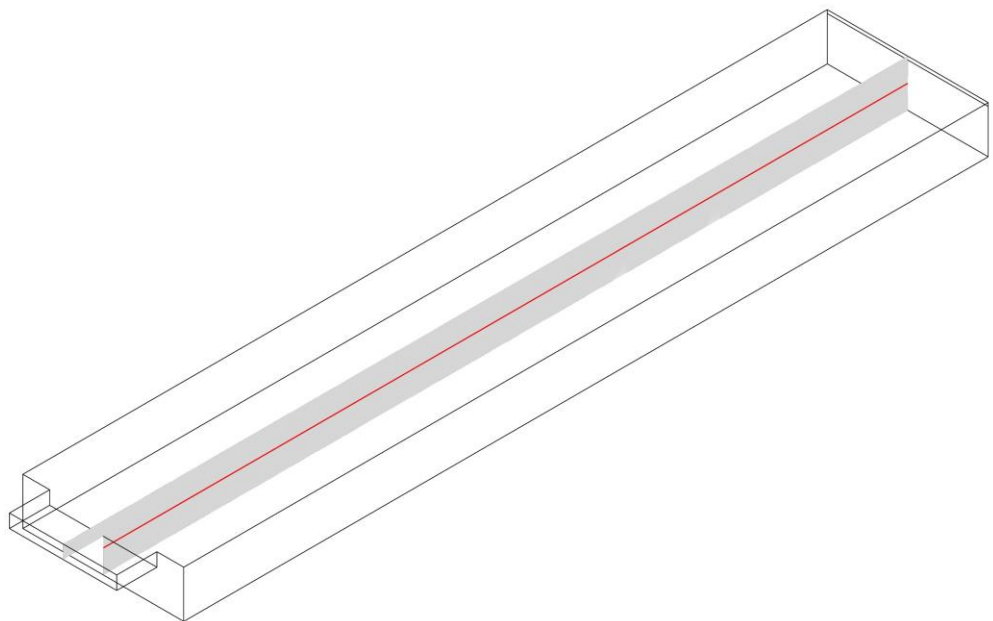


Figure 5.25. Location as indicated by a red line (Line Z) on middle section of YZ-midplane at 0 m on the X-axis.

Figure 5.26 shows the silicon nitride particle velocity and relative velocity results that were collected along Line Z and plotted with reference to the Z-axis. In Figure 5.26(a), the particle velocity close to the mould walls are low due to no-slip conditions. After the feedstock melts enters the cavity, it flows at a steady velocity to fill up the mould. In Figure 5.26(b), the relative velocity between silicon nitride particles and the binder is determined. Based on the distribution of relative velocity on Line Z and the shear strain rate results found in Figure 5.27, it is observed that the high relative velocity regions will result in high shear strain rates.

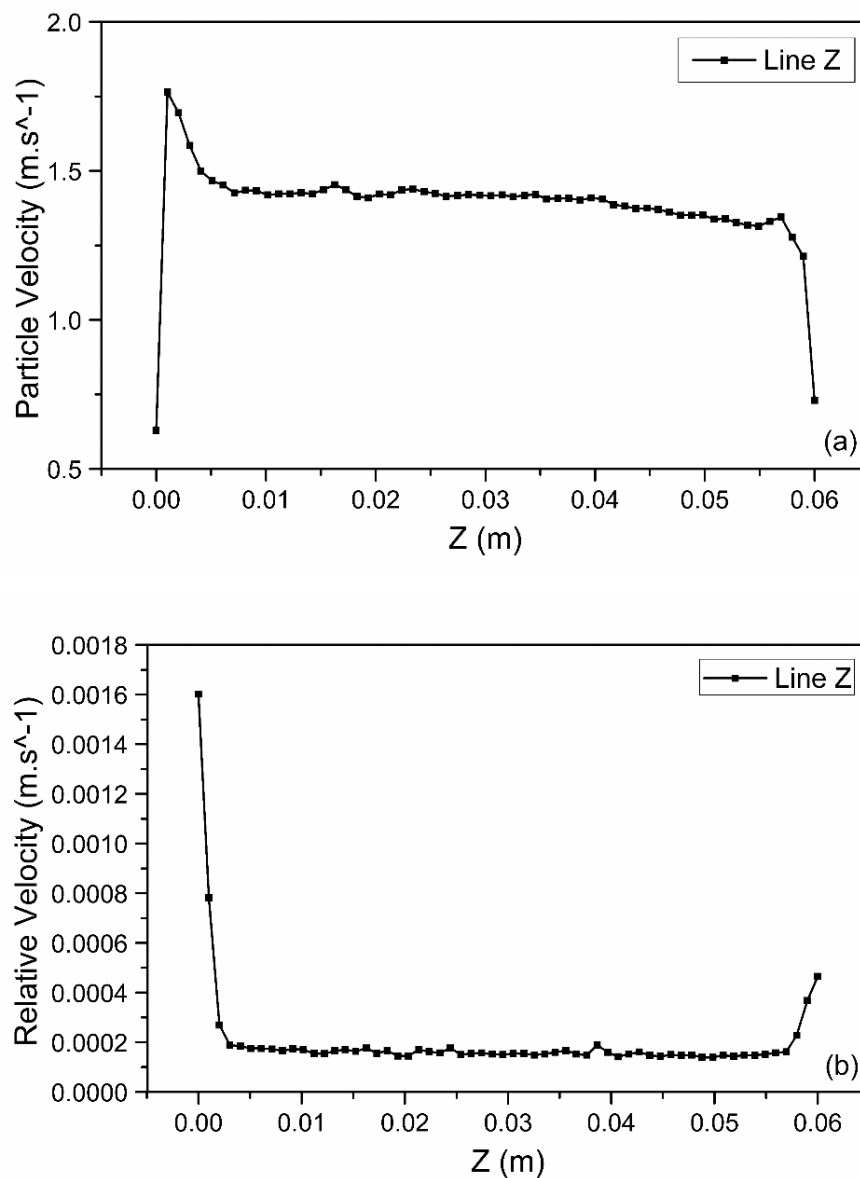


Figure 5.26. (a) Silicon nitride particle velocity and (b) relative velocity on Line Z with reference to the Z-axis.

Figure 5.27 shows the shear strain rate numerical results that were collected along Line Z and plotted with reference to the Z-axis. The shear strain rate observed closed to the mould

walls are high and the shear strain rate observed away from the mould walls are low. This is much like the relative velocity results between the binder system and silicon nitride powder. The fluctuation in shear strain rate can be explained by the distortion in the flow field caused by movement of particles. The same fluctuation can be observed from the distribution of viscosity and drag coefficient of the nodes along Line Z.

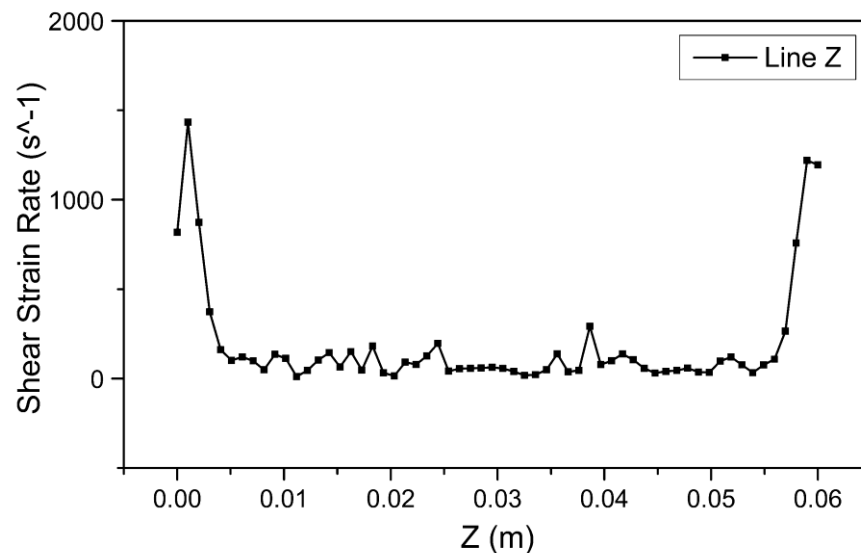


Figure 5.27. Shear strain rate of silicon nitride feedstock on Line Z with reference to the Z-axis.

Figure 5.28 shows the viscosity and drag coefficient numerical results in comparison. The numerical results were collected along Line Z and plotted with reference to the Z-axis. Higher viscosity and drag coefficient were observed in low shear strain rate region on Line Z. Fluctuation was observed along Line Z in the silicon nitride test-bar for viscosity and drag coefficient results. This are indications of distortion in the flow field experienced by the flow when filling up the mould which are caused by the movement of silicon nitride particles. In Figure 5.28, the drag coefficient for the interphase drag force between the binder and silicon powder can be observed to be directly proportional to the viscosity of the silicon nitride feedstock. This demonstrates that the viscosity of the silicon nitride feedstock is an essential component to the drag forces between the silicon nitride particles and binder.

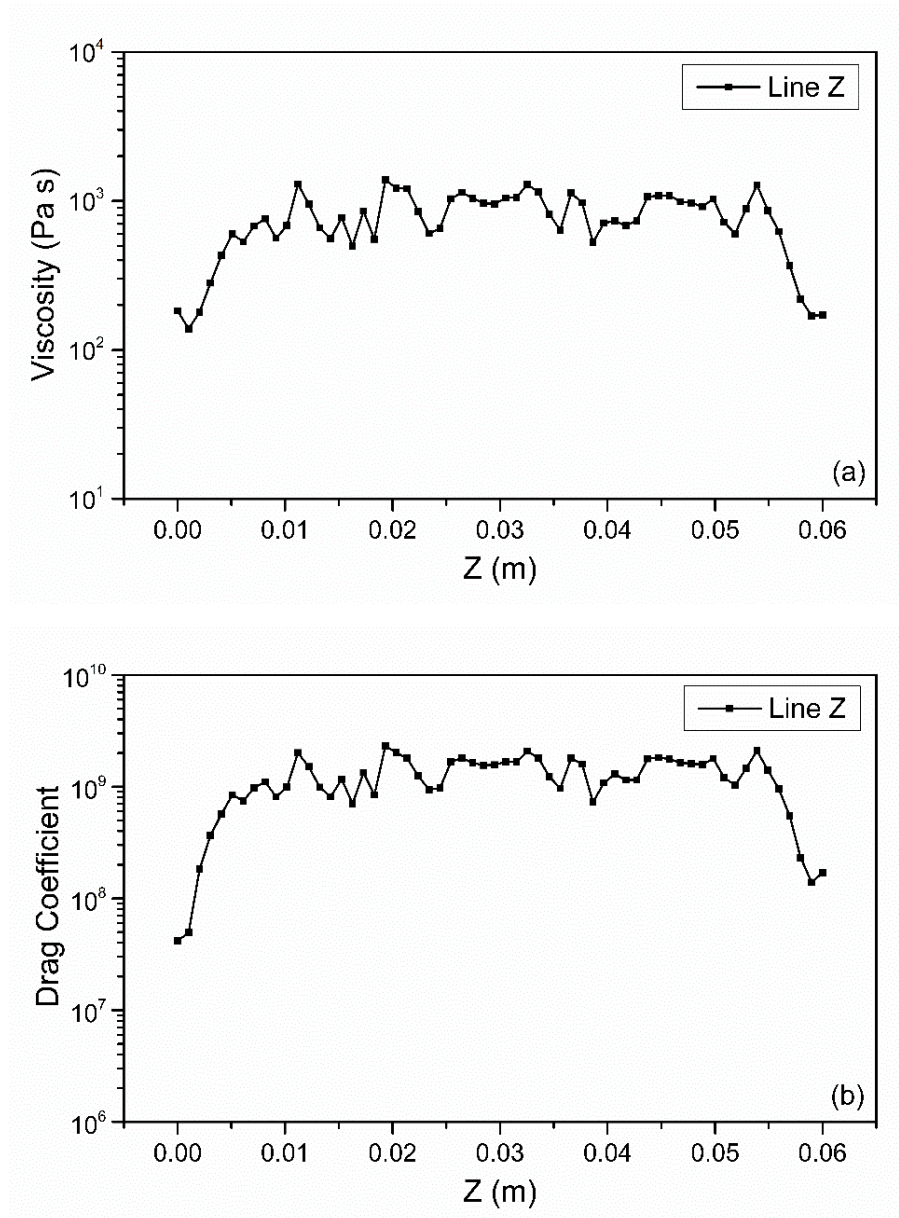


Figure 5.28. (a) Viscosity of silicon nitride feedstock and (b) drag coefficient of silicon nitride particles in binder on Line Z with reference to the Z-axis.

Figure 5.29 shows the silicon nitride volume fraction numerical results that were collected along Line Z and plotted with reference to the Z-axis. The silicon nitride powder volume fraction distributed along Line Z shows separation occurred at areas close to the mould walls at the gate region and the rear. This powder volume fraction distribution trend is similar to distribution observed in the simulation model developed by Fang et al. [72] on the mould filling of 316L stainless steel.

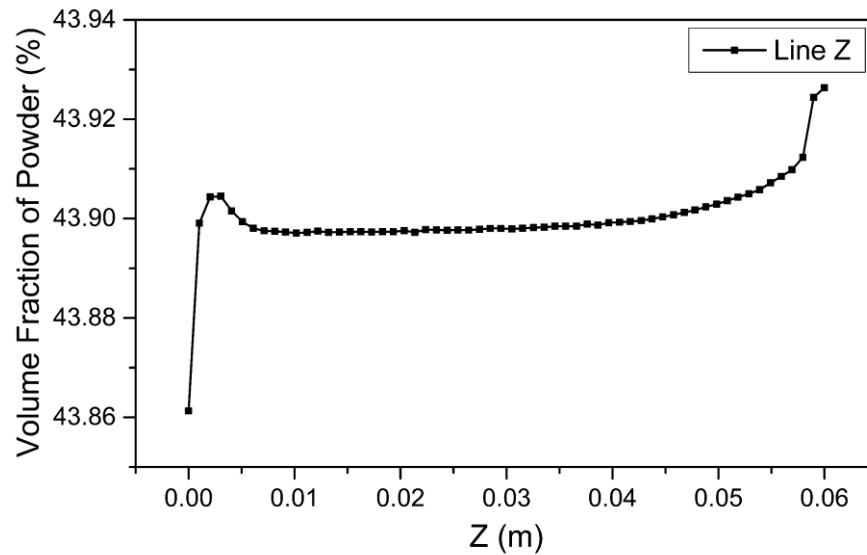


Figure 5.29. Volume fraction of silicon nitride powder on Line Z with reference to the Z-axis.

Figure 5.30 shows the temperature distribution results that were collected along Line Z and plotted with reference to the Z-axis. The temperatures along Line Z are close to the melt temperature (185°C) and a decrease in temperature was observed as it gets closer to the rear due to heat energy loss to the mould. The mould temperature observed on the nodes close to the mould walls were much lower and this temperature distribution trend was observed along Line Z. These observations were similar to the results found in the simulation model developed by Fang et al. [72].

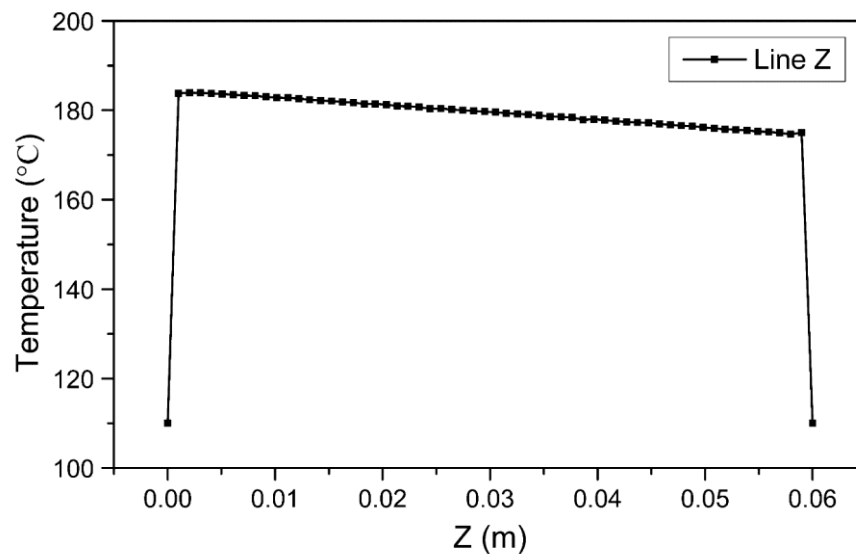


Figure 5.30. Temperature distribution of silicon nitride feedstock on Line Z with reference to the Z-axis.

In Figure 5.25, contours plot on the *YZ*-plane were plotted for numerical results such as shear strain rate, viscosity and drag coefficient to show a visual representation of the flow in the middle region of the flow. Figure 5.31(a) shows the shear strain rate distribution on the *YZ*-plane. High shear strain rates were observed at the lower left corner caused by restricted flow and the top right corner where the air is exiting the cavity. Low shear strain rate was observed in the middle region of the flow which is similar to the trend in Figure 5.22.

Figure 5.31(a) and (b) shows that the low shear strain rates observed in the middle region will result in high viscosity. As mentioned in the discussion for the previous figures, the high viscosity will lead to high drag coefficients and this is shown in Figure 5.31(c). It is a result of the high interphase drag forces between the silicon nitride particles and binder. The simulation results are further presented in Section 5.3, where the comparison between the TFM, SBM-NBV and SBM-V are made. Section 5.3 will present the experimental validation of the numerical models with the experimental data determined using the thermogravimetric analysis.

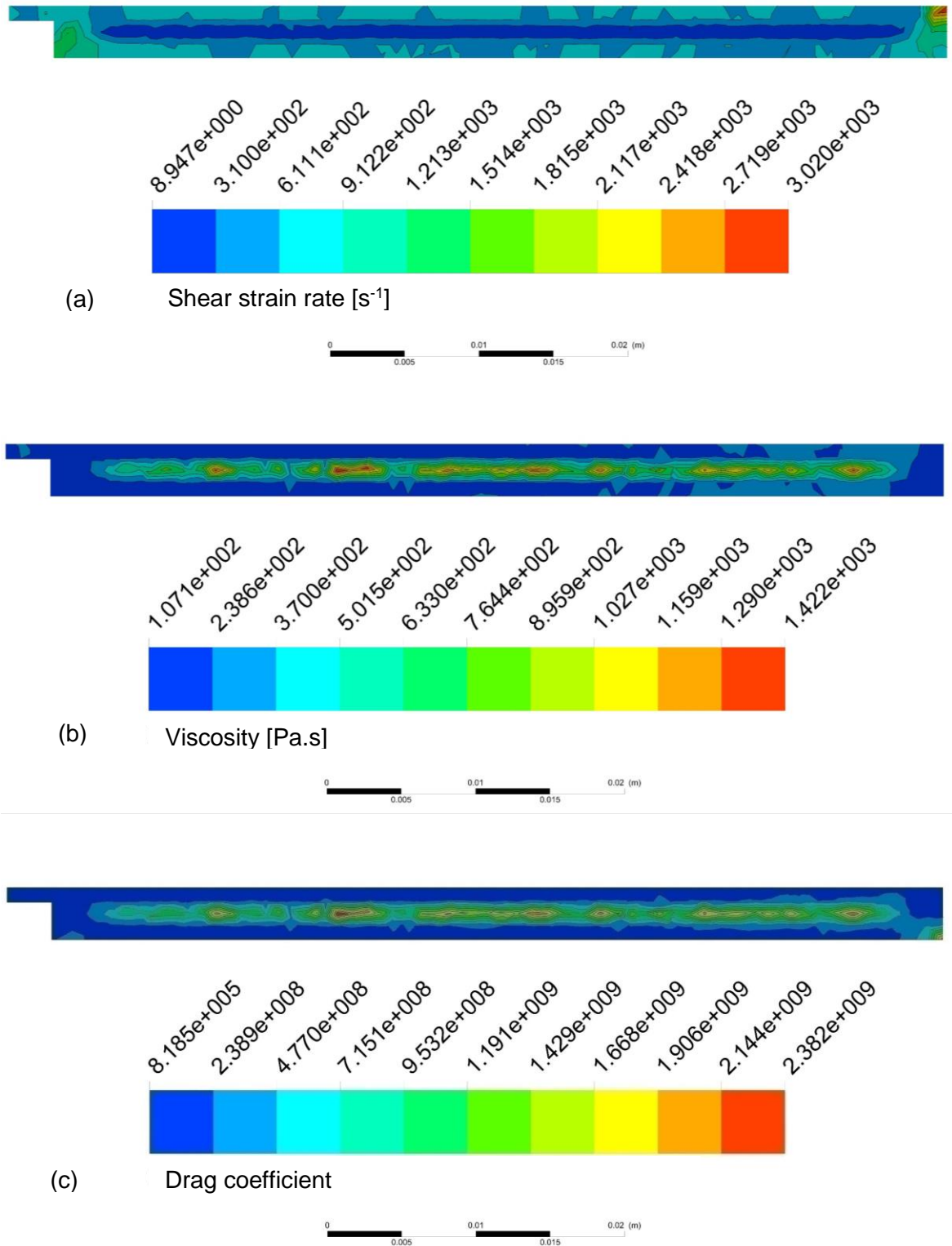


Figure 5.31. (a) Shear strain rate (b) viscosity and (c) drag coefficient distribution on the YZ-plane at 0 m on the X-axis.

5.3 Numerical results comparison and experimental validation

In this section, the numerical models developed in Section 5.1 and Section 5.2 to simulate the powder injection moulding of silicon nitride test-bar are presented in comparison. First, the filling pattern results of the simulation models (SBM-NBV, SBM-V and TFM) developed in this research work are presented in comparison. The simulation models (SBM-NBV and SBM-V) that simulate multiple stages of the injection moulding process will have powder distribution results from both the filling and packing stages.

Next, the parameters and conditions used for powder distribution study on the simulation models and experimental results are presented. A schematic diagram is shown for how the test-bar is segmented for the study and numerical data are collected for each section. Numerical data will determine the silicon nitride powder volume fraction in each section which represents the powder distribution results from the simulation models.

Lastly, thermogravimetric analysis results from Chapter 4 will be used to validate the silicon nitride powder distribution results from the simulation models. As presented Chapter 4, the thermogravimetric analysis was used to measure the volume fraction of silicon nitride powder and its distribution point to point along the injection moulded test-bar. The experimental method was presented to be able to measure the distribution of ceramic powder within the test-bar.

5.3.1 Filling patterns results of suspension balance models and two-fluid model

Presented in Section 5.1, SBMs developed with material data from HMD-NBV and HMD-V will be denoted as SBM-NBV and SBM-V. As presented in Section 5.2, the TFM developed with a drag coefficient will be denoted as TFM. The silicon nitride feedstock used in all three models have a silicon nitride volume fraction of 0.439 which was measured by the thermogravimetric analysis of the feedstock. All the simulation models were compared in terms of the filling time and the volume filled to observe the filling patterns. In Figure 5.32, the filling patterns from all three models are relatively similar other than at $T = 0.03$ s where the TFM starts to trail behind the suspension balance models.

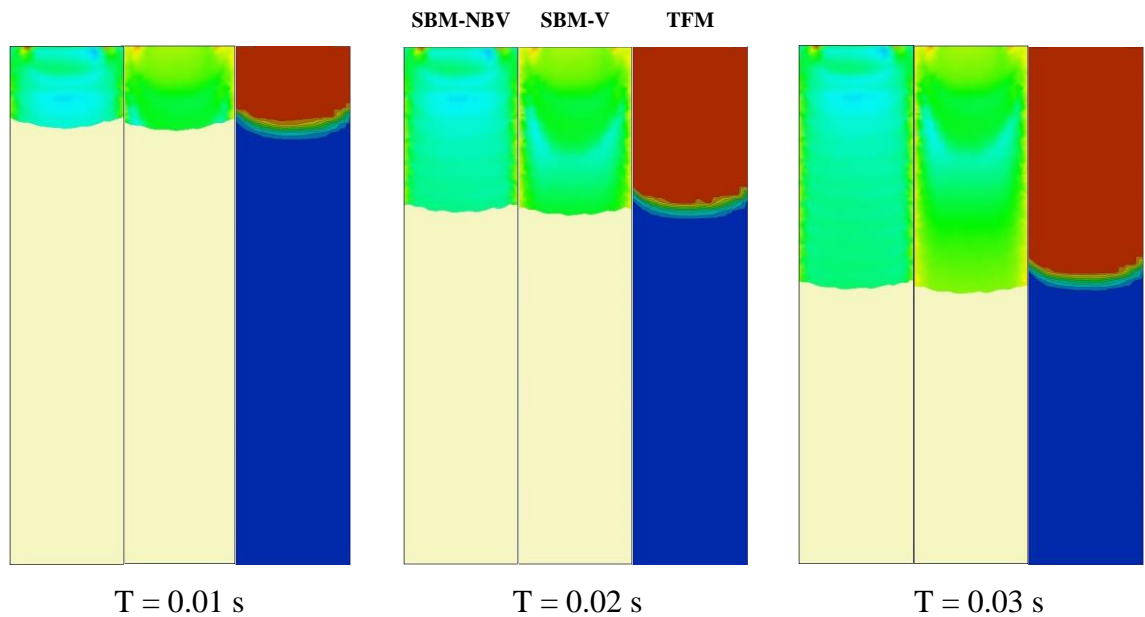


Figure 5.32. Filling patterns of SBM-NBV, SBM-V and TFM at $T = 0.01$ s, 0.02 s and 0.03 s.

In Figure 5.33, the filling patterns from both suspension balance models are rather similar from 0.04 s to 0.06 s. The TFM continues to trail behind the suspension balance model, showing that it takes more time to reach the end of filling for the TFM. This is likely due to the difference in outlet parameters used in the TFM. The parting line was defined for SBM-NBV and SBM-V which allows venting of the air in cavity to occur. Whereas for the sake of simplifying the TFM, the outlet is only set at the end of the test-bar.

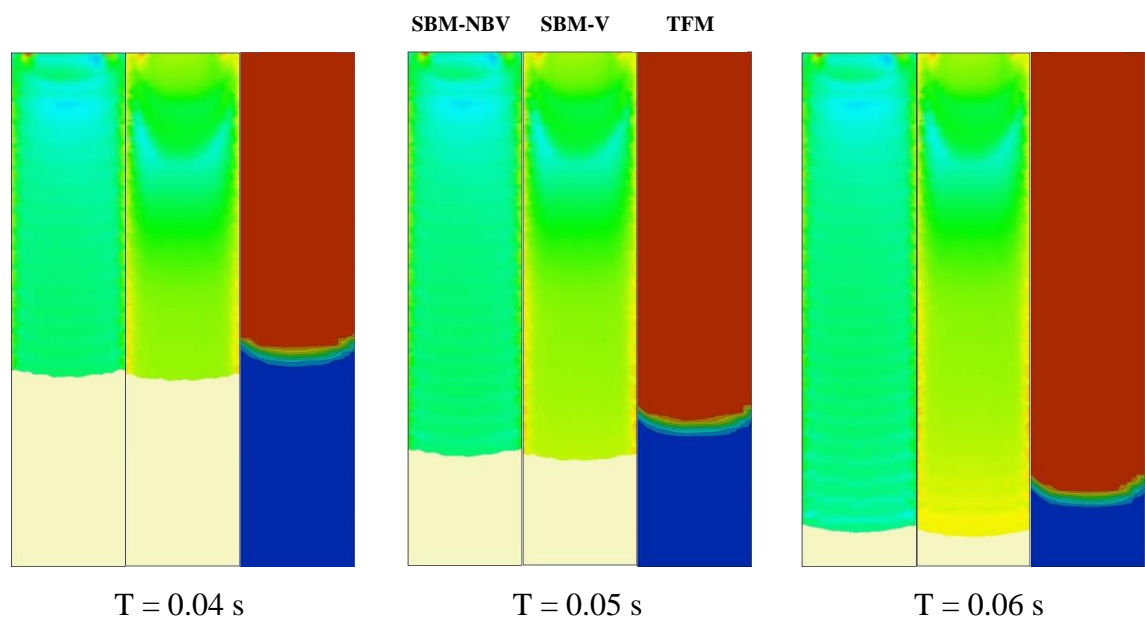


Figure 5.33. Filling patterns of SBM-NBV, SBM-V and TFM at $T = 0.04$ s, 0.05 s and 0.06 s.

Figure 5.34 shows the time taken to reach the end of filling for all three models and the powder distribution results. The SBM-NBV was the first to reach the end of filling at 0.066s and SBM-V was 0.067s while TFM took the longest time with 0.0715s. The numerical results from SBM-NBV, SBM-V and TFM are shown in similar powder concentration range where the SBMs are in volume (%) and the TFM is in volume fraction.

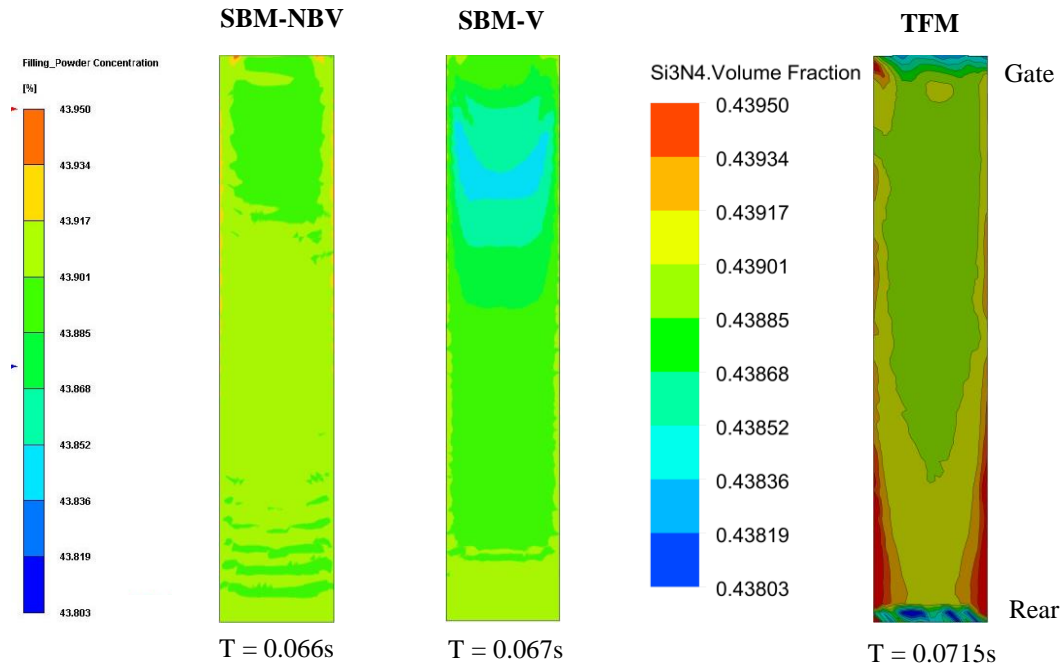


Figure 5.34. Silicon nitride volume fraction of SBM-NBV, SBM-V and TFM at the end of filling.

The numerical results from SBM-NBV and SBM-V show that lower powder concentration of silicon nitride is found in the regions close to the gate. The numerical results from TFM shows similar behaviour but closer to the gate and more segregation. The numerical results for maximum, minimum and mean powder concentration observed in the cavity for SBM-NBV, SBM-V and TFM are summarised in Table 5.16. In Table 5.16, the TFM noted higher maximum and lower minimum powder concentration which means that the TFM showed more powder-binder separation in the silicon nitride green body. The average powder concentration in SBM-NBV, SBM-V and TFM are similar.

Table 5.16. Powder concentration results from SBM-NBV, SBM-V and TFM.

	Max (vol%)	Min (vol%)	Mean (vol%)
SBM-NBV	43.950	43.875	43.902
SBM-V	43.936	43.803	43.907
TFM	44.214	43.674	43.907

The numerical results of SBM-NBV noted the least amount of the segregation as it has the smallest powder concentration difference. The numerical results of TFM noted that most of the segregation occurred at rear of the test-bar and high powder concentration close to the mould walls. The high segregation at the rear is likely due to the turbulence in the flow at the outlet where air is expected to exit the mould.

5.3.2 Powder distribution results of simulation models and thermogravimetric analysis

In Chapter 4, the experimental procedures to measure the powder volume fractions in the green bodies using thermogravimetric analysis (TGA) were presented. The test-bars had dimensions of $60 \times 12 \times 3.5$ mm and they were divided into 10 sections shown in Figure 5.35. Five TGA tests were carried out in each section to measure the residual weight after binder burnout. The remaining weight denotes the silicon nitride weight fraction in each section. In this powder distribution study, the experimental results of the test-bars were divided into 5 segments as denoted by 1 to 5 as seen in the schematic diagram. The weight fraction of silicon nitride in each section from 1 to 5 will be determined by the average weight fraction from the upper and lower sections.

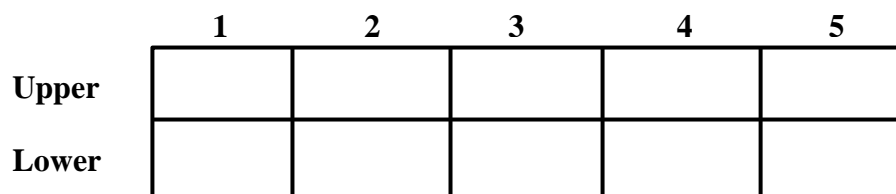


Figure 5.35. Schematic diagram for powder distribution study.

Figure 5.36 shows the experimental results from the TGA tests of five test-bars. The experimental test measured more consistent results in section 3 and 4 than other section therefore showing lower variations in results. Higher deviations are noted in section 1, 2 and 5 which suggest that segregation is more severe in these regions among the test-bars and there are less consistent volume fractions of silicon nitride in these regions from the injection moulding parameters.

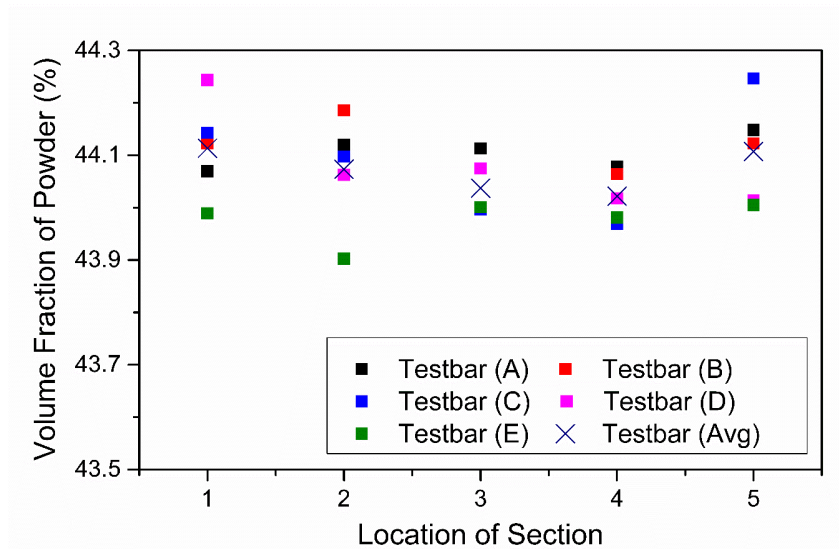


Figure 5.36. Silicon nitride powder volume fraction results from the TGA for five test-bars.

The simulation results from the numerical models are segmented and presented in the same way as the TGA experimental results shown in Figure 5.35. The numerical data for silicon nitride volume fraction was collected from 100 nodes in each section of the test-bar. The average value and the standard deviation of the numerical data were determined and plotted into graphs in comparison with the experimental results from TGA. The powder concentration results from the filling and packing stages of SBM-NBV and SBM-V were used. The TFM is a numerical simulation that only modelled the filling stage of the injection moulding process and the numerical results were in volume fractions. Therefore, the numerical results from the TFM were converted into volume percent which is the same as the results from SBM-NBV, SBM-V and TGA.

In Figure 5.37, the silicon nitride powder distribution results from the filling stage of all three models are compared. The simulation results for TFM and filling stage of SBM-NBV have almost identical volume fraction of powder in sections 1, 2 and 3 with slightly higher deviations seen in TFM. However, the volume fraction of powder from TFM starts to shift towards higher volume fractions in section 4 and 5 while the volume fraction of powder from SBM-NBV remained constant. On average silicon nitride powder distribution results of SBM-V has lower volume fraction compared to the results from TFM and SBM-NBV. The standard deviations of volume fractions of powder seen in each section can be regarded as the severity of powder-binder segregation in the sections.

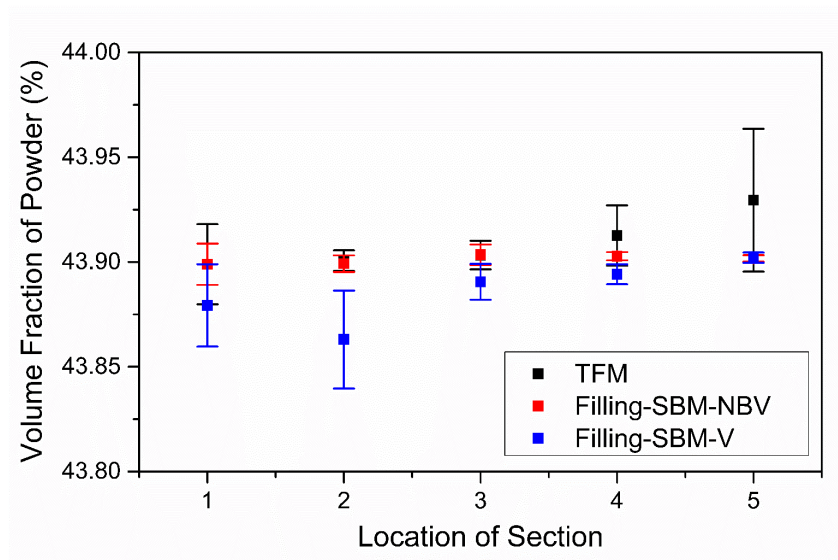


Figure 5.37. Silicon nitride powder distribution results from filling stage of SBM-NBV, SBM-V and TFM.

In Figure 5.38, the silicon nitride powder distribution results from the packing stage of SBM-NBV and SBM-V were selected and compared with results from the TFM. The numerical results from the filling stage and packing stage were from the same nodes. The packing stage of the SBMs had a holding pressure of 20.9 MPa applied to the green bodies. The holding pressure caused an increase in standard deviation of powder volume fraction in SBM-NBV (0.007 to 0.009) and in SBM-V (0.013 to 0.014). This meant that there is an increase in segregation in SBM-NBV and SBM-V from the packing stage. It is known that during the packing stage more molten feedstock is packed into the cavity to ensure that the green body is fully filled and have better shape retention when it contracts during the cooling down. Nonetheless, the segregation found in SBM-NBV remains lower than that in SBM-V. The SBM-NBV and SBM-V observed lower volume fraction of silicon nitride powder in the same nodes as compared to the numerical results from the filling stage. However, the average volume fraction of silicon nitride powder from the filling and pack stage were similar at 43.903 vol% and 43.908 vol% for SBM-NBV and SBM-V, respectively.

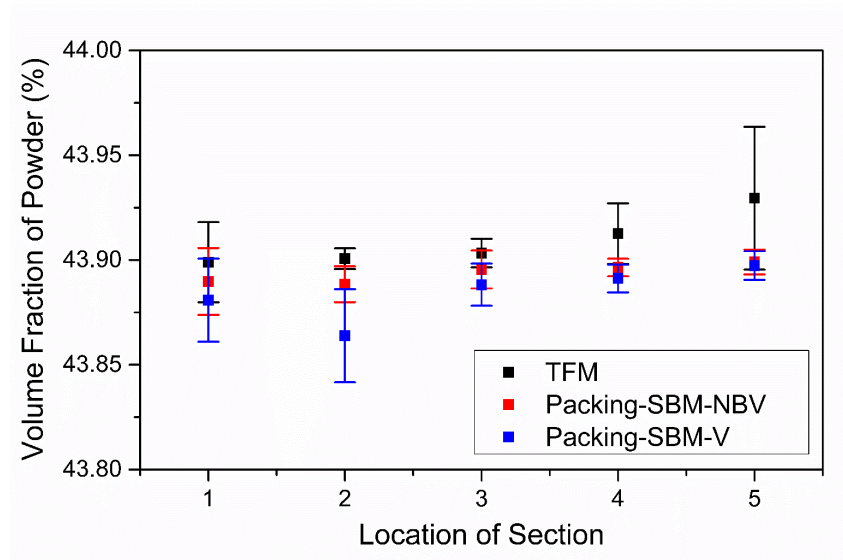


Figure 5.38. Silicon nitride powder distribution results from packing stage of SBM-NBV and SBM-V and filling stage of TFM.

Figure 5.39 shows the silicon nitride powder distribution results from the packing stage of SBM-NBV and SBM-V, filling stage of TFM and TGA experimental results. The segregation seen in the simulation models are considerably lesser when compared to the experimental results from the TGA tests. Nonetheless, both the experimental and simulation results of the powder distribution throughout the test-bar displayed higher segregations in areas close to the gate and rear of the test-bar. This is evident by the higher standard deviations observed in sections 1, 2 and 5. The input parameter for volume fraction of silicon nitride used in simulation models was measured by thermogravimetric analysis on the silicon nitride feedstock and the value was 43.9 vol%.

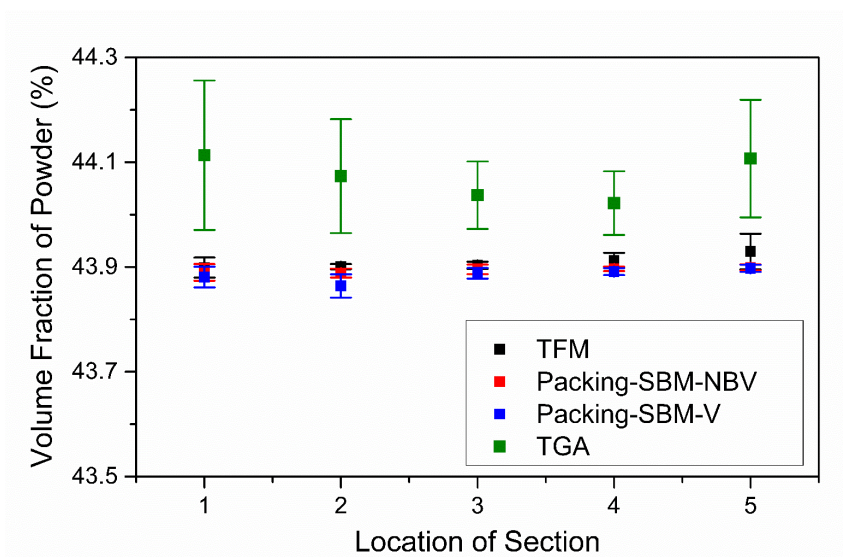


Figure 5.39. Silicon nitride powder distribution results from SBM-NBV, SBM-V, TFM and TGA.

The simulation models assumed ideal injection moulding conditions based on the input parameters used. It assumed the volume fraction of silicon nitride powder measured in the feedstock by the TGA as the input condition. However, the average volume fraction of silicon nitride powder measured in the test-bars have been shown to be higher than the volume fraction of silicon nitride powder measured in the feedstock. During an actual injection moulding process, multiple factors come into play that may affect the resultant injection moulded green bodies. Slight binder loss might have occurred when the silicon nitride feedstock was heated up in the barrel for extended periods of time during the injection moulding process. This may be the reason for high volume fractions of silicon nitride powder observed in the test-bar.

The difference in powder distribution results from SBM-NBV and SBM-V is considerably small. This is due to the fact the powder concentration results are computed at the end of the filling simulation using the velocity flow field. The difference in the thermal conductivity and elastic modulus between the material data had little influence on the powder concentration results. Nonetheless, the effects of overestimating these properties are largely observed in pressure and temperature related results. The difference in mean injection pressure was 10.9% and 5.7% for mean temperature. The difference in these results can hinder the optimising of injection moulding parameters. Therefore, it is still recommended that the estimation models used in HMB-NBV be to estimate material data for accurate numerical simulation. Using the estimation models to develop the HMD-NBV will provide the added flexibility to PIM simulation process.

5.4 Summary

In this chapter, simulation models developed to simulate powder injection moulding of silicon nitride test-bars are presented. The results from the models have been validated using the TGA experimental results. In Section 5.1, two simulation models are developed based on SBM and material data of HMD-NBV and HMD-V. Filling and packing results are used to study effects of overpredicting thermomechanical properties such as elastic modulus and thermal conductivity. In Section 5.2, a simulation model was developed based on a TFM. The TFM is developed using an empirical drag force coefficient as the interphase drag between the powder and the binder. In Section 5.3, filling patterns and powder distribution results are selected and compared between the simulation models. The numerical results show that the TFM took longer time to fill the cavity and had more segregation of powder and binder.

The TGA test results and numerical results from SBM-NBV, SBM-V and TFM showed lower volume fractions of silicon nitride powder in the middle of the test-bars and higher powder-binder segregation in the rear. The higher variations in TGA results in the gate and rear of the test-bar is an indication of the higher segregation observed in these areas. The TFM despite using a more accurate representation of powder and binder in PIM showed relative powder concentration results to the SBM-NBV and SBM-V.

Chapter 6. Conclusions and future work

6.1 Conclusions

This chapter presents the conclusions for this thesis and the recommendations for future work provided in this area of research. The aim of this research was to develop a holistic approach to study the injection moulding of ceramics using numerical models. This is achieved by developing validated numerical models to simulate the powder injection moulding process as well as providing flexibility in testing various feedstock materials and compositions. The conclusion drawn and contributions thereof are presented in the following sections, each addressing an objective of this thesis.

6.1.1 Hybrid material data of thermomechanical properties of a silicon nitride feedstock

In Chapter 3, two hybrid material data were developed based on a combination of experimental and estimated material properties. Experiments were carried out to measure the density, specific heat capacity, viscosity and particle size distribution. A comparative study was conducted on theoretical models that predict thermomechanical properties of powder-polymer mixture and experimental data found in literature. The fillers include alumina, HA, silica, SCAN and AlN while the matrixes include epoxy, PVDF, silicone rubber, ester and HDPE. The comparative study encompassed thermomechanical properties such as elastic modulus, thermal conductivity, CTE and specific volume.

Estimation models that provided the closest estimates to experimental data were selected and used in the first hybrid material data (HMD-NBV). The models selected were the Nielsen model for elastic modulus and thermal conductivity, Blackburn model for CTE and Voigt model for specific volume. The second hybrid material data (HMD-V) was developed using models used in previous studies which used mainly the Voigt model. Both hybrid material data, HMD-NBV and HMD-V, used the same experimental data for density, specific heat capacity, viscosity and particle size.

The contribution in part of the work was the development of a hybrid material data (HMD-NBV) that provided more accurate predictions for elastic modulus and thermal conductivity

based on the comparative study. The Nielsen model observed estimation ranging from 0.58 to 2.35 times the experimental data for elastic modulus and 0.57 to 3.91 times the experimental data for thermal conductivity. The Blackburn model observed estimation ranging from 0.86 to 2.47 times the experimental data for CTE. The Voigt model observed estimation ranging from 2.46 to 34.78 times the experimental data for elastic modulus, 1.44 to 99.85 times the experimental data for thermal conductivity and 1.05 to 3.18 times the experimental data for CTE. These results show that the Voigt model is unreliable at estimating elastic modulus and thermal conductivity of powder-polymer mixture. The HMD-V that uses the Voigt model to predict elastic modulus and thermal conductivity of the silicon nitride feedstock resulted in estimating elastic modulus and thermal conductivity that are 24.28 and 4.94 times of HMD-NBV. The CTE estimated from the HMD-V is only 4.79% higher than HMD-NBV. The thermomechanical properties based on HMD-NBV and HMD-V were used as material input data to simulate the injection moulding silicon nitride test-bars in Chapter 5. This allowed the effects of overpredicting thermomechanical properties to be studied from the numerical results.

6.1.2 Powder distribution analysis method to study the distribution of silicon nitride powder in silicon nitride green bodies

In Chapter 4, the DSC and TGA were developed to analyse the powder distribution in injection moulded ceramic green bodies. The work in this area have been published in Powder Technologies [83]. The DSC and TGA were used to measure the powder distribution along injection moulded silicon nitride test-bars.

Using the DSC test results, the ROM and EMP models were developed to determine the volume fractions of silicon nitride powder based on the heat of fusion measured. The ROM model considered that the heat of fusion measured from the samples are proportional to the weight fraction of binder system in the samples. The volume fraction of silicon nitride powder is then determined with the density of silicon nitride powder and binder system. The EMP model is established based on the experimental data of the binder system and silicon nitride feedstock. The volume fraction of silicon nitride powder in the test-bars are determined based on an empirical relationship using the model. The ROM predicted a volume fraction up to 52.04 vol% and a variation of 2.510 vol% while the EMP model predicted a highest volume fraction up to 46.96 vol% and a variation of 1.710 vol%. The EMP model developed in this study showed volume fractions closer to the nominal volume fraction and lower variation as compared to the ROM model.

TGA tests developed to measure the powder distribution in the silicon nitride test-bar by measuring the residual weight fraction after binder burnout along the test-bar. Volume fraction of the silicon nitride powder can be determined by the residual weight fraction and density of silicon nitride powder and binder system. The TGA measured low variations in volume fraction of silicon nitride powder in feedstock (0.240 vol%) and green bodies (0.177 vol%). The TGA results from the study showed that the TGA is suitable for quantifying the point to point powder fraction in ceramic green bodies. The TGA is also independent of the feedstock formulation as compared to the DSC methods that requires a calibration curve which is based on the heat flow data of binder components.

6.1.3 Develop numerical simulations to simulate moulding process of silicon nitride ceramics

In Chapter 5, two types of numerical models were developed to simulate the powder injection moulding of silicon nitride ceramics. In Section 5.1, the numerical models were developed based on SBM. Using the material input data from HMD-NBV and HMD-V, numerical models were developed based on SBM and implemented in Moldex3D. The CAE software was used to simulate the PIM process for filling and packing analysis. The overestimation of thermal conductivity by HMD-V observed differences in numerical results for outputs such as filling time, injection pressure, temperature distribution, viscosity and volumetric shrinkages. The elastic modulus and coefficient of thermal expansion of the feedstock only affected the thermal residual stress results. The pressure-volume-temperature data was shown to be an important material property of the feedstock as it affected the density, volumetric shrinkage, total displacement and thermal residual stress results.

In Section 5.2, a numerical model was developed based on the TFM using ANSYS-CFX to consider the interphase drag forces between particle and binder using an empirical drag coefficient from literature. The TFM focused on only filling stage of the injection moulding process to simulate the powder-binder separation phenomena. Unlike the SBM, the TFM does not predict the powder concentration in the injection moulded green body based on shear strain gradients. The TFM also considers two-phase where the silicon nitride particles are modelled as disperse fluids in a continuous fluid which is the binder system. The TFM considers a separate flow field for each phase. The TFM was able to simulate the silicon nitride particles and the relationship between shear rate, viscosity and drag coefficient parameters. The numerical model was used to study the viscosity and drag coefficient when silicon nitride particles move away from high to low shear rate gradient.

Both simulation methods were validated with the powder distribution results measured by the TGA. The TGA test results and numerical results from SBM-NBV, SBM-V and TFM showed lower volume fractions of silicon nitride powder in the middle of the test-bars and higher powder-binder segregation in the gate and rear of the test-bar. The higher segregation in the test-bar is indicated by the variations in the TGA results. Despite not simulating the powder and binder as individual phases which is considered a more accurate representation of the fluid mechanics in PIM, the SBMs showed relative powder concentration results as the TFM. HMD-NBV provides flexibility to estimate powder-based feedstock using experimental data of powder and binder. HMD-NBV was also shown to have better accuracy at estimating elastic modulus and thermal conductivity compared to HMD-V. Therefore, the SBM-NBV will be more suitable to be implemented into the holistic approach to study and develop the PIM process of ceramics.

6.2 Future work

The research work undertaken have encompassed a wide area of research and a holistic approach was developed to study the injection moulding of ceramic using numerical simulation tools which would allow future developments and improvements. However, there are still some improvements that can be made, and some interesting research topics have arisen from this research work. Indicated here are the following areas as recommended for further work.

- Future research should include full thermomechanical properties experimental data of the feedstock and each component. This will allow the hybrid material data (HMD-NBV) to be further validated or improved to provide better estimates. The PVT data have been shown to affect multiple numerical results therefore future studies will allow the observation of difference in numerical results from estimated and experimental PVT data. It would be interesting to consider other types of ceramic and metal feedstock in the injection moulding simulation. This will allow HMD-NBV to be studied at how well it estimates the thermomechanical properties of different types of feedstock material.
- A limitation of the current research is that the mean particle size is used as the function to determine the powder distribution in these numerical simulations. Future research can consider different particle sizes and particle size distributions to study the effects of particles on the estimation and accuracy of theoretical models. The effects of particle size and distribution can be observed through experimental analysis using DSC and TGA

and numerical simulations using the SBM and TFM. A narrower or wider distribution of particle size will provide more information in this area of research.

- The material input data required by commercial simulation software considers simplistic data for elastic modulus, thermal conductivity and CTE. The thermal conductivity of powder-based feedstock used in numerical models only considers temperature dependence. However, it was shown in experimental data found in literature that the thermal conductivity of polymers used in powder-based feedstock are dependent on temperature and pressure. The elastic modulus and CTE of powder-based feedstock are also shown to be dependent on temperature while numerical models only considers a single input value. Future research should include the pressure and temperature dependency for material properties such as elastic modulus, thermal conductivity and CTE in the material data. With sufficient experimental data, the HMD-NBV can be adapted to consider the pressure and temperature dependency for material properties such as elastic modulus, thermal conductivity and CTE.

References

- [1] J. Rödel *et al.*, “Development of a roadmap for advanced ceramics: 2010-2025,” *J. Eur. Ceram. Soc.*, vol. 29, no. 9, pp. 1549–1560, 2009.
- [2] O. Khasanov, E. Dvilis, V. Sokolov, and Y. Pokholkov, “Uniaxial dry pressing homogeneously dense powdered ceramic articles,” in *Proceedings - KORUS 2003: 7th Korea-Russia International Symposium on Science and Technology*, 2003.
- [3] J. Solarek, C. G. Aneziris, and H. Biermann, “A new method for manufacturing graded refractories by localized hot uniaxial pressing,” *Ceram. Int.*, 2017.
- [4] B. Zhao, H. Liu, C. Huang, J. Wang, and M. Cheng, “Fabrication and mechanical properties of Al₂O₃-SiC_w-TiC_{np} ceramic tool material,” *Ceram. Int.*, vol. 43, no. 13, pp. 10224–10230, 2017.
- [5] X. Bai, C. Huang, J. Wang, B. Zou, and H. Liu, “Fabrication and characterization of Si₃N₄ reinforced Al₂O₃-based ceramic tool materials,” *Ceram. Int.*, 2015.
- [6] D. Yao, Y. Xia, Y.-P. Zeng, K. Zuo, and D. Jiang, “Porous Si₃N₄ ceramics prepared via slip casting of Si and reaction bonded silicon nitride,” *Ceram. Int.*, 2011.
- [7] R. Ramachandra Rao and T. S. Kannan, “Slip cast nitride-bonded silicon carbide bodies,” in *Materials Chemistry and Physics*, 2002.
- [8] C. A. Gutiérrez and R. Moreno, “Tape casting of non-aqueous silicon nitride slips,” *J. Eur. Ceram. Soc.*, 2000.
- [9] M. Jabbari, R. Bulatova, A. I. Y. Tok, C. R. H. Bahl, E. Mitsoulis, and J. H. Hattel, “Ceramic tape casting: A review of current methods and trends with emphasis on rheological behaviour and flow analysis,” *Materials Science and Engineering B: Solid-State Materials for Advanced Technology*. 2016.
- [10] R. K. Nishihora, P. L. Rachadel, M. G. N. Quadri, and D. Hotza, “Manufacturing porous ceramic materials by tape casting—A review,” *Journal of the European Ceramic Society*. 2018.
- [11] H. Chen *et al.*, “Pressure filtration assisted gel casting in translucent alumina

References

- ceramics fabrication,” *Ceram. Int.*, 2018.
- [12] L. Han *et al.*, “Preparation of Si₃N₄porous ceramics via foam-gelcasting and microwave-nitridation method,” *Ceramics International*, 2018.
- [13] T. Moritz and S. Maleksaeedi, “4 - Additive manufacturing of ceramic components,” in *Additive Manufacturing*, 2018.
- [14] K. Liu *et al.*, “Laser additive manufacturing and homogeneous densification of complicated shape SiC ceramic parts,” *Ceram. Int.*, no. June, pp. 1–9, 2018.
- [15] L. Yang and H. Miyanaji, “Ceramic Additive Manufacturing: a review of current status and challenges,” in *Solid Freeform Fabrication 2017: Proceedings of the 28th Annual International*, 2017.
- [16] E. Champion, A. Magnaudeix, P. Pascaud-Mathieu, and T. Chartier, “Advanced processing techniques for customized ceramic medical devices,” in *Advances in Ceramic Biomaterials: Materials, Devices and Challenges: First Edition*, 2017.
- [17] M. J. Edirisinghe and J. R. G. Evans, “Review: Fabrication of engineering ceramics by injection moulding. I. Materials selection,” *Int. J. High Technol. Ceram.*, 1986.
- [18] M. J. Edirisinghe and J. R. G. Evans, “Review: Fabrication of engineering ceramics by injection moulding. II. Techniques,” *Int. J. High Technol. Ceram.*, 1986.
- [19] B. Hausnerova, “Powder Injection Moulding - An Alternative Processing Method for Automotive Items,” *New Trends Dev. Automot. Syst. Eng.*, 2011.
- [20] Z. Stanimirović and I. Stanimirović, “Ceramic Injection Molding,” *Some Crit. Issues Inject. Molding*, pp. 131–148, 1999.
- [21] J. Gonzlez-Gutierrez, G. Beulke, and I. Emri, “Powder Injection Molding of Metal and Ceramic Parts,” *Some Crit. Issues Inject. Molding*, 2012.
- [22] A. Lawley, “Powder Injection Molding,” *Advances in Powder Metallurgy and Particulate Materials*. 1993.
- [23] “PIM market to reach more than US\$3 billion,” *Metal Powder Report*. 2016.
- [24] G. Tosello, “Micro-injection Molding,” in *Micromanufacturing Engineering and Technology*, 2015.
- [25] L. Zema, G. Loreti, A. Melocchi, A. Maroni, and A. Gazzaniga, “Injection Molding

References

- and its application to drug delivery,” *Journal of Controlled Release*. 2012.
- [26] D. W. Richerson, “Modern Ceramic Engineering,” *Qual. Assur.*, 1992.
- [27] J. Szépvölgyi, I. Mohai, and J. Gubicza, “Atmospheric ageing of nanosized silicon nitride powders,” *J. Mater. Chem.*, 2001.
- [28] M. N. Rahaman, *Ceramic processing*. 2017.
- [29] T. Hanemann and O. Weber, “Polymethylmethacrylate/polyethyleneglycol-based partially water soluble binder system for micro ceramic injection moulding,” *Microsyst. Technol.*, vol. 20, no. 1, pp. 51–58, 2014.
- [30] R. Supati, N. H. Loh, K. A. Khor, and S. B. Tor, “Mixing and characterization of feedstock for powder injection molding,” *Mater. Lett.*, 2000.
- [31] R. M. German and A. Bose, *Injection Molding of Metals and Ceramics*. Metal Powder Industry, 1997.
- [32] K. S. Roetenberg, R. Raman, C. I. Whitman, I. F. Snider Jr., and R. M. German, “Optimization of the mixing process for powder injection molding,” in *Proceedings of the Powder Injection Molding Symposium*, 1992, pp. 119–130.
- [33] R. M. German and K. F. Hens, “Key Issues in Powder Injection Molding,” *Ceram. Bull.*, vol. 70, no. 8, pp. 1294–1302, 1991.
- [34] A. MANONUKUL *et al.*, “Study of Recycled and Virgin Compounded Metal Injection Moulded Feedstock for Stainless Steel 630,” *J. Solid Mech. Mater. Eng.*, vol. 1, no. 4, pp. 411–420, 2007.
- [35] S. Md Ani, A. Muchtar, N. Muhamad, and J. A. Ghani, “Binder removal via a two-stage debinding process for ceramic injection molding parts,” *Ceram. Int.*, 2014.
- [36] R. K. Enneti, S. J. Park, R. M. German, and S. V. Atre, “Review: Thermal debinding process in particulate materials processing,” *Materials and Manufacturing Processes*. 2012.
- [37] V. M. Kryachek, “Injection moulding (review),” *Powder Metallurgy and Metal Ceramics*. 2004.
- [38] M. R. Raza, F. Ahmad, M. A. Omar, R. M. German, and A. S. Muhsan, “Defect Analysis of 316LSS during the Powder Injection Moulding Process,” *Defect Diffus.*

References

- Forum*, vol. 329, no. July, pp. 35–43, 2012.
- [39] T. Zhang, S. Blackburn, and J. Bridgwater, “Debinding and sintering defects from particle orientation in ceramic injection moulding,” *J. Mater. Sci.*, 1996.
- [40] O. Weber, A. Rack, C. Redenbach, M. Schulz, and O. Wirjadi, “Micropowder injection molding: Investigation of powder-binder separation using synchrotron-based microtomography and 3D image analysis,” *J. Mater. Sci.*, 2011.
- [41] R. Heldele, S. Rath, L. Merz, R. Butzbach, M. Hagelstein, and J. Haußelt, “X-ray tomography of powder injection moulded micro parts using synchrotron radiation,” *Nucl. Instruments Methods Phys. Res. Sect. B Beam Interact. with Mater. Atoms*, 2006.
- [42] J. E. Zorzi, C. A. Perottoni, and J. A. H. Da Jornada, “Method for the measurement of powder distribution in green ceramic bodies,” *J. Mater. Sci. Lett.*, 2003.
- [43] T. Zhang, S. Blackburn, and J. Bridgwater, “The orientation of binders and particles during ceramic injection moulding,” *J. Eur. Ceram. Soc.*, 1997.
- [44] K. S. Hwang, *Common defects in metal injection molding (MIM)*, no. Mim. Woodhead Publishing Limited, 2012.
- [45] W. F. Zoetelief, L. F. A. Douven, and A. J. Ingen Housz, “Residual thermal stresses in injection molded products,” *Polym. Eng. Sci.*, 1996.
- [46] H. He, Y. Li, J. Lou, D. Li, and C. Liu, “Prediction of density variation in powder injection moulding-filling process by using granular modelling with interstitial power-law fluid,” *Powder Technol.*, 2016.
- [47] Z. Cheng, T. Barriere, B. Liu, and J. C. Gelin, “A vectorial algorithm with finite element method for prediction of powder segregation in metal injection molding,” *Int. J. Numer. Methods Fluids*, 2012.
- [48] T. Barriere, B. Liu, and J. C. Gelin, “Determination of the optimal process parameters in metal injection molding from experiments and numerical modeling,” in *Journal of Materials Processing Technology*, 2003.
- [49] M. R. Kamal, Y. Kuo, and P. H. Doan, “The injection molding behavior of thermoplastics in thin rectangular cavities,” *Polym. Eng. Sci.*, 1975.
- [50] B. S. Chen and W. H. Liu, “Numerical simulation of the post-filling stage in

References

- injection molding with a two-phase model,” *Polym. Eng. Sci.*, 1994.
- [51] K. H. Han and Y. T. Im, “Compressible flow analysis of filling and post-filling in injection molding with phase-change effect,” *Compos. Struct.*, 1997.
- [52] C. A. Hieber and S. F. Shen, “A finite-element/finite-difference simulation of the injection-molding filling process,” *J. Nonnewton. Fluid Mech.*, 1980.
- [53] F. Ilinca and J. F. Héту, “Three-dimensional filling and post-filling simulation of metal injection molding,” *Int. Polym. Process.*, vol. 16, no. 3, 2001.
- [54] F. Ilinca, J. F. Héту, A. Derdouri, and J. Stevenson, “Metal injection molding: 3D modeling of nonisothermal filling,” *Polym. Eng. Sci.*, 2002.
- [55] J. F. Héту, D. M. Gao, A. Garcia-Rejon, and G. Salloum, “3D finite element method for the simulation of the filling stage in injection molding,” *Polym. Eng. Sci.*, 1998.
- [56] T. S. Kwak, “A Study of Ceramic Injection Molding of Watch Case Composed of ZrO₂ Powder,” *Mater. Sci. Forum*, 2009.
- [57] S. Ahn, S. T. Chung, S. V. Atre, S. J. Park, and R. M. German, “Integrated filling, packing and cooling CAE analysis of powder injection moulding parts,” *Powder Metall.*, 2008.
- [58] S. Ahn, S. J. Park, S. Lee, S. V. Atre, and R. M. German, “Effect of powders and binders on material properties and molding parameters in iron and stainless steel powder injection molding process,” *Powder Technol.*, 2009.
- [59] H. Tseng, Y. Y.-J. Chang, C. Huang, C.-H. C. Tien, and C. C.-H. Hsu, “Prediction of powder concentration for filling simulation of metal injection molding,” *Annu. Tech. Conf. - ANTEC, Conf. Proc.*, 2014.
- [60] H. Tseng, Y. Chang, C. Hsu, and R. Chang, “Numerical Prediction of Powder Concentration for Mold Filling Simulations of Powder Injection Molding,” in *Proceedings of the Polymer Processing Society 29th Annual Meeting*, 2013.
- [61] J. F. Morris and F. Boulay, “Curvilinear flows of noncolloidal suspensions: The role of normal stresses,” *J. Rheol. (N. Y. N. Y.)*, 1999.
- [62] R. M. Miller, “Continuum Modeling of Liquid-Solid Suspensions for Nonviscometric Flows,” Georgia Institute of Technology, 2004.

References

- [63] M. Thornagel, “Simulating flow can help avoid mould mistakes,” *Met. Powder Rep.*, vol. 65, no. 3, pp. 26–29, 2010.
- [64] I. Duretek and C. Holzer, “Material flow data for numerical simulation of powder injection molding,” *J. Phys. Conf. Ser.*, vol. 790, no. 1, pp. 7–14, 2017.
- [65] R. J. Phillips, R. C. Armstrong, R. A. Brown, A. L. Graham, and J. R. Abbott, “A constitutive equation for concentrated suspensions that accounts for shear-induced particle migration,” *Phys. Fluids A*, 1992.
- [66] H. C. Tseng, R. Y. Chang, and C. H. Hsu, “Predictions of fiber concentration in injection molding simulation of fiber-reinforced composites,” *J. Thermoplast. Compos. Mater.*, no. 32, 2017.
- [67] D. Gidaspow, *Multiphase Flow and Fluidization*. 2016.
- [68] M. Ishii and K. Mishima, “Two-fluid model and hydrodynamic constitutive relations,” *Nucl. Eng. Des.*, 1984.
- [69] H. Enwald, E. Peirano, and A. E. Almstedt, “Eulerian two-phase flow theory applied to fluidization,” 1997.
- [70] Q. Wang, H. Yin, X. Qu, and J. L. Johnson, “Effects of mold dimensions on rheological of feedstock in micro powder injection molding,” *Powder Technol.*, 2009.
- [71] H. Yin, Q. Wang, X. Qu, C. Jia, and J. L. Johnson, “Computational simulation and experimental analysis of the mold-filling process in μ PIM,” *J. Micromechanics Microengineering*, 2011.
- [72] W. Fang, X. He, R. Zhang, S. Yang, and X. Qu, “The effects of filling patterns on the powder-binder separation in powder injection molding,” *Powder Technol.*, 2014.
- [73] V. V. Bilovol, “Mould filling simulations during powder injection moulding,” Delft University of Technology, 2003.
- [74] K. M. Tsai and H. J. Luo, “An inverse model for injection molding of optical lens using artificial neural network coupled with genetic algorithm,” *J. Intell. Manuf.*, 2017.
- [75] D. F. Heaney, R. Zauner, C. Binet, K. Cowan, and J. Piemme, “Variability of powder characteristics and their effect on dimensional variability of powder

- injection moulded components,” *Powder Metall.*, 2004.
- [76] W.-C. J. Wei, R.-Y. Wu, and S.-J. Ho, “Effects of pressure parameters on alumina made by powder injection moulding,” *J. Eur. Ceram. Soc.*, 2000.
- [77] Y. Li, L. Li, and K. A. Khalil, “Effect of powder loading on metal injection molding stainless steels,” *J. Mater. Process. Technol.*, 2007.
- [78] P. Pachauri and M. Hamiuddin, “Optimization of Injection Moulding Process Parameters in MIM for Impact Toughness of Sintered Parts,” *Cloud Publ. Int. J. Adv. Mater. Metall. Eng.*, 2015.
- [79] J. Lee and J. Kim, “Micro genetic algorithm based optimal gate positioning in injection molding design,” *J. Mech. Sci. Technol.*, 2007.
- [80] J. Zhao, G. Cheng, S. Ruan, and Z. Li, “Multi-objective optimization design of injection molding process parameters based on the improved efficient global optimization algorithm and non-dominated sorting-based genetic algorithm,” *Int. J. Adv. Manuf. Technol.*, vol. 78, no. 9–12, pp. 1813–1826, 2015.
- [81] C. Shen, L. Wang, and Q. Li, “Optimization of injection molding process parameters using combination of artificial neural network and genetic algorithm method,” *J. Mater. Process. Technol.*, 2007.
- [82] H. Shi, S. Xie, and X. Wang, “A warpage optimization method for injection molding using artificial neural network with parametric sampling evaluation strategy,” *Int. J. Adv. Manuf. Technol.*, 2013.
- [83] L. Poh, C. Della, S. Ying, C. Goh, and Y. Li, “Powder distribution on powder injection moulding of ceramic green compacts using thermogravimetric analysis and differential scanning calorimetry,” *Powder Technol.*, vol. 328, 2018.
- [84] R. Heldele, M. Schulz, D. Kauzlaric, J. G. Korvink, and J. Haußelt, “Micro powder injection molding: Process characterization and modeling,” in *Microsystem Technologies*, 2006.
- [85] A. Greiner *et al.*, “Simulation of micro powder injection moulding: Powder segregation and yield stress effects during form filling,” *J. Eur. Ceram. Soc.*, vol. 31, no. 14, pp. 2525–2534, Nov. 2011.
- [86] F. Ilinca, J.-F. Héту, and É. Baril, “Three-dimensional numerical modeling of

References

- segregation in powder injection molding,” in *International Conference on Powder Metallurgy & Particulate Materials (PowderMet 2009)*, 2009, vol. 1, no. 4.
- [87] F. Ilinca and J. F. Héту, “Three-dimensional numerical simulation of segregation in powder injection molding,” *Int. Polym. Process.*, vol. 23, no. 2, pp. 208–215, 2008.
- [88] M. Manninen, V. Taivassalo, and S. Kallio, “On the mixture model for multiphase flow,” *Vtt Publ.*, 1996.
- [89] P. R. Nott and J. F. Brady, “Pressure-driven flow of suspensions: Simulation and theory,” *J. Fluid Mech.*, 1994.
- [90] M. Jenni, L. Schimmer, R. Zauner, J. Stampfl, and J. Morris, “Quantitative Study of Powder Binder Separation of Feedstocks,” *PIM Int.*, vol. 2, no. 4, pp. 50–55, 2008.
- [91] H. Tseng, “The accurate prediction of surface defects with Powder Injection Moulding simulation,” no. May 2015, 2017.
- [92] M. Jenni, R. Zauner, J. Stampfl, and J. Morris, “Quantitative Study of Process and Material Parameters on Flow Behavior and Powder Binder Separation of Feedstocks: Experimental Design 3D Simulation Model and Balance Model for Separation in Suspensions,” in *World Congress on Powder Metallurgy & particulate Materials*, 2008, no. 1, pp. 169 – 178.
- [93] K. H. Kate, V. P. Onbattuvelli, R. K. Enneti, S. W. Lee, S. J. Park, and S. V. Atre, “Measurements of powder-polymer mixture properties and their use in powder injection molding simulations for aluminum nitride,” *JOM*, 2012.
- [94] D. F. Heaney, “Powders for metal injection molding (MIM),” *Handb. Met. Inject. Molding*, pp. 50–63, Jan. 2012.
- [95] J. Xu and L.-S. (Tom) Turng, *Microcellular injection molding*. Wiley, 2013.
- [96] Z. Y. Liu, N. H. Loh, S. B. Tor, and K. A. Khor, “Characterization of powder injection molding feedstock,” *Mater. Charact.*, 2003.
- [97] K. H. Kate, R. K. Enneti, and S. V. Atre, “Influence of feedstock properties on the injection molding of aluminum nitride,” *Int. J. Adv. Manuf. Technol.*, vol. 90, no. 9–12, pp. 2813–2826, 2017.
- [98] D. F. Heaney, *Handbook of Metal Injection Molding*. 2012.

References

- [99] S. Gaisford, V. Kett, and P. J. (Peter J. . Haines, *Principles of Thermal Analysis and Calorimetry*. 2002.
- [100] J. Wang, “PVT Properties of Polymers for Injection Molding, Some Critical Issues for Injection Molding,” *InTech*, 2012.
- [101] A. Eitzlmayr *et al.*, “Experimental characterization and modeling of twin-screw extruder elements for pharmaceutical hot melt extrusion,” *AIChE J.*, 2013.
- [102] X. Qu, J. Gao, M. Qin, and C. Lei, “Application of a wax-based binder in PIM of WC–TiC–Co cemented carbides,” *Int. J. Refract. Met. Hard Mater.*, vol. 23, no. 4–6, pp. 273–277, Jul. 2005.
- [103] V. Demers, S. Turenne, and O. Scalzo, “Segregation measurement of powder injection molding feedstock using thermogravimetric analysis, pycnometer density and differential scanning calorimetry techniques,” *Adv. Powder Technol.*, 2015.
- [104] L. Kowalski and J. Duszczuk, “Specific heat of metal powder-polymer feedstock for powder injection molding,” *J. Mater. Sci. Lett.*, vol. 18, no. 17, pp. 1417–1420, 1999.
- [105] L. Bergström, “Shear thinning and shear thickening of concentrated ceramic suspensions,” *Colloids Surfaces A Physicochem. Eng. Asp.*, 1998.
- [106] B. Hausnerova, L. Marcanikova, P. Filip, and P. Saha, “Rheological characterization of powder injection moulding using feedstock based on aluminium oxide and multicomponent water-soluble polymer binder,” *Recent Adv. Fluid Mech. Heat Mass Transf. - Proc. 9th IASME / WSEAS Int. Conf. Fluid Mech. Aerodyn. FMA’11, Proc. 9th IASME / WSEAS Int. Conf. HTE’11*, 2011.
- [107] J. Koszkuł and J. Nabialek, “Viscosity models in simulation of the filling stage of the injection molding process,” *J. Mater. Process. Technol.*, vol. 157–158, pp. 183–187, Dec. 2004.
- [108] P. Guerrier, G. Tosello, and J. H. Hattel, “Flow visualization and simulation of the filling process during injection molding,” *CIRP J. Manuf. Sci. Technol.*, 2017.
- [109] Z. S. Zheng and X. H. Qu, “Numerical simulation of powder injection moulding filling process for intricate parts,” *Powder Metall.*, vol. 49, no. 2, pp. 167–172, 2006.

References

- [110] T. Osswald, N. Rudolph, T. Osswald, and N. Rudolph, “Generalized Newtonian Fluid (GNF) Models,” *Polym. Rheol.*, pp. 59–99, Jan. 2015.
- [111] M. M. Cross, “Rheology of non-Newtonian fluids: A new flow equation for pseudoplastic systems,” *J. Colloid Sci.*, vol. 20, no. 5, pp. 417–437, Jun. 1965.
- [112] F. E. Weir, “Moldability of plastics based on melt rheology. Part 1-theoretical development,” *Polym. Eng. Sci.*, 1963.
- [113] G. Aggarwal, S. J. Park, and I. Smid, “Development of niobium powder injection molding: Part I. Feedstock and injection molding,” *Int. J. Refract. Met. Hard Mater.*, 2006.
- [114] A. Romero and G. Herranz, “Development of feedstocks based on steel matrix composites for metal injection moulding,” *Powder Technol.*, 2017.
- [115] J. P. Choi, J. S. Park, E. J. Hong, W. S. Lee, and J. S. Lee, “Analysis of the rheological behavior of Fe trimodal micro-nano powder feedstock in micro powder injection molding,” *Powder Technol.*, vol. 319, pp. 253–260, 2017.
- [116] J. Rajabi, N. Muhamad, and A. B. Sulong, “Effect of nano-sized powders on powder injection molding: A review,” *Microsystem Technologies*. 2012.
- [117] K. H. Kim, H. C. Youn, C. J. Choi, and B. T. Lee, “Fabrication and material properties of powder injection molded Fe sintered bodies using nano Fe powder,” *Mater. Lett.*, 2007.
- [118] S. J. Son, Y. S. Cho, and C. J. Choi, “Advanced micromanufacturing for high-precision micro bearing by nanopowder metallurgy and LIGA processing,” in *Reviews on Advanced Materials Science*, 2011.
- [119] G. Shu and K. Hwang, “High Density Powder Injection Molded Compacts Prepared from a Feedstock Containing Coarse Powders,” *Society*, vol. 45, no. 10, pp. 2999–3004, 2004.
- [120] J. M. Torralba, J. Hidalgo, and A. J. Morales, “Powder injection moulding: processing of small parts of complex shape,” *Int. J. Microstruct. Mater. Prop.*, 2013.
- [121] M. Trunec and J. Hrazdera, “Effect of ceramic nanopowders on rheology of thermoplastic suspensions,” *Ceram. Int.*, vol. 31, no. 6, pp. 845–849, Jan. 2005.
- [122] J. W. Oh, W. S. Lee, and S. J. Park, “Investigation and modeling of binder removal

References

- process in nano/micro bimodal powder injection molding,” *Int. J. Adv. Manuf. Technol.*, 2018.
- [123] H. K. Lin and K. S. Hwang, “In situ dimensional changes of powder injection-molded compacts during solvent debinding,” *Acta Mater.*, 1998.
- [124] J. W. Oh, R. Bollina, W. S. Lee, and S. J. Park, “Effect of nanopowder ratio in bimodal powder mixture on powder injection molding,” *Powder Technol.*, 2016.
- [125] M. Müller and W. Bauer, “Low-Pressure Injection Molding of Ceramic Micro Devices Using Sub-Micron and Nano Scaled Powders,” *4M Conf.*, no. C, pp. 203–206, 2005.
- [126] R. K. Enneti *et al.*, “Critical issues in manufacturing dental brackets by powder injection molding,” *Int. J. Powder Metall.*, 2012.
- [127] D. E. Niesz, “A review of ceramic powder compaction,” *KONA Powder and Particle Journal*. 1996.
- [128] T. Kikuchi, T. Takahashi, and K. Koyama, “Temperature and Pressure Dependence of Thermal Conductivity Measurements of High Density Polyethylene and Low Density Polyethylene,” *KOBUNSHI RONBUNSHU*, vol. 60, no. 7, pp. 347–353, 2003.
- [129] P. Andersson, G. Bäckström, and G. Backstrom, “Pressure dependence of the thermal conductivity, thermal diffusivity, and specific heat of polyethylene,” *J. Appl. Phys. Rev. Sci. Instruments MPa J. Phys. Chem. Ref. Data J. Appl. Phys.*, vol. 44, no. 44, pp. 2601–1545, 1973.
- [130] A. Dawson, M. Rides, and J. Nottay, “The effect of pressure on the thermal conductivity of polymer melts,” *Polym. Test.*, 2006.
- [131] T. Kikuchi, T. Takahashi, and K. Koyama, “Temperature and Pressure Dependence of Thermal Conductivity Measurement of Polystyrene and Polycarbonate,” *J. Macromol. Sci. Part B*, vol. 42, no. 5, pp. 1097–1110, 2003.
- [132] R. Simha, P. S. Wilson, and O. Olabisi, “Pressure-volume-temperature properties of amorphous polymers: empirical and theoretical predictions,” *Kolloid-Zeitschrift Zeitschrift für Polym.*, vol. 251, no. 6, pp. 402–408, 1973.
- [133] A. Quach and R. Simha, “Pressure-volume-temperature properties and transitions of

References

- amorphous polymers; polystyrene and poly (orthomethylstyrene),” *J. Appl. Phys.*, 1971.
- [134] K. H. Kate, R. K. Enneti, S. J. Park, R. M. German, and S. V. Atre, “Predicting powder-polymer mixture properties for PIM design,” *Critical Reviews in Solid State and Materials Sciences*. 2014.
- [135] K. H. Kate, R. K. Enneti, V. P. Onbattuvelli, and S. V. Atre, “Feedstock properties and injection molding simulations of bimodal mixtures of nanoscale and microscale aluminum nitride,” *Ceram. Int.*, 2013.
- [136] W. Voigt, “Über die Beziehung zwischen den beiden Elastizitätskonstanten isotroper Körper,” *Ann. Phys.*, vol. 274, no. 12, pp. 573–587, 1889.
- [137] K. H. Kate, “Material Properties in Ceramic Injection Molding Design,” Oregon State University, 2015.
- [138] B. P. Bandiwadekar, “Material properties design using simulations and experiments for powder injection molding of lead zirconate titanate,” University of Louisville, 2017.
- [139] C. J. Hwang and T. H. Kwon, “A full 3D finite element analysis of the powder injection molding filling process including slip phenomena,” *Polym. Eng. Sci.*, 2002.
- [140] T. Barrière, J. C. Gelin, and B. Liu, “Improving mould design and injection parameters in metal injection moulding by accurate 3D finite element simulation,” in *Journal of Materials Processing Technology*, 2002.
- [141] M. R. Kamal, A. I. Isayev, and S.-J. Liu, *Injection molding : technology and fundamentals*. 2009.
- [142] V. V. Bilovol, L. Kowalski, J. Duszczyk, and L. Katgerman, “Comparison of numerical codes for simulation of powder injection moulding,” *Powder Metall.*, vol. 46, no. 1, pp. 55–60, Apr. 2003.
- [143] P. Dvorak, T. Barriere, and J. C. Gelin, “Direct observation of mould cavity filling in ceramic injection moulding,” *J. Eur. Ceram. Soc.*, 2008.
- [144] P. Petera, “Holding pressure and its influence on quality in PIM technology,” *Acta Polytech.*, 2012.
- [145] D. H. Phillips and J. J. Lannutti, “Measuring physical density with X-ray computed

References

- tomography,” *NDT E Int.*, 1997.
- [146] S. Yang, R. Zhang, and X. Qu, “X-ray tomographic analysis of powder-binder separation in SiC green body,” *J. Eur. Ceram. Soc.*, 2013.
- [147] S. Yang, R. Zhang, and X. Qu, “X-ray analysis of powder-binder separation during SiC injection process in L-shaped mould,” *J. Eur. Ceram. Soc.*, 2015.
- [148] E. N. Landis and D. T. Keane, “X-ray microtomography,” *Materials Characterization*. 2010.
- [149] M. Seerane, “Exploring Micro-focus X-ray computed tomography for metal injection moulded green parts,” in *IOP Conference Series: Materials Science and Engineering*, 2018.
- [150] C.F.Buynaka and R.H.Bossi, “Applied X-ray computed tomography,” *Nucl. Instruments Methods Phys. Res. Sect. B Beam Interact. with Mater. Atoms*, no. 94, pp. 0–2, 1995.
- [151] S. R. Reid and G. Zhou, *Impact behaviour of fibre-reinforced composite materials and structures*. 2011.
- [152] J. Rosc, V. M. F. Hammer, and R. Brunner, “X-ray computed tomography for fast and non-destructive multiple pearl inspection,” *Case Stud. Nondestruct. Test. Eval.*, 2016.
- [153] M. Jenni, R. Zauner, and J. Stampfl, “Measurement Methods for Powder Binder Separation in PIM,” in *Euro PM2009 Proceedings*, 2009.
- [154] V. Demers, F. Fareh, S. Turenne, N. R. Demarquette, and O. Scalzo, “Experimental study on moldability and segregation of Inconel 718 feedstocks used in low-pressure powder injection molding,” *Adv. Powder Technol.*, 2018.
- [155] G. Aggarwal, I. Smid, S. J. Park, and R. M. German, “Development of niobium powder injection molding. Part II: Debinding and sintering,” *Int. J. Refract. Met. Hard Mater.*, 2007.
- [156] D. A. Ditmars, S. Ishihara, S. S. Chang, G. Bernstein, and E. D. West, “Enthalpy and Heat-Capacity Standard Reference Material: Synthetic Sapphire (Alpha-Al₂O₃) From 10 to 2250 K,” *J. Res. Natl. Bur. Stand. (1934)*, 2012.
- [157] L. Thomas, “Modulated DSC® Paper# 9 Measurement of Accurate Heat Capacity

References

- Values,” *TA Instruments, New Castle*, pp. 1–11, 2005.
- [158] D. Jamieson, *Properties of binary liquid mixtures : heat capacity*. Glasgow: National Engineering Laboratory, 1978.
- [159] A. S. Teja, “Simple Method for the Calculation of Heat Capacities of Liquid Mixtures,” *J. Chem. Eng. Data*, 1983.
- [160] J. J. Swab, A. A. Wereszczak, J. Tice, R. Caspe, R. H. Kraft, and J. W. Adams, “Mechanical and Thermal Properties of Advanced Ceramics for Gun Barrel Applications,” *Mater. Res.*, 2005.
- [161] A. Einstein, “Eine neue Bestimmung der Moleküldimensionen,” *Ann. Phys.*, 1906.
- [162] A. Einstein, “Berichtigung zu meiner Arbeit: Eine neue Bestimmung der Moleküldimensionen,” *Ann. Phys.*, 1911.
- [163] M. Mooney, “The viscosity of a concentrated suspension of spherical particles,” *J. Colloid Sci.*, 1951.
- [164] I. M. Krieger and T. J. Dougherty, “A Mechanism for Non-Newtonian Flow in Suspensions of Rigid Spheres,” *Trans. Soc. Rheol.*, 1959.
- [165] J. Gonzalez-Gutierrez *et al.*, “Models to Predict the Viscosity of Metal Injection Molding Feedstock Materials as Function of Their Formulation,” *Metals (Basel)*, 2016.
- [166] J. C. A. Weiss and R. D. Moser, “Sample Preparation of Nano-sized Inorganic Materials for Scanning Electron Microscopy or Transmission Electron Microscopy: Scientific Operating Procedure SOP-P-2.” 2015.
- [167] A. Reuss, “Berechnung der Fließgrenze von Mischkristallen auf Grund der Plastizitätsbedingung für Einkristalle .,” *ZAMM - J. Appl. Math. Mech. / Zeitschrift für Angew. Math. und Mech.*, 1929.
- [168] S. Y. Fu, X. Q. Feng, B. Lauke, and Y. W. Mai, “Effects of particle size, particle/matrix interface adhesion and particle loading on mechanical properties of particulate-polymer composites,” *Compos. Part B Eng.*, vol. 39, no. 6, pp. 933–961, 2008.
- [169] E. Guth, “Theory of filler reinforcement,” *J. Appl. Phys.*, 1945.

References

- [170] E. H. Kerner, "The elastic and Thermo-elastic properties of composite media," *Proc. Phys. Soc. Sect. B*, 1956.
- [171] L. E. Nielsen, "Generalized equation for the elastic moduli of composite materials," *J. Appl. Phys.*, 1970.
- [172] T. B. Lewis and L. E. Nielsen, "Dynamic mechanical properties of particulate-filled composites," *J. Appl. Polym. Sci.*, 1970.
- [173] L. E. Nielsen, "Morphology and the elastic modulus of block polymers and polyblends," *Rheol. Acta*, 1974.
- [174] L. E. Nielsen, "Thermal conductivity of particulate-filled polymers," *Journal of Applied Polymer Science*. 1973.
- [175] M. Wang, C. Berry, M. Braden, and W. Bonfield, "Young's and shear moduli of ceramic particle filled polyethylene," *J. Mater. Sci. Mater. Med.*, 1998.
- [176] T. J. Wooster, S. Abrol, J. M. Hey, and D. R. MacFarlane, "Thermal, mechanical, and conductivity properties of cyanate ester composites," *Compos. Part A Appl. Sci. Manuf.*, 2004.
- [177] C. P. Wong and R. S. Bollampally, "Thermal conductivity, elastic modulus, and coefficient of thermal expansion of polymer composites filled with ceramic particles for electronic packaging," *J. Appl. Polym. Sci.*, 1999.
- [178] R. Hill, "The elastic behaviour of a crystalline aggregate," *Proc. Phys. Soc. Sect. A*, 1952.
- [179] L. E. Nielsen, "The Thermal and Electrical Conductivity of Two-Phase Systems," *Ind. Eng. Chem. Fundam.*, 1974.
- [180] K. Lichtenecker, "Die dielektrizitätskonstante natürlicher und künstlicher mischkörper," *Phys. Z*, 1926.
- [181] M. James Clerk, *A treatise on electricity and magnetism*. 2010.
- [182] Y. Xu, D. D. L. Chung, and C. Mroz, "Thermally conducting aluminum nitride polymer-matrix composites," *Compos. - Part A Appl. Sci. Manuf.*, 2001.
- [183] A. Shimamura, Y. Hotta, H. Hyuga, N. Kondo, and K. Hirao, "Effect of amounts and types of silicon nitride on thermal conductivity of Si₃N₄/epoxy resin

References

- composite,” pp. 3–7, 2015.
- [184] W. Zhou, C. Wang, Q. An, and H. Ou, “Thermal properties of heat conductive silicone rubber filled with hybrid fillers,” *J. Compos. Mater.*, 2008.
- [185] P. S. Turner, “Thermal-expansion stresses in reinforced plastics,” *J. Res. Natl. Bur. Stand. (1934)*, 1946.
- [186] L. Holliday and J. Robinson, “Review: The thermal expansion of composites based on polymers,” *J. Mater. Sci.*, vol. 8, no. 3, pp. 301–311, 1973.
- [187] I. Sevostianov, “On the thermal expansion of composite materials and cross-property connection between thermal expansion and thermal conductivity,” *Mech. Mater.*, 2012.
- [188] A. Boudenne, L. Ibos, M. Fois, E. Gehin, and J. C. Majeste, “Thermophysical properties of polypropylene/aluminum composites,” *J. Polym. Sci. Part B Polym. Phys.*, vol. 42, no. 4, pp. 722–732, 2004.
- [189] F. Cardarelli, “Ceramics, Refractories, and Glasses,” in *Materials Handbook*, London: Springer, 2018.
- [190] W. Callister and D. Rethwisch, *Materials science and engineering: an introduction*. 2007.
- [191] P. Zoller and D. J. Walsh, “Standard pressure-volume-temperature data for polymers,” *IEEE Electr. Insul. Mag.*, 1996.
- [192] N. S. Cheng, “Comparison of formulas for drag coefficient and settling velocity of spherical particles,” *Powder Technol.*, 2009.
- [193] R. Chang and W. Yang, “Numerical simulation of mold filling in injection molding using a three-dimensional finite volume approach,” *Int. J. Numer. Methods Fluids*, 2001.
- [194] R. B. Bird, R. C. Armstrong, and O. Hassager, *Dynamics of polymeric liquids. Vol. 1, 2nd Ed. : Fluid mechanics*. 1987.
- [195] F. Boyer, O. Pouliquen, and É. Guazzelli, “Dense suspensions in rotating-rod flows: Normal stresses and particle migration,” *J. Fluid Mech.*, 2011.
- [196] J. F. Richardson and W. N. Zaki, “Sedimentation and fluidisation: Part I,” *Chem.*

References

Eng. Res. Des., 1997.

- [197] R. E. Hampton, A. A. Mammoli, A. L. Graham, N. Tetlow, and S. A. Altobelli, “Migration of particles undergoing pressure-driven flow in a circular conduit,” *J. Rheol. (N. Y. N. Y.)*, 1997.
- [198] A. Walale, A. Singh Chauhan, A. Satyanarayana, G. Venkatachalam, and R. Pradyumna, “Analysis of shrinkage & warpage in ceramic injection molding of HPT vane leading edge core of a gas turbine casting,” *Mater. Today Proc.*, vol. 5, no. 9, pp. 19471–19479, 2018.
- [199] P. Thakre, A. S. Chauhan, A. Satyanarayana, E. Raj Kumar, and R. Pradyumna, “Estimation of shrinkage & distortion in wax injection using moldex3D simulation,” *Mater. Today Proc.*, vol. 5, no. 9, pp. 19410–19417, 2018.